Doctorate Dissertation
博士論文

Stellar Inclinations from Asteroseismology and their Implications for Spin-Orbit Angles in Exoplanetary Systems

(星震学を応用した恒星の自転傾斜角測定と
太陽系外惑星系のスピン軌道傾斜角に与える示唆)

A Dissertation Submitted for Degree of Doctor of Philosophy
December 2018

平成30年12月　博士（理学）申請

Department of Physics, Graduate School of Science,
The University of Tokyo

東京大学大学院理学系研究科物理学専攻

Shoya Kamiaka

上赤　翔也

Abstract

A fraction of observed exoplanets are known to be in significantly oblique orbits with respect to the equatorial planes of their host stars unlike our solar system. Such a misalignment between the stellar spin and planetary orbital axes is characterized by the spin-orbit angle ψ. While the origin of the misalignment cannot be understood in the framework of the conventional planet formation theory, several scenarios have been proposed in which large misalignment results from the dynamical evolution of planetary orbits, the tilt of host stars, or the tilt of protoplanetary disks. Because different mechanisms predict different distributions of spin-orbit angles, measuring ψ is the key to understand the planet formation/migration history. However, the value of ψ has been measured mainly for planets larger than Neptune (e.g., hot Jupiters) because of the observational limitations.

Asteroseismology, the study of stellar pulsations, is now considered as a useful tool to characterize stars, thanks to successful space missions including CoRoT and *Kepler*. Asteroseismology also contributes to the understanding of exoplanetary systems because it provides precise measurements of stellar parameters such as mass, radius, and age. It also measures the inclination of stellar spin axis ($i_\star$) towards the observer, making possible to infer the orbital architecture of exoplanets. Because stellar pulsation signals are independent of the properties of planets, asteroseismology can potentially explore the orbital dynamics of small planets as well as giant planets. Besides, asteroseismology offers an independent measure of stellar rotational period ($P_{\rm rot}$).

In this thesis, we systematically analyze stellar inclinations and rotational periods with asteroseismology for 33 *Kepler* planet-host stars with detectable pulsations. This is the largest asteroseismic catalogue of stellar inclinations and rotation periods ever for planet-host stars. In addition, we analyze 61 *Kepler* stars without known planetary companions for a reference sample. With these 94 stars, we investigate the possible constraints on the stellar inclinations and therefore spin-orbit angles for planet-host stars.

First, we derive the analytic criteria for reliable determination of stellar inclination and rotation. These criteria are then verified to work well in the actual asteroseismic analysis by performing intensive numerical simulations. Applying these criteria to the sample above leaves 9 and 22 reliable stars with and without planets, respectively. This is the first systematic study of reliability of parameters derived with asteroseismology.

Among 9 reliable planet-hosts analyzed in this work, Kepler-408 is the unique star whose planetary orbit is estimated to be misaligned with more than 2σ significance. In addition, asteroseismic rotation period is found to be consistent with that derived from photometric

variation, indicating that this misalignment is quite robust. Kepler-408 has an Earth-sized planet, for which the conventional Rossiter-McLaughlin method is not feasible to prove the misalignment. Consequently, this is the first discovery of significant spin-orbit misalignment for a planet smaller than Neptune. This finding indicates that misalignment-generating processes should work also for small planets.

Because rotation periods derived from photometric variation ($P_{\rm rot,photo}$) are known to be occasionally uncertain, independent validation with asteroseismology ($P_{\rm rot,astero}$) is essential. We find 13 stars among 33 planet-hosts above show consistent periods between asteroseismology and photometry ($P_{\rm rot,astero} \approx P_{\rm rot,photo}$). Therefore rotational periods are considered to be measured accurately for these 13 stars. We also discover an interesting regularity between stellar rotational period $P_{\rm rot}$ and orbital period of their planetary companions $P_{\rm orb}$ in some of 13 systems. In fact it turns out that their values of $P_{\rm orb}/P_{\rm rot}$ are not randomly distributed, but preferentially take rational numbers. Similar regularities have been reported among orbital periods of planets, indicating that they are in orbital resonances. In this work, we report the first observational signatures of the resonance between stellar rotations and planetary orbits. This result is unlikely explained in terms of the conventional model of star-planet tidal interaction, implying that more effective interaction may be at play in the actual star-planet systems.

These discoveries revealed new aspects of exoplanetary systems with asteroseismology, which may be difficult to be accomplished by other observations. In fact, asteroseismology makes possible quite robust characterizations of exoplanetary systems when combined with photometry and spectroscopy as we demonstrate in this work. Our work offers many possibilities for asteroseismology to play a useful and unique role in unveiling the nature of exoplanetary systems.

Contents

Chapter 1

Introduction

The last two decades since the first detection of an extrasolar planet (hereafter, exoplanet) around a solar-like star by Mayor & Queloz (1995) were particularly dramatic among the long history of astronomy from the prehistoric era of human beings. This is because the exoplanetary worlds revealed by subsequent studies until today are found to be completely different from what we had imagined from the analogy of our solar system. Since the planet formation and evolution theory was originally established to account for the current architecture of our solar system, the unexpected properties of observed exoplanets drastically altered our perspective on the planetary science. Based on the recent observations suggesting that our solar system might not be *a typical* planetary system in the universe, the standard model of planet formation (known as the Kyoto model or Hayashi model; Hayashi et al. 1985) now needs to be extended so that it can reconcile the observed diversity of exoplanets.

Since the first detection, a significant number of exoplanets have been discovered, approaching 4,000 in total. Figure 1.1 illustrates the cumulative number of exoplanets detected until today, with different colors for different detection methods. Among them, the transit method (green bar) is one of the most successful methods (e.g., Winn 2010). The planet passing the front of the central star produces periodical light reduction in the observed stellar flux, which is known as "transit" event (Brown et al. 2001, Winn et al. 2010a). This method allows us to obtain the period of planetary orbital motion, and the size of the planet by the amplitude of light reduction.

Planetary transits have been surveyed mostly by space instruments, including CoRoT (Convection, Rotation and planetary Transits; Baglin et al. 2006a,b) and *Kepler* (Borucki et al. 2010). The continuous and uninterrupted photometry performed by these space satellites led to the detection of thousands of exoplanets, including small planets (down to sub-Earth size). Indeed CoRoT and *Kepler* made possible the careful characterization of each exoplanet by combining other observations such as spectroscopy (e.g., High Accuracy Radial Velocity Planet Searcher; HARPS; Mayor et al. 2003) and astrometry (e.g., GAIA; Berger et al. 2018).

Figure 1.2 describes the radius distribution of the observed exoplanets as a function of orbital semi-major axis. It is important to note that a significant number of Jupiter-sized planets (gas-giants) are found in the orbits smaller than 0.1 au (top left region in the panel).

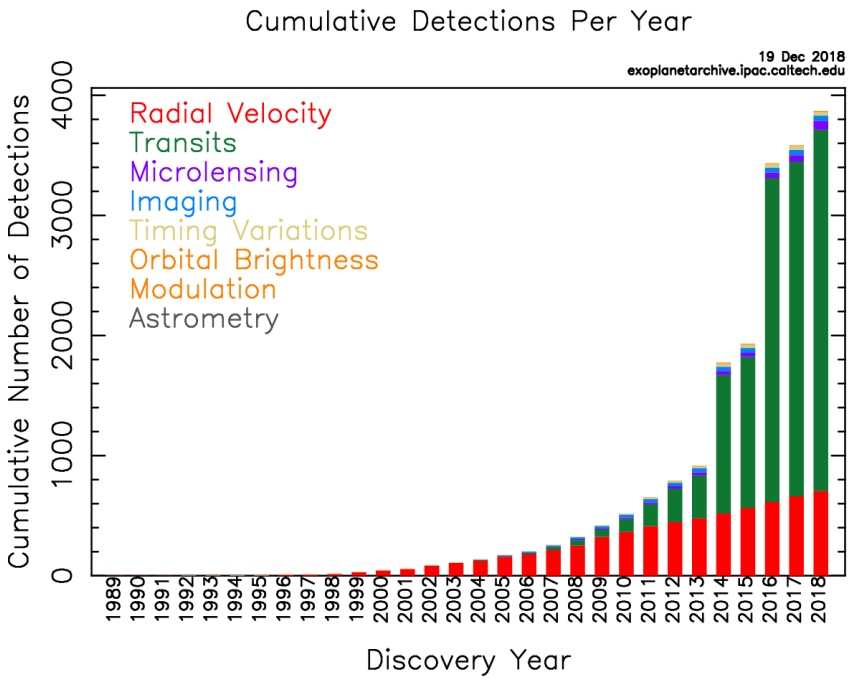

Figure 1.1: Cumulative number of exoplanets discovered per year. Different colors correspond to different detection methods. Figure is taken from NASA Exoplanet Archive; `http://exoplanetarchive.ipac.caltech.edu/index.html`.

In fact the first discovered exoplanet, 51 Pegasi b, is found to revolve around a G dwarf similar to the Sun, but has substantially large mass ($> 0.472\,M_{\rm Jupiter}$) compared to its short orbital period (in 4.2-day orbit, much inside than Mercury's orbit in the solar system). Nowadays more than 100 gas-giants in short orbits have been discovered, and then they are often referred to as "hot Jupiters". We also find from Figure 1.2 that the majority of detected exoplanets are Earth-sized planets (planets with $R_{\rm p} \lesssim 4\,R_{\rm Earth}$), and then they are often referred to as "super Earths" (Winn & Fabrycky 2015 and references therein).

In addition to the radius and orbital semi-major axis distribution, recent observations revealed the diversity in their orbital dynamics around central stars (Howard 2013, Winn & Fabrycky 2015). In the solar system, all the 8 planets are orbiting in a plane almost perpendicular to the solar spin axis, within the range of $\approx 7°$. On the contrary, non-negligible number of exoplanets are found to have highly oblique orbits compared to the spin axes of their host stars (Winn et al. 2011). Surprisingly, some of them have polar (Johnson et al. 2011), or even retrograde orbits (Narita et al. 2009, Winn et al. 2009, Anderson et al. 2010, and Albrecht et al. 2012). The discovery of oblique orbits seriously challenges the conventional planet formation and evolution theory, because it predicts that planets will be born to orbit within the stellar equatorial plane as planets do in our solar system. Recently some promising models of planetary formation and evolution have been proposed to reconcile the observed diversity of planetary orbits. Therefore observational constraints on the obliquity of planetary orbit are the key to obtain the unified picture of the formation and evolution history of

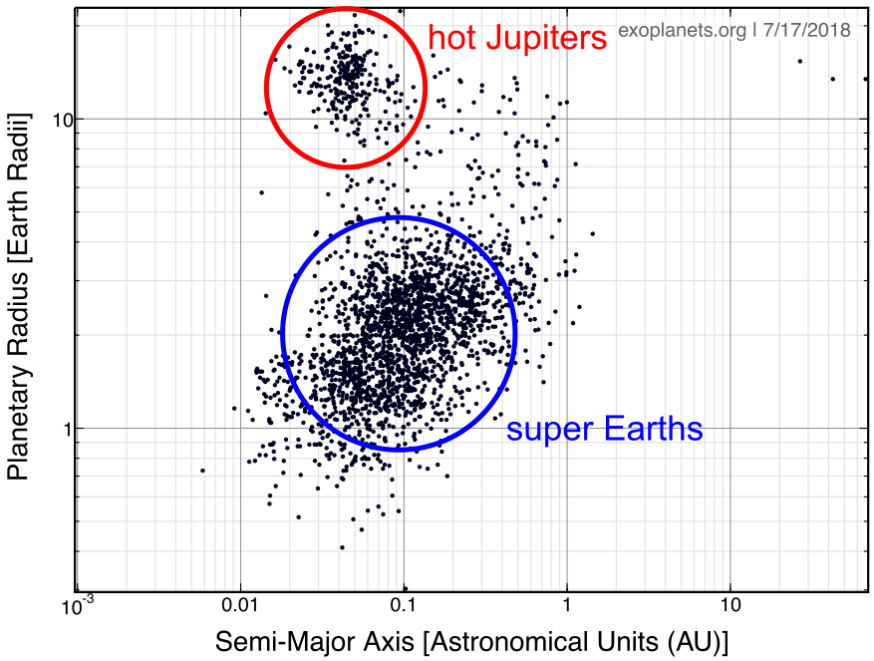

Figure 1.2: Planetary radius distribution as a function of orbital semi-major axis of observed exoplanets. Figures are taken from Exoplanet Orbit Database - Exoplanet Data Explorer; `http://exoplanets.org/`.

planetary systems.

Although the primary missions of CoRoT and *Kepler* are planet hunting, they also enabled the science that studies the pulsations of stars, which is known as "asteroseismology" (Chaplin et al. 2011, Chaplin & Miglio 2013, Huber 2016). Asteroseismology is the frequency analysis of stellar lightcurves with high precision, and makes possible precise and accurate determination of stellar properties such as mass and radius. Therefore asteroseismology greatly contributes to characterize exoplanets by means of better understanding of planet-host stars. However, the synergy between planetary science and asteroseismology has not been dedicated intensively. Then the work bridging exoplanets and asteroseismology is now highly demanded to put our knowledge on planetary science forward.

Asteroseismology has the same theoretical background as helioseismology, the frequency analysis of the Sun (Harvey 1985). The Sun is known for its acoustic "5-minute oscillation", corresponding to the dynamical timescale for the sound waves to travel across solar interior. Helioseismology accelerated our understanding on the Sun with both ground and space-based observatory in last several decades. In the same way, the stars with similar mass to the Sun ("solar-like stars") are expected to show the acoustic oscillation. Thanks to its well-developed theoretical background of acoustic pulsation of stars, asteroseismology is now widely used to characterize solar-like stars (Huber 2016). In this thesis, we focus especially on the ability of asteroseismology to measure the direction of stellar spin axis. By applying asteroseismology to planet-host stars, we can examine orbital dynamics of exoplanetary systems.

This thesis is organized as follows.

- In chapter 2, we define the spin-orbit angle in exoplanetary systems, describe its implication for planetary formation and evolution theory, and summarize current results from observations.

- Chapter 3 introduces basics of asteroseismology, mainly focusing on its potential to determine the stellar inclinations from stellar pulsation signals.

- Chapter 4 discusses the possible uncertainty in measuring stellar inclination with asteroseismology, and performs the analytical and numerical studies to derive the conditions necessary for the secure inclination measurement. We also derive the stellar inclinations for 94 main-sequence solar-like stars observed by *Kepler*. This chapter is based on Kamiaka et al. (2018).

- In chapter 5, we study further a misaligned Earth-sized planet Kepler-408b analyzed in chapter 4. We also examine its validity by comparing our asteroseismic results with other observations. This chapter is based on Kamiaka et al. (2019).

- Chapter 6 claims the observed resonance of stellar rotation periods measured from asteroseismology and planetary orbital periods determined from transits. We also discuss the possible mechanism to enable this resonance, such as tidal interaction between stars and planets. This chapter is based on Suto et al. (2019).

- Chapter 7 is devoted to summarize the achievements of this work and implications for the future study.

Chapter 2

Backgrounds of spin-orbit angles in exoplanetary systems

We find some exoplanets are in the orbits highly tilted with respect to the equatorial plane of their host stars. This is one of the most surprising discoveries in exoplanetary science. This misalignment between stellar spin and planetary orbital axes is characterized by "spin-orbit angle" (or, "stellar obliquity") ψ.

2.1 Spin-orbit angles and its implication for planetary formation/migration

Large misalignment is inconsistent with what we know about the solar system, in which all 8 planets are almost coplanar and aligned to solar equator within $\approx 7^\circ$. In the standard model of planet formation/evolution, planets are considered to be born within protoplanetary disk around the star. To begin with, stars form due to the gravitational collapse of molecular cloud. And then protoplanetary disk is the disk-like remnant of the cloud that remains around the protostar because of their non-zero angular momentum. Planets form within this disk, and may experience inward/outward migration through angular momentum exchange with disk materials. Therefore planetary orbits are thought to trace in most cases the plane of protoplanetary disks, even after disk dispersal ($\lesssim 10\,\mathrm{Myr}$ after star formation). As long as protostar and protoplanetary disk share the same direction of rotation, the spin-orbit misalignment seems to be unlikely.

In the last two decades, intensive theoretical works have been made to link the observed misalignments to the formation and/or migration histories that exoplanets must have experienced. Therefore, the tilt of planetary orbit is now considered to be an important diagnostic to investigate the formation and evolution history of planetary systems. In this section, we summarize possible scenarios to enhance/suppress the misalignment proposed by theoretical consideration of stellar and planetary dynamics. There are three major ways to enhance the misalignment; (1) tilt the planetary orbit, (2) tilt the protoplanetary disk, where exoplanets are considered to be born, or (3) tilt the central star. In principle, the observed misalign-

ments can be explained by at least one of these scenarios. On the other hand, we need to keep in mind that some other mechanisms are known to be able to suppress the misalignment enhanced by the dynamics above.

2.1.1 The mechanisms to tilt the planetary orbit

The mechanisms below can tilt the planetary orbits during the dynamical evolution of planets, causing spin-orbit misalignment.

- **Planet-planet scattering.** Planet-planet scattering is the gravitational scattering of more than one orbiting planets [1] (Rasio & Ford 1996, Weidenschilling & Marzari 1996, Lin & Ida 1997). In most cases, the gravitational interaction among planets are much weaker than that between planet and star, so that planetary orbital motion can be well approximated by two-body description between star and planet. If planets get quite close each other, however, this two-body approximation never holds. This is because in that situation gravitational interaction *between planets* dominates their orbital motion than that with central star. To be more specific, planets which have mutual separation $r_{1,2}$ smaller than their mutual Hill radius, defined with their masses ($M_{1,2}$) and semi-major axes ($a_{1,2}$) as

$$r_{1,2} < R_{\rm H} \equiv \left(\frac{M_1 + M_2}{3M_\star}\right)^{1/3} \left(\frac{a_1 + a_2}{2}\right), \tag{2.1}$$

  experience gravitational scattering and exchange their orbital angular momenta. And then the geometry of their orbital motion changes drastically. For example, this may result in the ejection of one planet from planetary system (due to the gain of angular momentum), whereas the other falls inward (due to the loss of angular momentum). Because there is no reason for planets to keep their initial orbital inclination in this scenario, this mechanism can randomize the orientation of the planet that survived the scattering. Many numerical works have performed to study the outcome of scattering (e.g., Chatterjee et al. 2008) by N-body simulation, concluding that a variety of orbital orientation is possible even from fairly ordered initial state. In addition, this scenario can account for the presence of recently-observed close-in planets (e.g., hot Jupiters), which are very challenging to the in-situ formation.

- **Kozai-Lidov cycles.** Planetary orbit can be tilted even without experiencing violent processes like scattering. One well-known mechanism is the Kozai-Lidov cycle, the oscillatory evolution of planetary orbital parameters induced by distant perturber (Kozai 1962). Suppose the star-planet system has distant and massive stellar/planetary companion, and they satisfy hierarchical condition ($a_{\rm out} \gg a_{\rm in}$ and $M_{\rm out} \gg M_{\rm in}$) [2]. If initial

[1] It does not necessary require direct collision, because gravitational interaction enhances the scattering cross section rather than their physical radii.

[2] Binary systems in which planet revolves around one of them are very likely to satisfy this condition.

mutual inclination between planet and outer perturber exceeds the critical value

$$i_{\rm mut} > \cos^{-1}[(3/5)^{1/2}] = 39.2^\circ, \tag{2.2}$$

orbital inclination and eccentricity e of inner body will be oscillatory so that it preserves $\sqrt{1-e^2}\cos i_{\rm mut}$. Specifically, inclination becomes maximum (minimum) when eccentricity becomes minimum (maximum), making possible highly inclined planetary orbit. Kozai cycles are now often used to characterize the observed exoplanetary systems and predict their future evolution (Mazeh et al. 1997, Fabrycky & Tremaine 2007, Naoz et al. 2011). Again, this scenario is compatible with observed close-in planets when coupled with tidal dissipation (see below).

These two mechanisms are not necessarily exclusive, but can occur sequentially. For instance, Nagasawa et al. (2008) showed that planet-planet scattering and the subsequent Kozai-Lidov effect in multi-planetary systems modify the orbital plane of the close-in planets that survive the orbit crossing.

2.1.2 The mechanisms to tilt the protoplanetary disk

Stars and planets do not always form in perfect isolation, but mostly under the influence of other nearby systems and/or accreting materials onto the system. The mechanisms below can tilt protoplanetary disks by significant torque in these non-static environments, allowing spin-orbit misalignment.

- **Torque from distant perturber.** The Kozai-Lidov effect is shown to be at play also for protoplanetary disk around one component of binary stars, as long as self-gravity within the disk is strong enough to keep the structure of the disk (Batygin et al. 2011). Besides, Batygin (2012) demonstrated that torque by distant perturber (e.g., binary companion) can drive the precession of central star's spin and disk's normal axes. In this scenario, both of these axes precess around orbital axis of binary motion with different time scale, causing periodic variation of spin-orbit angle ψ [3]. These mechanisms lead to inherently inclined disks at the time of planet formation, making possible the spin-orbit misalignment.

- **Chaotic accretion.** This scenario considers the observed misalignments as a common outcome of star formation. In fact the molecular cloud, within which stars form through the gravitational collapse, is not static but highly turbulent. This property is also the case for gas and solid materials accreting onto the protoplanetary disk [4]. This chaotic nature of mass accretion allows anisotropic and variable gain of angular momentum to the protoplanetary disk so that it can be tilted away from stellar spin axis during its evolution. Recent numerical works found that especially inner disk orientation is highly vulnerable to what falls into them in the last phase of accretion (e.g., Bate et al. 2010, Thies et al. 2011, Fielding et al. 2015).

[3] Binary orbit remains almost intact because it is the largest reservour of angular momentum of the system.

[4] Because of the non-zero angular momentum, most materials accrete onto the disk first, not the star. Subsequently it flows into the star through the disk inward.

2.1.3 The mechanisms to tilt the stellar spin axis

The mechanisms below can tilt the stellar spin axis, allowing spin-orbit misalignment.

- **Stat-disk magnetic interactions.** Lai et al. (2011) proposed a possible channel of the misalignments in which magnetic interaction between star and inner disk may push stellar spin away from the normal of protoplanetary disk, even into retrograde state. Therefore this process can deliver the birthplace of planets misaligned with respect to stellar spin from the beginning. Since this scenario never assumes outer companion, this is possible to occur in any star-planet systems.

- **Internal gravity waves.** Rogers et al. (2012) developed a scenario in which stellar spin changes its orientation spontaneously, without any interactions with planets or disks. This model is amenable to hot stars, which have convective interior and radiative envelope. The physics behind is that the internal gravity waves excited at convective-radiative interface will transport the considerable amount of angular momentum and deposit it to radiative envelope. This re-distributes angular momentum within stellar interior, making radiative envelope rotate in a different direction from the convective interior. Since this mechanism works mainly for hot stars, it is consistent with the presence of misaligned hot Jupiters around hot stars (see section 2.6).

2.1.4 The mechanisms for the re-alignment

Even if star and/or planet become highly oblique, some processes to suppress the misalignment are known to work especially for systems with close-in planets.

- **Tidal dissipation.** Tidal interaction between star and planet affects the orbital dynamics of the planet in many aspects. Because tidal force scales inversely with the cubic star-planet separation, it becomes highly effective for close-in planets. Tidal interaction accompanies the dissipation of energy and angular momentum in stellar (or planetary) convective layers. Therefore, it becomes more dominant for the planets around cooler stars, which are known to have thicker convective envelopes (see section 2.6).

  Tidal dissipation (1) makes planetary orbit shrink ($a \to 0$), (2) circlizes the orbit ($e \to 0$), and (3) aligns the orbit to equatorial plane of the star ($\psi \to 0$). One possible prediction by this nature is that close-in planets around cooler stars are more likely to be aligned, even if their orbital orientation is initially random. In addition, this naturally explains the formation of close-in planets when coupled with the Kozai-Lidov mechanism. Since highly eccentric planets get close to the central star at pericenter ($r_{\rm peri} = a(1-e)$), planet under the Kozai-Lidov cycles will tidally-interact with the star mainly at pericenter. This causes orbit and eccentricity shrink, leaving close-in and circular orbit.

  Because accurate modelling of tidal process requires the understanding of the physics inside the star and planet in detail, the reliability of current tidal model could be still

rather limited. Equilibrium tide is often taken as the standard model of tidal dissipation, based on weak friction theory of convective layers (e.g., Zahn 1977, Zahn 1989, Correia et al. 2011). Later Lai (2012) extended the equilibrium model by incorporating inertial waves excited in the convective-radiative interface of the star. This model enabled tidal theory to explain the presence of hot Jupiters more naturally [5].

- **Star-disk magnetic interactions.** Magnetic interaction between star and inner disk may also align stellar spin towards the disk's normal. This process enables the birthplace of planets aligned to stellar spin, regardless of the origin of star-disk misalignment.

2.2 Geometry of spin-orbit misalignment

As described above, the spin-orbit angle ψ is an important diagnostic for the formation and evolution history of planetary systems. However, it is difficult to measure ψ directly in most cases. Therefore we often appeal to other three direct-observable angles associated with ψ; planetary orbital inclination angle ($i_{\rm orb}$), stellar inclination angle ($i_\star$), and spin-orbit angle *projected* onto the sky plane (λ). Here $i_{\rm orb}$ and $i_\star$ are the inclination angles, the angle of the axis from the line of sight, whereas λ is the position angle, the compass direction of the axis's projection onto the sky plane. Figure 2.1 introduces geometrical relation among these angles. And then the methods to determine $i_{\rm orb}$, λ, and $i_\star$ are presented later in sections 2.3, 2.4, and 2.5, respectively.

The unit vector of stellar spin ($\boldsymbol{s}$) and planetary spin ($\boldsymbol{l}$) are given in coordinates in Figure 2.1 as

$$\boldsymbol{s} = \begin{pmatrix} 0 \\ \sin i_\star \\ \cos i_\star \end{pmatrix}, \ \boldsymbol{l} = \begin{pmatrix} \sin i_{\rm orb} \sin\lambda \\ \sin i_{\rm orb} \cos\lambda \\ \cos i_{\rm orb} \end{pmatrix}, \tag{2.3}$$

and thus

$$\cos\psi = \boldsymbol{s}\cdot\boldsymbol{l} = \sin i_\star \sin i_{\rm orb} \cos\lambda + \cos i_\star \cos i_{\rm orb}. \tag{2.4}$$

Since $i_{\rm orb}$ is close 90° for transiting planets [6] , this equation reduces to

$$\cos\psi \approx \sin i_\star \cos\lambda. \tag{2.5}$$

Therefore the measurements of $i_\star$ and λ are required to determine the spin-orbit angle ψ.

[5] Standard model predicts that hot Jupiters will be engulfed by the star due to the orbital shrink ($a \to 0$), which is incompatible with the observations. Indeed, Lai model enabled the survival of close-in and circular hot Jupiters by retarding orbital shrink (Xue et al. 2014).

[6] Orbital inclination angle too away from 90° cannot carry planet to the front of the star at any phase of its orbital motion. For circular orbits, for example, $\cos i_{\rm orb} < R_\star/a$ ($R_\star$ and a are stellar radius and orbital semi-major axis) is required for transits to occur.

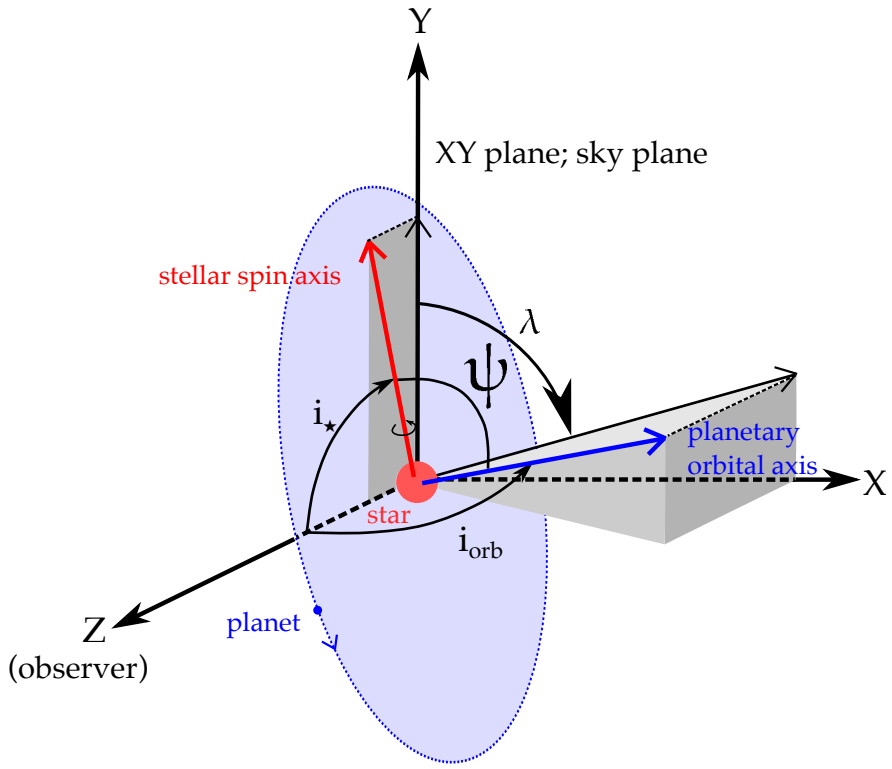

Figure 2.1: Schematic illustration of the geometric configuration of star-planet system. The coordinates are set with the origin centered on the star with XY plane corresponding the sky plane, and positive Z-direction pointing toward the observer. Positive Y-direction are defined so that stellar spin axis (red) projected onto the sky plane coincides with it, forming a right-handed triad with Z and X-axes. Spin-orbit angle ψ, the angle between stellar spin (red) and planetary orbital (blue) axes, can be decomposed into three angles associated with this coordinate; stellar spin inclination measured from positive Z-axis ($i_\star$), planetary orbital inclination measured from positive Z-axis ($i_{\rm orb}$), and spin-orbit angle *projected* onto sky plane (λ).

2.3 Transit photometry and constraints on orbital inclination

Transit is the eclipse of the star by the planet. During that event, the star looks fainter because the stellar flux is partially blocked by the planet. This phenomenon provides lots of information on the stellar and planetary properties [7]. In this section, we briefly review the way to constrain the orbit of transiting planet, following Winn (2010).

[7]Eclipse of the planet by the star (i.e., the event where star blocks the planet) also provides the clues on mainly planetary surface environment or composition. This is because flux emitted by planet will be fully masked during that event. This is contrary to the ordinary transit event, at which stellar flux alone is partially blocked. This type of eclipse is often called "secondary eclipse", "superior conjunction", or "occultation".

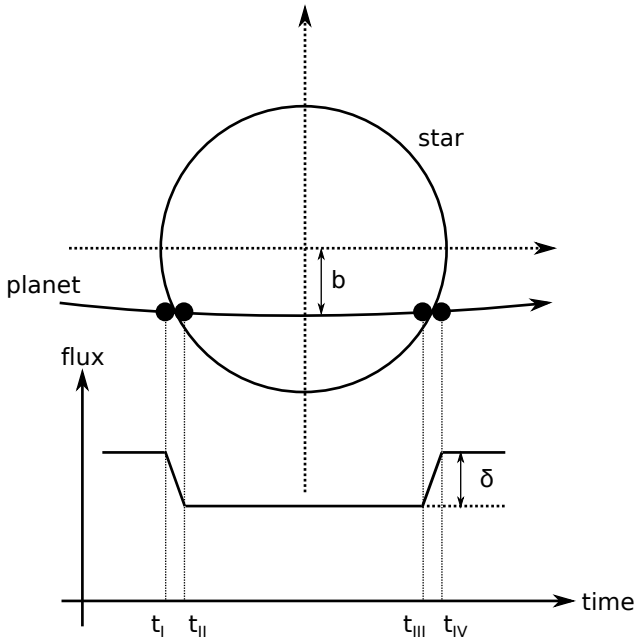

Figure 2.2: Schematic illustration of planetary transit with impact parameter b. Planetary eclipse induces the dip in flux by δ. Four contact times ($t_{\rm I}$, $t_{\rm II}$, $t_{\rm III}$, $t_{\rm IV}$) are defined.

Figure 2.2 illustrates the geometry of transit with impact parameter b (upper panel). The stellar flux decreases by δ during transit (lower panel), which corresponds to planet-to-star size ratio, $R_{\rm p}^2/R_\star^2$. We define four contact times ($t_{\rm I}$, $t_{\rm II}$, $t_{\rm III}$, and $t_{\rm IV}$), the moments when planet touches stellar circumference while it passes the stellar front. To be more exact, stellar flux decreases in "ingress" ($t_{\rm I} - t_{\rm II}$), reaches minimum during "full transit" ($t_{\rm II} - t_{\rm III}$), and increases again in "egress" ($t_{\rm III} - t_{\rm IV}$). Note that transit lightcurve in Figure 2.2 is oversimplified, because for example no limb-darkening of the star is assumed for easy understanding.

To be specific, what we obtain from transit lightcurve is transit depth δ, four contact times ($t_{\rm I}$, $t_{\rm II}$, $t_{\rm III}$, $t_{\rm IV}$), and planetary orbital period $P_{\rm orb}$ that corresponds to the separation of transit events in time series. As will be shown below, the modelling planetary transit can convert parameters above into physical ones, such as orbital semi-major axis scaled by stellar radius $a/R_\star$ and orbital inclination angle $i_{\rm orb}$ as follows.

First, we define the planetary orbital parameters. In general we need six parameters to define the motion of the planet uniquely (three in position, and three in momentum). By solving Kepler problem, they are replaced by six orbital parameters, a, e, $i_{\rm orb}$, ω, Ω, and f as defined in Figure 2.3 (see Table 2.1 and caption of Figure 2.3 for further description). The position of the planet relative to the star, $\boldsymbol{r}$, is given by

$$\boldsymbol{r} = \begin{pmatrix} X \\ Y \\ Z \end{pmatrix} = r \begin{pmatrix} \cos\Omega\cos(\omega+f) - \sin\Omega\sin(\omega+f)\cos i_{\rm orb} \\ \sin\Omega\cos(\omega+f) + \cos\Omega\sin(\omega+f)\cos i_{\rm orb} \\ \sin(\omega+f)\sin i_{\rm orb} \end{pmatrix}, \tag{2.6}$$

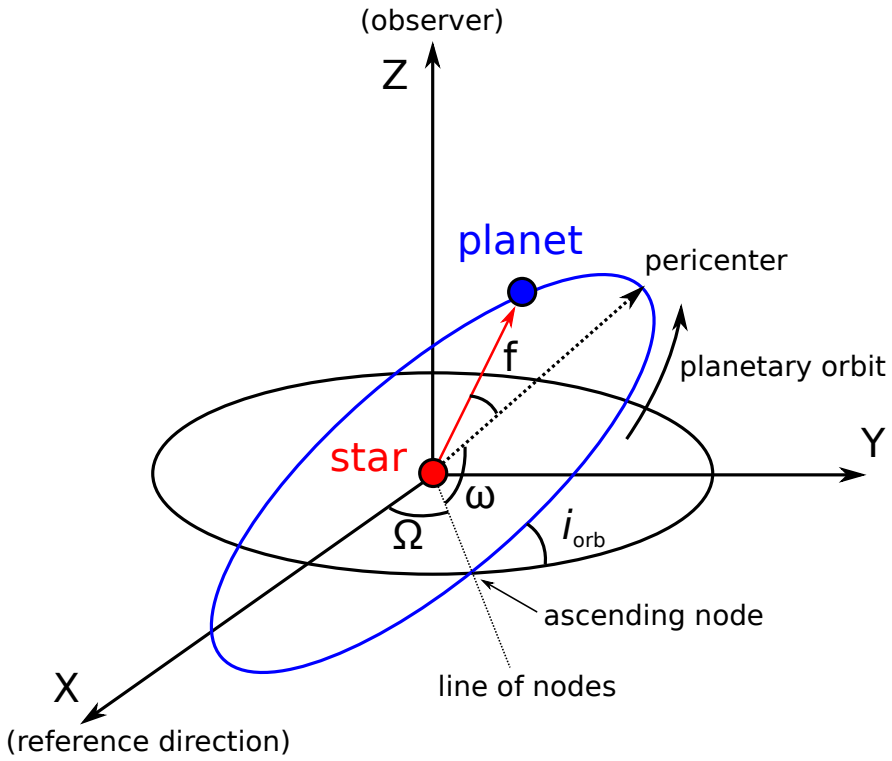

Figure 2.3: The coordinates defined for the planetary orbital motion. The star is centered at origin. Positive Z-direction is pointing towards the observer, and XY plane defines sky plane. Planetary orbit is inclined from sky plane by $i_{\rm orb}$, and planet crosses sky plane towards observer at ascending node. Longitude of ascending node, Ω, is the angle between line of nodes and positive X-direction (reference direction). Argument of pericenter, ω, is defined as the angle between line of nodes and line pointing pericenter of the orbit. True anomaly, f, is a phase parameter describing the position of planet measured from pericenter.

Table 2.1: The planetary orbital parameters

symbol	name
a	orbital semi-major axis
e	orbital eccentricity
$i_{\rm orb}$	orbital inclination
ω	argument of pericenter
Ω	longitude of ascending node
f	true anomaly

where r is the separation between star and planet:

$$r = \frac{a(1-e^2)}{1+e\cos f}. \tag{2.7}$$

The position of planet in the sky plane ($X-Y$ plane) is given by

$$r_{\rm sky} \equiv \sqrt{X^2+Y^2} = \frac{a(1-e^2)}{1+e\cos f}\sqrt{1-\sin^2(\omega+f)\sin^2 i_{\rm orb}}. \tag{2.8}$$

Thus mid-transit phase is defined so that it minimizes $r_{\rm sky}$ [8] as

$$f = +\frac{\pi}{2} - \omega. \tag{2.9}$$

Then the impact parameter b of transit is defined as

$$b \equiv \frac{r_{\rm sky}|_{f=+\pi/2-\omega}}{R_\star} = \frac{a\cos i_{\rm orb}}{R_\star}\left(\frac{1-e^2}{1+e\sin\omega}\right). \tag{2.10}$$

To proceed further, we use the Kepler's second law:

$$r^2\dot{f} = \frac{2\pi}{P_{\rm orb}}a^2\sqrt{1-e^2}. \tag{2.11}$$

Then the total duration of transit and the duration of full transit are respectively expressed as

$$T_{\rm tot} \equiv t_{\rm IV}-t_{\rm I} = \frac{P_{\rm orb}}{2\pi\sqrt{1-e^2}}\int_{f_{\rm I}}^{f_{\rm IV}}\left[\frac{r(f)}{a}\right]^2 {\rm d}f, \tag{2.12}$$

$$T_{\rm full} \equiv t_{\rm III}-t_{\rm II} = \frac{P_{\rm orb}}{2\pi\sqrt{1-e^2}}\int_{f_{\rm II}}^{f_{\rm III}}\left[\frac{r(f)}{a}\right]^2 {\rm d}f. \tag{2.13}$$

The integration above can be approximated by

$$T_{\rm tot} \approx \frac{P_{\rm orb}}{\pi}\sin^{-1}\left[\frac{R_\star}{a}\frac{\sqrt{(1+k)^2-b^2}}{\sin i_{\rm orb}}\right]\frac{\sqrt{1-e^2}}{1+e\sin\omega}, \tag{2.14}$$

$$T_{\rm full} \approx \frac{P_{\rm orb}}{\pi}\sin^{-1}\left[\frac{R_\star}{a}\frac{\sqrt{(1-k)^2-b^2}}{\sin i_{\rm orb}}\right]\frac{\sqrt{1-e^2}}{1+e\sin\omega}, \tag{2.15}$$

where $k \equiv \sqrt{\delta} = R_{\rm p}/R_\star$ is planet-to-star radius ratio, and is a direct observable. For the case of $R_{\rm p} \ll R_\star \ll a$, these equations can be rewritten as

$$b^2 \approx \frac{(1-k)^2-(T_{\rm full}/T_{\rm tot})^2(1+k)^2}{1-(T_{\rm full}/T_{\rm tot})^2} \tag{2.16}$$

$$\frac{R_\star}{a} \approx \frac{\pi}{2\sqrt{k}}\frac{\sqrt{T_{\rm tot}^2-T_{\rm full}^2}}{P_{\rm orb}}\left(\frac{1+e\cos\omega}{\sqrt{1-e^2}}\right). \tag{2.17}$$

Equations (2.10), (2.16), and (2.17) enable to derive $a/R_\star$ and $i_{\rm orb}$ from direct observables, given e and ω from other observations such as radial velocity measurements.

[8] There is another solution that minimizes $r_{\rm sky}$, $f = -\frac{\pi}{2}-\omega$. This corresponds to mid-occultation phase.

2.4 Spectroscopic observations to determine projected spin-orbit angle

Spectroscopic measurement of the star with planetary companion also offers unique information on the dynamical state of star-planet system. Here we review what we learn from stellar spectroscopy, focusing on the measurement of the projected spin-orbit angle λ by the Rossiter-McLaughlin (RM) effect (e.g., Winn & Fabrycky 2015, Triaud 2017).

In general, the star with a planetary companion revolves around the center of mass (CM) of the system. This induces the reflex motion of the central star accompanied by the orbital motion of the planet, and appears as the periodic Doppler shift of absorption lines in stellar spectra. This periodic Doppler shift is often used to detect exoplanets, which is known as spectroscopic radial velocity (RV) method. The first exoplanet 51 Pegasi b, indeed, was detected with the RV measurement. Over the decades this method has successfully discovered ≈ 700 exoplanets, and is now one of the most successful methods to detect exoplanets.

The stellar reflex motion along with line of sight is given by converting the planetary motion relative to the star (equation 2.6) to the stellar motion relative to CM;

$$v_{\rm rad} = -\frac{M_{\rm p}}{M_\star + M_{\rm p}}\dot{Z} = -\frac{M_{\rm p}}{M_\star + M_{\rm p}}\frac{na\sin i_{\rm orb}}{\sqrt{1-e^2}}[\cos(\omega + f) + e\cos\omega], \tag{2.18}$$

where $n = 2\pi/P_{\rm orb} = \sqrt{G(M_\star + M_{\rm p})/a^3}$ is the orbital frequency of planet, and is called mean motion. Thus the orbital eccentricity e, argument of pericenter ω, and $M_{\rm p}\sin i_{\rm orb}$ are estimated from RV data. Therefore RV measurement can predict lower limit of planetary mass $M_{\rm p}\sin i_{\rm orb}$. This enables to infer planetary material density (moreover, the composition of planet) when combined with transit method, which gives an estimate of planetary radius $R_{\rm p}$.

During transits, there appears the anomaly on the measured radial velocity. This is related to stellar rotation as follows. Due to the stellar rotation, the flux from stellar surface approaching towards observer is blue-shifted, while receding half is red-shifted. During out of transit, the contributions of these two are canceled so that no blue/red-shift anomaly will be present in RV curve. During transits, on the other hand, planet masks either blue or red part of stellar surface. When planet masks blue part, stellar radial velocity becomes slightly red-shifted because contribution from blue part decreases. This anomaly of radial velocity during transit is knows as the Rossiter-McLaughlin (RM) effect (Holt 1893, Schlesinger 1910, Rossiter 1924, McLaughlin 1924), whose theory had initially been developed to model eclipsing binaries.

Figure 2.4 visualizes the modelling of RM anomalies in RV curve for three different transit chords. Top panel brackets the entire orbital phase of the star, and gray-shaded region is in-transit phase where RM anomalies arise. Conventionally positive radial velocity is defined for the motion moving away from the observer. Bottom panels provide close-up views of the RM anomalies during transit (lower panels), and corresponding geometry of planetary transit. From left to right, transits with $\lambda = 30^\circ$, 90°, and 150° are illustrated. In the case of $\lambda = 30^\circ$, planet passes the blue-shifted half of stellar surface first, and red-half after

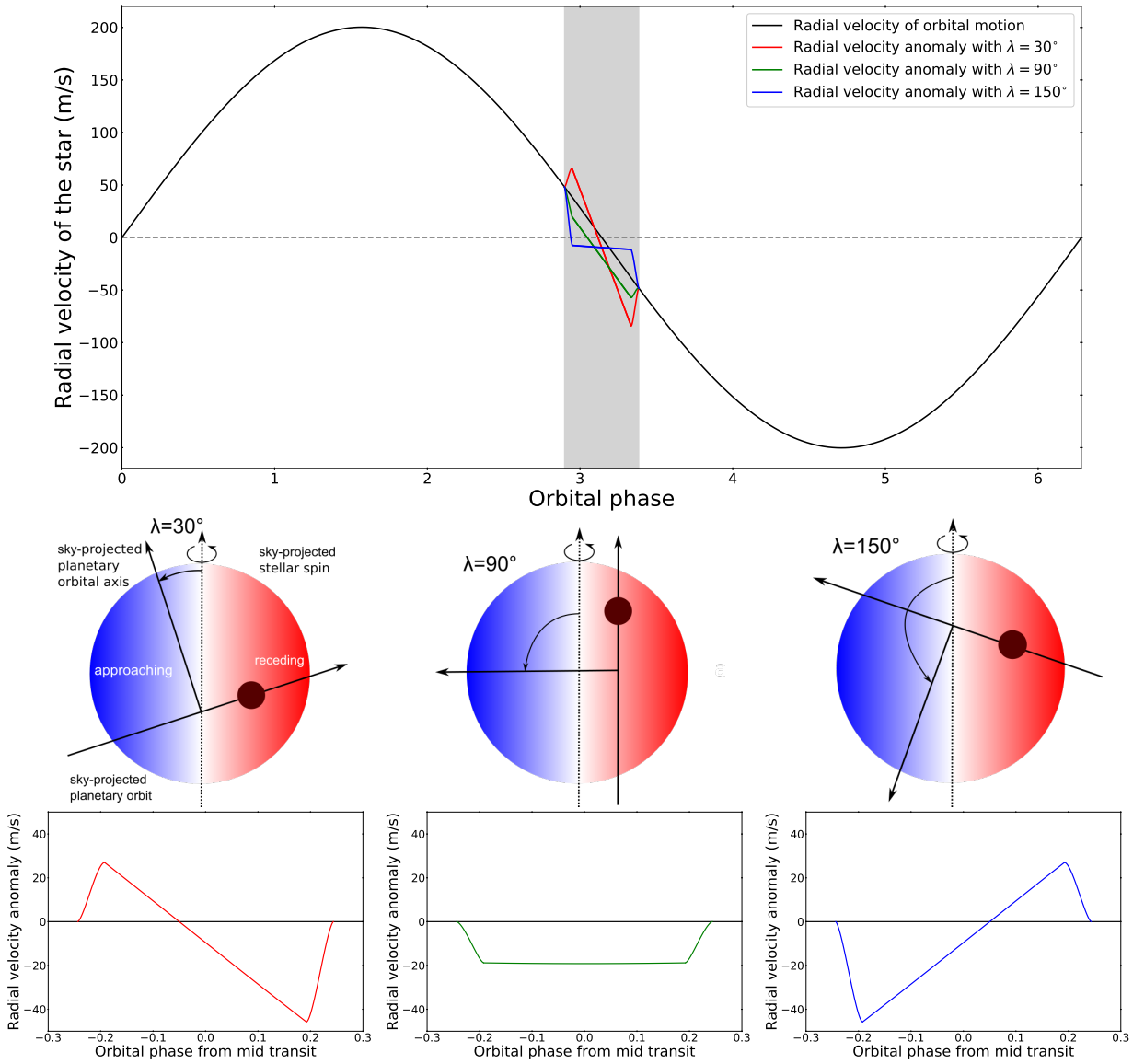

Figure 2.4: Modelled radial velocity curve of exoplanetary system based on the formulation by Ohta et al. (2005). Star and planet with $M_\star = 1\,M_\odot$, $M_\mathrm{p} = 1\,M_\mathrm{J}$, $a = 0.02\,\mathrm{au}$, $e = 0$, $i_\star = 90°$, $i_\mathrm{orb} = 85°$, $\omega = 90°$, $P_\mathrm{rot} = 10\,\mathrm{days}$, $R_\star = 1\,R_\odot$, and $k = 0.1$ are assumed. No limb darkening is taken into account. *Top*: Radial velocity over full orbital phase ($[0, 2\pi]$). Shaded region denotes transit window, and red, green, and blue lines correspond to the Rossiter-McLaughlin anomalies with $\lambda = 30°$, $90°$, and $150°$, respectively. *Bottom*: Close-up views of the RM anomalies during transit (lower panels) and schematic descriptions of corresponding transit geometry (upper panels). Blue half is the stellar surface where rotation makes it approach towards the observer, while red is receding half. From left to right, we assume $\lambda = 30°$, $90°$, and $150°$, respectively.

that. Accordingly, radial velocity shifts to positive side first, and to negative side later. The situation is completely opposite for $\lambda = 150°$; radial velocity shifts blueward first, and redward later. For transit with $\lambda = 90°$, RM anomaly is always negative, because planet keeps masking only red side.

This RM anomalies has been modelled as a function of λ by Ohta et al. (2005). For example, the RM anomaly in full transit ($t_{\rm II} - t_{\rm III}$ in Figure 2.2) can be formulated as

$$\Delta v_{\rm rad} = r_\lambda \frac{2\pi}{P_{\rm rot}} \sin i_\star \frac{k^2}{1-k^2}, \tag{2.19}$$

where

$$r_\lambda = r[-\cos\lambda\cos(\omega+f) - \sin\lambda\sin(\omega+f)\cos i_{\rm orb}] \tag{2.20}$$

in the absence of stellar limb-darkening. Now the RM model has been developed further by taking into account the realistic stellar absorption line profiles (Hirano et al. 2011), enabling more accurate determination of λ. As demonstrated here, proper modelling of the RM anomalies makes possible to derive projected spin-orbit angle λ.

In order for the RM anomalies to be detectable, larger planets are favored because they give larger amplitude of the RM anomaly (equation 2.19). Besides, planets in shorter orbital period (i.e., close-in planets) are advantageous because we have more opportunities to observe planetary transit, and then multiple RM anomaly measurement contributes to reduce the noise level of the resulting radial velocity. More frequent transit is favorable also because transit window (shaded zone in upper panel of Figure 2.4) takes larger fraction in the entire orbital phase.

2.5 Methods to derive stellar inclination

Stellar inclination angles measured from line of sight ($i_\star$) deliver the clues on dynamical state of star-planet system with different and complementary viewpoint from that of λ. Here we summarize the methods to derive $i_\star$, highlighting the sensitivity of each method to stellar and planetary characteristics.

2.5.1 Spectroscopic line broadening and photometric variation

Stellar inclination $i_\star$ can be derived by combining spectroscopic and photometric observations. In doing so, we need three variables; projected stellar rotation velocity ($v \sin i_\star$), stellar rotational period ($P_{\rm rot}$), and stellar radius ($R_\star$). Once these three parameters are given, $i_\star$ is easily estimated as

$$i_\star = \sin^{-1}\left(\frac{v\sin i_\star}{2\pi R_\star / P_{\rm rot}}\right), \tag{2.21}$$

because $2\pi R_\star / P_{\rm rot}$ is a proxy for the equatorial rotation velocity of the stellar surface. In what follows, we refer to this as "combined method" when deriving $i_\star$. Here we present the remark on the measurement of each parameter.

- Stellar rotation broadens the absorption line profile in the spectra. Therefore we can get line of sight component of stellar rotation velocity ($v \sin i_\star$) by modelling line broadening properly. In the actual measurement, however, special care is necessary to distinguish two contributions to line broadening; stellar rotation and (macro-)turbulence. In other words, poor modelling of turbulence may lead to incorrect measurement of surface rotational velocity $v \sin i_\star$. Actually, it is difficult to isolate stellar rotation from turbulence unless rotation is fast enough (e.g., $v \sin i_\star \gtrsim 5\,\mathrm{km/s}$).

- The measurement of rotational period $P_{\rm rot}$ is based on the periodic signal encoded in time series of stellar brightness. If there is inhomogeneity of brightness on the stellar surface (star-spots and/or faculae), there happens periodic variation of the total stellar flux as star rotates, whose period is identical to stellar rotation. However, this method relies on some assumptions of the nature of star-spots. First, the lifetime of star-spots needs to be long enough to be able to follow stellar rotational motion. If star-spot appears or vanishes many times during one rotational period, it is no longer proper tracer of stellar rotation. Second, a single-spotted star is preferable, because for multi-spotted stars time series may suffer from high overtones of rotational periods ($P_{\rm rot}/2$, $P_{\rm rot}/3$, ...). Third, we need to assume the latitudes the star-spots appear. Since it is possible that different latitude rotates with different period (as is the case for the Sun), derived periods always have uncertainty of up to $\approx 30\%$ due to poor understanding of spot-emerging latitudes.

- Stellar radius $R_\star$ cannot be derived directly from observations. Instead, it is derived by modelling stellar evolution, which adopts spectroscopic parameters such as $v \sin i_\star$, surface gravity ($\log g$), and metallicity ([Fe/H]) as input parameters.

We note here that three independent measurements are necessary for spectroscopic estimate of $i_\star$. We may apply this method to a large number of stars [9], but $i_\star$ derived from the combined method most likely suffer from large uncertainties.

In this combined method, relatively fast rotation of the stars are required for line broadening to be detectable ($v \sin i_\star \gtrsim 5\,\mathrm{km/s}$). In addition, photometrically active stars are unfavorable because flux variation not originating from star-spot modulation will be present in stellar time series.

2.5.2 Asteroseismic estimate of the stellar inclination

Asteroseismology is a study of stars with their pulsations. Among stars, main-sequence solar-like stars are known to show pulsations with amplitudes of a few parts per million in time series. Through the analysis of this pulsation, asteroseismology is now expected to deliver very accurate measurements of stellar parameters including stellar inclination $i_\star$. In this thesis, we focus on photometric variation induced by stellar acoustic oscillation with

[9] Large scale observations have been operated to get $v \sin i_\star$ and $R_\star$, such as Spectroscopic Properties of Cool Stars (SPOCS) project (Valenti & Fischer 2005) and California *Kepler* Survey (CKS) project (Petigura et al. 2017, Johnson et al. 2017).

a few minutes period (frequencies with the order of a few thousand μHz). The review of asteroseismology is given in chapter 3 in great detail, and in this subsection we briefly describe the basic principle.

In asteroseismic analysis, we do not deal with stellar photometric time series directly, but its Fourier-transforms ("power spectrum") to extract periodicity within it. In addition, the shape of this power spectrum is tightly dependent on the viewing angle of star ($i_\star$) in sub-μHz scale. The change of the shape is so tiny that $i_\star$ measurement had been almost impossible until the advent of high precision space telescopes such as CoRoT and *Kepler*, which can describe "fine structure" of power spectrum with sub-μHz resolution.

The advantage of asteroseismic determination of $i_\star$ is mainly two-fold. First, the shape of power spectrum is directly sensitive to the value of $i_\star$. This is not the case for the combined method of spectroscopy and photometry. Therefore asteroseismic $i_\star$ measurement is relatively model-independent, unlike combined method that assumes line broadening model, spot generation/annihilation model, and stellar evolution model. Second, the applicability of asteroseismology does not depend on the properties of planets. This is clearly contrary to the RM measurement, which prefers deep and frequent transits (i.e., those by hot Jupiters) for the detectable anomalies. Actually the RM measurements have been made mostly for hot Jupiters, as we see in section 2.6. Because most of detected exoplanets are Earth-sized planets (rather than hot Jupiters), indeed, asteroseismology has great potential to explore smaller and more distant planets for the study of the misalignment.

Measuring the spin-orbit angle for smaller and/or more distant planets may not immediately lead to the strong quantitative constraints on the possible planet formation scenarios. However, it will provide a significant implication to the possible scenarios.

As described above, the discovery of misaligned exoplanets has triggered the development of various planet formation scenarios that account for such misalignments. For example, intensive effort has been made to predict the evolution of the spin-obit angle of exoplanets numerically (e.g., Nagasawa et al. 2008). However, the quantitative understanding of the outcome of orbital evolution is hampered by the arbitrariness of the initial conditions adopted there; e.g., the number of planets, planet masses, and planet orbital periods. Recently, ALMA observation discovered the gapped structure in some protoplanetary disks. It is presumed that these gaps are formed by the protoplanets, which provides realistic initial conditions for the planetary orbital evolution (e.g., Tamayo et al. 2015).

As this example demonstrates well, new observations can lead to the great progress in the theory, making possible the quantitative comparison of the theory with the observations. In the same way, the measured misalignments for small and/or distant planets will provide realistic conditions of planet formation. Of particular importance is measuring the spin-orbit angles in various kinds of exoplanetary systems including e.g., small or distant planet systems, and multi-planet systems. Once enough number of measurements are achieved, the statistics of the spin-orbit angles will not only valify the already known models of planet formation/evolution, but also contribute to establish more realistic models. In this sense, measuring the inclination angle for planet-host stars with asteroseismology is a basic observational research to establish the comprehensive planet formation scenario.

Table 2.2: Summary of derived ψ in literatures.

System	ψ (deg)	Method to measure $i_\star$	Reference
CoRoT-18	20 ± 20	combined method	Hébrard et al. (2011)
GJ 436	80^{+20}_{-18}	combined method	Bourrier et al. (2018)
HAT-P-7	$94.6^{+5.5}_{-3.0}$	combined method	Winn et al. (2009)
	115^{+19}_{-16}	asteroseismology	Benomar et al. (2014)
	97 ± 14	asteroseismology	Lund et al. (2014b)
	$116.4^{+30.2}_{-14.7}$	asteroseismology	Campante et al. (2016)
HAT-P-20	36^{+10}_{-12}	combined method	Esposito et al. (2017)
HAT-P-22	24 ± 18	combined method	Mancini et al. (2018)
HAT-P-36	< 63	combined method	Mancini et al. (2015)
Kepler-25	$26.9^{+7.0}_{-9.2}$	asteroseismology	Benomar et al. (2014)
	$12.6^{+6.7}_{-11.0}$	asteroseismology	Campante et al. (2016)
Kepler-63	104^{+9}_{-14}	combined method	Sanchis-Ojeda et al. (2013)
Qatar-2	< 43	combined method	Esposito et al. (2017)
WASP-19	0 ± 20	combined method	Hellier et al. (2011)
WASP-32	11 ± 14	combined method	Brothwell et al. (2014)
WASP-43	< 20	combined method	Esposito et al. (2017)
WASP-84	17.3 ± 7.7	combined method	Anderson et al. (2015)
WASP-117	$69.5^{+3.6}_{-3.1}$	combined method	Lendl et al. (2014)
XO-2	27^{+12}_{-27}	combined method	Damasso et al. (2015)

2.6 Current results of spin-orbit angle distribution

If we can measure all of $i_{\rm orb}$, λ, and $i_\star$, spin-orbit angle (ψ) can be given uniquely (equation 2.4). However, measuring these three angles simultaneously for one system is quite demanding in most cases The reasons are two-fold. First, the RM measurement is most likely for hot Jupiters as we noted. On the other hand, asteroseismology has no requirement on the properties of planets around the star. Therefore most planet-host stars with detectable acoustic oscillations have Earth-sized planets, which are the most common exoplanets. Second, *Kepler*, the satellite that had detected acoustic oscillations for many stars, had been dedicated to $10^\circ\times10^\circ$ field of view around Cygnus. Because *Kepler* stars are quite distant (as deep as up to 1,000 persec), spectroscopic follow-up is difficult in most cases. For these reasons, the RM measurement and asteroseismology have few common stars.

Table 2.2 summarizes 15 confirmed exoplanetary systems with measured spin-orbit angle ψ. In fact, there are only two planetary systems for which spin-orbit angle ψ is successfully derived with asteroseismology; HAT-P-7 (Benomar et al. 2014, Lund et al. 2014b, Campante et al. 2016) and Kepler-25 (Benomar et al. 2014, Campante et al. 2016). Because of small number statistics, the discussion on the spin-orbit angle distribution has been mainly made in terms of either λ or $i_\star$. In what follows we briefly highlight the previous works on the spin-orbit angle distribution.

2.6.1 Spin-orbit angle distribution revealed by λ

Projected spin-orbit angle λ has been measured for more than 120 exoplanets so far. Figure 2.5 summarizes the values of λ for 124 planets taken from TEPCat sample (Southworth 2011) [10] [11]. It is again clear from this figure that almost all measurements are limited for close-in ($P_{\rm orb} \lesssim 1\,$week) gas-giants ($R_{\rm p} \gtrsim 4\,R_{\oplus}$). In addition, it is important to note that more than half planets in this sample are consistent with spin-orbit alignment [12] (the gray-shaded region), while non-negligible fraction of planets are known to be misaligned. Some of them are found in polar ($\lambda \approx 90°, 270°$), retrograde ($90° \lesssim \lambda \lesssim 270°$), or even counter-orbiting ($\lambda \approx 180°$) orbits.

Fabrycky & Winn (2009) first performed statistical study in terms of λ by using 11 measurement of λ at the time of their writing. They assumed two possible populations of λ to describe the entire distribution of known values; Gaussian distribution around $\lambda = 0°$ and isotropic distribution. The former is to describe aligned systems, while the latter is for misaligned systems. Authors estimated how likely the data suggest each model is. They found observation favors $< 36\%$ probability for isotropic distribution, suggesting that up to 30% of the systems was not necessarily in the aligned state. Despite the small number of measured λ, this trend seems to hold even with much more observations until today (Figure 2.5).

When classified in terms of the spectral types of host stars, statistics of the RM samples helps us understand the possible origin of these misalignments (Winn et al. 2010a, Albrecht et al. 2012, Dawson 2014, Winn & Fabrycky 2015). Figure 2.6 compares measured values of λ and effective temperatures of host stars ($T_{\rm eff}$) for hot Jupiters ($0.7\,{\rm days} < P_{\rm orb} < 7\,{\rm days}$). Planets around stars below $T_{\rm eff} = 6{,}100\,$K show the trend of alignment, while large scatter of the values of λ is found for planets around hotter stars. In addition, more massive planets ($M_{\rm p} > 3\,M_{\rm J}$) are likely to be aligned regardless of temperature of their host stars. Recently, Muñoz & Perets (2018) verified this distinction in quantitative fashion. With 118 samples (74 around cooler stars, 44 around hotter stars), they found that cooler and hotter samples obey different distribution with 4σ significance.

It is interesting to note that this boundary of 6,100 K coincides with the discontinuity of stellar potation profile, which is also known as "Kraft break" (Kraft 1967). To be specific, hotter stars tend to rotate more rapidly, while cooler ones rotate slowly. This distinction would be attributed to the internal structure of the stars. Cooler stars have radiative core and thick convective envelope, while hotter stars have convective core and radiative envelope covered by thin convective layer. Since convective motion is known to be responsible for the generation of magnetic field, it suggests that magnetic breaking through the mass ejection works more effectively for cooler stars. This naturally explains the observed profiles of stellar rotation.

Because the excitation mechanisms of spin-orbit misalignment presented in section 2.1 are not necessarily exclusive each other, the profiles of λ distribution in Figure 2.6 may

[10] `http://www.astro.keele.ac.uk/jkt/tepcat/`

[11] We removed 55 Cnc e and WASP-2b, for which earlier measurement of λ is disputed by later study.

[12] In this thesis we define "alignment" as $|\lambda| \lesssim 30°$.

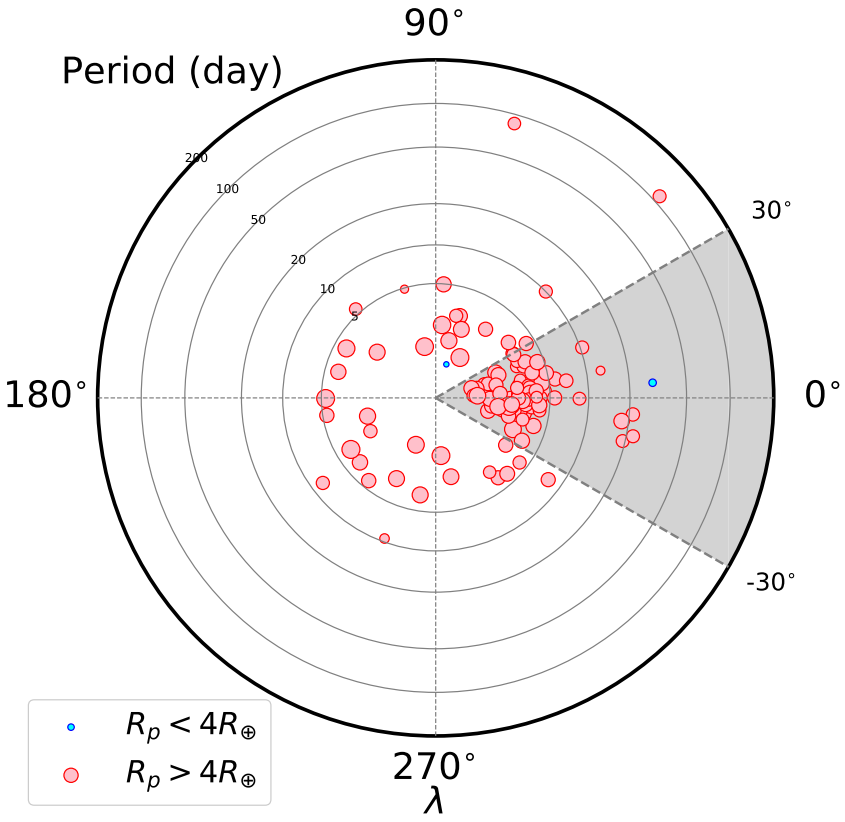

Figure 2.5: The distribution of observed values of λ with the Rossiter-McLaughlin measurements for 124 planetary systems. Radial coordinate corresponds to the planetary orbital period ($P_{\rm orb}$) in logarithmic scale, while angular coordinate represents λ. The size of symbols is proportional to planetary radius ($R_{\rm p}$), and planets larger (smaller) than $4\,R_\oplus$ are colored in red (blue). The shaded area denotes aligned systems ($|\lambda| < 30°$). The sample is taken from TEPCat (Southworth 2011; `http://www.astro.keele.ac.uk/jkt/tepcat/`).

have various origins. Indeed, the key to infer the planet formation/evolution history is to know how likely each mechanism is. When interpreting the observation, the gap at 6,100 K suggests that some of misalignments have the origin of dynamical excitation followed by tidal realignment. As we introduced, one promising scenario for the observed distribution of λ is planet-planet scattering or Kozai-Lidov migration followed by tidal realignment (section 2.1). Tidal interaction is theoretically based on tidal dissipation in stellar convective layers. Since cooler stars tend to have thicker convective envelopes, it predicts that tidal force works more effectively for planets around cooler stars. Figure 2.6 is consistent with this hypothesis; even if spin-orbit misalignment can be excited for all planets regardless of the type of central star, misalignments around cooler stars are preferentially suppressed due to the stronger star-planet tidal interaction. Because larger planets are expected to have thicker envelope, tidal force will work more effectively for larger hot Juiters. This is again consistent with the

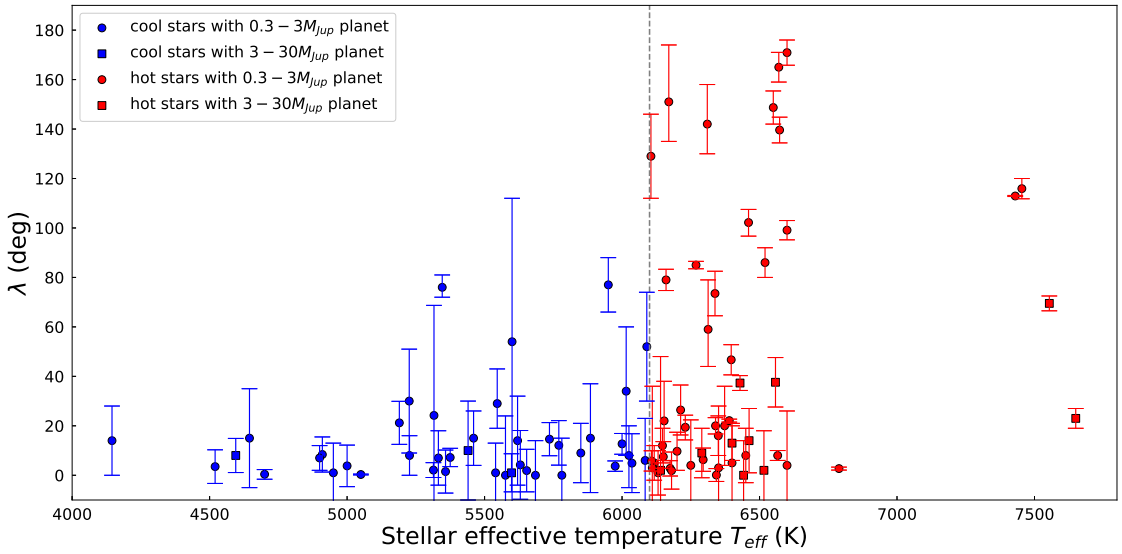

Figure 2.6: Distribution of the values of λ as a function of stellar effective temperature $T_{\rm eff}$ for stars with secure measurements. Close-in planets ($P_{\rm orb} = 0.7 - 7$ days) are shown. The vertical dashed line represents $T_{\rm eff} = 6{,}100$ K, below (above) which stars are marked in blue (red). Planets with $0.3 - 3\,M_{\rm Jup}$ are marked in circle, while those with $3 - 30\,M_{\rm Jup}$ are in squares.

overall alignment for more massive hot Jupiters ($3 - 30\,M_{\rm Jup}$), as we find in Figure 2.6.

Figure 2.7 plots measured values of λ against theoretically-estimated realignment timescale; $\tau_{\rm CE}$ (CE; convective envelopes) for cooler stars and $\tau_{\rm RA}$ (RA; radiative envelopes) for hotter stars. The explicit forms of these timescales are given by Zahn (1977);

$$\tau_{\rm CE} = 10 q^{-2} \left(\frac{a/R_\star}{40} \right)^6 \ {\rm Gyr}, \tag{2.22}$$

and

$$\tau_{\rm RA} = 1.25 q^{-2} (1+q)^{-5/6} \left(\frac{a/R_\star}{6} \right)^{17/2} \ {\rm Gyr}, \tag{2.23}$$

where $q \equiv M_{\rm p}/M_\star$ is the planet-to-star mass ratio. Figure 2.7 reveals that most of misaligned systems, mainly planets around hotter stars (red), are found in timescale longer than even the age of the universe. On the other hand, planets whose timescale is less than the age of the universe are mostly in aligned states $|\lambda| < 30^\circ$. All of the observational evidences are in favor of planet-planet scattering or Kozai-Lidov cycles followed by tidal dissipation for observed hot Jupiters. However, it is not well understood if the same mechanism will work also for Earth-sized planets, mainly because of the small number statistics. This emphasizes the importance of asteroseismology, which can unveil the geometry of small and distant planets, that is, the planets that have been less explored so far.

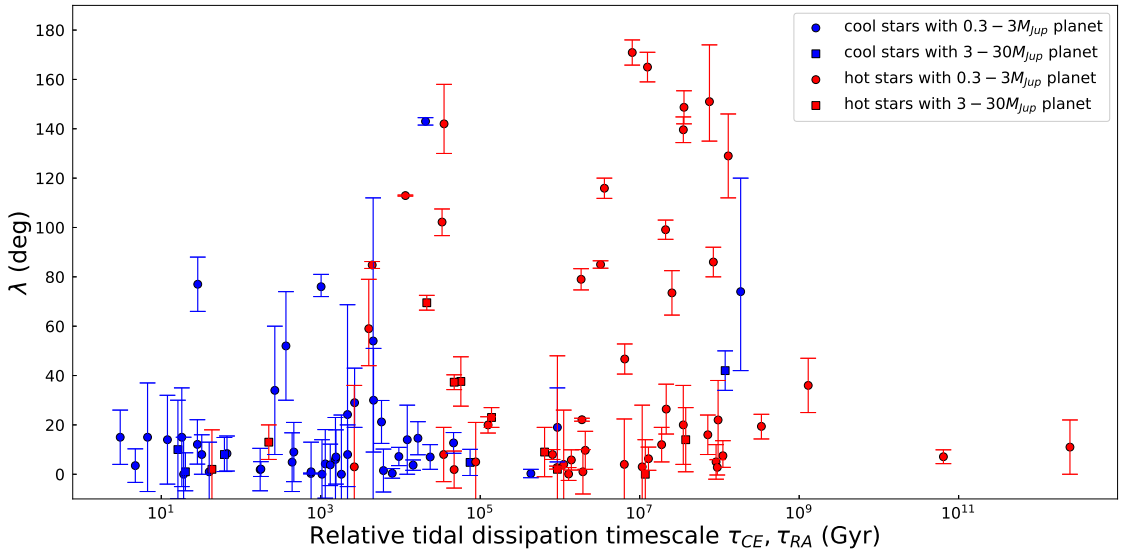

Figure 2.7: Distribution of λ values as a function of tidal dissipation timescale for stars with secure measurements. The colors and symbols share the same meanings as those in Figure 2.6. Timescale $\tau_{\rm CE}$ (equation 2.22) is computed for cooler stars, while $\tau_{\rm RA}$ (equation 2.23) is for hotter stars.

2.6.2 Spin-orbit angle distribution revealed by $i_\star$

Stellar inclination $i_\star$ is another tracer of spin-orbit angle ψ. Misalignment can be proved even if λ is not measured, because low $i_\star$ corresponds to large misalignment for *any* values of λ (equation 2.5) for transiting systems. By measuring $i_\star$, we may be able to reveal spin-orbit angle distribution of Earth-sized planets, because combined method and asteroseismic method rely on observing signals that are independent of planet size.

The statistical studies of $i_\star$ have been given by several authors based on the rich samples of spectroscopic observations. Hirano et al. (2012, 2014) derived $i_\star$ for total 33 planetary systems with combined method based on their own spectroscopic observations. They reported possible misalignments for single-transiting super-Earth system Kepler-96 and for three multi-transiting systems (Kepler-261, 518, and 1164), although their constraints are not strong enough to draw firm conclusion in the absence of follow-up studies. Winn et al. (2017a) derived $i_\star$ with combined method for the largest sample (156 planetary systems) ever as part of California *Kepler* Survey (CKS) project, and found all stars to be compatible with high inclination (i.e., spin-orbit alignment). In summary, combined method measured stellar inclination angles $i_\star$ for hundreds of planetary systems, and none of them are undoubtedly verified to be misaligned because of their weak constraints.

As introduced above, asteroseismology is another method to measure $i_\star$. As a pioneering work that applied asteroseismology to the planetary dynamics, Chaplin et al. (2013) confirmed high stellar inclination (implying spin-orbit alignment) for double-transiting system Kepler-50 and triple-transiting system Kepler-65.

One of the most epoch-making works with asteroseismology for planet-host stars was presented by Huber et al. (2013a). They found a significant misalignment ($i_\star = 43 \pm 4$ degrees) for a red-giant star Kepler-56 with double-transiting gas-giant planets. Because Kepler-56 is an evolved star with expanded radius such that the RM anomaly is almost undetectable, this discovery undoubtedly demonstrated the potential of asteroseismology to investigate spin-orbit angle in complementary manner with the conventional RM method. In addition, it is worth emphasizing that it is the first discovery of a significant misalignment for multi-planet system.

Statistical study on spin-orbit angle with asteroseismology was first presented by Campante et al. (2016). They analyzed the acoustic oscillation of 25 main-sequence solar-like stars with transiting planet(s), and found that all systems are compatible with aligned orbits within 2σ ($i_\star \approx 90^\circ$).

In summary, there are $\approx$ 30 measurements of stellar inclination angles $i_\star$ with asteroseismology. However, we need to keep in mind that some authors raised the caution that asteroseismology may give inaccurate measurements of $i_\star$, unless the stellar rotation is rapid enough (Gizon & Solanki 2003, Ballot et al. 2006). Therefore a substantial proportion of these measurements could be inaccurate, expect the unambiguous case Kepler-56. Motivated by this situation, we mainly focus on the reliability assessment of parameters derived by asteroseismology in next chapters 3 and 4.

Chapter 3

Basics of asteroseismology

3.1 History of the study of stellar pulsations

3.1.1 History of the discovery of variable stars

The variability of some stars has been known since centuries. Mira (a red-giant), observed by David Fabricius (1564-1617) and Johannes Holwarda (1618-1651), is the first star known to have luminosity variation recorded over time. With the development of photography, quantitative methods to evaluate the stellar luminosities were eventually made possible, so that more variable stars were found. The first mention of the term "stellar pulsation" was made by Arthur Eddington (1882-1944). Around the same time, major advances in astrophysics were achieved due to the characterization of Cepheids (a class of pulsator named after δ Cephei). These stars show luminosity variations of several magnitude. Leavitt & Pickering (1912) established that there was a direct dependence of the luminosity and pulsation period. This is possible only if those stars have similar mass and temperature, so that they can be used as "cosmic ruler". Based on that, distances of observed astronomical objects could be finally estimated. For example, the Magellanic cloud, which has been thought to be a part of our galaxy, was found to be outside the Milky Way. Edwin Hubble (1889-1953) used Cepheids to show that the universe is expanding, contrary to the dominant vision from Albert Einstein (1879-1955) at that time that the common view was that the universe was static. Stellar pulsations therefore allowed radical changes in our perception of the universe. With the resent advent of space missions such as SOHO, CoRoT, and *Kepler*, new major discoveries are made possible.

3.1.2 Understanding the Sun: History of the study of solar pulsations

The solar oscillations have been first detected by Leighton et al. (1962) and Evans & Michard (1962), whose origin could not be understood at all at that time. This has been known as solar 5-minute oscillation. The interpretation in terms of global oscillations due to solar acoustic waves was then given by Ulrich (1970) and Leibacher & Stein (1971), and later verified by

Deubner (1975). This is the birth of helioseismology, and enabled for the first time to probe the interior of the star with high precision, in a similar way to what Earth seismology can do. This is because the oscillation of stars induced by acoustic waves is tightly related to its internal structure. Sound waves travel at sound speed, which depends on the internal properties of the stars including pressure and density. Based on that, seismic investigation of the stars can uniquely deliver lots of information on the stellar interior for which other observation methods may not. Under the hydrostatic equilibrium, for example, the sound travel timescale is identical to the dynamical timescale of stars:

$$t_{\rm dyn} = \left(\frac{R_\star^3}{GM_\star}\right)^{1/2} \approx (G\rho_\star)^{-1/2}, \tag{3.1}$$

which clearly gives the stellar mean density. It predicts that younger stars, such as those in main-sequence phase, will oscillate with higher frequency, while evolved stars will oscillate with longer timescale. This is because stellar radius expands over the evolution while the mass remains almost constant. Furthermore, by looking at waves traveling in different layers of stellar interior, we can also probe density, pressure and temperature profiles inside the star (see below).

In principle, local sound waves (also called "p modes") are stochastically excited and damped due to the turbulent motion in the stellar outer convective layers. This excitation occurs at various frequencies. Waves produced locally near the surface of the star then interfere between each other to form global waves traveling within the stellar cavity. The process of excitation and damping of p mode oscillations can take place in any star which has a significant outer convective layer, i.e., stars with masses ranging from $0.8 - 1.6\,M_\odot$ for main-sequence stars. This is why solar-like stars, namely F, G, and K-type stars including the Sun, are likely to be the targets of frequency analysis.

Oscillatory phenomena can be observed as recurring expansion and contraction patterns of stellar surface because of the nature of the density waves. This type of oscillation can be observable both in photometry (intensity variation measurement) and spectroscopy (radial velocity variation measurement), because surface dynamical motion of expansion/contraction always accompanies with intensity variation via temperature variation [1]. It is clear that variations in intensity and radial velocity share a common period. For example, surface temperature (and intensity) becomes maximum when the surface is contracted the most, while minimum when the surface is expanded the most. Variation pattern of intensity can be seen in principle in the stellar time series, and variation pattern of radial velocity can be observed as periodic Doppler shift of stellar spectra.

In the case of the Sun, intensive and continuous observation has been operated to reveal the physics happening inside the Sun, both from ground and space-based observatories. There are some famous ground-based project of helioseismology such as Birmingham Solar Oscillations Network (BiSON) and Global Oscillations Network Group (GONG). For instance, BiSON is a global network of 6 ground-based instruments located at various longitudes on

[1] $I = \sigma_{\rm SB} T_{\rm eff}^4$, where I is intensity, $\sigma_{\rm SB}$ is Stefan-Boltzmann constant, and $T_{\rm eff}$ is stellar surface temperature.

the Earth; north/south America, north/south Africa, and west/east Australia. They are located so as to be able to continuously monitor the Sun and avoid observational interruptions due to day/night shifts. On the other hand, there are space-based instruments optimized for helioseismology, such as Solar and Heliospheric Observatory (SOHO) and Solar Dynamics Observatory (SDO). For instance, SOHO is located at the Lagrange point between Sun and Earth so that it can always keep the Sun in its view. The common characteristic of these instruments is that they are designed so that they can perform continuous monitoring of the Sun. Since helioseismology is analysis of the Solar photometry/spectroscopy in frequency domain, long and uninterrupted observation is highly required.

Helioseismology revealed the internal profiles of the Sun in great detail due to observations since decades. One of the most successful discovery is the precise identification of the base of the solar convective zone by detecting the sudden change of sound speed across the radiative/convective boundary (Basu et al. 1996). Moreover, the rotation profile inside the Sun has been found to be different from what the theory predicts (Schou et al. 1998, Thompson et al. 2003). Solar evolution model in the absence of angular momentum transport expects that the deep interior rotates ≈ 100 times faster than the envelope. Helioseismology demonstrated that this was not the case, suggesting that angular momentum transport should be more effective inside the Sun. Furthermore, current observation revealed that solar interior rotates as solid body, and solar envelope rotates faster at equator than at higher latitudes (latitudinal differential rotation). This discovery contributed to the advance of the stellar dynamics theory, involving any mechanisms at play inside the star such as dynamo motion, magnetic field, and angular momentum transport/redistribution.

Another important topic that helioseismology considerably contributed to, is the understanding of neutrino physics. It had been long know that the amount of neutrino detected in ground-based facilities is approximately half of what is predicted by the solar model theoretically. This neutrino deficit problem has been under debate whether it comes from poor modelling of solar interior or poor understanding of neutrino properties. Because helioseismology is a unique tool to model solar interior, it is recognized to be the key to reconcile this problem. Later a new model of neutrino was proposed, predicting that a e neutrino generated inside the Sun will change flavor possibly among μ or τ neutrino. This is known as the neutrino oscillation, and was confirmed later by detecting anomalous neutrino in Earth atmosphere by Super-Kamiokande (Fukuda et al. 1998). Therefore precise description of solar interior by helioseismology indeed promoted our understanding of not only astrophysics, but also particle physics.

As given above, the benefits from helioseismology has been delivered to various fields of (astro-)physics. Now we have the data from new observatories (CoRoT and *Kepler*) that can lead to great discovery again, which is discussed in next subsection.

3.1.3 The study of solar-like pulsations

Asteroseismology is the seismic investigation of the stars other than the Sun. Although theoretical background of asteroseismology is identical to that of helioseismology, its applicability has been rather limited, and only the Sun has been the major target for decades. This results

from the difficulty to conduct the long and uninterrupted monitoring for the stars other than the Sun, and due to the great distance separating us from stars. Before the launch of the space telescopes CoRoT and *Kepler*, there were a handful of stars for which asteroseismic analysis was possible. This includes the main solar-like stars; η Bootis (Bedding & Kjeldsen 1995), Procyon A (Barban et al. 1999), β Hydri (Bedding et al. 2001), α Centauri A (Bouchy & Carrier 2001, Bazot et al. 2007), μ Herculis (Bonanno et al. 2008), and 18 Scorpii (Bazot et al. 2011).

MOST (Microvariability and Oscillations of Stars; 2003-2014; Walker et al. 2003) and CoRoT (2006-2013) have entirely changed the situation and thoroughly demonstrated how powerful asteroseismology with space-borne instruments is (e.g., Benomar et al. 2009). MOST and CoRoT have been succeeded by *Kepler* (2009-2018), allowing to observe thousands of stars. These space telescopes performed photometric asteroseismology, because they do not have spectroscopic instruments on board. *Kepler* has observed $\approx 1.5\times10^5$ stars over 4 years of its primary operation mainly with 29.4 minutes exposure, with the so-called long cadence mode (LC, Gilliland et al. 2010). It also has 512 slots with 58.8 seconds exposure (short cadence; SC) to detect precise transit timing variation (TTV; Holman & Murray 2005, Agol et al. 2005) or follow the shape of transit ingress/egress in details (Winn 2010). Here exposure time (Δt) defines the maximum frequency that can be uniquely extracted in Fourier spectra from time series (Nyquist frequency); $\nu_{\rm Nyq} = 1/(2\Delta t) \approx 293\,\mu$Hz for LC and 8,496 μHz for SC. *Kepler* LC mode has been successful in detecting more than 15,000 solar-like pulsators in the evolved phase. Because typical oscillation frequency of the stars in main-sequence phase is found for frequencies higher than $\approx 1{,}000\,\mu$Hz, we need to rely solely on SC mode to detect their pulsations. By making use of 512 slots for SC mode, *Kepler* has detected ≈ 200 solar-like oscillators in main-sequence phase.

Figure 3.1 illustrates how stellar acoustic oscillations look like in Fourier spectra of time series (hereafter, "power spectra") for a typical main-sequence solar-like star Kepler-408. The *forest* of power excess (blue) at a few thousand μHz are the peaks corresponding to eigen-frequencies, and standing upon monotonically decreasing noise background (red). This noise is mostly due to the convective motion at the surface of the star (see subsection 3.2.5).

The fundamental properties of the star are related to the profiles of the observed peaks of eigen-modes. For example, the frequency of maximum amplitude, $\nu_{\rm max}$ ($\approx 2{,}100\,\mu$Hz in Figure 3.1), is supposed to scale with the stellar mass $M_\star$, radius $R_\star$, and effective temperature $T_{\rm eff}$ (e.g., Brown et al. 1991, Bedding & Kjeldsen 2003, Chaplin et al. 2008) as

$$\nu_{\rm max} \propto M_\star R_\star^{-2} T_{\rm eff}^{-1/2}. \tag{3.2}$$

Besides, Figure 3.1 suggests that the peaks of eigen-modes are regularly located with almost equal separation. This separation is approximated as $\approx\Delta\nu/2$, where $\Delta\nu$ (called "large separation" as will be shown in later sections) is directly related to the sound travel time across the stellar diameter, and is therefore sensitive to the mean stellar density $\bar{\rho}$ (e.g., Ulrich 1986) as

$$\Delta\nu \propto \bar{\rho}^{1/2} \propto M_\star^{1/2} R_\star^{-3/2}. \tag{3.3}$$

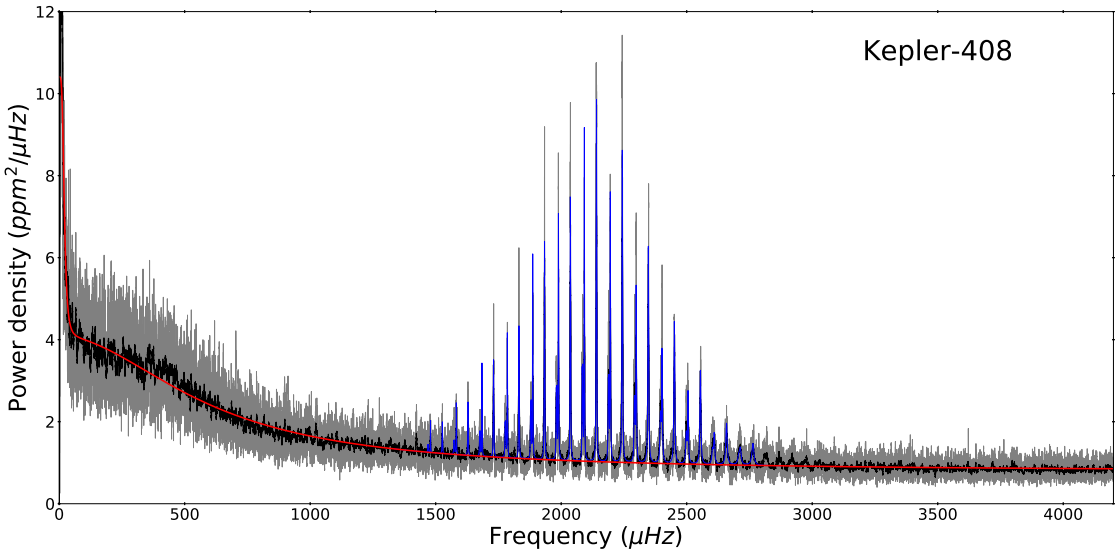

Figure 3.1: The overview of power spectra of main-sequence solar-like oscillator (Kepler-408). Gray and black correspond to different levels of smoothing of spectra. Red line is the modeled noise background, and blue is the fit to acoustic oscillation modes (see section 3.2). Although power spectra ranges up to Nyquist frequency of short cadence sampling ($\approx 8{,}500\,\mu$Hz), spectra only around power excess are shown just for clarity.

Table 3.1: Number of target stars of space instruments.

instrument	number of stars
before CoRoT	$\approx 100 - 1{,}000$
CoRoT	$\approx 10{,}000$
Kepler	$\approx 150{,}000$
TESS	$\approx 200{,}000$
PLATO	$\approx 1{,}000{,}000$

The full width at half maximum of the mode peak, or more commonly mode width Γ, is related to the mode lifetime $\tau = 1/\pi\Gamma$. Mode width increases with stellar effective temperature (Chaplin et al. 2009), reflecting shorter mode lifetimes τ in hotter stars. Therefore mode width is an indicator of the stellar spectrum type. In summary, the properties of oscillation modes in power spectra are tightly related to the fundamental stellar properties including mass, radius, and effective temperature. Therefore these scaling relations can be used to estimate the stellar fundamental properties from measured oscillation properties.

In the coming years, we expect some additional results from new space missions; TESS (Transiting Exoplanet Survey Satellite; already under operation) and PLATO (PLAnetary Transits and Oscillations of stars; planned for 2026). Table 3.1 summarizes the number of stars that was and will be observed for each space instrument. These promising future instruments are expected to make possible the full study of pulsators in all directions in the

sky with high completeness. Among them, it is of particular interest to study solar-like stars. This is because they are low mass stars and the most common stars in the universe, and also because they can be understood in details as we have the prototype of solar-like star next to us; the Sun.

The benefit from asteroseismology has been delivered in various aspects of astrophysics, both in stellar physics and stellar population. With small number of stars, a pioneering example of stellar physics revealed by asteroseismology is the fact that stellar internal rotation period is likely to be almost consistent with surface rotation (Benomar et al. 2015; Nielsen et al. 2015, 2017). Similarly to the Sun, this suggests that uniform rotation along with radial direction is likely to be achieved in main-sequence solar-like stars. This significantly contributes to evaluate the efficiency of angular momentum transport within each star during its evolution. Another leading work is on the spin-axis alignment of the stars that belong to the same open cluster (Corsaro et al. 2017). Thanks to the ability of asteroseismology to measure stellar inclination angle seen from us (sections 2.5, 3.2), Corsaro et al. (2017) reported a clustering of spin-axes in open clusters NGC 6791 (25 stars) and NGC 6819 (23 stars), which is very unlikely to happen by chance. Because the birth of stars is associated with the collapse of gas cloud, this could be the key to understand the angular momentum redistribution of molecular cloud to the dynamics of stars (proper motion, orbital motion, and rotation) due to the turbulence.

Moreover, asteroseismology is becoming an important method to study stellar populations across the Milky Way. This is because asteroseismology enables very precise and accurate measurements of stellar fundamental parameters such as radius (down to ≈ 2 percent) and mass (down to ≈ 4 percent), as well as age (down to ≈ 10 percent) with the stellar modeling [2]. These precisely-measured parameters are used to understand the structure of Milky Way, such as vertical age distribution of the galactic disk (Casagrande et al. 2016) and age distribution in globular clusters (Miglio et al. 2016). A series of these study is now established as an important field of astrophysics, "Galactic archaeology" (Miglio et al. 2017).

Asteroseismology can also play an essential role in current and future characterization of exoplanets (Ragazzoni et al. 2016). Indeed, the most basic parameters such as the radius and mass of exoplanets are usually derived on the basis of those of their host stars. This is because, for example, transit method gives planet-to-star size ratio alone. Thus the precise determination of the fundamental parameters of host stars are of significant importance. Another important quantity that asteroseismology can also deliver uniquely is the tilt of stellar spin axis measured from line of sight; stellar inclination angle $i_\star$ as introduced in chapter 2. This angle can be helpful in constraining planetary orbits, inferring possible planet migration scenario. Such synergies between exoplanets and asteroseismology can lead to breakthrough in our understanding of the planet formation and evolution.

In recent works, actually, more and more authors have been getting interested in asteroseismology of solar-like stars with exoplanets. Consequently, statistical works on asteroseis-

[2]For example, there are 66 best-studied dwarfs for which radii, masses, and ages are determined with comparison with the stellar models. They have been observed for at least ≈ 1 year and at best ≈ 4 years campaign and are called the *Kepler* asteroseismic LEGACY sample after the end of *Kepler* primary mission (Lund et al. 2017, Silva Aguirre et al. 2017).

mic characterization of planets has been presented (Huber et al. 2013b, Silva Aguirre et al. 2015, Campante et al. 2016, Davies et al. 2016). In addition, some focused on the orientation of stellar spin axis with asteroseismology; Kepler-50 and 65 (Chaplin et al. 2013), Kepler-56 (Huber et al. 2013a), HAT-P-7 (Lund et al. 2014b, Benomar et al. 2014), and Kepler-25 (Benomar et al. 2014). Because the ability of asteroseismology to measure stellar inclination is one of the most important topics in this thesis, we introduce theories of stellar acoustic oscillation and demonstrate how stellar inclination can be determined within that framework in the next section.

3.2 Theory of stellar internal structure and pulsations

Star is a ball of plasma gas at thermal and hydrostatic equilibrium maintained by a balance between nuclear fusion and gravity. Because nuclear fusion of hydrogen does not occur in the gaseous body below $\approx 0.08\,M_\odot$, it defines the minimum mass for "stars". Low mass gaseous body that cannot ignite hydrogen is called either "brown dwarf", that mildly shines by the nuclear fusion of deuterium, or "planet", that faintly shines by its gravitational contraction [3]. All gaseous bodies across the entire HR diagram are known to pulsate, even including dead stars (white dwarf, neutron stars, pulsar, ...) and planets (e.g., global Jovian pulsation detected by Gaulme et al. 2011). Among such pulsators, low mass stars ($0.8\,M_\odot \lesssim M_\star \lesssim 2.5\,M_\odot$) are often referred as solar-like stars. The Sun, the best known solar-like star, has radiative core ($R \lesssim 0.7\,R_\odot$) in which energy is transported by radiation. This radiative core is covered by convective envelope ($R \gtrsim 0.7\,R_\odot$) in which energy is transported by convection of fluid materials. The solar convective layer is thick enough to sustain long-lived global acoustic oscillation, which enabled helioseismology to investigate the solar internal structure and rotation profiles as mentioned in section 3.1. Any other main-sequence solar-like stars are expected to have similar property, except those with $M_\star \gtrsim 1.1\,M_\odot$ that begin to have a convective core according to theory and recent observations from CoRoT and *Kepler*. Evolved solar-like stars (stars that have depleted their core hydrogen) are found to have very different internal properties, but they are not the topic of this thesis and they will not be discussed here.

3.2.1 Equations of internal structure and stellar pulsations

Based on physical properties, the internal structure of the stars can be described in the basic equations below;

- The equation of continuity

$$\frac{\partial \rho}{\partial t} + \nabla\cdot(\rho \boldsymbol{v}) = 0, \tag{3.4}$$

[3] The mass that separates the brown dwarfs and the planets is $\approx 13\,M_{\rm J}$.

where $\rho = \rho(t, \boldsymbol{r})$ and $\boldsymbol{v} = \boldsymbol{v}(t, \boldsymbol{r})$ are density and local instantaneous velocity of fluid element at time t and position $\boldsymbol{r}$. The local time derivative $\partial/\partial t$ is the time derivative at a fixed point.

- Equations of motion

$$\frac{\partial \boldsymbol{v}}{\partial t} + (\boldsymbol{v}\cdot\nabla)\boldsymbol{v} = -\frac{1}{\rho}\nabla p + \nabla\Phi, \tag{3.5}$$

where $p = p(t, \boldsymbol{r})$ and $\Phi = \Phi(\boldsymbol{r})$ are pressure and gravitational potential at time t and position $\boldsymbol{r}$.

- Poisson's equation

$$\nabla^2\Phi = 4\pi G\rho, \tag{3.6}$$

where G is gravitational constant.

- Energy equation

$$\rho T\left(\frac{\partial}{\partial t} + \boldsymbol{v}\cdot\nabla\right) S = \rho\epsilon - \nabla\boldsymbol{F}, \tag{3.7}$$

where $T = T(t, \boldsymbol{r})$, $S = S(t, \boldsymbol{r})$, $\epsilon = \epsilon(t, \boldsymbol{r})$, and $\boldsymbol{F} = \boldsymbol{F}(t, \boldsymbol{r})$ are temperature, entropy, the rate of energy generation per unit mass (e.g., mostly from nuclear reactions in the core), and the density of energy flux. In general, $\boldsymbol{F}$ describes any ways of energy transportation; radiation, convection, and conduction. In most cases molecular conduction is almost negligible. The term $\nabla\boldsymbol{F}$ term depends on the location inside the star; radiative energy transport dominates in the inner core, while convective energy transport dominates in outer envelope. In most cases, convective motion of fluid materials is too complex to be handled in analytically or numerically. Therefore they are often described by performing averages over the typical scales of convective motion, whose familiar example is the mixing-length theory.

Based on these basic equations, stellar pulsations can be modelled by a first order perturbative approach;

$$X = X_0 + \delta X, \tag{3.8}$$

where X_0 represents equilibrium (static) states of physical parameter X, and δX describes perturbation imposed on X.

In addition, we assume the adiabatic pulsations of stars; heating timescale (principally the order of Kelvin-Helmholtz timescale) is much longer than pulsation timescale (the order of minutes to hours). This adiabatic approximation states that time-derivative terms are much larger than heating terms in equation (3.7), therefore enabling to neglect the terms in right-hand side. This simplifies equation (3.7) to

$$\frac{\mathrm{d}p}{\mathrm{d}t} = \frac{\Gamma_1 p}{\rho}\frac{\mathrm{d}\rho}{\mathrm{d}t}, \tag{3.9}$$

where

$$\Gamma_1 = \left(\frac{\partial \ln p}{\partial \ln \rho}\right)_{\rm ad} \tag{3.10}$$

is an adiabatic exponent, and the time derivative

$$\frac{\mathrm{d}}{\mathrm{d}t} = \frac{\partial}{\partial t} + (\boldsymbol{v}\cdot\nabla), \tag{3.11}$$

following the motion of the gas, is the material time derivative. This equation is identical to equation of state, relating p and ρ of the gas element in the star.

To enable the simple analytic approach, we further assume spherical star; $X_0(t, \boldsymbol{r}) = X_0(t, r)$. This implies that stellar equilibrium state varies only with time and radius and does not depend on polar and azimuthal angle. This leaves basic equations to 1-dimensional problem. Moreover, we assume stationary equilibrium; $X_0(t, \boldsymbol{r}) = X_0(r)$. This allows us to eliminate time-derivative terms in the basic equations; $\mathrm{d}X_0/\mathrm{d}t = 0$.

Based on these equations and simplifications, we can analytically get perturbations on p, $\boldsymbol{r}$, Φ, namely, δp, $\delta \boldsymbol{r}$, $\delta\Phi$. Stationary equilibrium implies the independence between space and time variables. Therefore solution of perturbative approach to scalar variable (p and Φ) takes the form of

$$\delta X(t, \boldsymbol{r}) = \delta X(\boldsymbol{r}) \exp(-i\omega t). \tag{3.12}$$

Consequently δX is eigen-function of the operator defined by spherical harmonics as

$$Y_l^m(\theta, \phi) = (-1)^m \sqrt{\frac{(2l+1)(l-m)!}{4\pi(l+m)!}} P_l^m(\cos\theta) \exp(im\phi), \tag{3.13}$$

where P_l^m is the associated Legendre polynomials with degree l and order m. Angular variables θ and ϕ correspond to co-latitude (polar angle measured from north pole) and longitude on the sphere, respectively. It is then possible to show that the solutions for the perturbed quantities can be written as

$$\delta X(t, r, \theta, \phi) = X_{\alpha,l,m}(r) Y_l^m(\theta, \phi) \exp(-i\omega_{\alpha,l,m} t) \tag{3.14}$$

with $\omega_{\alpha,l,m} = 2\pi\nu_{\alpha,l,m}$ being pulsation frequency of the modes (α, l, m). In addition, the displacement eigen-functions $\delta\boldsymbol{r}$ can be written in the form of

$$\boldsymbol{\delta r} = \begin{pmatrix} \xi_r(r) Y_l^m(\theta,\phi) \boldsymbol{e}_r \\ \xi_\perp(r) \frac{\partial Y_l^m(\theta,\phi)}{\partial\theta} \exp(-i\omega_{\alpha,l,m}t) \boldsymbol{e}_\theta \\ \xi_\perp(r) \frac{1}{\sin\theta} \frac{\partial Y_l^m(\theta,\phi)}{\partial\phi} \exp(-i\omega_{\alpha,l,m}t) \boldsymbol{e}_\phi \end{pmatrix}, \tag{3.15}$$

where $\xi_r(r)$ and $\xi_\perp(r)$ are the amplitudes of the spatial displacement along with radial and tangential direction, respectively. The unit vectors of radial, polar, and azimuthal direction are given by $\boldsymbol{e}_r$, $\boldsymbol{e}_\theta$, and $\boldsymbol{e}_\phi$, respectively. In the expressions above α is an arbitrary real

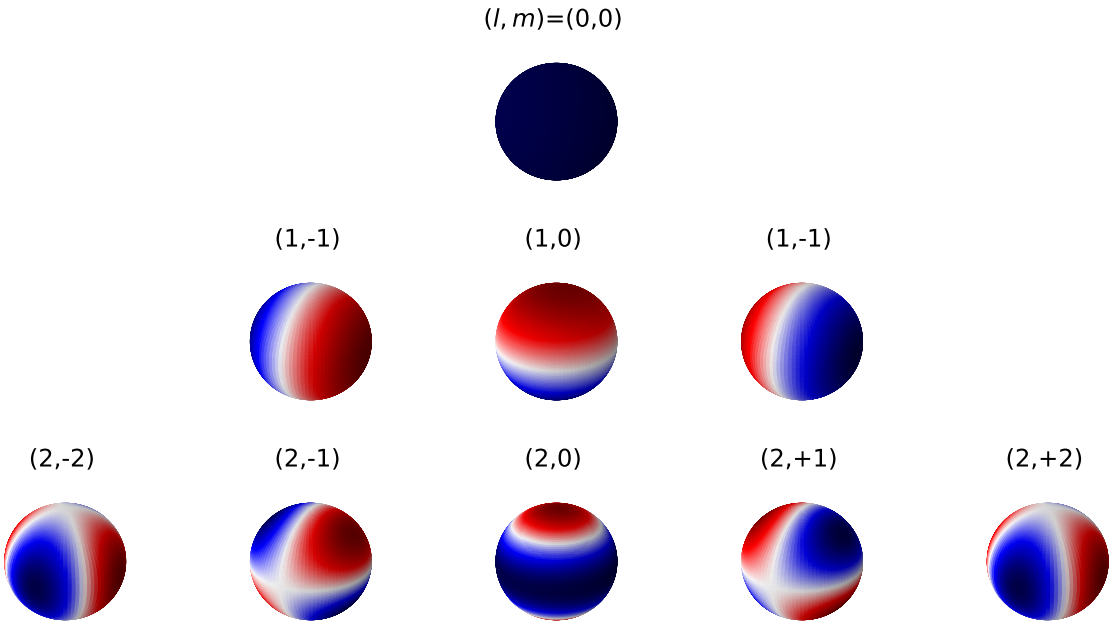

Figure 3.2: Contour maps of the real part of spherical harmonics $Y_l^m(\theta, \phi)$ (equation 3.8) for $l = 0$ (top), $l = 1$ (middle), and $l = 2$ (bottom) modes. Blue and red colors have the opposite phases of stellar pulsation motion. The $\theta = 0^\circ$ axis is inclined towards the viewer for the clearer visibility.

number, but due to boundary conditions at the surface and in the interior, we can replace it by an integer n such that each pulsation is described by (n, l, m).

Among three indices (n, l, m), the index n is referred to as a radial order, corresponding to the number of nodes of sound wave along with radial direction. Second, the index l is referred to as an angular degree, representing the number of nodes of sound wave on stellar surface. Third, the index m is referred to as an azimuthal order, counting the number of nodes of sound wave *across an equator* on the stellar surface. Obviously, m cannot be greater than l ($-l < m < +l$). Figure 3.2 introduces the examples of oscillation patterns and their visibilities for various combination of (l, m). Mode with $l = 0$ is a simple radial oscillation, at which all the stellar surfaces pulsate with common phase, preserving spherical symmetry. As l increases, however, the stellar oscillation becomes more complicated. Mode with $l > 0$ is called non-radial pulsation, where different area of stellar surface has different phase of oscillation. For example, the mode with $(l, m) = (1, 0)$ corresponds to the hemispherical oscillation, at which northern (southern) hemisphere expands (contracts) while the other contracts (expands) in turn. What we actually observe is the superposition of all possible modes, especially high radial orders ($10 \lesssim n \lesssim 25$) and low angular degree ($l \lesssim 3$) (see Figures 3.1 and 3.5).

We cannot resolve the oscillatory motion over the stellar disk in *Kepler* stars, and then

they show themselves only as point sources. In other words, we are observing the flux integrated over the stellar disk for *Kepler* stars. Since oscillation mode gets much more complicated as angular degree l increases, the mode patterns with higher l are more likely canceled out. Therefore the modes with higher l have very small amplitudes in the integrated flux. Actually, mode patterns are visible typically up to $l = 2$ for *Kepler* stars [4] , unlike the Sun for which we can resolve disk intensity/velocity such that it is possible to observe up to $l\approx$1,500.

3.2.2 Properties of the oscillations: The Cowling approximation

In the perturbative approach, assumptions of adiabaticity and sphericity greatly help modelling the stellar internal structure. Here we impose another approximation that the perturbation to the gravitational potential can often be neglected ($\delta\Phi \approx 0$) in order to enable the simple analytic description of stellar interiors. This approximation is valid when either l or n is large, and for the stars observed by CoRoT and/or *Kepler* the latter is often the case. Indeed we often observe modes of $n = 10 - 20$ for main-sequence solar-like stars. For large n, the density profile inside the star rapidly changes in radial direction so that most perturbations will be canceled out when integrated over radius. This allows us to safely neglect $\delta\Phi$ in differential equations. In addition, it is also reasonable for higher n modes to assume that pressure scale height ($H_p \equiv \left(-\frac{\mathrm{dln}p}{\mathrm{d}r}\right)^{-1}$) is much larger than the varying scale of eigen-functions (δp or ξ_r). This enables to ignore the terms that have $\delta p/H_p$ or ξ_r/H_p in differential equations.

All approximations above leave a single second-order differential equation for ξ_r as

$$\frac{\mathrm{d}^2\xi_r}{\mathrm{d}r^2} = -K(r)\xi_r, \tag{3.16}$$

where $K(r)$ is

$$K(r) = -\frac{\omega^2}{c^2}\left(1 - \frac{N^2}{\omega^2}\right)\left(1 - \frac{S_l^2}{\omega^2}\right), \tag{3.17}$$

and $c = \sqrt{\Gamma_1 p/\rho}$ is the adiabatic sound speed. In equation (3.17), two characteristic frequencies are introduced; acoustic frequency S_l (also called *Lamb* frequency) and buoyancy frequency N (also called *Brunt-Väisälä* frequency). They are written as

$$S_l^2 = \frac{l(l+1)c^2}{r^2}, \tag{3.18}$$

and

$$N^2 = g\left(\frac{1}{\Gamma_1 p}\frac{\mathrm{d}p}{\mathrm{d}r} - \frac{1}{\rho}\frac{\mathrm{d}\rho}{\mathrm{d}r}\right), \tag{3.19}$$

[4]For high signal-to-noise ratio stars, namely *Kepler* magnitude of $V \lesssim 7$, even $l = 3$ modes can be apparent in power spectra and useful to the analysis; for example, 16 Cyg A and B with $V = 5.86$ and 6.09 (Davies et al. 2015).

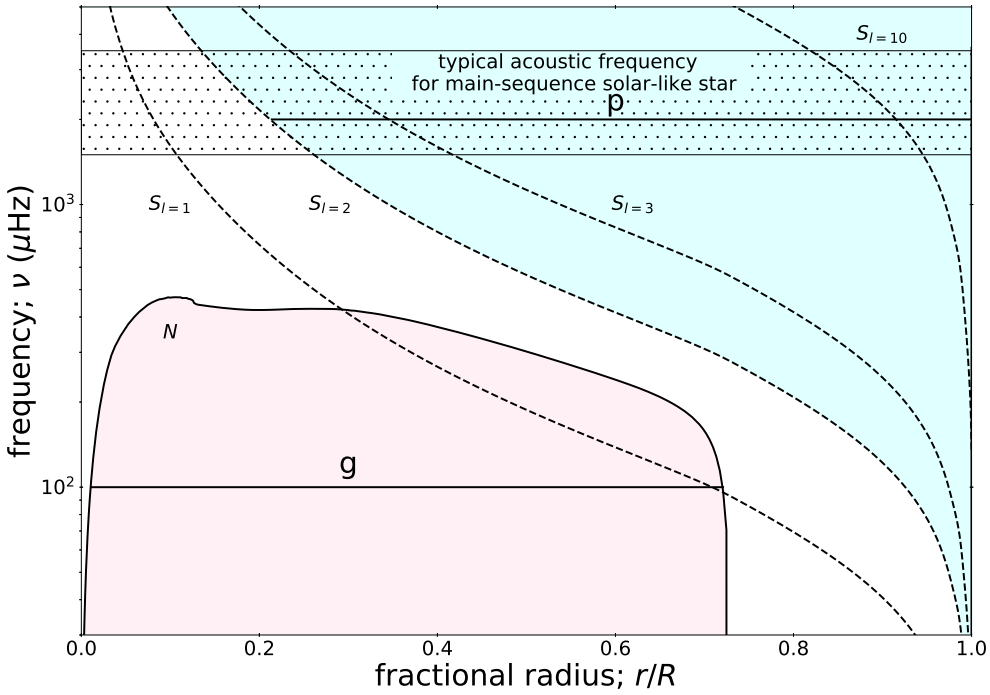

Figure 3.3: Propagation diagram of p and g modes for a star with $M_\star = 1.0\,M_\odot$ and [Fe/H] = 0.0 at the age of 4.6 Gyr. Acoustic frequency S_l is drawn in dashed lines for $l = 1$, $l = 2$, $l = 3$, and $l = 10$. Buoyancy frequency N is drawn in solid line. This diagram is computed by MESA code (Modules for Experiments in Stellar Astrophysics; Paxton et al. 2011, 2013, 2015, 2018). Blue region shows trapping region of quadrupole p mode (condition a), while red region represents trapping region of g modes (condition b). Black dotted band represents the typical frequency range of acoustic oscillation for main-sequence solar-like star ($1{,}500 - 3{,}500\,\mu$Hz).

where $g = -\frac{1}{\rho}\frac{\mathrm{d}p}{\mathrm{d}r}$ is the gravitational acceleration inside the star.

Equations (3.16) obviously predicts that the perturbation can be oscillatory when $K(r) > 0$, while decays exponentially when $K(r) < 0$. The former case can be reduced to two conditions;

a) $\omega > |N|$ and $\omega > S_l$,

b) $\omega < |N|$ and $\omega < S_l$.

For a given frequency, there may be several regions where wave oscillates, intervened by the regions where it decays. The solution is then said to be *trapped* in the region that satisfies condition a) or b). The boundary between trapping zone and decaying zone is defined by $K(r) = 0$, which is known as *turning points* of propagating waves.

Figure 3.3 describes acoustic frequency S_l and buoyancy frequency N as a function of fractional radius of the star. This diagram allows to visualize the behavior of these characteristic frequencies. For example, S_l decreases from the stellar core to surface, while N

takes positive values only at stellar interior. The region that satisfies condition a) for $l = 2$ is colored in blue, while condition b) is in red. For these modes, the white region is the zone in which waves cannot live long and then distinguishes the trapping zones. In the blue region, the modes behave as "p modes" (higher frequency, where the pressure force dominates in equation 3.16), while in the red region the modes behave as "g modes" (lower frequency, where the buoyancy force dominates). On one hand, p modes are standing acoustic waves, whose restoring force is pressure gradient. On the other hand, g modes have gravity as restoring force (see next subsection for details). Figure 3.3 predicts that p modes exists mainly outer layer of the star (the horizontal solid bar labelled "p"), while g modes are trapped deep inside the star (the horizontal solid bar labelled "g"). We will discuss mainly p modes in what follows because g modes cannot be observed in main-sequence stars (even in the Sun), that is, the stars which will be analyzed in later chapters.

3.2.3 Acoustic waves: p modes

Acoustic p modes are trapped between inner turning point $r = r_t$ and the surface. In other words, sound waves can be oscillatory in $r \in [r_t, R]$, while damps exponentially in $r \in [0, r_t]$. Here the inner turning point is defined by $S_l(r_t) = \omega$ so that $K(r) = 0$, which gives

$$\frac{c^2(r_t)}{r_t^2} = \frac{\omega^2}{l(l+1)}. \tag{3.20}$$

This r_t defines the deepest stellar layer that acoustic wave can propagate as a function of l and ω.

For p modes, which have typical frequency of a few thousand μHz, we usually suppose $\omega \gg N$. Therefore $K(r)$ can be approximated to be

$$K(r) \approx \frac{1}{c^2}(\omega^2 - S_l^2). \tag{3.21}$$

Because of the similarity of this relation to a plane sound wave (i.e., $\omega^2 = c^2k^2$ with k being the wave number), it can be said that the dynamics of p modes is solely determined by the variation of the sound speed with r. This is why p modes can be understood as acoustic waves [5].

The dynamics of p modes inside the star can be understood in terms of ray theory. As the wave dives into the star more deeply, the material density gets higher ($\partial\rho/\partial r < 0$) such that the deeper parts of the wave fronts experience a higher sound speed and therefore travels faster. Consequently, the direction of propagation will be bent away from radial direction. This is the nature of waves traveling across medium with varying density. This

[5]On the other hand, g modes have gravity as the restoring force. The buoyancy frequency N corresponds to the frequency of the motion of "blob" in convective stability. If fluid element is displaced adiabatically and the density of surroundings is smaller than the element, then buoyancy forces it back towards original position. This leads to oscillatory motion of fluid elements around equilibrium position. Because g modes cannot be present in convective layer, the sudden drop of buoyancy frequency N toward zero at $r/R \approx 0.7$ in Figure 3.3 indicates the base of convective zone.

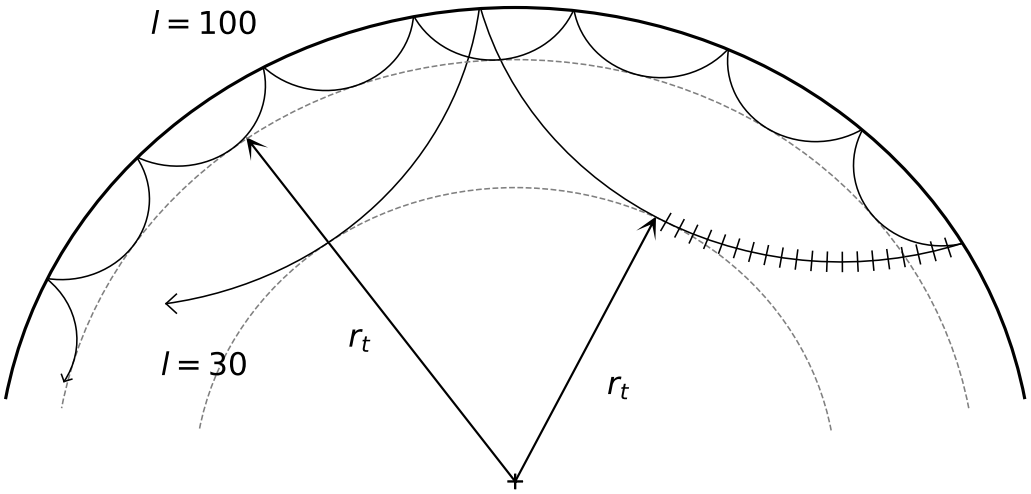

Figure 3.4: Schematic illustration of acoustic wave propagation. Deeply (shallowly) penetrating rays correspond to $l = 30$ ($l = 100$) modes with the frequency of $\nu = 3{,}000\,\mu$Hz. The lines orthogonal to the former path of propagation correspond to the wave fronts.

is schematically illustrated in Figure 3.4. The standing acoustic wave that departs from the stellar surface inwards will be bent as it travels, and mostly goes back to the surface after reflected by the turning point r_t. It will be also essentially reflected by stellar surface R because of the sharp density gradient near the surface, and again dives into stellar interior. Global acoustic oscillation of the star is the recurring process of this phenomena.

Solutions of equation (3.16) also predict that modes with smaller l penetrates the star more deeply, while modes with higher l will be essentially trapped in outer layer (see also Figure 3.3). To be extreme, $l = 0$ will no longer experience the refraction, and penetrate stellar core, and reaches the stellar surface opposite to the starting point. This is the theoretical basis for the property of asteroseismology that different l modes can reveal different layers of stellar interior.

Tassoul (1980) showed that in first approximation, the pulsation frequency of p modes is a linear function of n and l;

$$\nu(n,l) = \frac{\omega(n,l)}{2\pi} \approx \left(n + \frac{l}{2} + \varepsilon_{n,l}\right)\Delta\nu + \delta_{n,l}, \tag{3.22}$$

where

$$\Delta\nu = \left(2\int_0^R \frac{\mathrm{d}r}{c(r)}\right)^{-1} \tag{3.23}$$

is the inverse of the sound travel time inside the star. Then $\varepsilon_{n,l}$ is a small correction of order

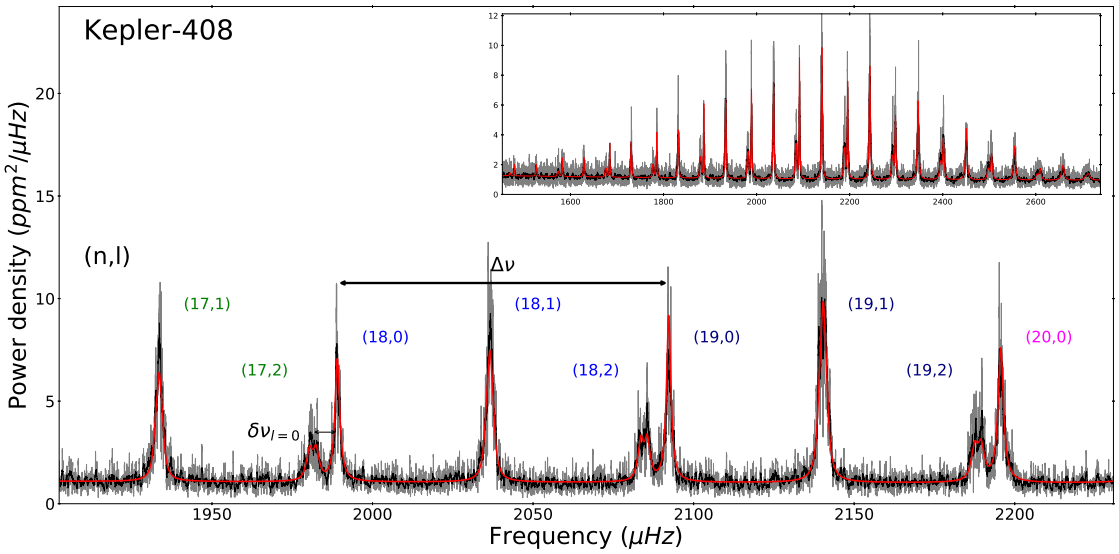

Figure 3.5: Zoom-in view around maximal power of stellar oscillation modes for typical main-sequence solar-like oscillator Kepler-408. Gray and black correspond to different levels of smoothing of spectra, and red is the best fit. Radial orders and angular degrees (n, l) are accompanied next to each mode. Long arrow indicates the extent of large separation $\Delta\nu$, and short arrow is for small separation $\delta\nu_l$ (see text). The upper inset describes the entire power excess due to acoustic oscillation as in Figure 3.1.

unity [6] (e.g., Tassoul 1980, 1990, Mosser et al. 2013). The additional term $\delta_{n,l}$ is related to the sound speed at different depths (see below).

Equation (3.22) clearly predicts that any radial order modes n belonging to the same degree l show up with regular spacing of $\Delta\nu$, and in similar way, any degree modes l belonging to the same radial order n with regular spacing of $\Delta\nu/2$ (Figure 3.5). For this reason $\Delta\nu$ is referred to as a *large separation* (a frequency spacing between consecutive radial modes). Based on this property, the modes of $(n, l) = (n_0 - 1, 2)$ and $(n_0, 0)$ will be found close to each other, and the same is the case with $(n_0 - 1, 3)$ and $(n_0, 1)$ for the stars with visible $l = 3$ modes. Figure 3.5 provides close-up view of three sequential radial order modes n for typical main-sequence solar-like oscillator. We find modes are located fairly regularly, and $l = 0$ and $l = 2$ modes appear together. Furthermore, the additional term $\delta_{n,l}$ is written as

$$\delta_{n,l} = -l(l+1)D_0, \tag{3.24}$$

where D_0 is positive constant that reflects the conditions in the stellar core. This is based on the fact that different l modes have different sensitivity to stellar interior along with radial direction (i.e., small l modes dive star into the radiative core, while large l modes are bound

[6] Actually, observations find $0.8 \lesssim \varepsilon_{n,l} \lesssim 1.6$ for main-sequence solar-like stars (White et al. 2012). Since the (n, l) dependence (i.e., frequency dependence) of $\varepsilon_{n,l}$ is very weak, $\varepsilon_{n,l}$ does not violate the regularity of the location of eigen-modes.

in outer convective layer). Therefore, $l = 2\,(3)$ modes appear always in slightly smaller frequency than $l = 0\,(1)$ by

$$\delta\nu_l = \nu(n,l) - \nu(n-1,l+2) \approx \delta_{n,l} - \delta_{n-1,l+2} = (4l+6)D_0. \tag{3.25}$$

This difference in frequency $\delta\nu_l$ is called *small separation*, and useful to infer the physics at different stellar radii.

This regularity of modes becomes fairly apparent when we plot the spectra modulo $\Delta\nu$ (Échelle diagram, Figure 3.6). This figure includes entire frequency range of oscillation over y-axis, and x-axis is frequency modulo $\Delta\nu$ so that each $l = 0, 1, 2$ mode shows up only once along with x-axis. The power density of modes is described as contour map. The sequence of $l = 1$ modes for different n (green) is apparent on the right side of Figure 3.6, while $l = 0$ (red) and 2 (blue) are on the left side together. This Échelle diagram greatly helps the correct identification of oscillation modes, especially for lower/higher ends of frequency where modes are difficult to be identified because of noise.

The m dependence of eigen-frequencies, that we did not discuss above, shows up in much smaller frequency scale ($\approx$ a few μHz) and is tightly related to the stellar rotation. Since the estimate of the stellar inclination relies on the slight difference among m modes (as will be discussed later), the frequency resolution of power spectra [7] needs to be fine enough. This is why $i_\star$ measurement through asteroseismology has not been made possible until the onset of long observation with space observatories.

For non-rotating stars, the eigen-frequency is independent of m (equation 3.22). On the other hand, the central frequency for rotating stars becomes

$$\nu(n,l,m) = \nu(n,l) + m\delta\nu_\star \approx \left(n + \frac{l}{2} + \varepsilon_{n,l}\right)\Delta\nu + \delta_{n,l} + m\delta\nu_\star, \tag{3.26}$$

where $\delta\nu_\star$ is approximately the inverse of an *average* of the rotational period over the stellar interior, and is called stellar rotational splitting (see e.g., Appourchaux et al. 2008). Thus, the degeneracy among m modes can be broken due to the stellar rotation; rotation makes the frequency of modes with $m \neq 0$ in power spectra shifted by rotational frequency of the star ($\delta\nu_\star \approx 1/P_{\rm rot}$). Equation (3.26) predicts that due to rotation $l = 1$ modes will be split into three ($m = -1, 0, +1$) with equal spacing of $\delta\nu_\star$ [8] , and $l = 2$ into five ($m = -2, -1, 0, +1, +2$). Radial mode ($l = 0$) is not affected by rotation because it does not propagates along horizontal direction.

[7] Frequency resolution is inversely proportional to total observational duration $T_{\rm obs}$.

[8] Departures from this regularity can be used to infer the stellar sphericity. It is known that stellar rotation and magnetic field cause distortion of the star into either oblate or prolate shape. In the distorted star the acoustic distance for the sound wave slightly changes, which is understood as asymmetrical location among m-components. Gizon et al. (2016) measured the oblateness of KIC 11145123 and found $\Delta R/R = (1.8 \pm 0.6)\times10^{-6}$ ($\Delta R \approx 3\,$km for $R = 1.56\times10^6\,$km), concluding that this star is the most *round* object in the entire universe. We do not take into account mode asymmetry in this thesis, because it is beyond the scope of the purpose of this work.

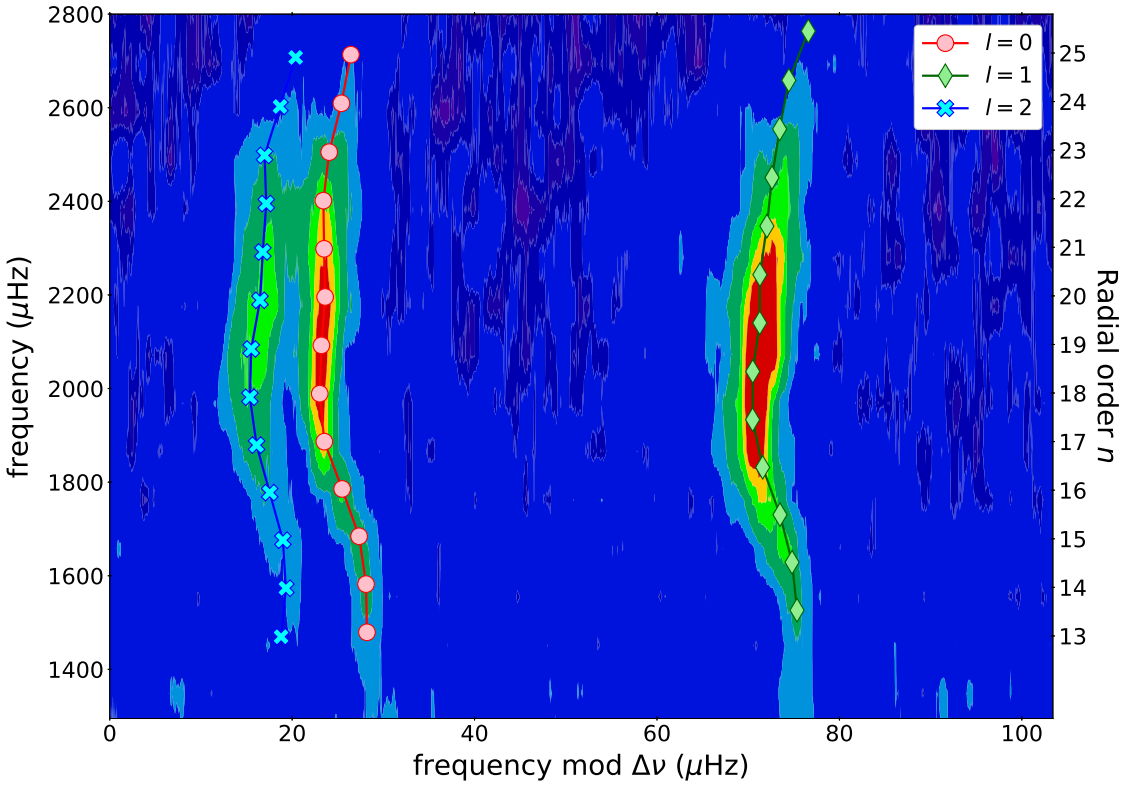

Figure 3.6: Échelle diagram of main-sequence solar-like oscillator Kepler-408. y-axis is the entire frequency range within which power excess due to acoustic oscillation is found. x-axis is frequency modulo large separation ($\Delta\nu = 102.6\,\mu$Hz). Color contour shows the power density at each frequency. Radial order n increased from bottom to top, and red, green and blue symbols connect a series of $l = 0$, 1, and 2 modes with different n, respectively.

3.2.4 Excitation mechanism of p modes

Understanding the mode excitation mechanism is necessary to derive the shape of the mode profile. The mechanism proposed by Goldreich & Keeley (1977) assumes that stellar modes are stochastically excited by convection motions and damped by dynamical and thermal effects. This profile is the consecutive re-excitations of surface waves in random phase and amplitude. Because of the broad spectrum of the energy offered by convective phenomena (e.g., Kolmogorov 1941a,b), this mechanism allows the excitation of a large number of eigen-modes.

At first approximations, each eigen-mode can be represented by a damped and randomly re-excited oscillation by interaction with turbulent convection. The amplitude of these modes is therefore the solution of the forced oscillation (Anderson et al. 1990),

$$\frac{1}{\omega_0^2}\frac{\mathrm{d}^2 y(t)}{\mathrm{d}t^2} + \frac{2\pi\Gamma}{\omega_0^2}\frac{\mathrm{d}y(t)}{\mathrm{d}t} + y(t) = f(t), \tag{3.27}$$

where $y(t)$ represents the spatial displacement, ω_0 is the proper pulsation frequency of the undamped oscillator, Γ (time-independent constant) is the inverse of characteristic damping timescale, and $f(t)$ is a stochastic function that describes the excitation source. A series of solutions from equation (3.27) can be formulated as a convolution;

$$y(t) = (h*f)(t) = \int_{-\infty}^{+\infty} h(u)f(t-u)\mathrm{d}u, \tag{3.28}$$

where $h(u)$ is the response to the impulse of the system, which is of peculiar interest to model the mode profile. Fourier transform of equation (3.28) gives

$$Y(\nu) = H(\nu)F(\nu), \tag{3.29}$$

where $Y(\nu)$, $H(\nu)$, and $F(\nu)$ denote the Fourier transforms of $y(t)$, $h(t)$, and $f(t)$, respectively. By replacing $f(t) = \delta(t - t_0)$ with t_0 being the moment of the impulse, we calculate the response to the impulse from equation (3.27),

$$H(\nu) = \frac{\nu_0^2 e^{2i\pi\nu t_0}}{\nu_0^2 - \nu^2 + i\Gamma\nu}. \tag{3.30}$$

For main-sequence stars, the frequency of pulsations is relatively high ($\nu_0 \gtrsim 1{,}000\,\mu$Hz). Assuming that solar-like stars take similar values of Γ to that of the Sun ($\approx 1\,\mu$Hz), it can be estimated that $\Gamma \ll \nu_0$. Thus the profile of a mode in the power spectra can be easily deduced as

$$P(\nu) \propto |H(\nu)|^2 \approx \frac{H}{1 + 4(\nu - \nu_0)^2/\Gamma^2}. \tag{3.31}$$

Therefore each mode of damped stellar pulsation, whose excitation source is turbulent convection, is theoretically well represented by a Lorentzian in the power spectra.

As a consequence, the entire power spectra $P(\nu)$ are well approximated by superposition of all possible oscillation modes (n, l, m):

$$P(\nu) = \sum_{n=n_{\min}}^{n_{\max}} \sum_{l=0}^{l_{\max}} \sum_{m=-l}^{+l} \frac{H(n,l,m,i_\star)}{1 + 4[\nu - \nu(n,l,m)]^2/\Gamma^2(n,l,m)} + N(\nu), \tag{3.32}$$

where $N(\nu)$ is a background model (see next subsection). Here $H(n, l, m, i_\star)$, $\Gamma(n, l, m)$, and $\nu(n, l, m)$ are height, width (inverse of characteristic lifetime), and central frequency of mode with (n, l, m), respectively. Note that the dependence on $i_\star$ is entirely imprinted in its height $H(n, l, m, i_\star)$ as we demonstrate later. The asteroseismic analysis in this work is the fit of the model above against stellar power spectra, optimizing model parameters in the Bayesian manner with Markov Chain Monte Carlo (MCMC) sampling method (Details are described in section 3.3).

3.2.5 Noise background: Origin and modelling

On the surface of the Sun, convective phenomena are visible in the form of granules. Any stars with convective envelope have this type of surface structure (up to $\approx 2.5\,M_\odot$). A granule corresponds to rising bubble of a hot plasma from the depths to the surface. Around granule, on the other hand, there is the flow of descending cold material that enters the deeper layers of the stellar surface. By this contrast effect, the hotter surface areas appear shiny, while cooler areas are dark. It is difficult to quantify the size and lifetime of granules because there is a whole spectrum of almost continuous sizes of convective structure ranging from a few 10^5 m (granulation) to about 5×10^7 m (super-granulation). The associated characteristic lifetimes range from a few minutes (transporting small amount of energy) to several tens of hours (transporting lots of energy). This convective phenomena are also manifested in time series.

Another source of periodicity in the solar time series comes from the active regions. Active regions are the areas of intense magnetic field, and the convective movements are inhibited by the field there. As a result, the active regions correspond to the plasma cooler than the surrounding environment (up to 2,000 K less), known as spots.

In the power spectrum, these two phenomena are fairly well reproduced by a generalized semi-Lorentzian

$$L(\nu) = \frac{4\sigma^2\tau}{1 + (2\pi\tau\nu)^p} = \frac{A}{1 + (B\nu)^p}, \tag{3.33}$$

where σ is the intensity of the process, τ is characteristic lifetime, and p is a parameter depending on the nature of the phenomenon and its degree of spatial and temporal coherence. Empirically Harvey (1985) used this formula to describe the solar power spectra with $p = 2$, and then equation (3.33) is also called Harvey-like profile.

Because the pulsation in main-sequence stars occurs at high frequency, it suffices to consider only two Harvey-like profiles for the total background model (Appourchaux et al.

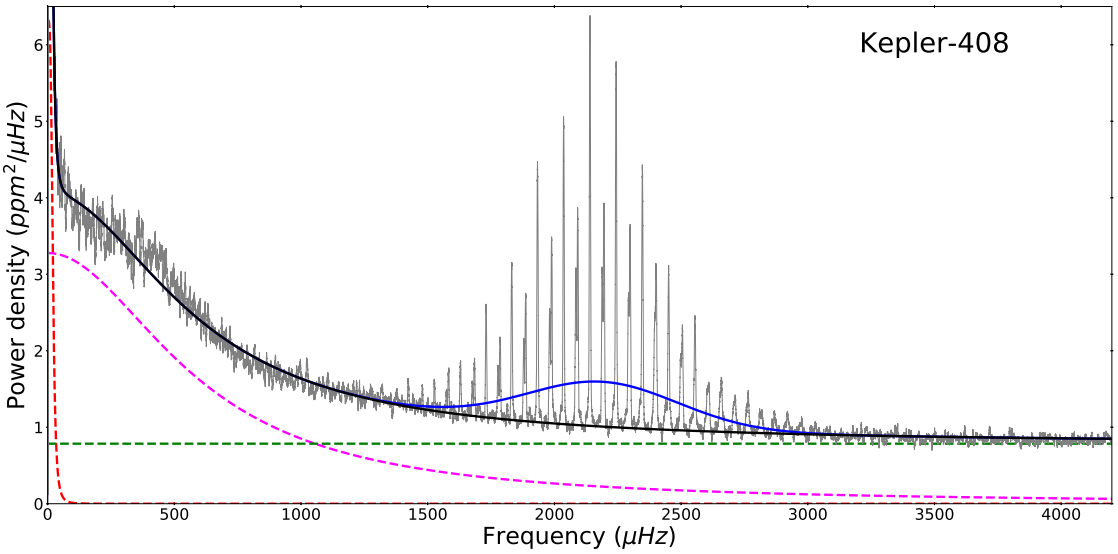

Figure 3.7: The noise background and mode envelope of power spectra. The smoothed spectra is shown in gray. Mode envelope (blue solid) is upon the noise background (black solid), which can be separated into there components; two Harvey-like profiles (red and magenta dashed) and white shot noise (green dashed).

2009, Karoff et al. 2013)

$$N(\nu) = \sum_{i=1}^{2} \frac{A_i}{1 + (B_i \nu)^{p_i}} + N_0, \tag{3.34}$$

where N_0 is the white noise, mostly due to the instrumental photon shot noise. One Harvey-like profile corresponds to stellar granulation, while the other is to model active regions.

Figure 3.7 illustrates a typical noise background in *Kepler* star (black solid line). As in equation (3.34), we model total background with three different contributions; two Harvey-like profiles (red and magenta dashed lines) and white shot noise (green dashed line). The profile describing stellar active region (red) is dominant only at very low frequency, while white noise (green) surpasses the other two at very high frequency.

3.2.6 Power distribution among azimuthal components

As mentioned above, the dependence of the Lorentzian profile on $i_\star$ is incorporated into mode heights $H(n, l, m, i_\star)$. The structure is as follows. Under the assumption of energy equipartition among different m-components associated with the same degree l, Gizon & Solanki (2003) showed that the height $H(n, l, m, i_\star)$ of the mode is given by

$$H(n, l, m, i_\star) = \mathcal{E}(l, m, i_\star) H(n, l), \tag{3.35}$$

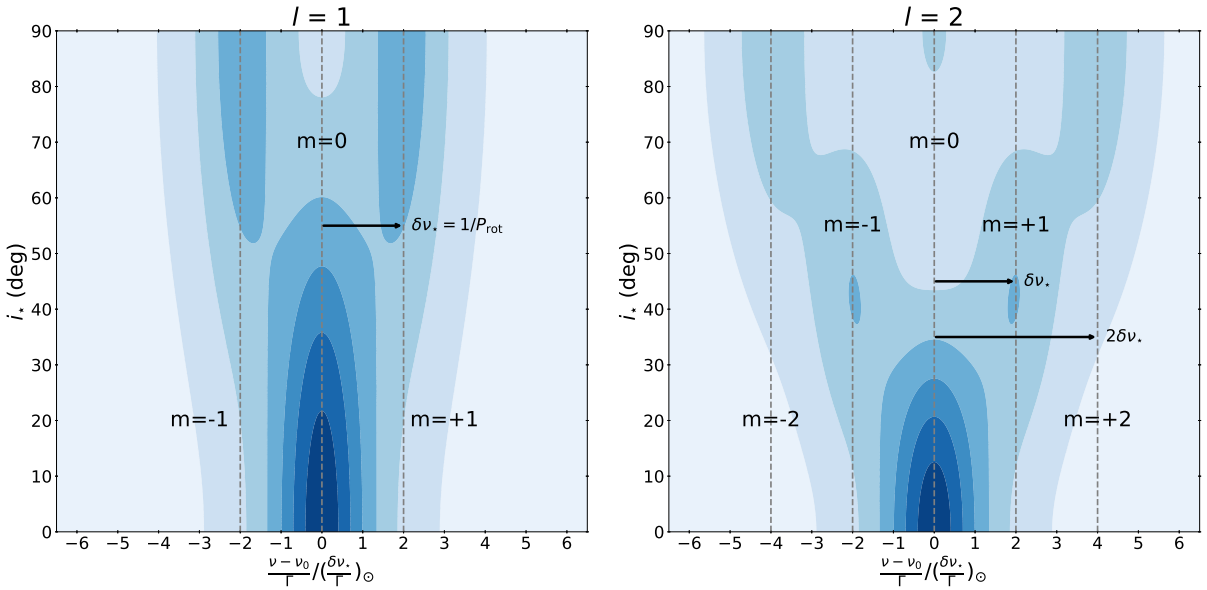

Figure 3.8: Schematic illustration of the power distribution among m-components for varying $i_\star$ for dipole ($l = 1$; left) and quadrupole ($l = 2$; right) modes. x-axis corresponds to the frequency in units of $(\delta\nu_\star/\Gamma)_\odot$, and y-axis is $i_\star$. Power for each m-component is represented by contour. Stellar rotation twice faster than the Sun is assumed, and vertical dashed lines indicate central frequencies of the multiplets m.

where

$$\mathcal{E}(l, m, i_\star) = \frac{(l - |m|)!}{(l + |m|)!} \left[P_l^{|m|}(\cos i_\star)\right]^2, \tag{3.36}$$

and $P_l^{|m|}$ is the associated Legendre polynomials with degree l and order m (Toutain & Gouttebroze 1993, Gizon & Solanki 2003). For instance,

$$\mathcal{E}(0, 0, i_\star) = 1, \tag{3.37}$$
$$\mathcal{E}(1, 0, i_\star) = \cos^2 i_\star, \tag{3.38}$$
$$\mathcal{E}(1, \pm1, i_\star) = \frac{1}{2}\sin^2 i_\star, \tag{3.39}$$
$$\mathcal{E}(2, 0, i_\star) = \frac{1}{4}\left(3\cos^2 i_\star - 1\right)^2, \tag{3.40}$$
$$\mathcal{E}(2, \pm1, i_\star) = \frac{3}{2}\cos^2 i_\star \sin^2 i_\star, \tag{3.41}$$
$$\mathcal{E}(2, \pm2, i_\star) = \frac{3}{8}\sin^4 i_\star. \tag{3.42}$$

It is clear that $l = 0$ modes cannot be used to infer stellar inclination because of its insensitivity to $i_\star$. We also note that viewing angle $i_\star$ is irrelevant to the total amount of energy distributed to the particular angular degree l; $\sum_{m=-1}^{m=+1} \mathcal{E}(1, m, i_\star) = 1$ and $\sum_{m=-2}^{m=+2} \mathcal{E}(2, m, i_\star) = 1$.

Although energy is expected to be equally distributed among different m-components intrinsically, the viewing angle $i_\star$ changes the energy balance appearing in the observed power spectra simply due to the geometrical effect. This is because different m-components have different sensitivity to latitudes (Lund et al. 2014a, Benomar et al. 2015). More specifically, $m = \pm l$ modes are sensitive to the equatorial region, while $0 < |m| < l$ modes are sensitive to higher latitudes. For example, $(l, m) = (2, 2)$ mode has maximal sensitivity to $\theta = 90°$ (equator), while $(l, m) = (2, 1)$ mode is peaked around $\theta = 51°$. Modes with $m = 0$ have no particular sensitivity to latitudes. When viewed from north/south pole (i.e., $\theta = 0°$), therefore, $m = 0$ alone will be visible, while $m = \pm l$ modes surpass the others ($-l < m < +l$) when viewed from the equator.

For this reason, if the power of each m-mode associated to the same degree l is properly identified in $P(\nu)$, the ratio of their heights can be used to determine $i_\star$. Figure 3.8 clearly demonstrates this gradual shift of relative power density for varying $i_\star$. As $i_\star$ increases, energy of $m = 0$ mode will be re-distributed into $|m| > 0$ modes.

We again note that equation (3.36) is derived by assuming energy equipartition among different m-components. This assumption is actually consistent with the solar data (Gizon & Solanki 2003). Because 94 stars we will analyze in this work (chapter 4) are low mass stars in main-sequence phase, similarly to the Sun, we consider this assumption is still valid for them.

Stellar rotation may break the energy equipartition, because $m > 0$ ($m < 0$) modes are forward (backward) propagating waves along with rotational motion. One way to evaluate the effect of rotation on the stars is to compare the centrifugal force and surface gravity of the star as

$$\left(\frac{2\pi}{P_{\rm rot}}\right)^2 \frac{R_\star^3}{GM_\star} \approx 1.3{\times}10^{-4} \left(\frac{P_{\rm rot}}{10\,{\rm days}}\right)^{-2} \left(\frac{R_\star}{R_\odot}\right)^3 \left(\frac{M_\star}{M_\odot}\right)^{-1}, \tag{3.43}$$

where G is the gravitational constant. Based on that, we estimate that the deviation from spherical symmetry is very small, at least for 94 stars we will analyze. Although this discussion does not refer to the explicit relation between rotation and mode excitation, we suppose that the rotation will rarely affect the energy equipartition among m-modes, due to its small contribution to the spherical asymmetry ($\approx \mathcal{O}(10^{-4})$). [9].

3.3 Procedure in the fit of stellar oscillations

Asteroseismic analysis in this thesis is the fit of the model power spectrum (equation 3.32) to the observed power spectra, to search for the parameters that represents the observation best. In doing so, we fit the spectrum in two steps because of the large number of free parameters. Before describing the steps of the analysis, we introduce the conventional approximations

[9] As an observational clue, it is worth introducing a rapidly-rotating F-type star KIC 3424541 (Appourchaux et al. 2012a, Benomar et al. 2015). Although this star shows very rapid rotation of $P_{\rm rot} \approx 3.5$ days, its rotationally-split $m = -1$ and $m = +1$ components of $l = 1$ modes are found to have almost the same amplitudes in the observed spectra (see Figure B1 of Benomar et al. 2015).

often adopted in the actual spectra fitting (subsection 3.3.1). The first step of the analysis is the fit of the background, using a single Gaussian function to model the envelope of excess power from the oscillation modes (subsection 3.3.2). The next step is MCMC fit for the parameters of the oscillation modes (subsection 3.3.3).

3.3.1 Conventional approximations for modes in spectra fitting

An asteroseismic analysis performed in this work requires to identify the indices (n, l, m) for each mode from the noisy spectra, and then preferably fit many lines simultaneously to determine the global parameters $i_\star$ and $\delta\nu_\star$. In fact, since each Lorentzian profile has three parameters (central frequency, height, and width), total number of parameters to be fitted increases dramatically as we adopt more modes (n, l, and m). It is typical that high signal-to-noise ratio stars have more than 20 detectable radial orders, leading to more than 100 parameters to be fitted, which requires very long computation for a reliable parameter estimation. Therefore one has to adopt several approximations in order to reduce the number of free parameters as much as possible. We summarize conventional assumptions often adopted in asteroseismology below.

Since it is known for the Sun that height ratio of non-radial ($l \neq 0$) and radial ($l = 0$) modes is uniform over the range of pulsation frequency (Salabert et al. 2011, and references therein), the intrinsic height of the oscillation for $l \neq 0$ modes can be scaled with those of $l = 0$ as

$$H(n, l) = V_l^2 H(n, l = 0), \tag{3.44}$$

where V_l^2 is referred to as the *mode visibility* and independent of the radial orders n. This removes the degrees of freedom for $H(n, l \neq 0)$. We adopt a slightly different sets of values, $(V_1^2, V_2^2) = (1.449, 0.6589)$ for simulations in section 4.2 and $(1.447, 0.5485)$ for the real data analysis in section 4.3, as described later in detail.

As for the mode width $\Gamma(n, l, m)$, earlier analysis of the Sun and solar-like stars found that it does not dramatically change with frequency, but shows gradual increase from lower to higher frequency (Toutain & Froehlich 1992, García et al. 2004). Figure 3.9 illustrates this profile for one of the *Kepler* stars. Therefore we first neglect the m-dependence of $\Gamma(n, l, m)$, because frequency shift given by rotation is at best a few μHz, small enough to assume almost the same width.

The remaining l-dependence is empirically modeled from the set of the fitted values of $\nu(n, l)$ and $\Gamma(n, l = 0)$ as follows. First we identify the modes (n, l) for $n_{\min} \leq n \leq n_{\max}$ from the spectra, and obtain the corresponding eigen-frequency $\nu(n, l)$ and mode width $\Gamma(n, l = 0)$. Then we estimate $\Gamma(n, l \neq 0)$ by linear interpolation of $\Gamma(n, l = 0)$ with respect to $\nu(n, l)$. For example, $\Gamma(n_0, l = 1)$ is given by a set of parameters; $\nu(n_0, l = 0)$, $\nu(n_0, l = 1)$, $\nu(n_0{+}1, l = 0)$, $\Gamma(n_0, l = 0)$, $\Gamma(n_0 + 1, l = 0)$. The same is the case for $\Gamma(n_0, l = 2)$. Again this removes the degrees of freedom for $\Gamma(n, l \neq 0)$.

In summary, under the assumptions above, the free parameters characterizing the entire power spectra are as follows.

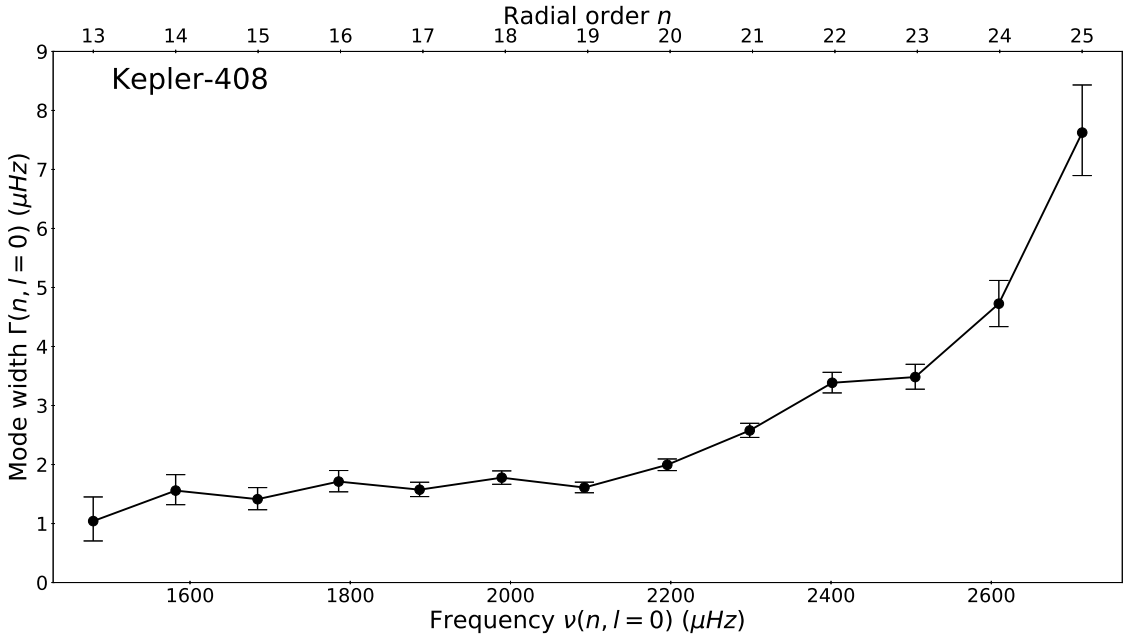

Figure 3.9: Mode width profile of main-sequence solar-like star Kepler-408. Width of radial modes ($l = 0$) are shown. Width of non-radial modes ($l \neq 0$) are interpolated linearly with $\nu(n, l)$ and $\Gamma(n, l = 0)$.

- Central mode frequency for each (n, l) mode: $\nu(n, l)$
- Mode height for each $(n, l = 0)$ mode: $H(n, l = 0)$
- Mode width for each $(n, l = 0)$ mode: $\Gamma(n, l = 0)$
- Global parameters: $i_\star$, $\delta\nu_\star$
- Background parameters: $A_{1,2}$, $\tau_{1,2}$, $p_{1,2}$, and N_0.

Eventually, the total number of fitting parameters is $(n_{\max} - n_{\min} + 1)(l_{\max} + 3) + 9$. In what follows we describe the parameter set above as $\boldsymbol{\theta}$.

3.3.2 Noise background and oscillation envelope fit

The power excess of acoustic oscillation is standing atop the noise background (equation 3.32). Therefore, poor modelling of the noise background may accidentally lead to the inaccurate estimate of model parameters, especially those responsible for mode heights, e.g., height $H(n, l)$ and stellar inclination angle $i_\star$. Before attempting to fit the m-mode splittings of power spectra, we begin with the rough estimate of the noise background level and the envelope of the acoustic modes. In doing so, we assume two Harvey-like profiles with white shot noise (equation 3.34), and a single Gaussian envelope to model the entire power excess over the oscillation frequencies. This model has 7 (noise background) + 3 (Gaussian) =

10 parameters in total. Figure 3.7 illustrates the result of this simple fit; the entire noise background (black solid line) and Gaussian envelope (blue solid line) model with optimized parameters. The errors of the noise background parameters derived here are used as priors in the following MCMC analysis. The Gaussian envelope is used to guess the frequency range of possible oscillation modes.

After fitting the noise background correctly, we attempt to identify each eigen-mode. In this step, we define angular degree ($l = 0, 1, 2$) to all possible eigen-modes and set the priors of mode center, which will be used in the following analysis. This process is conducted visually on mode by mode basis. Top panel of Figure 3.10 shows the eigen-modes identified in this procedure. All peaks are attributed to either $l = 0$, 1, or 2. In doing so, the fact that eigen-modes are regularly spaced makes the visual and correct identification feasible. Moreover, the échelle diagram (Figure 3.6) is helpful to find correct eigen-modes at lower/higher frequency end of power excess, where modes have so small amplitudes that they are possible to be misidentified.

3.3.3 Bayesian-MCMC approach

In the Bayesian-MCMC sampling approach, we adopt the algorithm developed by Benomar et al. (2009). In this subsection we briefly summarize the formulation behind the algorithm and setups for the MCMC run.

Bayesian formulation

In Bayesian approach, the derived values and errors of mode parameters $\boldsymbol{\theta}$ are discussed through Bayes' theorem:

$$\pi(\boldsymbol{\theta}|y, \mathcal{M}) = \frac{\pi(\boldsymbol{\theta}|\mathcal{M})\pi(y|\boldsymbol{\theta}, \mathcal{M})}{\pi(y|\mathcal{M})}, \tag{3.45}$$

where y is the observed power spectra and $\mathcal{M}$ is the model parametrized with $\boldsymbol{\theta}$, i.e., the model power spectrum $P(\nu)$ (equation 3.32)

$$\begin{aligned} \mathcal{M}(\nu, \boldsymbol{\theta}) &= P(\nu) \\ &= \sum_{n=n_{\min}}^{n_{\max}} \sum_{l=0}^{l_{\max}} \sum_{m=-l}^{+l} \frac{H(n, l, m, i_\star)}{1 + 4[\nu - \nu(n, l, m)]^2/\Gamma^2(n, l, m)} \\ &+ \sum_{i=1}^{2} \frac{A_i}{1 + (B_i\nu)^{p_i}} + N_0. \end{aligned} \tag{3.46}$$

In equation (3.45), $\pi(\boldsymbol{\theta}|y, \mathcal{M})$ is the posterior probability distribution (PPD) of parameters $\boldsymbol{\theta}$ for given data y and model $\mathcal{M}$. Besides, $\pi(y|\boldsymbol{\theta}, \mathcal{M})$ is the *likelihood* function and represents the probability of observing data y given the model $\mathcal{M}$. Lastly, $\pi(\boldsymbol{\theta}|\mathcal{M})$ is a priori knowledge of the model parameters $\boldsymbol{\theta}$. The denominator $\pi(y|\mathcal{M})$ is the total probability of the model $\mathcal{M}$ describing the data y, and is used as normalizing factor in equation (3.45).

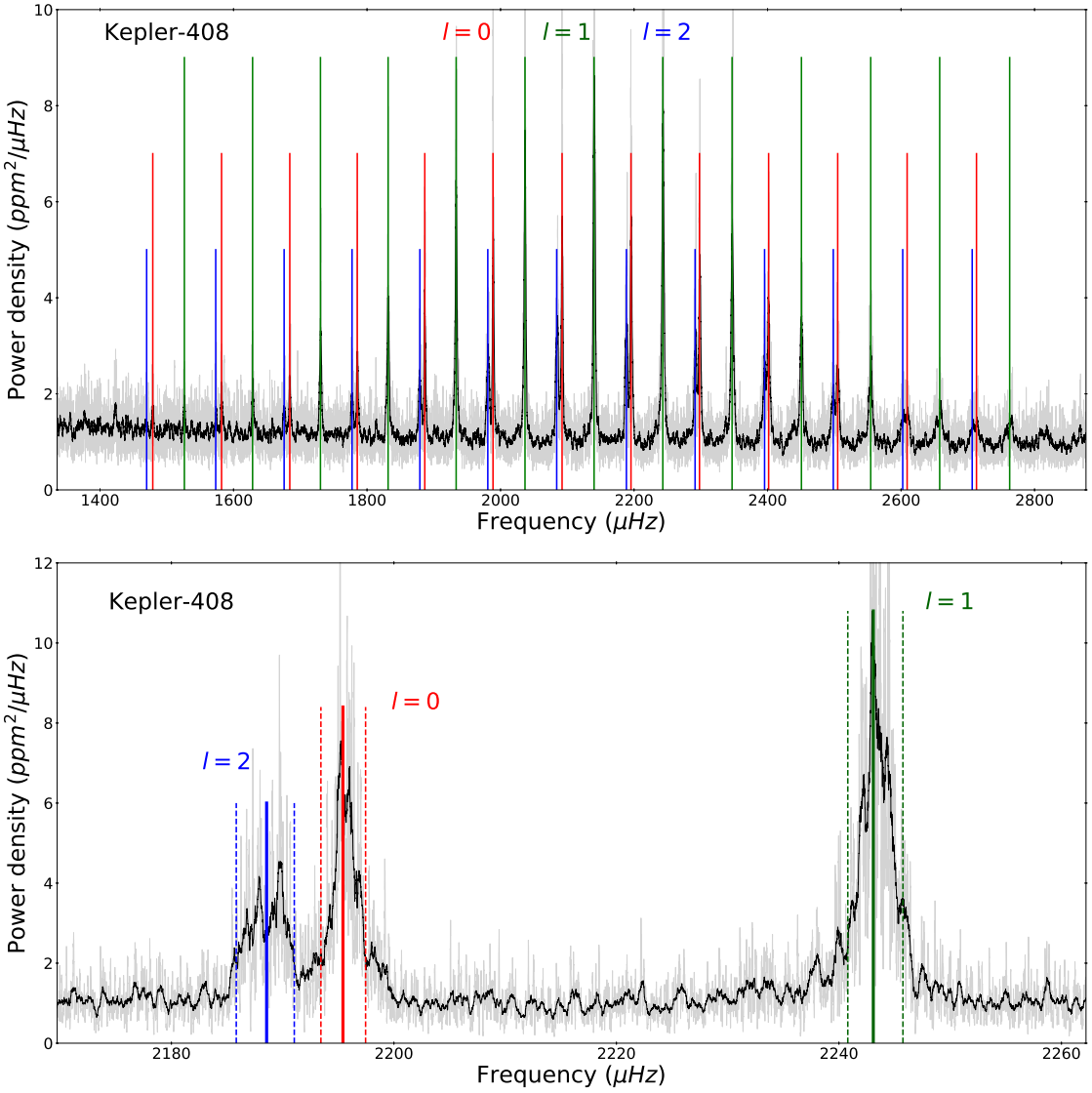

Figure 3.10: *Top*: The positions of eigen-modes that are identified as $l = 0$ (red), $l = 1$ (green), or $l = 2$ (blue). *Bottom*: The close-up view of a single set of $l = 0$, 1, and 2 modes around $\nu_{\rm max}$. Solid vertical line represents the frequency assumed as the mode center $\nu(n, l)$, and two vertical dashed lines represent the priors set for $\nu(n, l)$ for the MCMC sampling.

Likelihood function

The noise in the power spectrum follows χ^2 distribution with two degrees of freedom (Duvall & Harvey 1986). Knowing the noise statistics of the power spectrum gives the likelihood function in the form of

$$\pi(y|\boldsymbol{\theta},\mathcal{M}) = \prod_{i=1}^{N} \frac{1}{\mathcal{M}(\nu_i,\boldsymbol{\theta})} \exp\left(-\frac{y_i}{\mathcal{M}(\nu_i,\boldsymbol{\theta})}\right), \tag{3.47}$$

where the product is performed for all frequency samples ν_i.

Priors

The prior on each parameter is defined as follows.

- Prior on $\nu(n,l)$:
  We set un-informative, uniform prior on $\nu(n,l)$ as

$$p(\nu(n,l)|M) = \begin{cases} \frac{1}{\nu(n,l)^{\max} - \nu(n,l)^{\min}} & \text{if } \nu(n,l)^{\min} < \nu(n,l) < \nu(n,l)^{\max} \\ 0 & \text{otherwise,} \end{cases} \tag{3.48}$$

  where $\nu(n,l)^{\min}$ and $\nu(n,l)^{\max}$ are set by the visual inspection of the power spectra. The vertical dashed lines in the bottom panel of Figure 3.10 show the example of $\nu(n,l)^{\min}$ and $\nu(n,l)^{\max}$ set for each mode.

- Priors on $H(n,l=0)$ and $\Gamma(n,l=0)$:
  We set the truncated Jeffreys priors on $H(n,l=0)$ and $\Gamma(n,l=0)$ as

$$p(x|M) = \begin{cases} \frac{\ln\left(1+\frac{x^{\max}}{x^{\min}}\right)}{x+x^{\min}} & \text{if } x^{\min} < x < x^{\max} \\ 0 & \text{otherwise,} \end{cases} \tag{3.49}$$

  where $(x^{\min}, x^{\max}) = (1,10)\,\mathrm{ppm}^2/\mu\mathrm{Hz}$ for $H(n,l=0)$, and $(x^{\min}, x^{\max}) = (5,25)\,\mu\mathrm{Hz}$ for $\Gamma(n,l=0)$.

- Prior on $\delta\nu_\star$:
  We set un-informative, uniform prior on $\delta\nu_\star$ as

$$p(\delta\nu_\star|M) = \begin{cases} \frac{1}{\delta\nu_\star^{\max}} & \text{if } 0 < \delta\nu_\star < \delta\nu_\star^{\max} \\ 0 & \text{otherwise,} \end{cases} \tag{3.50}$$

  where $\delta\nu_\star^{\max}$ is set to be $5\,\mu$Hz (corresponding to 2.3-day rotational period), beyond which is unlikely for the main-sequence solar-like stars.

- Prior on $i_\star$:
  We set an isotropic prior on $i_\star$ (i.e., uniform prior on $\cos i_\star$) as

$$p(i_\star|M) = \begin{cases} \sin i_\star & \text{if } 0^\circ < i_\star < 90^\circ \\ 0 & \text{otherwise.} \end{cases} \tag{3.51}$$

- Priors on noise background parameters:
  We set un-informative, uniform priors on noise background parameters (A_i, τ_i, p_i, and N_0) as

$$p(x|M) = \begin{cases} \frac{1}{x^{\max} - x^{\min}} & \text{if } x^{\min} < x < x^{\max} \\ 0 & \text{otherwise,} \end{cases} \tag{3.52}$$

  where $(x^{\min}, x^{\max})$ is set to be 1σ error range derived in the earlier fit (subsection 3.3.2).

MCMC sampling

The power spectrum is then analyzed using a Markov Chain Monte Carlo (MCMC) algorithm based on a Metropolis-Hasting scheme, with parallel tempering (e.g., Gregory 2005, Benomar et al. 2009, Handberg & Campante 2011). The MCMC algorithm works so as not only to find the maxima of the posterior probability $\pi(\boldsymbol{\theta}|y, \mathcal{M})$ (maximum a posteriori), but also to give conservative and robust estimate on the uncertainties by sampling the probability around the maxima effectively. The number of parallel chains is fixed to $c_{\rm mac} = 5$, with a temperature distribution following a geometric law $T = \lambda^{c-1}$ with $(T_{\min}, T_{\max}) = (1, 70)$.

We divide the analysis into three steps: the burn-in phase, training phase, and acquire phase. The burn-in phase (40,000 samples) ensures that we reach the region of interest in the parameter space. The training phase (700,000 samples) employs an adaptive algorithm to optimize the covariance matrix of the Gaussian proposal probability density function to achieve the ideal acceptance rate of 23.4% (Atchade 2006). During the acquire phase (1,000,000 samples), the optimal covariance matrix is used to sample the posterior distribution. This phase ensures that we reach an acceptance rate near 23.4% that remains stable along the acquisition phase. Convergence of the posterior distribution is confirmed through the visual inspection.

The MCMC sampling method makes it easy to obtain the marginal probability distribution for each of the model parameters. We define median 1σ, and 2σ error of each parameter as its median, 68% credible interval, and 95% credible interval of the marginal probability distribution, respectively.

Chapter 4

Reliability assessment of asteroseismic measurement of stellar inclination

The number of transiting exoplanetary systems with measured ψ using asteroseismology is hampered by the required signal-to-noise ratio (SNR) and the relatively high stellar rotation rate. In reality, a majority of transiting exoplanets have been searched around F, G, and K type stars in their main-sequence phase. For such main-sequence stars, $i_\star$ is difficult to measure. Their oscillation modes exhibit low amplitudes and suffer from severe blending among modes (see e.g., Appourchaux et al. 2008). Therefore the systematic verification of the reliability of $i_\star$ derived from asteroseismology is of fundamental importance.

As shown by Gizon & Solanki (2003) and Ballot et al. (2008, 2006) using a limited number of simulations, the inferred value of $i_\star$ is not so accurate if modes are of insufficient SNR or not properly identified. This is why we attempt in this chapter to perform systematic mock simulations to examine the reliability of $i_\star$ determination from asteroseismology. In this work, we focus on main-sequence stars, but our method could be applied to evolved stars as well. This is because the fundamental physical reason allowing us to infer the inclination are the same (Beck et al. 2012, Benomar et al. 2013, Mosser et al. 2017). In the future, it is worthwhile to extend our methodology for those evolved stars, as discussed in more details in section 4.4.

4.1 Analytic criteria to distinguish among different azimuthal orders

As suggested in the previous chapter, accurate measurement of $i_\star$ crucially depends on the ability of identifying the frequencies and heights of different m-modes associated with the same degree l. Ideally, the higher amplitude and the wider separation between different m-modes are required. More specifically, the former is represented by the ratio of the mode height $H(n, l, m, i_\star)$ and the noise level, and the latter, by the ratio of the stellar rotational splitting and the mode width, $\delta\nu_\star/\Gamma(n, l)$. This consideration may be translated into analytic criteria that are necessary to distinguish among different m-modes.

Because $l = 0$ modes are insensitive to either rotation ($\delta\nu_\star$) or inclination ($i_\star$), $i_\star$ can be determined by non-radial modes ($l \neq 0$). For a majority of main-sequence stars whose pulsations are detected, their visible modes are limited up to $l = 2$. Moreover, the amplitudes of $l = 1$ modes are roughly three times larger than those of $l = 2$ modes ($V_1^2/V_2^2 \approx 3$). Thus $l = 1$ modes are most likely to play a key role in the ability to determine $i_\star$ in practice, and we consider analytic criteria to separate $m = 0$ and $m = \pm 1$ modes for $l = 1$ below.

A difficulty to distinguish among different m-modes may be understood from Figure 4.1, in which model profiles of power spectra around the central frequency ν_0 for different values of $i_\star$ and $\delta\nu_\star/\Gamma$ are plotted; $i_\star = 30°$, $60°$, and $80°$ from left to right panels, and $(\delta\nu_\star/\Gamma)/(\delta\nu_\star/\Gamma)_\odot = 2.0$, 1.0, and 0.5 from top to bottom panels, with $(\delta\nu_\star/\Gamma)_\odot \approx 0.42\,\mu\mathrm{Hz}/0.95\,\mu\mathrm{Hz} \approx 0.44$ being the solar value near the maximum of mode amplitude. The horizontal axis corresponds to $(\nu - \nu_0)/\Gamma$ in units of $(\delta\nu_\star/\Gamma)_\odot$.

Hereafter, we note the contribution of $m = -1, 0, +1$ to the power spectra as $P_{l=1,m=-1,0,+1}(\nu)$. From equations (3.32), (3.26), and (3.42), $P_{l=1,m=0}(\nu)$ and $P_{l=1,m=\pm1}(\nu)$ are explicitly written as

$$P_{l=1,m=0}(\nu) = H(n, l=1)\frac{\cos^2 i_\star}{1 + 4(\nu - \nu_0)^2/\Gamma^2}, \tag{4.1}$$

$$P_{l=1,m\pm1}(\nu) = H(n, l=1)\frac{\sin^2 i_\star}{2[1 + 4(\nu - \nu_0 \mp \delta\nu_\star)^2/\Gamma^2)]}. \tag{4.2}$$

Figure 4.1 is normalized so that $H(n, l = 1)$ is unity.

The reliability of the estimate of $i_\star$ and $\delta\nu_\star$ is crucially determined by how well one can separate the contributions from three different m-modes encoded in the total profile (black solid curve in Figure 4.1). To be more specific, their separate contributions to the total power are computed as

$$\int_0^\infty \mathrm{d}\nu P_{l=1,m=0}(\nu) \approx \frac{H(n, l=1)\Gamma(n, l=1)}{2}\cos^2 i_\star, \tag{4.3}$$

$$\int_0^\infty \mathrm{d}\nu P_{l=1,m=\pm1}(\nu) \approx \frac{H(n, l=1)\Gamma(n, l=1)}{4}\sin^2 i_\star. \tag{4.4}$$

These need to be much larger than the *resolvable element* of the power, which is roughly given by the product of the root mean square (rms) noise level σ_n in the observed power spectra and the frequency resolution $\delta f \approx 1/T_{\mathrm{obs}}$ with T_{obs} being the total observational duration.

The consideration above leads to the following qualitative and analytic criteria.

(I) The identification of $m = 0$ mode requires

$$\frac{H(n, l=1)\Gamma(n, l=1)}{2}\cos^2 i_\star > \alpha\,\sigma_n \delta f, \tag{4.5}$$

where we introduce a fudge constant α that will be empirically determined later through the comparison with mock simulations. The condition (4.5) becomes

$$\cos^2 i_\star > \alpha\,\frac{2}{\mathrm{SNR}}\frac{\delta f}{\Gamma}, \tag{4.6}$$

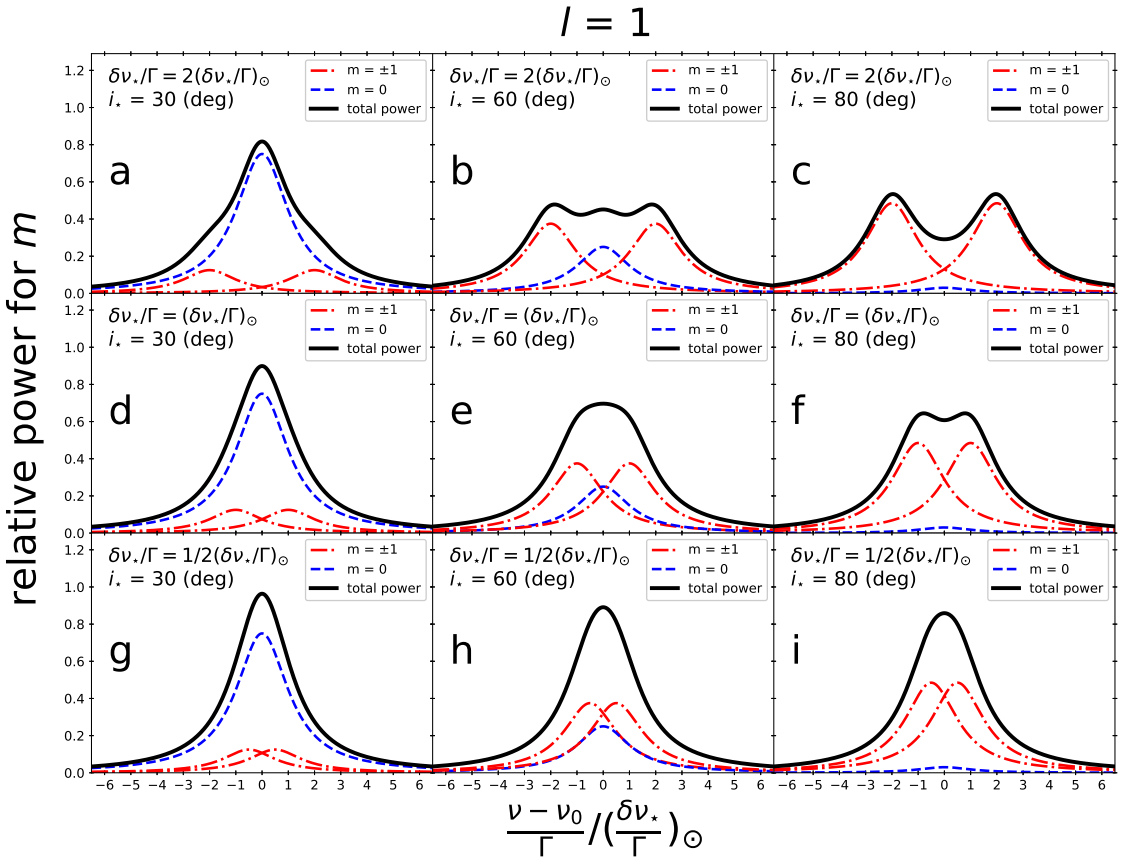

Figure 4.1: Model power spectra of dipole ($l = 1$) mode with central frequency ν_0. x and y- axes correspond to the frequency in units of $(\delta\nu_\star/\Gamma)_\odot$ and relative power for different m components in units of the height of $m = 0$ mode with $i_\star = 0\,(\mathrm{deg})$, respectively. Blue dashed (red dotted-dashed) line represents the contribution of $m = 0$ ($m = \pm 1$) modes, and black solid line shows the consequent total power spectra. Different panel corresponds to the different combination of $\delta\nu_\star/\Gamma$ and $i_\star$, ranging from faster (upper; twice solar rotation) to slower (lower; half solar rotation) rotation and from lower (left) to higher (right) inclination.

where we define the *signal-to-noise ratio* SNR:

$$\mathrm{SNR} \equiv \frac{H(n, l=1)}{\sigma_n}. \tag{4.7}$$

Then the inequality (4.6) leads to an upper limit on the detectable $i_\star$;

$$i_\star < \cos^{-1} \sqrt{\alpha \frac{2}{\mathrm{SNR}} \frac{\delta f}{\Gamma}}. \tag{4.8}$$

In other words, we cannot reliably estimate the true value of $i_\star$ if it is larger than the threshold value in the right-hand-side of the inequality above. For instance, a reliable estimate of $i_\star = 90^\circ$ is very demanding and requires an ideal observation with either $\mathrm{SNR} = \infty$ or $\delta f = 0$ (i.e., observation with infinite time).

(II) Similarly, the identification of $m = \pm 1$ mode requires

$$\frac{H(n, l=1)\Gamma(n, l=1)}{4} \sin^2 i_\star > \beta\, \sigma_n \delta f, \tag{4.9}$$

with β being another fudge factor to be estimated later. In this case, we obtain a lower limit on the measurable $i_\star$ as

$$i_\star > \sin^{-1} \sqrt{\beta \frac{4}{\mathrm{SNR}} \frac{\delta f}{\Gamma}}. \tag{4.10}$$

Again this condition implies that either $\mathrm{SNR} = \infty$ or $\delta f = 0$ is needed for $i_\star$ to be measurable down to 0°.

The two criteria above are independent of the rotational splitting $\delta\nu_\star$. Indeed if we take into account conditions to distinguish among the peak height of different m-modes, instead of their total area (i.e., power), we obtain criteria dependent on $\delta\nu_\star/\Gamma$. In this case, however, the dependence on the frequency resolution δf is neglected. In principle, we could combine those conditions to improve our analytic criteria, but the results become complicated so that it may lose easy applicability. Therefore we decide to consider the condition on $\delta\nu_\star$ separately as follows.

(III) The requirement that the peaks of $m = \pm 1$ modes need to be distinguished from the sum of the $m = \pm 1$ modes at $\nu = \nu_0$ is written as

$$P_{l=1,m\pm1}(\nu_0 \pm \delta\nu_\star) > [P_{l=1,m=+1}(\nu_0) + P_{l=1,m=-1}(\nu_0)], \tag{4.11}$$

which reduces to the simple form of

$$\frac{\delta\nu_\star}{\Gamma} > 0.5. \tag{4.12}$$

This is insensitive to $i_\star$, and a very basic requirement on $\delta\nu_\star/\Gamma$ to reliably estimate $i_\star$. We note that interestingly the solar value ≈ 0.44 is very close to this threshold just by chance.

4.2 Mock simulations to extract stellar inclinations from power spectra

Measurement of the stellar inclination from asteroseismology is based on several complicated procedures and their validity can be examined quantitatively only through the analysis of simulated power spectra. Thus we here carry out intensive analyses of systematic mock spectra.

In this simulation, we try to clarify the condition(s) of the stars necessary for the reliable measurement of $i_\star$. We generate simulated power spectra of the stars assuming various stellar properties and observational conditions (long/short observational duration, high/low signal-to-noise ratio, fast/slow rotation, and high/low inclination angle). We perform asteroseismic analysis to these simulated spectra, mainly focusing on the derived values of $i_\star$. The reliability of the analysis is judged by checking if output $i_\star$ is close to input value or not. By performing this test to the simulated spectra above, we attempt to map the parameter space where reliable measurement of $i_\star$ is feasible (i.e., output $i_\star \approx$ input $i_\star$).

We first describe how to generate simulated power spectra, and then present the results against our analytic criteria discussed in the previous section.

4.2.1 Generating mock power spectra scaled from a reference star KIC 12069424

As we demonstrated in the previous section, the precision and accuracy of the estimate of the stellar inclination depend sensitively on the splitting-to-width ratio $\delta\nu_\star/\Gamma$ and on the signal-to-noise ratio SNR. In the present simulation, we have not implemented realistic noises except for the background noise level of N_0 in equation (3.34). Thus the SNR $\equiv H(n, l = 1)/\sigma_n$ defined in section 4.1 is not easy to be assigned properly. Instead, we use height-to-background ratio HBR $\equiv H(n, l)/N_0$ as a proxy for SNR throughout the following analysis. In practice, the difference between HBR and SNR is expected to be incorporated by renormalizing the values of α and β in inequalities (4.8) and (4.10). The relation of HBR and SNR will be revisited in subsection 4.2.3.

We take the HBR and $\delta\nu_\star/\Gamma$ as our primary variables in simulated power spectra, and generate realistic mock spectra covering a wide range of their values. In practice, we choose KIC 12069424 (16 Cyg A) as our reference star, which is one of the brightest stars monitored by *Kepler*. It has one of the highest HBR among the observed main-sequence stars, and therefore is one of the most studied stars in the *Kepler* field (Metcalfe et al. 2012, Metcalfe et al. 2014, Davies et al. 2015). The observed power spectrum for KIC 12069424 is shown in Figure 4.2.

We first extract the mode parameters (frequency, height, width, noise background parameters, rotational splitting and inclination) of the reference star by following the asteroseismic analysis method described in section 3.3. We fit a total of 17 radial orders with associated degrees $l = 0$, 1, and 2. While $l = 3$ degree is identifiable for this reference star due to its high brightness, it is not the case for most of other stars. Therefore we do not incorporate

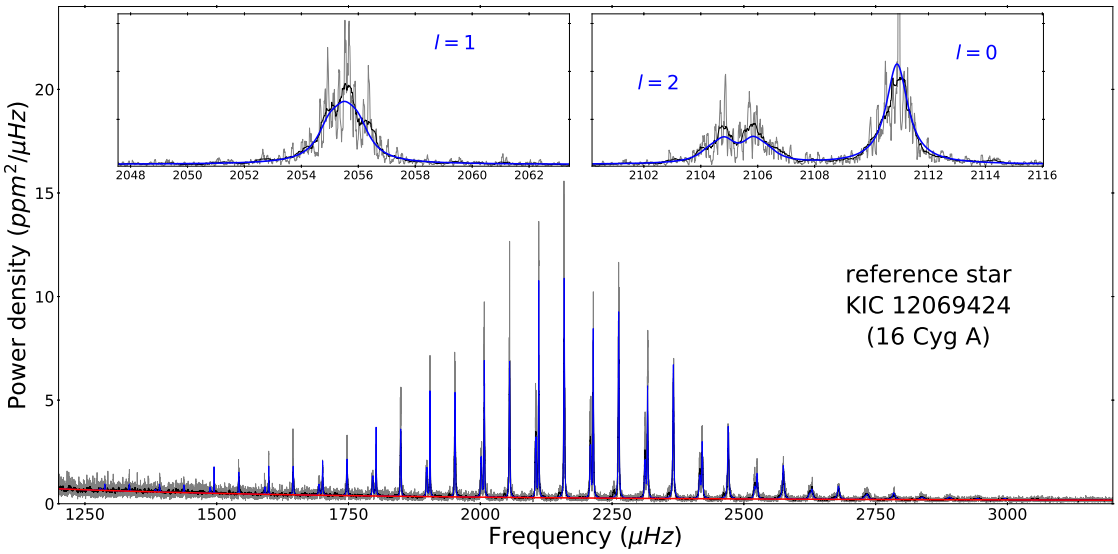

Figure 4.2: Observed power spectra of the reference star KIC 12069424 (16 Cyg A). Asteroseismic power spectra smoothed with a boxcar filter over 0.2 μHz (gray) and 2.0 μHz (black) are shown. Superimposed is the background level (red) and the fitted oscillation modes (blue). The inset shows the modes of degree $l = 0, 1, 2$ around highest amplitude.

the modes of $l \geq 3$ for the reference star and for the simulated spectra. We verified that frequencies, rotational splitting and stellar inclination are all consistent with the result derived by Davies et al. (2015) within 2σ significance. Figure 4.3 shows the measured profile of HBR ($\mathrm{HBR_{ref}}$) and the splitting-to-width ratio ($(\delta\nu_\star/\Gamma)_{\mathrm{ref}}$) of KIC 12069424 as a function of the radial mode frequency. These profiles are fairly representative of other solar-like stars (see e.g., Appourchaux et al. 2012a).

As shown in Figure 4.3, the height-to-background ratio $\mathrm{HBR}(n, l = 0)$ as a function of the radial mode frequency has a peak at $\nu_{\mathrm{max,ref}}$, and the corresponding peak value of HBR is defined as $\mathrm{HBR_{max,ref}}$. We scale those reference parameters to generate mock spectra covering a range of HBR and $\delta\nu_\star/\Gamma$ as described below. Hereafter, the subscript "sim" indicates the variables of simulated stars scaled from a reference star.

The mode heights $H_{\mathrm{sim}}(n, l = 0)$ of a simulated star are specified by its maximum value of HBR at $\nu_{\mathrm{max,sim}}$; $\mathrm{HBR_{max,sim}}$, and are scaled as

$$H_{\mathrm{sim}}(n, l = 0) = \mathrm{HBR_{sim}}(n, l = 0) N_0 \tag{4.13}$$

$$= \frac{\mathrm{HBR_{max,sim}}}{\mathrm{HBR_{max,ref}}} \mathrm{HBR_{ref}}(n, l = 0) N_0. \tag{4.14}$$

In reality, the noise background of the spectrum of actual main-sequence solar-like stars weakly depends on frequency (see section 3.2). It typically decreases by a factor of a few between modes with the lowest measurable frequency and the highest measurable frequency. Figure 4.2 illustrates this profile for KIC 12069424 (red solid line). Here, for simplicity we neglect the frequency dependence in equation (4.13). We include only the constant power N_0,

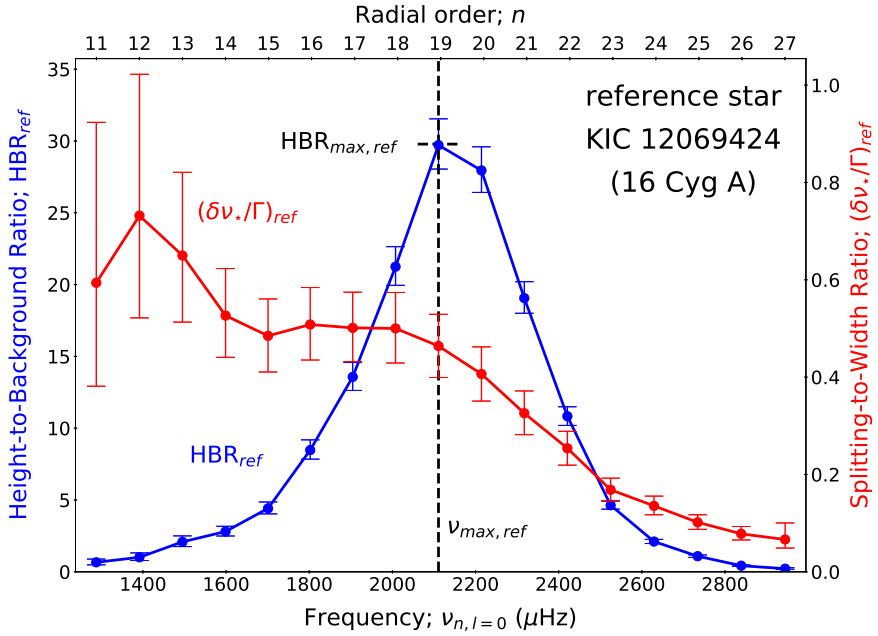

Figure 4.3: Measured profiles of the reference star KIC 12069424 (16 Cyg A). Measured height-to-background ratio (HBR; blue) and splitting-to-width ratio ($\delta\nu_\star/\Gamma$; red) of the radial modes are shown as a function of the radial mode frequency $\nu(n, l = 0)$. These reference profiles are scaled and used in simulated power spectra in section 4.2.

and adopt the value of the reference star $N_{0,\mathrm{ref}} = 0.0857\,\mathrm{ppm}^2/\mu\mathrm{Hz}$. The height $H_{\mathrm{sim}}(n, l)$ for $l = 1$ and $l = 2$ are scaled using the visibilities of the reference star, $V^2_{1,\mathrm{ref}} = 1.449$ and $V^2_{2,\mathrm{ref}} = 0.659$, from equations (3.44) and (4.13).

The other primary parameter that controls the reliability of the estimate of $i_\star$ is the splitting-to-width ratio $\delta\nu_\star/\Gamma(n, l)$. It measures the influence of the overlap between split components (see section 4.1) on the inclination. In the current simulation, we fix the width of the mode $\Gamma(n, l)$ to the reference value $\Gamma_{\mathrm{ref}}(n, l)$. On the other hand, we modify the rotational splitting $\delta\nu_{\star,\mathrm{sim}}$ so that

$$\delta\nu_{\star,\mathrm{sim}} = \gamma_{\mathrm{sim}}\,\Gamma_{\mathrm{max,ref}}, \tag{4.15}$$

where $\Gamma_{\mathrm{max,ref}} = 1.08\,\mu\mathrm{Hz}$ is the width of the mode that corresponds to $\mathrm{HBR}_{\mathrm{max,ref}}$. Here, γ_{sim} is the splitting-to-width ratio at $\mathrm{HBR}_{\mathrm{max,sim}}$.

Obviously the observation duration T_{obs} is another important factor that defines the number of independent data points sampling mode profiles. The longer T_{obs} improves the frequency resolution $\delta f \propto 1/T_{\mathrm{obs}}$. It also improves the description of the mode profile, which in turns can enhance the accuracy on the stellar inclination. To assess this effect, we consider $T_{\mathrm{obs}} = 1$ and 4 years, corresponding to the minimal and maximal observation duration of the *Kepler* LEGACY sample (Lund et al. 2017).

In summary, we generate simulated power spectra for various combination of four parameters; T_{obs}, HBR, $\delta\nu_\star/\Gamma$, and $i_\star$. The ranges of these parameters are carefully chosen to be

Table 4.1: Value and range of the control parameters in simulated spectra.

parameter	value and range
$T_{\rm obs}$ (year)	[1, 4]
$\mathrm{HBR}_{\rm max,sim}$	[0, 1, ..., 29, 30]
$\gamma_{\rm sim} = \delta\nu_{\star,\rm sim}/\Gamma_{\rm max,ref}$	[0.1, 0.2, ..., 0.9, 1.0]
$i_{\star,\rm sim}$ (deg)	[0, 10, ..., 80, 90]

representative of the *Kepler* stars [1]. Table 4.2.1 summarizes the ranges of the four control parameters for the simulated spectra; $T_{\rm obs}$, $\mathrm{HBR}_{\rm max,sim}$, $\gamma_{\rm sim}$ and the inclination angle $i_{\star,\rm sim}$. Eventually, a grid with a total of 3,000 artificial spectra is generated each for $T_{\rm obs}$ =1 and 4 years. In the next subsection, we perform asteroseismic analysis to those simulated spectra and then evaluate how output $i_\star$ and $\delta\nu_\star/\Gamma$ are different from inputs. This test reveals the parameter space where $i_\star$ measurement is reliable (input $\approx$ output) as a function of four control parameters $T_{\rm obs}$, HBR, $\delta\nu_\star/\Gamma$, and $i_\star$. In addition, it serves as a check for the robustness of the analytic criteria above.

4.2.2 Results of mock spectra analysis

Figure 4.4 plots the result of mock spectra analysis on $i_\star$-$\delta\nu_\star/\Gamma$ plane. Specifically, it shows the difference between the true input value and the median of the inferred posterior probability distribution (PPD) for $i_\star$ and $\delta\nu_\star/\Gamma$. As we will show later, the median value does not necessarily represent the best-fit, but we use it here just for simplicity. The base of the gray arrows indicates the input value, and the tip is the measured median value. Left panels are for $T_{\rm obs}$ = 4 years, while right panels are for $T_{\rm obs}$ = 1 year. Top, middle, and bottom panels correspond to $\mathrm{HBR}_{\rm max,sim}$ = 30, 5, and 3, respectively. Note that $\mathrm{HBR}_{\rm max,sim}$ = 3-5 are representative of the maximum HBR of the modes for *Kepler* stars with detected pulsations. In practice, below $\mathrm{HBR}_{\rm max}$ = 3 the noise makes difficult to observe the individual pulsation modes, so that the asteroseismic analysis is often limited to the measure of the central frequency at maximum power $\nu_{\rm max}$ and of the large separation $\Delta\nu$. The case with $\mathrm{HBR}_{\rm max,sim}$ = 30 corresponds to the best cases, such as KIC 12069424 (the reference star).

Clearly there exists a coherent pattern of arrow distribution over the plane, suggesting the presence of the large uncertainty in the parameter estimation. The length of each arrow reflects the amplitude of the uncertainty. The possible cause of these uncertainty will be discussed in next subsection. Labels of "a" to "i" in the top-left panel of Figure 4.4 indicate the locations of ($i_\star$, $\delta\nu_\star/\Gamma$) in the corresponding panels of Figure 4.1. The comparison of Figure 4.4 with Figure 4.1 helps intuitive understanding of this result.

To proceed further, we overlay the analytic criteria (I)-(III) on each panel of Figure 4.4. The three blue vertical lines in the right part indicate the criterion (I) with α = 15 (left dashed), 10 (middle solid) and 5 (right dashed). Similarly, the three red vertical lines in the left part indicate the criterion (II) with β = 10 (left dashed), 15 (middle solid) and 20

[1] Specifically, *Kepler* stars analyzed in this work have been observed typically for 1-4 years. Their SNRs are 30 (best case) or below. Few stars show extreme rapid rotation, leading to $\delta\nu_\star/\Gamma \lesssim 1.0$ in most cases.

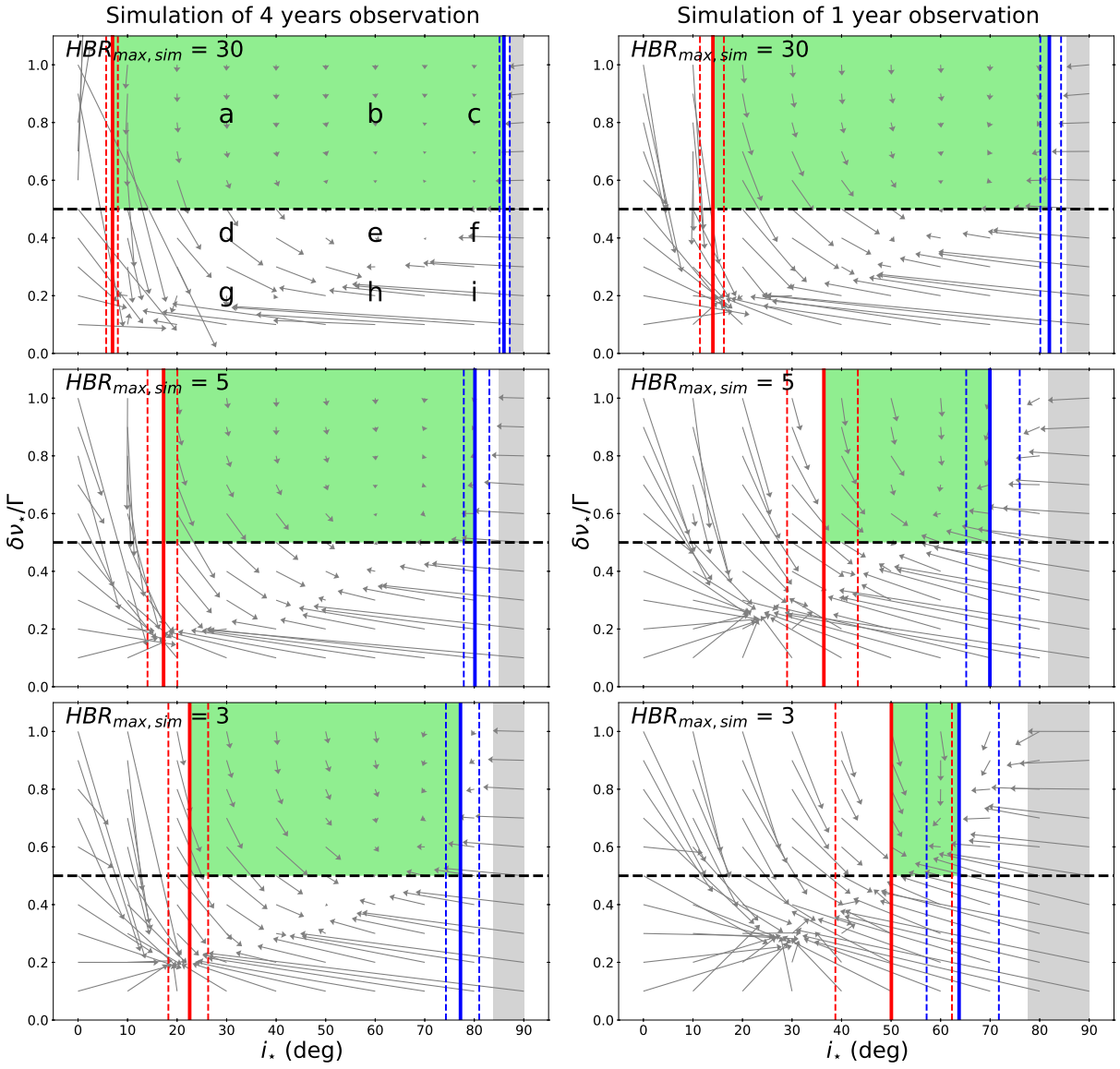

Figure 4.4: Comparison of asteroseismically-derived values and true inputs of $i_\star$ and $\delta\nu_\star/\Gamma$ for the simulated spectra. Arrows in each panel start from the true values and end at the estimated values. Left and right panels show the results for $T_{\rm obs}$ = 4 years and 1 year, respectively. Top, middle, and bottom panels correspond to $\mathrm{HBR}_{\rm max,sim}$ = 30, 5, and 3, respectively. Nine alphabets in the top-left panel indicate the set of ($i_\star$, $\delta\nu_\star/\Gamma$) assumed in the the corresponding panel of Figure 4.1. Blue lines, red lines and horizontal black dashed lines correspond to analytic criteria (I), (II), and (III) discussed in section 4.1, respectively.

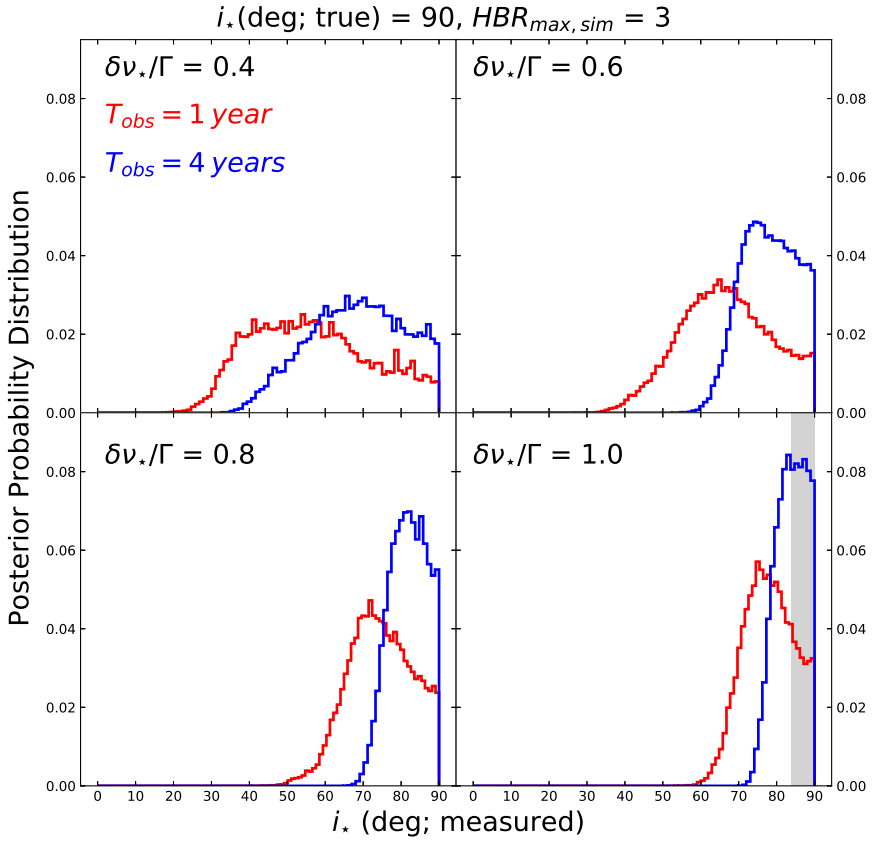

Figure 4.5: Posterior probability distribution (PPD) of measured $i_\star$ for simulated spectra with input $i_\star = 90°$ with different input $\delta\nu_\star/\Gamma$. $\mathrm{HBR}_{\mathrm{max,sim}} = 3$ is assumed. These are shown as histograms, with the number of bins defined according to Scott's normal reference rule (Scott 1992). Red and blue histograms show the results for $T_{\mathrm{obs}} = 1$ year and 4 years, respectively. Gray area in the lower-right panel indicates the region from the median of the 4 year PPD ($i_\star = 83.8°$) to the input value ($i_\star = 90°$).

(right dashed). Finally the horizontal black dashed line corresponds to the criterion (III), $\delta\nu_\star/\Gamma = 0.5$. In doing so, we set $\mathrm{SNR} = \mathrm{HBR}_{\mathrm{max}}$ just for simplicity. As we remarked above, those criteria are not expected to be strict, and the adopted values of α and β are merely empirical. Nevertheless the regions bounded by the criteria agree with those in which the input parameters are reproduced fairly accurately from the mock simulation. We also note that the length of the arrows for $T_{\mathrm{obs}} = 4$ years becomes approximately half with respect to that for 1 year on average. This indicates that the accuracy of the estimate scales as $1/\sqrt{T_{\mathrm{obs}}}$.

On the basis of the empirical comparison above, we divide the observed *Kepler* stars into two different categories by using $\alpha = 10$ and $\beta = 15$ in the next section. Although these three analytic criteria are helpful in getting a qualitative understanding of the condition necessary for reliable $i_\star$ measurement, they do not always ensure the reliability of measured $i_\star$ quantitatively.

Before finishing this section, we emphasize the limitation of using the median value of the derived PPD in estimating the inclination angle. For that purpose, we compute the derived PPD of the inclination angle for a simulated star assigned $i_\star = 90°$ as an input value. The resulting PPDs are plotted in Figure 4.5 for different values of $\delta\nu_\star/\Gamma$. Red and blue histograms correspond to 1 year and 4 years simulations, respectively, for $\mathrm{HBR}_{\mathrm{max,sim}} = 3$. While the true value (90°) can be measured better for higher $\delta\nu_\star/\Gamma$ and longer observation, the measured value always becomes less than 90°. For example, the gray regions in the bottom-right panel brackets between the measured and true values. This is because we employ the sampling method for inclination over the range of $[0°, 90°]$. In similar fashion, the derived inclination for true inclination of 0° is always greater than 0°. Therefore the uncertainty indicated in Figure 4.4 may be partly, even though not entirely, due to the use of the median value of the entire PPD.

4.2.3 Possible interpretation of the large uncertainty in mock spectra analysis

Since our simulated spectra are not noised, one may expect that the input parameters will be uniquely retrieved, as is mostly the case in the parameter space regarded as *reliable* (green area in Figure 4.4). However, it is clearly not the case outside this region, where we found long arrows suggesting large uncertainty. In practice, there exists large uncertainty for small input $\delta\nu_\star/\Gamma$ (lower region in the Figure 4.4) or small input $i_\star$ (leftmost region in the Figure 4.4). These long arrows cannot represent a systematic error of the analysis, because the model used to generate the simulated spectra and that used in the fitting are identical.

We argue that this uncertainty for small input $\delta\nu_\star/\Gamma$ or $i_\star$ is caused by strong degeneracy between $\delta\nu_\star/\Gamma$ and $i_\star$. As introduced in panels "a", "d", "g", "h", and "i" in Figure 4.1, the shape of $l = 1$ mode profiles are insensitive to $\delta\nu_\star/\Gamma$ and $i_\star$ when either $\delta\nu_\star/\Gamma$ or $i_\star$ is small. Such a degeneracy leads to the broad distribution of the resulting posterior probability density of $\delta\nu_\star/\Gamma$ and $i_\star$. Indeed, the broadness of the posterior distribution is the essential problem that makes precise parameter estimation quite difficult. When posterior is broad over the range of parameter space, the parameter estimation always suffers from large uncertainty. The probability distribution described in red in Figure 4.6 demonstrates such underlying difficulty in parameter estimation for broad distribution, which is actually what we observed in small input $\delta\nu_\star/\Gamma$ or $i_\star$ area in Figure 4.4.

On the other hand, input parameters could be successfully found in green area in Figure 4.4, because the mode profile is quite sensitive to $i_\star$ and $\delta\nu_\star/\Gamma$ and then they do not suffer from a strong degeneracy as observed above. Consequently, the output parameter can be estimated with high precision (see probability distribution described in blue in Figure 4.6).

Obviously, the real observed spectra are noisy data. For these noisy spectra it must be more difficult to find true values of $\delta\nu_\star/\Gamma$ and $i_\star$ when true $\delta\nu_\star/\Gamma$ or $i_\star$ is small, because noise makes it difficult to identify the correct shape of mode profiles. Therefore, estimating statistical errors for the noisy spectra is of another particular importance.

When generating the simulated spectra, we used the ratio of the mode height and constant background power ($\mathrm{HBR} \equiv H/N_0$) as a proxy for SNR of the real spectra. Although "SNR"

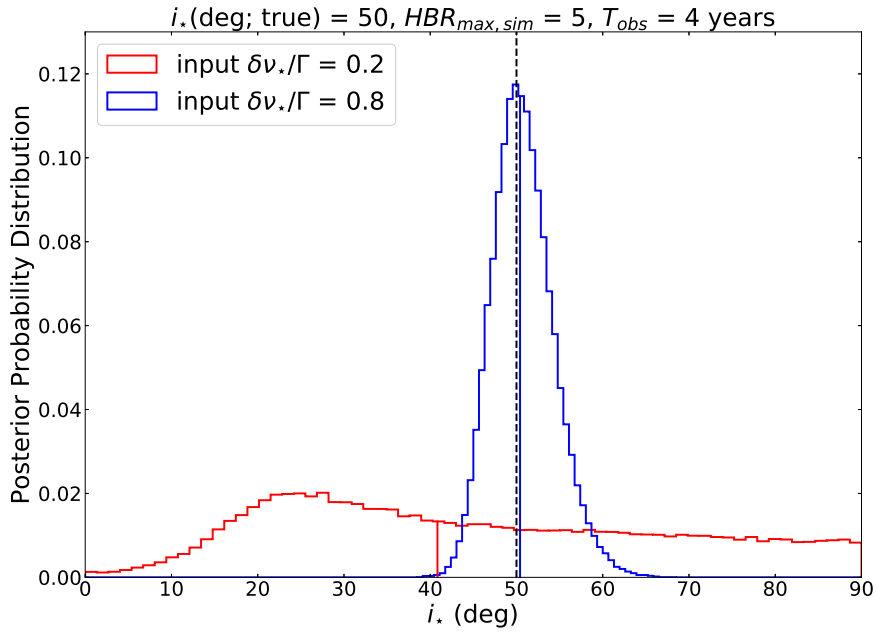

Figure 4.6: Posterior probability distribution of $i_\star$ of the simulation with input $\delta\nu_\star/\Gamma = 0.2$ (red) and $\delta\nu_\star/\Gamma = 0.8$ (blue). The other input values are $i_\star = 50°$, HBR = 5 and $T_{\rm obs} = 4$ years. Black vertical dashed line represents input $i_\star$, while red and blue vertical lines are medians of these distributions.

should account for how noisy the observed spectrum is, the realistic noise is not assigned in our simulated spectra. Based on this situation, proper relation between HBR and SNR is not obvious. Thus considering noisy simulated spectra may allow more realistic evaluation of SNR in relation with HBR.

The noise in power spectrum is known to follow a χ^2 distribution with 2 degree of freedom (e.g., Duvall & Harvey 1986). Based on this property, we generate the noisy simulated spectra with 10 different noise realizations for the case of input HBR = 5, $T_{\rm obs} = 4$ years, and $(i_\star, \delta\nu_\star/\Gamma) = (10°, 0.2), (50°, 0.2), (90°, 0.2), (10°, 0.6), (50°, 0.6), (90°, 0.6)$. Their results of asteroseismic analysis are given in Figure 4.7. Total 10 arrows begins from each combination of input $(i_\star, \delta\nu_\star/\Gamma)$ above. And then the distribution of the endpoints of arrows indicates the statistical error expected at each point in $i_\star$-$\delta\nu_\star/\Gamma$ diagram. As we suspected, there exist large statistical errors for small $\delta\nu_\star/\Gamma$ or $i_\star$.

This result does not change our qualitative understanding that reliable measurement of stellar inclination prefers substantially fast rotation $\delta\nu_\star/\Gamma$ and more or less intermediate inclination. Moreover, it will not affect the results and conclusions in later chapters, because we will focus on the stars whose parameters are reliably determined there. However, the additional simulations with noised spectra are necessary to understand and evaluate the statistical errors of asteroseismic analysis. These tests will help us probe more realistic relation between HBR and SNR.

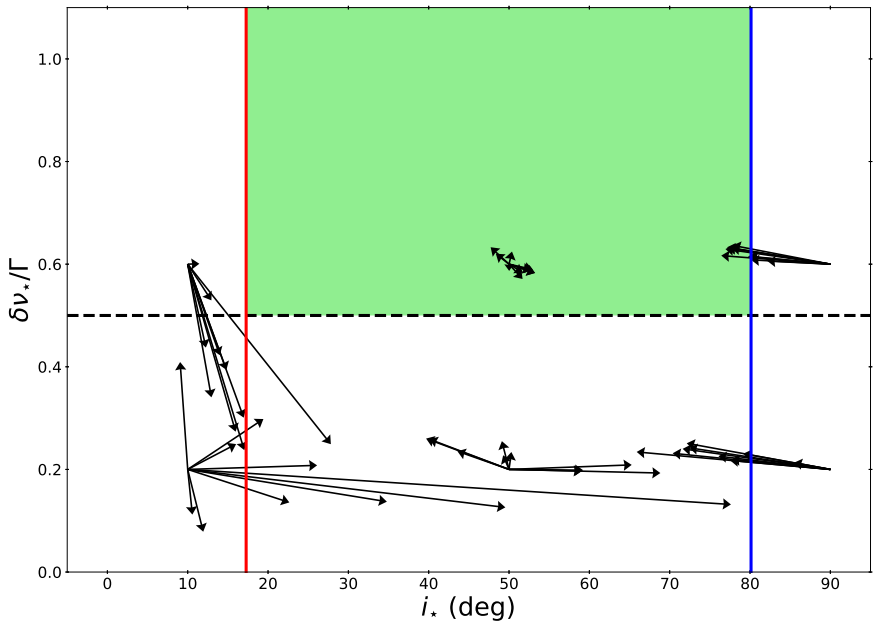

Figure 4.7: Same as Figure 4.4, but for the simulated spectra of HBR=5 and $T_{\rm obs}$=4 years with realistic noise. At each combination of input $(i_\star, \delta\nu_\star/\Gamma) = (10°, 0.2), (50°, 0.2), (90°, 0.2), (10°, 0.6), (50°, 0.6), (90°, 0.6)$, we create the mock power spectra with 10 different noise realizations. Each black arrow at each combination of input $(i_\star, \delta\nu_\star/\Gamma)$ represents the result of the analysis for each simulated spectrum. Scatter of the endpoints of 10 arrows indicates the statistical error expected at each input $(i_\star, \delta\nu_\star/\Gamma)$.

4.3 Application to *Kepler* data

4.3.1 Target star selection

We analyze stars monitored by *Kepler* during its initial 4 years mission. In total, we consider 33 stars with transiting planets and 61 stars without known transiting planets. The stars without known planets in this work are taken from LEGACY sample (Lund et al. 2017, Silva Aguirre et al. 2017). This sample consists of 66 main-sequence solar-like stars observed in short cadence for at least $\approx$ 1 year by *Kepler*. Out of the 66 stars, we select 61 stars that do not have known planets (the remaining 5 stars with planets are also analyzed below). We re-analyze 25 stars with planets in Campante et al. (2016), which include 4 stars (KIC 3632418, 9414417, 9955598, and 10963065) with planets from the LEGACY sample above. In addition, we analyze 8 stars with planets whose asteroseismic analysis has not yet been published elsewhere, including one star (KIC 7296438) from LEGACY sample.

Figure 4.8 is the surface gravity and effective temperature diagram of these 94 stars in our sample. We find all stars are predominantly in main-sequence phase and in range of spectral type from early K to late F (i.e., $5{,}000\,{\rm K} \lesssim T_{\rm eff} \lesssim 6{,}500\,{\rm K}$). Actually, we find no signature of mixed modes, which is typical for evolved stars (sub-giants and red-giants), in the power

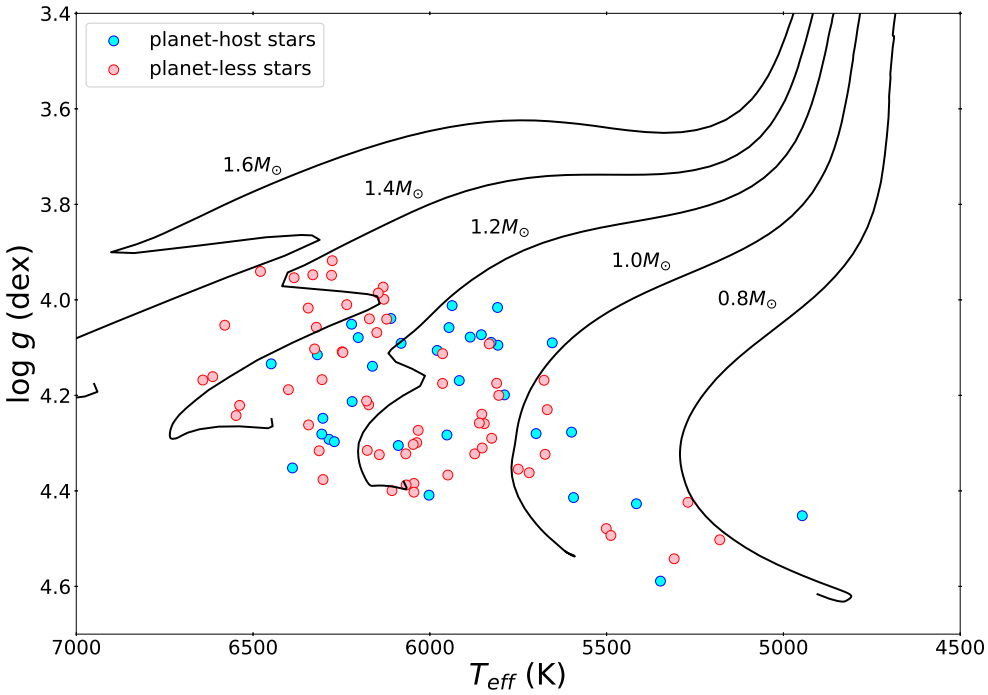

Figure 4.8: Surface gravity and effective temperature diagram for 33 planet-host (blue circle) and 61 planet-less (red circle) stars in our sample. Stellar evolutionary tracks ranging from 0.8 to 1.6 $M_\odot$ in step of 0.2 $M_\odot$ are drawn as continuous lines. These tracks are computed by MESA code by assuming solar values as initial condition except for the mass.

spectra of any stars.

The power spectra prepared using the method of Handberg & Lund (2014), are downloaded from Kepler Asteroseismic Science Operations Center (KASOC) database [2]. There are two different spectra available, with and without weighting of the photometric flux with the flux uncertainty. We use unweighted spectra for 42 targets since their weighted spectra are not available. Otherwise we use the weighted spectra for 51 stars. For KIC 11401755, the latest weighted spectra are not available, and we decided to use its unweighted spectra. We adopt $V_1^2 = 1.447$ and $V_2^2 = 0.5485$, the mean of visibility of the Sun in green and red VIRGO/SPM channels from Salabert et al. (2011). This averaging might give visibilities representative of the *Kepler* visibilities (Ballot et al. 2011).

4.3.2 Asteroseismic inference of *Kepler* stars

We perform asteroseismic analysis using the MCMC method, and summarize the main results in Tables 4.2, 4.3 and 4.4, 4.5 for stars with and without planets, respectively. We classify stars as category A if their measured values of $(i_\star, \delta\nu_\star/\Gamma)$ satisfy the three analytic criteria (I), (II), and (III) with $\alpha = 10$ and $\beta = 15$. Otherwise the stars are classified as category

[2] `http://kasoc.phys.au.dk`

Table 4.2: Results on *Kepler* planet-host stars in category A

KIC	KOI	*Kepler* ID	$\mathrm{HBR}_{\max}$	$\delta\nu_\star/\Gamma$	$i_\star$(16%, 50%, 84%) (deg)	$\delta\nu_\star$(16%, 50%, 84%) (μHz)
3544595	69	93	2.25	1.01	[49.9, 58.0, 70.4]	[0.42, 0.49, 0.56]
4141376	280	1655	0.69	0.70	[41.2, 58.9, 77.7]	[0.80, 0.98, 1.37]
6521045	41	100	3.13	0.51	[62.3, 75.2, 85.6]	[0.43, 0.46, 0.51]
8077137	274	128	1.45	0.65	[56.5, 67.4, 80.1]	[0.84, 0.93, 1.05]
8494142	370	145	0.80	0.51	[38.9, 60.0, 80.1]	[0.89, 1.09, 1.72]
9955598	1925	409	2.91	0.50	[40.3, 49.8, 66.3]	[0.32, 0.41, 0.49]
10963065	1612	408	7.79	0.61	[38.2, 41.7, 46.8]	[0.88, 0.99, 1.08]
11401755	277	36	1.19	0.54	[42.5, 60.0, 79.5]	[0.53, 0.65, 0.84]
11807274	262	50	1.61	0.73	[59.9, 71.6, 83.9]	[1.41, 1.52, 1.70]

Table 4.3: Results on *Kepler* planet-host stars in category B

KIC	KOI	*Kepler* ID	$\mathrm{HBR}_{\max}$	$\delta\nu_\star/\Gamma$	$i_\star$(16%, 50%, 84%) (deg)	$\delta\nu_\star$(16%, 50%, 84%) (μHz)
3425851	268	...	0.78	0.84	[32.3, 52.0, 75.1]	[1.37, 1.98, 3.01]
3632418	975	21	7.92	0.40	[60.3, 71.3, 83.3]	[0.88, 0.94, 1.04]
4143755	281	510	1.67	0.43	[4.6, 20.7, 55.4]	[0.09, 0.32, 0.91]
4349452	244	25	0.94	0.91	[71.3, 80.6, 87.1]	[1.41, 1.49, 1.59]
4914423	108	103	0.63	0.42	[16.0, 43.4, 73.2]	[0.34, 0.62, 1.44]
5094751	123	109	0.54	0.40	[3.7, 15.9, 49.9]	[0.12, 0.60, 2.12]
5866724	85	65	1.07	0.85	[66.4, 75.0, 84.5]	[1.32, 1.41, 1.52]
6196457	285	92	1.62	1.76	[4.5, 14.5, 35.8]	[0.24, 1.90, 3.97]
6278762	3158	444	3.95	2.39	[48.4, 64.8, 78.6]	[0.35, 0.39, 0.49]
7296438	364	...	6.12	0.57	[6.8, 19.2, 48.7]	[0.15, 0.50, 1.11]
7670943	269	...	0.81	0.76	[66.8, 77.3, 86.0]	[1.79, 1.90, 2.05]
8292840	260	126	1.32	0.61	[64.4, 75.6, 85.3]	[1.37, 1.47, 1.59]
8349582	122	95	1.17	0.54	[10.8, 34.8, 66.1]	[0.12, 0.27, 0.55]
8478994	245	37	1.09	1.53	[19.9, 38.7, 64.6]	[0.43, 0.71, 1.16]
8554498	5	...	0.78	0.42	[2.3, 11.9, 49.6]	[0.07, 0.44, 1.67]
8866102	42	410	2.28	0.66	[78.4, 83.6, 88.0]	[2.03, 2.07, 2.12]
9414417	974	...	3.88	0.37	[46.0, 58.7, 76.9]	[0.92, 1.05, 1.25]
9592705	288	...	1.55	0.44	[42.7, 52.2, 65.3]	[0.90, 1.08, 1.30]
10586004	275	129	2.16	0.95	[19.7, 42.9, 69.5]	[0.38, 0.70, 1.12]
10666592	2	2	1.60	0.21	[28.6, 41.8, 61.4]	[0.66, 0.95, 1.29]
11133306	276	509	0.75	0.86	[7.6, 27.1, 62.4]	[0.21, 0.61, 1.53]
11295426	246	68	5.86	0.32	[27.6, 43.1, 70.2]	[0.21, 0.30, 0.46]
11853905	7	4	0.98	0.42	[8.0, 36.2, 66.9]	[0.19, 0.38, 0.92]
11904151	72	10	1.58	0.85	[8.6, 40.5, 74.0]	[0.16, 0.33, 0.80]

Table 4.4: Results on *Kepler* planet-less stars in category A

KIC	$\mathrm{HBR}_{\mathrm{max}}$	$\delta\nu_\star/\Gamma$	$i_\star$(16%, 50%, 84%) (deg)	$\delta\nu_\star$(16%, 50%, 84%) (μHz)
1435467	3.35	0.52	[52.7, 59.5, 70.4]	[1.46, 1.64, 1.82]
4914923	10.58	0.56	[36.4, 43.3, 51.7]	[0.49, 0.58, 0.69]
5773345	5.06	0.67	[27.5, 31.2, 35.4]	[1.50, 1.78, 2.13]
6225718	10.21	0.70	[25.1, 27.2, 29.8]	[1.52, 1.70, 1.85]
6679371	2.71	0.53	[69.9, 78.5, 86.3]	[1.78, 1.86, 1.97]
7103006	2.97	0.51	[41.9, 46.2, 51.5]	[1.76, 1.96, 2.16]
7206837	1.80	0.93	[32.3, 35.4, 38.8]	[2.46, 2.74, 3.03]
7510397	8.76	0.67	[13.9, 17.6, 21.7]	[0.99, 1.37, 1.66]
7680114	5.55	0.51	[15.9, 24.3, 52.0]	[0.26, 0.59, 0.93]
7871531	2.91	0.60	[50.7, 64.1, 81.2]	[0.34, 0.40, 0.47]
7970740	4.66	0.57	[40.2, 48.5, 61.5]	[0.29, 0.37, 0.46]
8006161	8.78	0.62	[33.1, 39.6, 47.5]	[0.45, 0.54, 0.64]
8179536	2.37	0.71	[47.8, 53.3, 60.3]	[1.55, 1.72, 1.91]
8379927	8.21	0.54	[67.0, 71.9, 78.8]	[1.10, 1.15, 1.20]
8394589	3.33	0.70	[63.7, 69.1, 76.0]	[1.00, 1.06, 1.11]
9025370	2.75	0.60	[52.5, 69.9, 83.6]	[0.41, 0.47, 0.55]
9139151	3.37	0.57	[61.0, 71.2, 83.0]	[0.93, 1.00, 1.09]
9139163	2.88	0.83	[23.1, 25.1, 27.6]	[3.09, 3.50, 3.85]
9965715	3.10	0.62	[55.5, 60.3, 66.2]	[1.83, 1.96, 2.09]
11253226	2.31	0.53	[45.8, 48.3, 50.9]	[3.10, 3.24, 3.39]
12009504	3.83	0.53	[63.6, 69.2, 77.1]	[1.12, 1.20, 1.27]
12069424	35.68	0.54	[45.9, 51.9, 60.2]	[0.45, 0.50, 0.55]

B. We find 9 stars with planets of category A, and 22 without planets. The classification is admittedly not strict, because it is based on the measured median values neglecting the quoted errors, in addition to the qualitative nature of the criteria themselves. Nevertheless such a classification is useful as a rough measure of the reliability of the inference.

Top and bottom panels in Figure 4.9 plot the distribution of measured $i_\star$ and $\delta\nu_\star/\Gamma$ for stars with and without planets, respectively. Stars belonging to categories A and B are plotted in filled circles with error-bars and in crosses, respectively. Also we indicate the KOI number for category A stars with planets in top panel. Since the target selection is somewhat heterogeneous, we cannot put any strong conclusion at this point. Nevertheless it is interesting to note that the category A stars with planets are preferentially located around the large $i_\star$ region relative to those without planets, suggesting a general spin-orbit alignment of transiting planets.

Figures 4.10 and 4.11 show examples of power spectra and the resulting two dimensional PPD of $i_\star$ and $\delta\nu_\star$ for categories A and B stars. They present the difference of the ability to constrain $i_\star$ and $\delta\nu_\star$ between categories A and B. Note, however, that these two may be extreme examples, and in some cases the difference between A and B is milder.

Table 4.5: Results on *Kepler* planet-less stars in category B

KIC	$\mathrm{HBR}_{\max}$	$\delta\nu_\star/\Gamma$	$i_\star$(16%, 50%, 84%) (deg)	$\delta\nu_\star$(16%, 50%, 84%) (μHz)
2837475	1.74	0.46	[70.9, 76.6, 83.6]	[3.01, 3.10, 3.20]
3427720	3.18	0.31	[12.4, 28.5, 61.0]	[0.19, 0.43, 0.88]
3456181	3.52	0.28	[34.5, 48.6, 72.0]	[0.75, 0.99, 1.36]
3656476	11.57	0.42	[34.6, 48.8, 73.1]	[0.24, 0.31, 0.42]
3735871	1.42	0.38	[42.9, 66.2, 83.1]	[0.62, 0.72, 0.98]
5184732	13.74	0.43	[58.8, 70.8, 83.0]	[0.53, 0.57, 0.63]
5950854	2.16	1.04	[1.7, 8.2, 27.6]	[0.05, 1.15, 2.35]
6106415	19.61	0.44	[67.0, 75.9, 85.1]	[0.68, 0.71, 0.75]
6116048	12.58	0.42	[62.8, 73.0, 83.7]	[0.61, 0.64, 0.70]
6508366	2.56	0.49	[80.9, 85.6, 88.7]	[2.12, 2.19, 2.26]
6603624	17.93	0.44	[2.0, 4.2, 38.7]	[0.30, 1.44, 2.00]
6933899	10.51	0.31	[48.9, 64.2, 81.0]	[0.33, 0.37, 0.45]
7106245	1.65	0.43	[13.5, 28.6, 62.6]	[0.27, 0.57, 1.36]
7771282	1.17	0.39	[48.6, 67.0, 82.0]	[1.05, 1.19, 1.39]
7940546	9.25	0.35	[52.5, 63.0, 76.6]	[0.97, 1.08, 1.23]
8150065	1.39	0.28	[5.2, 26.0, 65.8]	[0.15, 0.49, 1.37]
8228742	6.52	0.44	[29.9, 38.5, 58.6]	[0.56, 0.83, 1.11]
8424992	2.72	0.41	[4.0, 19.2, 59.3]	[0.08, 0.31, 1.04]
8694723	7.59	0.46	[32.4, 37.4, 43.0]	[1.10, 1.25, 1.46]
8760414	7.19	0.43	[2.1, 8.1, 40.4]	[0.04, 0.48, 1.74]
8938364	8.91	0.31	[7.8, 25.0, 61.7]	[0.10, 0.23, 0.65]
9098294	3.86	0.36	[30.8, 49.9, 75.1]	[0.33, 0.43, 0.66]
9206432	1.62	0.30	[21.1, 36.2, 59.6]	[1.06, 1.73, 2.77]
9353712	1.78	0.87	[21.0, 28.9, 53.8]	[0.86, 1.84, 2.65]
9410862	1.66	0.78	[13.7, 21.2, 45.3]	[0.47, 1.16, 2.01]
9812850	1.82	0.38	[50.7, 64.7, 81.3]	[1.40, 1.57, 1.87]
10068307	11.91	0.40	[33.4, 41.9, 58.4]	[0.58, 0.77, 0.96]
10079226	2.23	2.50	[49.8, 71.6, 84.0]	[0.64, 0.75, 0.93]
10162436	6.61	0.29	[28.7, 44.6, 62.2]	[0.48, 0.65, 1.02]
10454113	3.23	0.42	[26.4, 34.5, 47.6]	[0.83, 1.16, 1.53]
10516096	6.79	0.33	[53.2, 70.2, 83.8]	[0.45, 0.49, 0.58]
10644253	1.86	0.21	[2.5, 13.9, 54.4]	[0.06, 0.34, 1.36]
10730618	1.01	0.31	[11.4, 24.6, 52.8]	[0.52, 1.32, 2.65]
11081729	1.32	2.30	[80.7, 85.4, 88.6]	[3.22, 3.40, 3.51]
11772920	1.93	0.49	[51.1, 67.0, 81.8]	[0.28, 0.33, 0.40]
12069127	1.66	0.19	[16.9, 40.4, 70.3]	[0.35, 0.65, 1.16]
12069449	29.29	0.37	[33.1, 47.0, 70.7]	[0.27, 0.35, 0.49]
12258514	13.77	0.30	[19.9, 34.0, 64.6]	[0.28, 0.46, 0.81]
12317678	2.74	0.20	[46.1, 62.4, 80.5]	[0.92, 1.06, 1.34]

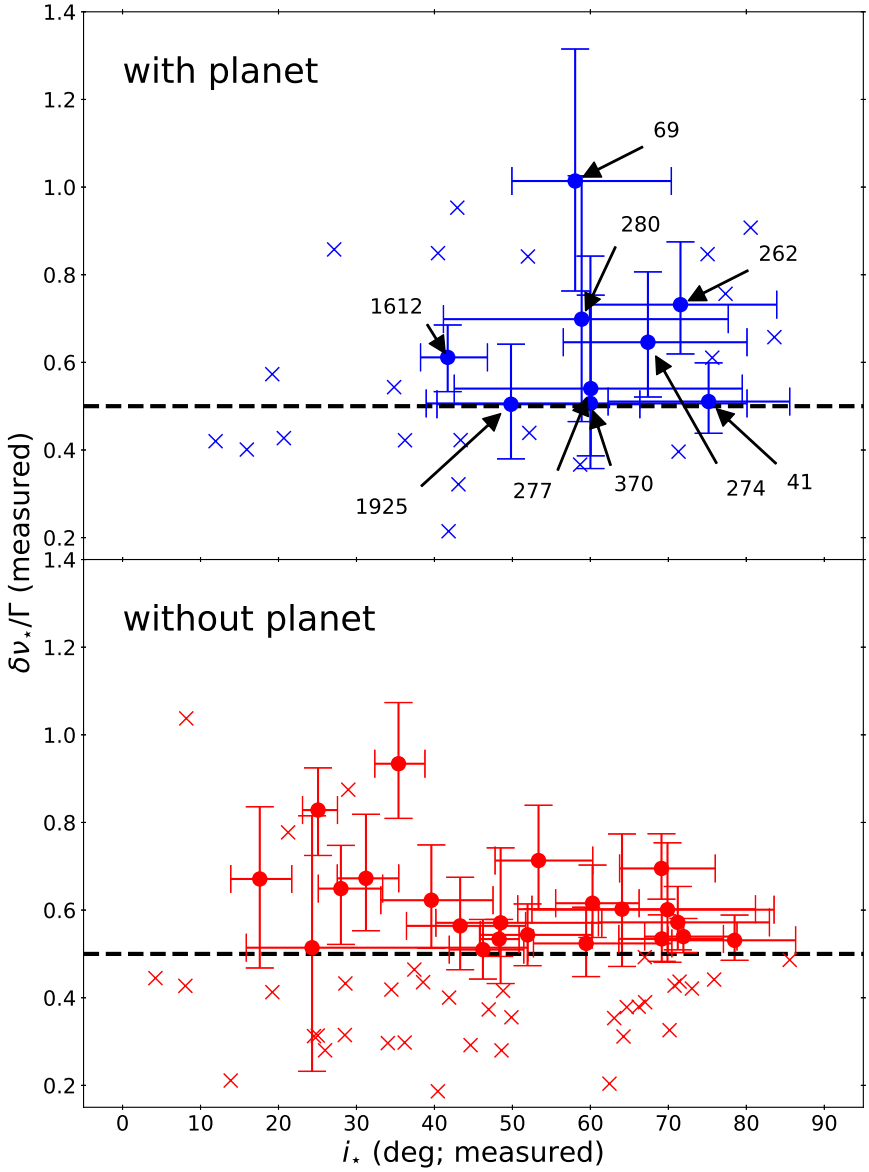

Figure 4.9: Measured values of $i_\star$ and $\delta\nu_\star/\Gamma$ for *Kepler* stars with (top) and without (bottom) known planetary companions. The black solid horizontal line represents $\delta\nu_\star/\Gamma = 0.5$ (equation 4.12). Filled circles indicate category A stars, while crosses correspond to category B stars. The numbers labelling the filled circles denote the KOI IDs for stars with planets.

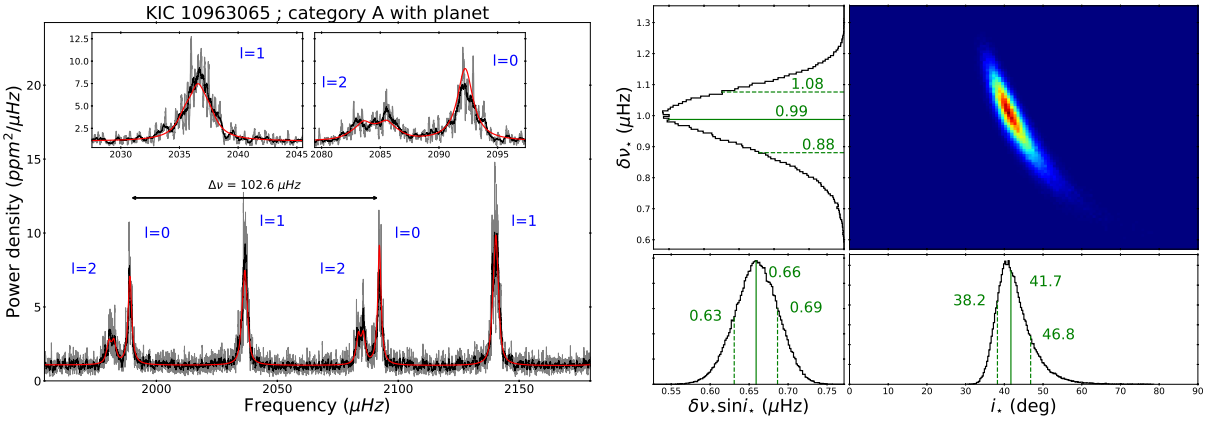

Figure 4.10: Results of our asteroseismic analysis for KIC 10963065 (KOI 1612, Kepler-408), as a typical example of planet-host stars in category A. *Left*: Power spectra around $\nu_{\rm max}$ along with the best-fit model curve (red solid line). Black and gray lines indicate spectra smoothed over the width of $0.2\,\mu$Hz and $2.0\,\mu$Hz, respectively. The upper insets display the zoom-in views of the spectra, around $l = 1$ (left) and $l = 0 + 2$ (right) modes. Black and gray lines in these insets are smoothed over $0.15\,\mu$Hz and $0.75\,\mu$Hz. *Right*: Upper-right panel is the two-dimensional correlation map of $i_\star$ and $\delta\nu_\star$ obtained from the MCMC sampling. Top-left and bottom-right panels are the corresponding marginalized PPD for $\delta\nu_\star$ and $i_\star$, respectively. Bottom-left panel is the PPD of the combined quantity, $\delta\nu_\star \sin i_\star$. Green vertical lines in these histograms indicate the median and 1σ credible regions.

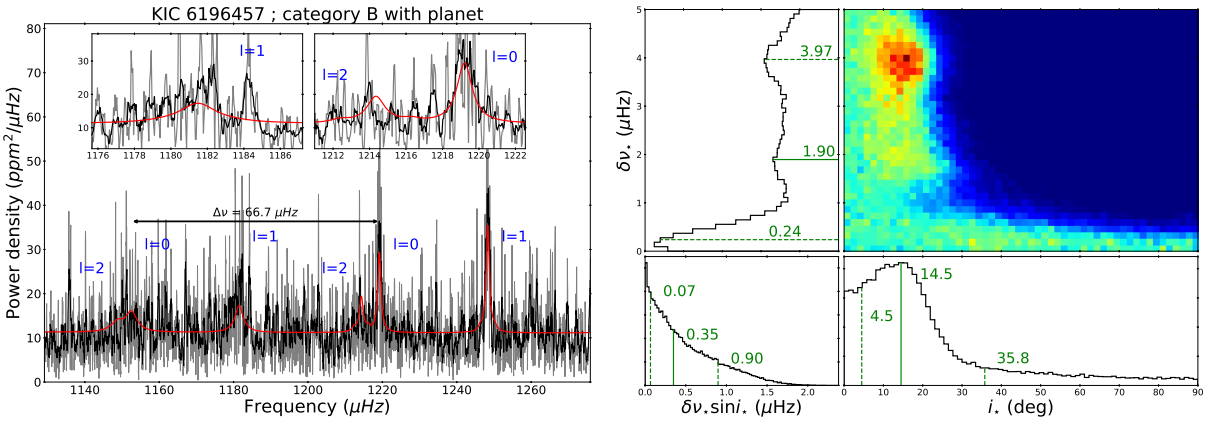

Figure 4.11: Same as Figure 4.10, but for category B star KIC 6196457.

4.3.3 Consistency with other observations

Unlike for simulated stars, the true values of the stellar parameters for actual *Kepler* stars are obviously not known. Thus it is important to compare our asteroseismic estimates of stellar parameters with other independent observations, which is attempted in this subsection. In this subsection we present a brief comparison of $v \sin i_\star$, $\delta\nu_\star$, and $i_\star$ with other observations to discuss the overall trend. Then more dedicated study for some particular stars will be given in later chapters, in terms of $i_\star$ (chapter 5) and $P_{\rm rot} = 1/\delta\nu_\star$ (chapter 6).

We first consider $v \sin i_\star$ that can be measured also from line widths of spectroscopically observed stars. For 33 stars with planets, we use the spectroscopic $v \sin i_\star$ from California-*Kepler* Survey (CKS) [3], except one from Huber et al. (2013b). For 61 stars without planets, we consider two different spectroscopic datasets from Bruntt et al. (2012) and Molenda-Żakowicz et al. (2013). First we adopt the data for 43 stars from Bruntt et al. (2012). Out of the remaining 18 stars not listed in their catalog, we adopt the data from Lund et al. (2017) for 11 stars. Next we repeat the same procedure starting with the dataset of Molenda-Żakowicz et al. (2013). In this case, we combine 46 stars from Molenda-Żakowicz et al. (2013), and 11 stars from Lund et al. (2017). Note that $v \sin i_\star$ in Huber et al. (2013b) and Lund et al. (2017) is calculated on the basis of the Stellar Parameter Classification pipeline (SPC; Buchhave et al. 2012), while CKS, Bruntt et al. (2012), and Molenda-Żakowicz et al. (2013) developed their own pipelines in computing $v \sin i_\star$.

While $v \sin i_\star$ can be directly estimated from spectroscopic data, it is not the case for asteroseismology. We estimate the stellar radius $R_\star$ from the scaling relation calibrated with the Sun:

$$\frac{R_\star}{R_\odot} = \left(\frac{\nu_{\rm max,\star}}{\nu_{\rm max,\odot}}\right)\left(\frac{\Delta\nu_\star}{\Delta\nu_\odot}\right)^{-2}\left(\frac{T_{\rm eff,\star}}{T_{\rm eff,\odot}}\right)^{1/2}, \tag{4.16}$$

where $\nu_{\rm max,\star}$ is the frequency corresponds to the peak of the mode heights (see Figure 4.3), $\Delta\nu_\star$ is the large separation, and $T_{\rm eff,\star}$ is the effective temperature of the star. Thus $R_\star$ can be estimated from the two asteroseismic observables, $\nu_{\rm max,\star}$ and $\Delta\nu_\star$, along with $T_{\rm eff,\star}$, which leads to asteroseismic estimate of $v \sin i_\star$:

$$v \sin i_\star = 2\pi R_\star \delta\nu_\star \sin i_\star. \tag{4.17}$$

We adopt $\nu_{\rm max,\odot} = 3{,}100\,\mu$Hz, $\Delta\nu_\odot = 134.9\,\mu$Hz, and $\rm T_{eff,\odot} = 5{,}777\,K$ (Broomhall et al. 2009, Gaulme et al. 2016).

Figure 4.12 compares $v \sin i_\star$ from asteroseismic and spectroscopic data. The left panel shows planet-hosting stars in blue (32 from CKS and 1 from Huber et al. 2013b), and also stars without planets, 11 from Lund et al. (2017) in black, 43 from Bruntt et al. (2012) in red, and 46 from Molenda-Żakowicz et al. (2013) in green. Since a significant fraction of stars without planets overlaps in the two sources, we distinguish them using different colors. Filled circles and crosses correspond to categories A and B stars, respectively. We do not quote error-bars for Bruntt et al. (2012) since they are not available from their published table.

[3] `https://california-planet-search.github.io/cks-website/`

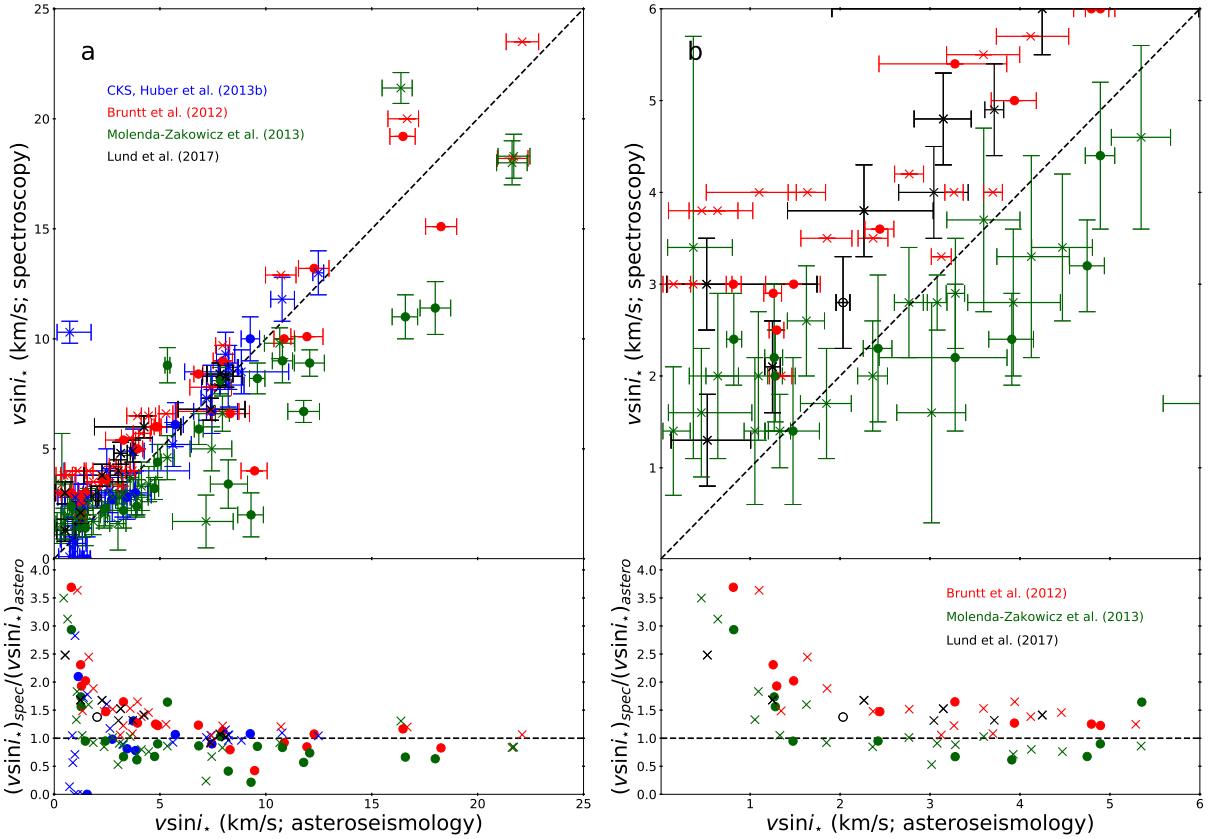

Figure 4.12: Comparison of $v \sin i_\star$ estimated from spectroscopy and those from asteroseismology. Filled circles and crosses correspond to categories A and B stars, respectively. Panel a shows stars with planets (blue), with spectroscopic values from CKS (32 stars) and Huber et al. (2013b) (1 star). Shown stars without planets use values from Lund et al. (2017) in black (11 stars), from Bruntt et al. (2012) in red (43 stars), and from Molenda-Żakowicz et al. (2013) in green (46 stars). Panel b is an enlarged view for stars without planet whose $v \sin i_\star$ is less than 6 km/s.

The left panel of Figure 4.12 suggests that asteroseismic and spectroscopic $v \sin i_\star$ are in reasonable agreement. However, a closer look at $v \sin i_\star < 6$ km/s data in the right panel reveals an interesting feature; the estimates by Bruntt et al. (2012) (red) are systematically larger than our asteroseismic values, while those by Molenda-Żakowicz et al. (2013) (green) are systematically smaller. Our result are somewhere in-between, except for $v \sin i_\star \lesssim 2$ km/s. Since these authors have a large fraction of stars in common, the feature should not be due to differences in the stellar properties. We suspect that the difference between the two spectroscopic results comes from the subtle modelling of micro/macro-turbulence effects in spectroscopic data. We would like to point that "the roundest A-type star" KIC 11145123 (Kurtz et al. 2014, Gizon et al. 2016) presents an interesting example in this context. Takada-Hidai et al. (2017) found that the spectroscopically measured value

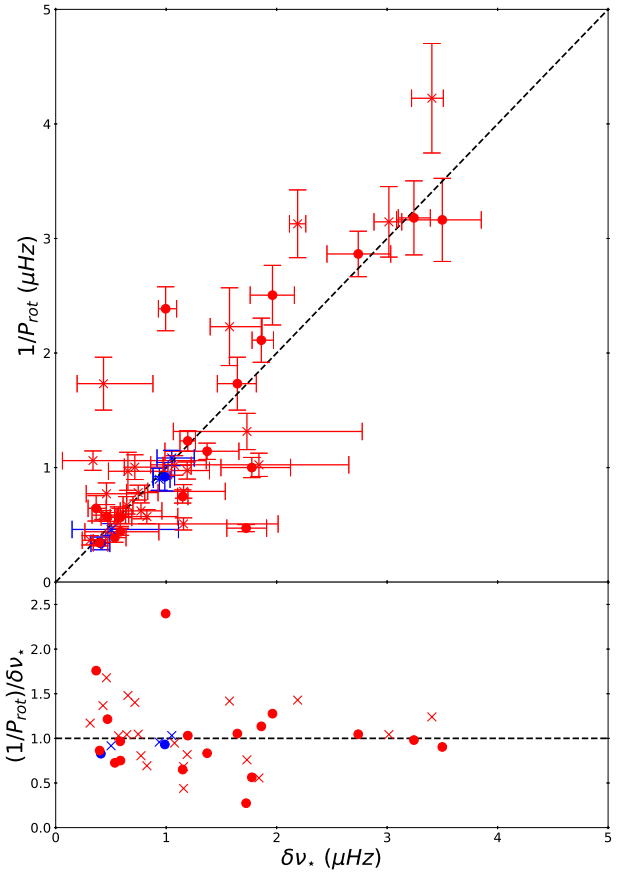

Figure 4.13: Comparison of $\delta\nu_\star$ derived from asteroseismology and the inverse of the stellar rotation period derived from photometric variations, whenever available. Stars with and without planets are plotted in blue and red, respectively. Filled circles and crosses correspond to categories A and B stars.

of $v \sin i_\star \approx 5$ km/s suffers from systematic overestimate, and asteroseismically derived equatorial rotation velocity of $v \sin i_\star \approx 1$ km/s proved to be more reliable. This suggests that the spectroscopic measurement of $v \sin i_\star$ for slowly rotating stars needs to be interpreted with caution, which is in good agreement with our conclusions from Figure 4.12. The importance of the careful calibration of turbulence has been well recognized in earlier publications, for instance by Bruntt et al. (2012). The lower panels of Figure 4.12 provide observational evidences of this problem. Incidentally, the overall consistency between asteroseismic and spectroscopic $v \sin i_\star$ ($>$ a few km/s) may also reinforce the nearly-uniform rotation of stars as stated by Benomar et al. (2015). This is because asteroseismology measures the stellar rotation averaged over its interior, while spectroscopy measures its surface rotation.

Figure 4.13 compares asteroseismic $\delta\nu_\star$ and the inverse of stellar rotation period measured from photometric variability for 46 stars (García et al. 2014). While they agree reasonably on average, individual agreement is not good except for $\delta\nu_\star \gtrsim 2\,\mu$Hz ($P_{\rm rot} \lesssim 6$ days). Again

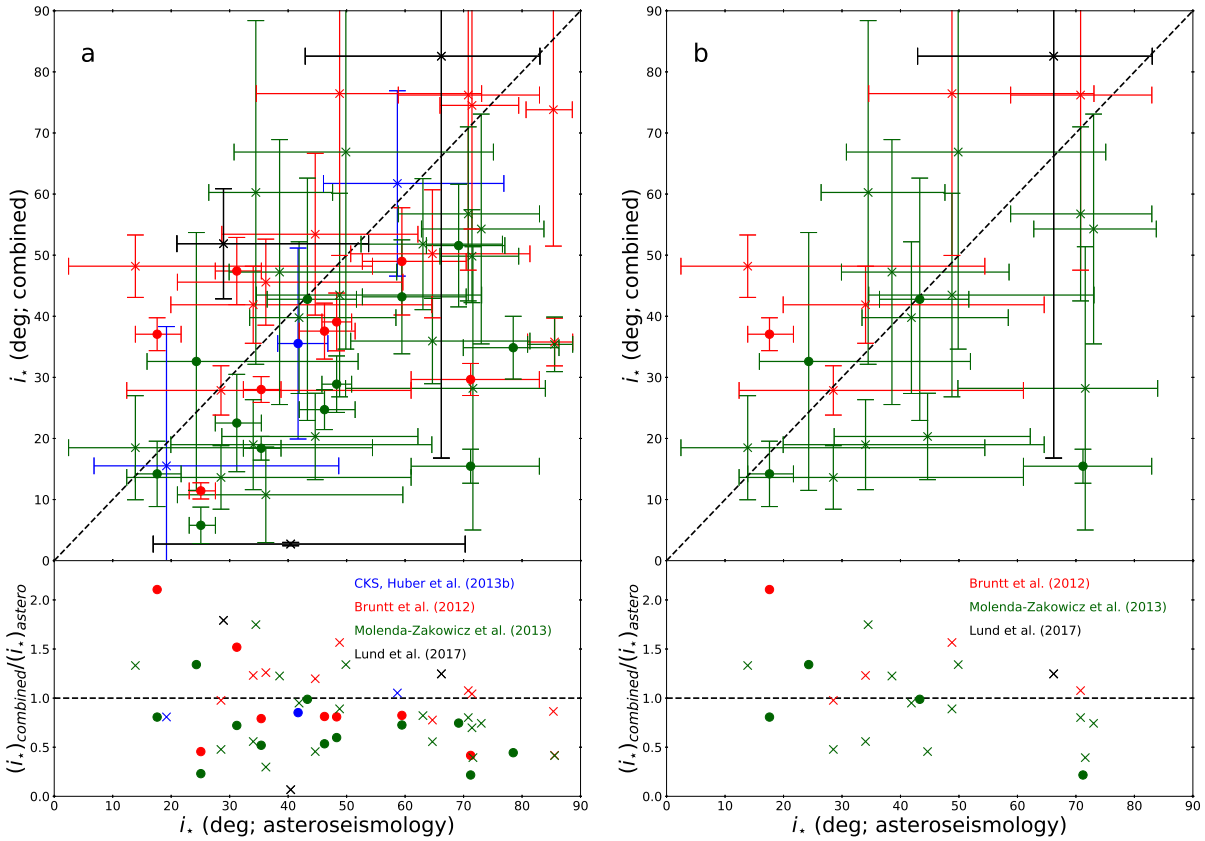

Figure 4.14: Comparison of $i_\star$ derived from asteroseismology and those derived from spectroscopic and time-domain photometric observations (equation 2.21). The colors and symbols are the same as those in Figure 4.12.

both the photometric variation and rotational splitting are not reliably identified for slowly rotating stars.

Combining the spectroscopic $v \sin i_\star$, asteroseismic $R_\star$, and photometric $P_{\rm rot}$, we can estimate $i_\star$ by equation (2.21). Figure 4.14 is similar to Figure 4.12, but instead, compares $i_\star$ estimated from equation (2.21) with the asteroseismic $i_\star$. Panel a (left) shows the stars whose $i_\star$ is derived from the combined analysis, while panel b (right) shows planet-less stars with $v \sin i_\star < 6\,$km/s alone, similarly to Figure 4.12. The large scatter, that is mainly due to the photometric variation uncertainty, makes it difficult to draw any definite conclusion at this point. Indeed, the lightcurve modulation attributed to star-spots could be affected by the fact that the number, lifetime and latitude of the star-spots are not understood well. It is therefore difficult to identify the reason of the scatter at this stage. However, this is the current status of the mutual comparison of independently measured $i_\star$, which needs to be kept in mind in considering the implications of the distribution of $i_\star$.

This caution may be relevant to interpret the recent results by Kovacs (2018), which reports the possible alignment of stellar inclinations in the Praesepe cluster from the combined

analysis of photometric rotation periods ($P_{\rm rot}$), spectroscopic rotation velocities ($v \sin i_\star$), and estimated stellar radii ($R_\star$). Figures 3 and 4 of Kovacs (2018) indicate that the cumulative distribution of $i_\star$ for the cluster is biased toward the larger value relative to the isotropic distribution. This could be explained as well if the macro-turbulence is underestimated as it might be the case for Bruntt et al. (2012). It is premature to firmly conclude at this point, but it clearly indicates the importance of our current findings exhibited in Figure 4.12, and the necessity to perform in the future a thorough comparative study of methods for inferring the stellar inclination.

4.4 Discussion and conclusion

One of our main findings in this chapter is that the asteroseismology provides reliable stellar inclination only for stars with at least $20^\circ \lesssim i_\star \lesssim 80^\circ$, $\delta\nu_\star/\Gamma \gtrsim 0.5$, with higher signal-to-noise ratio, and with longer observations. A significant uncertainty arises when this is not the case, so that the stellar inclination could be overestimated for low inclinations and underestimated otherwise. Below we discuss more broadly its implication on previous results.

4.4.1 Inclinations for CoRoT stars

Although the statistics is low, it is interesting to note that the analysis of solar-like stars observed by CoRoT (Baglin et al. 2006a,b) often led to low and medium stellar inclinations. An isotropic distribution of stellar spins in the sky should give instead a larger proportion of stars with high inclination. We have $i_\star = 45 \pm 4$ (deg) for HD 181420 (Barban et al. 2009), $i_\star = 24 \pm 3$ (deg) for HD 181906 (García et al. 2009), and in fact they are based on the low SNR. On the other hand, we have $i_\star = 17 \pm 9$ (deg) or $i_\star = 26^{+17}_{-7}$ (deg) for HD 49933 (Benomar et al. 2009, Benomar et al. 2015) and $i_\star = 71 \pm 6$ (deg) for HD 49385 (Deheuvels et al. 2010) with high SNR.

Those CoRoT stars were observed only for 90 to 180 days, with a signal-to-noise that does not exceed $\approx$ 5. From Figure 4.4, we expect that a substantial uncertainty covering lower inclinations should be present for most of the CoRoT stars, which is in agreement with the apparent excess of low to medium stellar inclinations. This is also largely consistent with our *Kepler* data analysis plotted in Figure 4.9, especially for stars without planet in which the correlation with the transiting planetary orbital plane should not exist.

4.4.2 Inclinations for evolved stars

While the current work is specifically dedicated to low-mass main-sequence stars, our results can be of importance also for evolved stars. Sub-giants and red-giants show mixed modes, arising from the coupling between pressure modes and gravity modes. Mixed modes can be mostly sensitive either to the envelope (pressure-like modes) or to the interior (gravity-like modes). The large number of $l = 1$ mixed modes observed in evolved stars has enabled

detailed studies of the interior and evolution of those stars (e.g., Deheuvels et al. 2012, Mosser et al. 2014).

Because pressure-like modes are short-lived [4] and probe the slowly rotating envelope (e.g., rotations of the order $\approx$ 100 days in red-giants), it is expected that split-components of $l = 1$ modes suffer from a severe blending ($\delta\nu_\star \ll \Gamma$). On the contrary, gravity-like modes have lifetimes of the order of years and probe regions that mostly rotate faster than the envelope (Beck et al. 2012, Deheuvels et al. 2012, Benomar 2013, Deheuvels et al. 2014, Deheuvels et al. 2015, Mosser et al. 2017), so that split-components are well separated ($\delta\nu_\star \gg \Gamma$).

In these conditions and as suggested by Figure 4.4, it is likely that gravity-like modes allow an accurate determination of the stellar inclination, provided that they have a significant signal-to-noise ratio. However, we need to be cautious when determining the stellar inclination from pressure-like modes. We also stress that when modes of evolved stars are fitted individually (e.g., using a local fit, rather than a global fit as performed in this study), inclinations of blended modes or low signal-to-noise modes are expected to be significantly misled towards lower values. This suggest that the asteroseismic determination of the stellar inclination for the red-giant Kepler-56 (Huber et al. 2013a), reported to have a large $i_\star$ and to host multiple transiting planets, remains certainly accurate because the analyzed split component of the $l = 1$ modes are clearly well resolved and of high signal-to-noise ratio (see their Figure 1). However, results from Corsaro et al. (2017) on spin alignment of star clusters may require a careful interpretation because they fit different modes independently and determine *a posteriori* the stellar inclination. In addition, the clusters consist of faint stars with modes of relatively low amplitudes. As suggested by Figure 4.4, this may mislead stellar inclinations towards $\approx$ 30 degrees. This indicates the importance of studying a potential uncertainty on stellar inclination for sub-giants and red-giants as we have performed for main-sequence stars.

4.5 Summary of this chapter

The measurement of the stellar inclination angle $i_\star$ is particularly important to probe the spin-orbit alignment of transiting exoplanetary systems in an independent and complementary manner to the projected angle λ from the Rossiter-McLaughlin measurement (Ohta et al. 2005). The statistical distribution of $i_\star$ and λ provides a quantitative test for theories of the origin and evolution of planetary systems. While the majority of transiting exoplanets are found around F, G, and K type stars in their main-sequence phase, those are harder to measure $i_\star$ compared to evolved solar-like stars (red-giants and sub-giants). This is mostly due to the relatively lower oscillation amplitude and the sever mode blending of main-sequence solar-like stars. Therefore, it is of fundamental importance to perform a systematic verification of the reliability of $i_\star$ derived from asteroseismology for those stars.

We generated 3,000 simulated oscillation power spectra scaled from a reference star KIC 12069424 (16 Cyg A) that span a wide range of the height-to-background ratio, rotational splitting $\delta\nu_\star$, and inclination angle $i_\star$, each for 1 year and 4 years observation duration.

[4] The lifetime of the modes is inversely proportional to the mode width.

Then we performed systematic mock simulations of asteroseismic analysis, and examined the reliability of $i_\star$ derived from asteroseismic analysis with a Bayesian-MCMC sampling method. We find that the low signal-to-noise ratio of the power spectra induces a systematic under-estimation (over-estimation) for stars with high (low) inclinations. The combination of analytical consideration and mock simulation results revealed three empirical criteria on ($i_\star$, $\delta\nu_\star/\Gamma$) plane as a function of the power, height-to-background ratio HBR, and the observation duration $T_{\rm obs}$, which are required for a reliable estimate of $i_\star$. These criteria indicate that for the reliable measurements stars need to be at least in the range of $20^\circ \lesssim i_\star \lesssim 80^\circ$ with high HBR, high $\delta\nu_\star/\Gamma$, and longer $T_{\rm obs}$.

We also performed asteroseismic analysis of 94 main-sequence solar-like stars in *Kepler* short cadence data using the same Bayesian-MCMC sampling method; 33 and 61 are stars with and without known planetary companions, respectively. We find that 9 stars with planet and 22 stars without planet satisfy the criteria above.

The stellar inclination and rotation, $i_\star$ and $\delta\nu_\star$, that we derived asteroseismically for those *Kepler* stars are compared with those derived photometrically and spectroscopically. We find that our asteroseismic $v \sin i_\star$ is in good agreement with the *average* of two independent spectroscopic analysis by Bruntt et al. (2012) and Molenda-Żakowicz et al. (2013). This suggests that a careful modelling of macro-turbulence is crucial in estimating $v \sin i_\star$ from spectroscopic data, especially for slowly rotating stars.

The rotation period $P_{\rm rot}$ derived from the photometric variability of the stellar light curve shows reasonable, even if not good, agreement with $\delta\nu_\star$. The combined estimate of $i_\star$, however, is very limited both observationally and statistically, and does not show strong agreement with its asteroseismic estimate at this point, indicating that further quantitative study is necessary. Some important implications of our asteroseismic results for the *Kepler* stars will be revisited in later chapters.

Chapter 5

Highly oblique exoplanetary system Kepler-408

As we reviewed in section 2.6, all previous detections of misaligned orbits are for planets larger than Neptune. Smaller planets are relatively unexplored because of the difficulty of the relevant measurements.

One of the most successful techniques for investigating spin-orbit misalignment, the Rossiter-McLaughlin effect, requires the observation of signals for which the amplitude is proportional to the loss of light during planetary transits. Hence, it is much easier to apply to giant planets than small planets. Two other techniques introduced in chapter 2, the asteroseismic method and the combined method, rely on observing signals that are independent of planet size. However, the asteroseismic method has only been applied to 33 stars, because it requires an unusually bright star with large-amplitude p mode oscillations. The combined method has been applied to samples of hundreds of stars, but in most cases it only provides weak constraints (Schlaufman 2010, Winn et al. 2017b). Due to these limitations, it is unclear whether the misalignments are the result of processes specific to giant planets, or whether they also occur for terrestrial planets.

In this chapter, we report the detection of a gross misalignment between the equator of the star Kepler-408 and the orbital plane of a planet comparable in size to the Earth.

5.1 Basic properties of Kepler-408 system

Kepler-408 (also known as KIC 10963065 and KOI-1612), one of 33 planet-host stars analyzed with asteroseismology in previous chapter, has been monitored for 4 years by *Kepler*. Transit signal of only one planet has been detected, with a period of 2.5 days, a duration of 1.3 hours, and a fractional transit depth of 3.1×10^{-5} (Thompson et al. 2018). Table 5.1 summarizes the known characteristics of the system. With a *Kepler* apparent magnitude of 8.8, the host star is the third brightest of all the *Kepler* stars with confirmed planets. This unusual brightness enables an investigation of the stellar obliquity using asteroseismology. In practice, Kepler-408 is classified as category A according to the analytic criteria. This is because this unusual

Table 5.1: System parameters of Kepler-408

Parameter	Value	Reference
Stellar parameters		
Effective temperature, $T_{\rm eff}$ [K]	6088 ± 65	Petigura et al. (2017)
Surface gravity, $\log(g/{\rm cm\,s^{-2}})$	$4.318^{+0.08}_{-0.089}$	Petigura et al. (2017)
Metallicity, [Fe/H]	$-0.138^{+0.043}_{-0.042}$	Petigura et al. (2017)
Mass, $M_\star\,[M_\odot]$	1.05 ± 0.04	Johnson et al. (2017)
Radius, $R_\star\,[R_\odot]$	1.253 ± 0.051	Berger et al. (2018)
Age [Gyr]	4.7 ± 1.2	Johnson et al. (2017)
Projected rotation rate, $v \sin i_\star$ [km/s]	2.8 ± 1.0	Petigura et al. (2017)
Rotation period, $P_{\rm rot}$ [days]	12.89 ± 0.19	Angus et al. (2018)
Planetary parameters		
Planet-to-star radius ratio, $R_{\rm p}/R_\star$	0.0063 ± 0.0003	This work
Radius, $R_{\rm p}\,[R_\oplus]$	0.86 ± 0.04	This work
Time of inferior conjunction [BJD]	2454965.6804 ± 0.0003	This work
Orbital period, $P_{\rm orb}$ [days]	2.465024 ± 0.000005	Thompson et al. (2018)
Orbital inclination, $i_{\rm orb}$ [deg]	81.85 ± 0.10	This work

brightness enables high SNR and frequency resolution fine enough. Moreover, it is important to note that Kepler-408 is an unique system that shows significantly low stellar inclination among 33 planet-host sample.

However, there are conflicting reports in the literature. Campante et al. (2016) found the inclination to be consistent with 90° and set a lower limit of 54°. This was part of a homogeneous study of 25 stars with transiting planets. In contrast, Nielsen et al. (2017) found the inclination to be between 40 and 45 degrees. This finding was incidental to the main purpose of that study, which was to probe the internal rotation profiles of 6 stars. The authors did not remark on the transiting planet, nor on the conflict with Campante et al. (2016).

We have examined the case of Kepler-408 in greater detail, to try and resolve this conflict. This is motivated by the numerical simulations in chapter 4, which established the observational requirements for the reliable inference of the rotational inclination, and found that the characteristics of Kepler-408 should allow for reliable results. Section 5.2 describes the transit analysis. Section 5.3 presents some independent checks on the previous measurements of the stellar rotation period, which plays a key role in the asteroseismic analysis. Section 5.4 describes the asteroseismic analysis, and resolves the prior discrepancy by identifying a problem with the analysis by Campante et al. (2016). Section 5.5 shows that our asteroseismic estimate of $i_\star$ agrees with the constraint that is obtained by combining measurements of the stellar radius, rotation period, and sky-projected rotation velocity. Our findings and some implications are summarized in section 5.6.

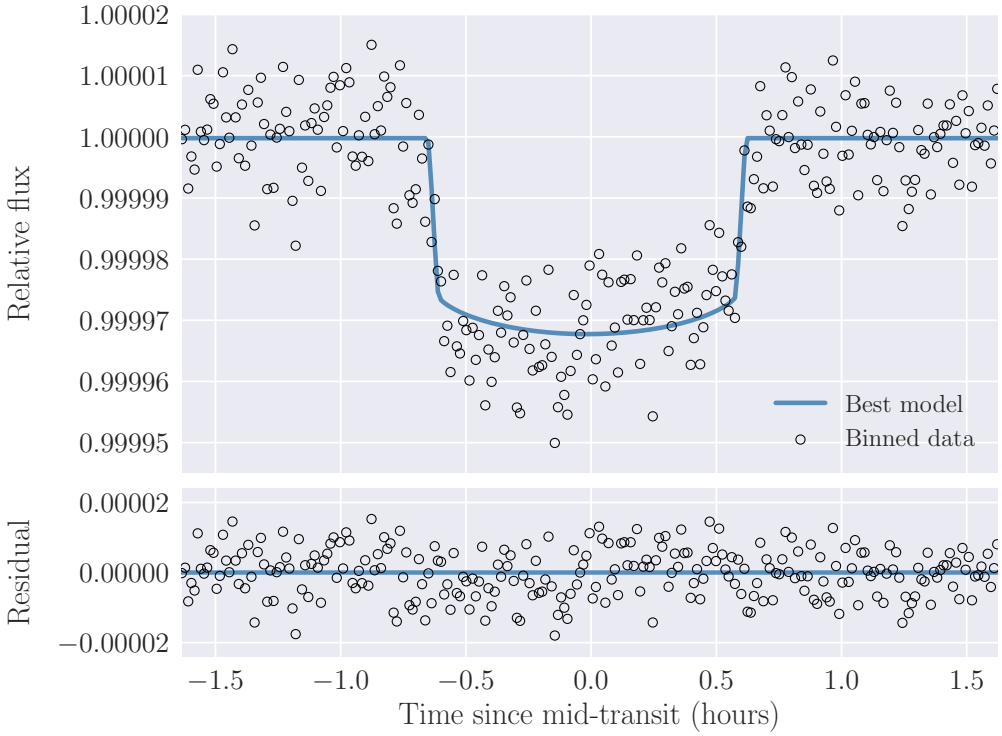

Figure 5.1: Phase-folded transit light curve of Kepler-408b. *Upper panel*: Binned data (open circles) with the best-fitting model (thick line). *Lower panel*: Residuals between the data and the best-fitting model.

5.2 Transit modelling

The orbital inclination, $i_{\rm orb}$, of a transiting planet is always close to 90°. For a precise measurement, we modeled the *Kepler* transit light curve. We downloaded the short-cadence, pre-search data conditioning (PDC) light curves from the Mikulski Archive for Space Telescopes. The data surrounding each transit were fitted with a standard model for the loss of light (Mandel & Agol 2002), assuming the orbit to be circular and accounting for stellar variability with a locally quadratic function of time. After dividing through by the best-fitting quadratic functions, the transit data were phase-folded and averaged, giving a mean light curve with a higher signal-to-noise ratio (Figure 5.1).

This light curve was then fitted to obtain our final estimates for the transit parameters (Table 5.1). Uniform priors were adopted for the logarithm of the planet-to-star radius ratio ($R_{\rm p}/R_\star$), the cosine of the orbital inclination ($\cos i_{\rm orb}$), the normalization of the light curve, the two coefficients of the quadratic limb-darkening profile, and the logarithm of a noise term to account for the scatter of the residuals between the data and the model. A Gaussian prior was adopted for the mean stellar density ($\rho_\star = 0.816 \pm 0.025\,{\rm g/cm^3}$) based on the asteroseismic analysis in chapter 4. The posterior distributions for the model parameters were obtained with a nested sampling code (Feroz et al. 2009). The result for the orbital

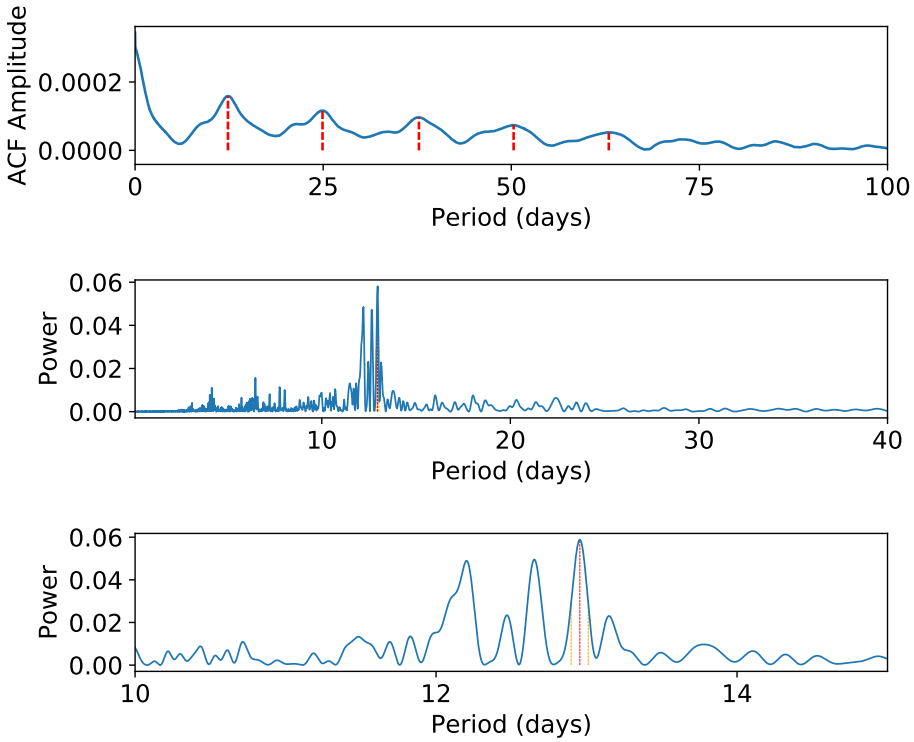

Figure 5.2: Two methods for determining the stellar rotation period. *Top*: Auto-correlation function. *Middle*: Lomb-Scargle periodogram. *Lower*: Close-up of the periodogram near the most significant peaks.

inclination was $i_{\rm orb} = 81.85 \pm 0.10$ (deg).

We also tried allowing the planet's orbit to be eccentric. In that case, although the mode of the eccentricity posterior was about 0.7, the circular solution was not excluded with a high significance. These results are in agreement with the previous light-curve analysis of Van Eylen et al. (2018), who found that the eccentricity was consistent with zero within 95% confidence.

5.3 Stellar rotation period from photometric variability

The *Kepler* photometric time series exhibits quasi-periodic modulation that is presumably due to the rotation of surface inhomogeneities across the star's visible hemisphere. By computing the autocorrelation function, McQuillan et al. (2013) determined the photometric rotation period to be 12.44 ± 0.17 days. Angus et al. (2018) reported a value of 12.89 ± 0.19 days by modeling the *Kepler* data as a Gaussian process with a quasi-periodic covariance kernel function.

To perform an independent check on the determination of the stellar rotation period, we

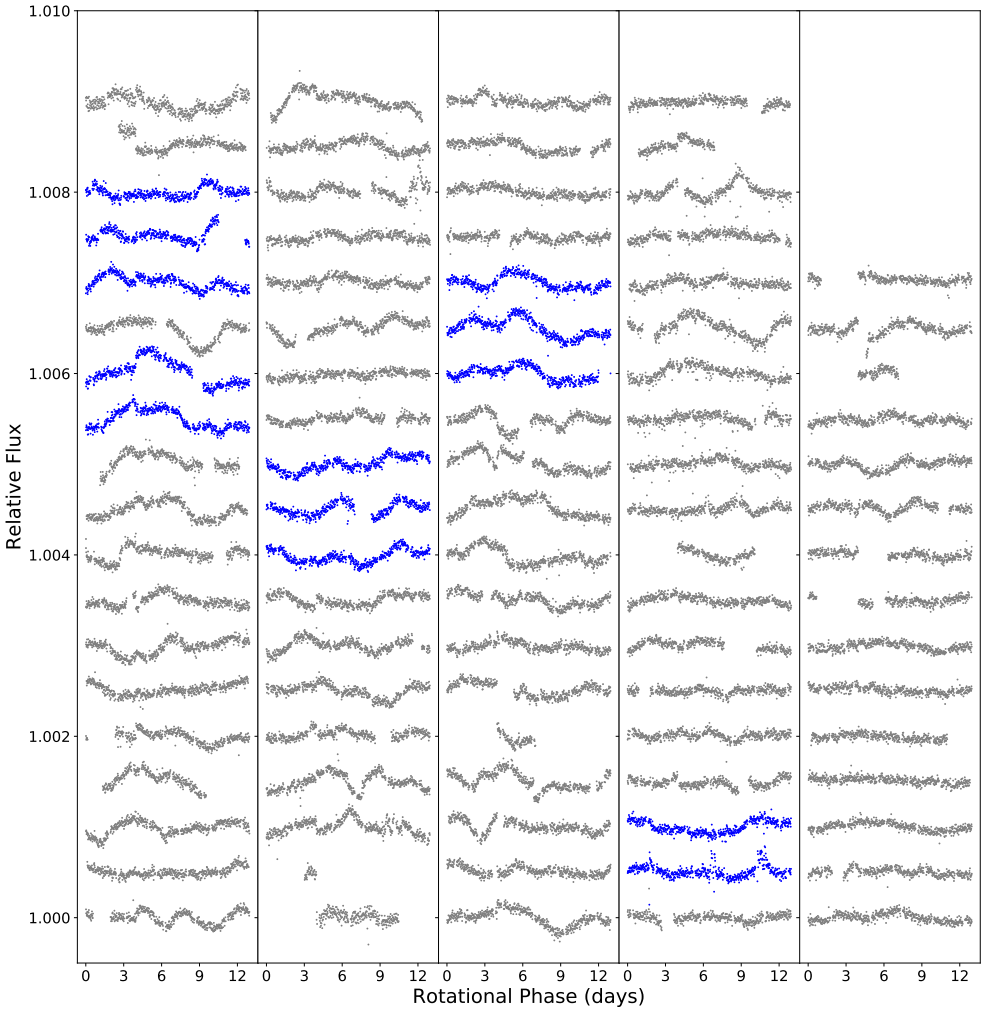

Figure 5.3: Confirmation of the rotation period through visual inspection. Shown is the entire *Kepler* light curve, folded with the candidate 12.94-day period. Vertical offsets have been applied to each cycle of data in order to separate them; they are organized like the lines of text on a page. Highlighted in blue are several occasions where the pattern of flux variation is similar from one rotation to the next. This would be unlikely if the rotation period had been misidentified.

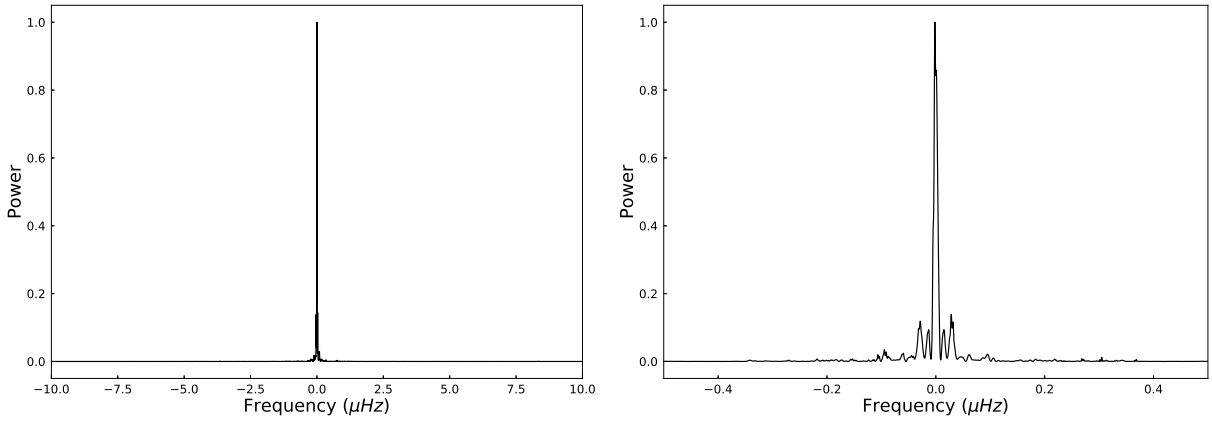

Figure 5.4: Spectral window function of Kepler-408 for the frequency range of $[-10, +10]\,\mu$Hz (left) and $[-0.5, +0.5]\,\mu$Hz (right).

analyzed the *Kepler* data outside of transits. We normalized the data from each quarter by setting the median flux equal to unity. A Lomb-Scargle periodogram of the resulting time series has its most prominent peak at 12.96 ± 0.07 days, and the auto-correlation function shows a series of peaks spaced by 12.94 ± 0.22 days (Figure 5.2). Previous experience has shown that the strongest photometric periodicity sometimes occurs at harmonics of the true rotation period, presumably because there are several active regions on the star. In the present case, visual inspection of the light curve confirms that the true period is close to 12.9 days. We were able to identify several time intervals in which a complex pattern of variations repeats nearly exactly after 12.9 days (Figure 5.3), which would be an unlikely coincidence if the true period were different.

In what follows, we adopt the value $P_{\rm rot} = 12.89 \pm 0.19$ days based on the work of Angus et al. (2018), since their analysis appears to be the most rigorous with regard to the quoted uncertainty. The reciprocal of the rotation period, which is most relevant to the asteroseismic analysis, is $1/P_{\rm rot} = 0.898 \pm 0.013\,\mu$Hz.

5.4 Asteroseismic analysis

5.4.1 Power spectrum of Kepler-408

The power spectrum of Kepler-408, available on KASOC database, is computed from its time series with the pipeline by Handberg & Lund (2014) as follows. Kepler-408 has been observed from Aug. 2009 to May 2013 in 1 minute time sampling (short cadence mode). However, it lacks the observation from Sep. 2009 to Mar. 2010, from Dec. 2010 to June 2011, from Jan. 2012 to Mar. 2012, and from Jan. 2013 to Apr. 2013 (Lund et al. 2017). For this original time series, the pipeline by Handberg & Lund (2014) corrects the sudden jumps in measured flux between observing windows, separated by the gaps above. And then it removes long-term trends (e.g., stellar activity), instrumental effects, and signals of planetary origin (e.g.,

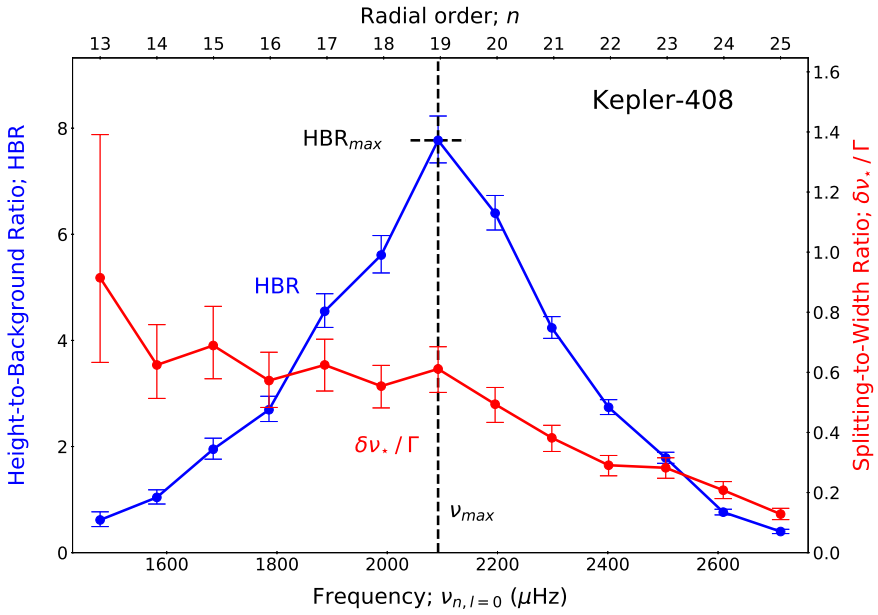

Figure 5.5: Key parameters for the reliable inference of rotational inclination. The blue curve shows the height-to-background ratio (HBR) for the $l = 0$ modes. The red curve shows the ratio between the frequency splitting $\delta\nu_\star$ and the line width Γ for the $l = 0$ modes.

planetary transits). The power spectrum for asteroseismic analysis is prepared by computing the Lomb-Scargle periodogram of the corrected time series (Lomb 1976, Scargle 1982).

The observed spectra calculated above will be given by the underlying stellar spectrum convolved with the spectral window, i.e., the power spectrum of time window function. In principle, finite observation duration and the gaps in the time series result in the spurious peaks (e.g., side-lobes) in the spectral window. This may complicate the correct identification of the oscillation modes in the observed spectrum by generating artificial peaks (aliases).

In order to evaluate this effect in the case of Kepler-408, we calculate the spectral window of Kepler-408 following Handberg & Lund (2014) (Figure 5.4). We find that the spectral window has the strongest peak at the center, along with the side-lobes with small but significant power around $[-0.05, +0.05]\,\mu$Hz. Beyond that frequency range the power of side-lobes is no more than a few percent of that of the central peak, predicting no detectable aliases in the observed noisy power spectra. The spread of non-negligible power in the spectral window is so narrow ($[-0.05, +0.05]\,\mu$Hz around the center) that we conclude that the aliases will not complicate the mode identification of the rotationally-split m-components (in separation of $\delta\nu_\star \approx 0.9\,\mu$Hz), and (n, l) modes (in separation of $\Delta\nu/2 \approx 50\,\mu$Hz).

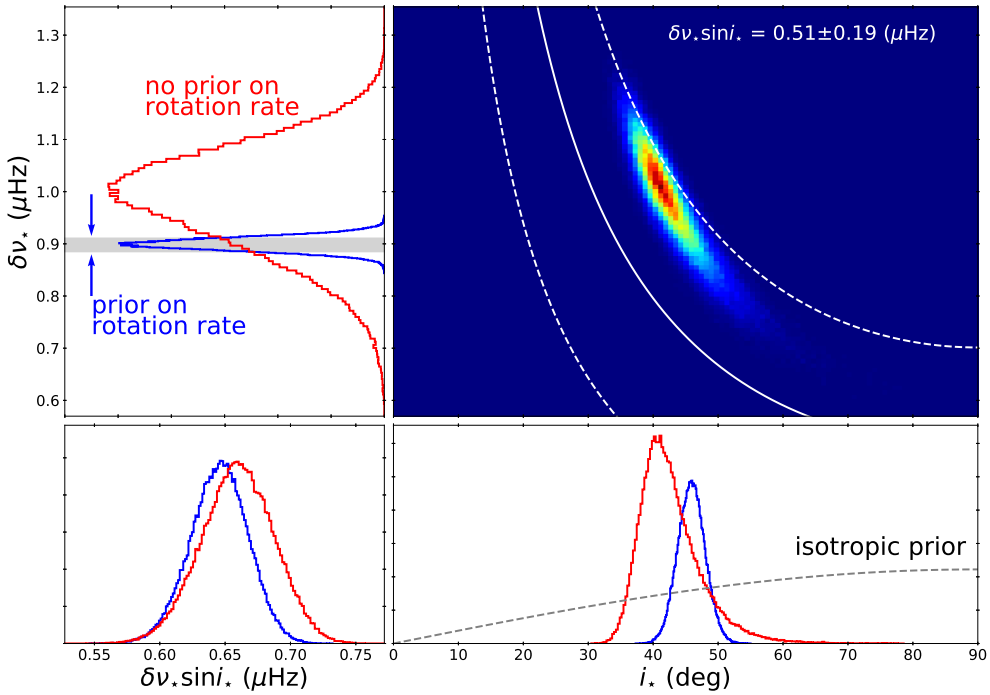

Figure 5.6: Constraints on rotational inclination and frequency splitting. Shown is the posterior probability density (PPD) in the space of $i_\star$ and $\delta\nu_\star$, marginalized over all other parameters. The one-dimensional marginalized densities are also shown to the left and below the axes. The panel in the bottom left is the PPD of $\delta\nu_\star \sin i_\star$, which is more tightly constrained than either $\delta\nu_\star$ or $i_\star$. The red and blue histograms are the PPDs without and with a prior constraint of $\delta\nu_\star = 0.898 \pm 0.013\,\mu$Hz based on the measured rotation period. The white lines identify the region where $\delta\nu_\star \sin i_\star = 0.51 \pm 0.19\,\mu$Hz, the value that is independently determined from measurements of $v \sin i_\star$ and $R_\star$ (see section 5.5).

5.4.2 Checks for consistency and robustness

Key results of asteroseismic inference

Figure 5.5 provides the profiles of pulsation modes of Kepler-408. We find that height-to-background ratio (HBR) and splitting-to-width ratio $\delta\nu_\star/\Gamma$ are sufficiently high, such that reliable inference of $i_\star$ is possible for this system. The key results were $i_\star = 42^{+5}_{-4}$ degrees and $\delta\nu_\star = 0.99 \pm 0.10\,\mu$Hz (see Figure 5.6). The measured splitting is in agreement with the value of $1/P_{\rm rot} = 0.898 \pm 0.013\,\mu$Hz based on the photometric rotation period, thereby providing a successful consistency check. We also tried using the photometric rotation period as a prior constraint on the asteroseismic analysis, which sharpened the constraint on the stellar inclination angle to 45.9±2.1 degrees (see the blue curves in Figure 5.6).

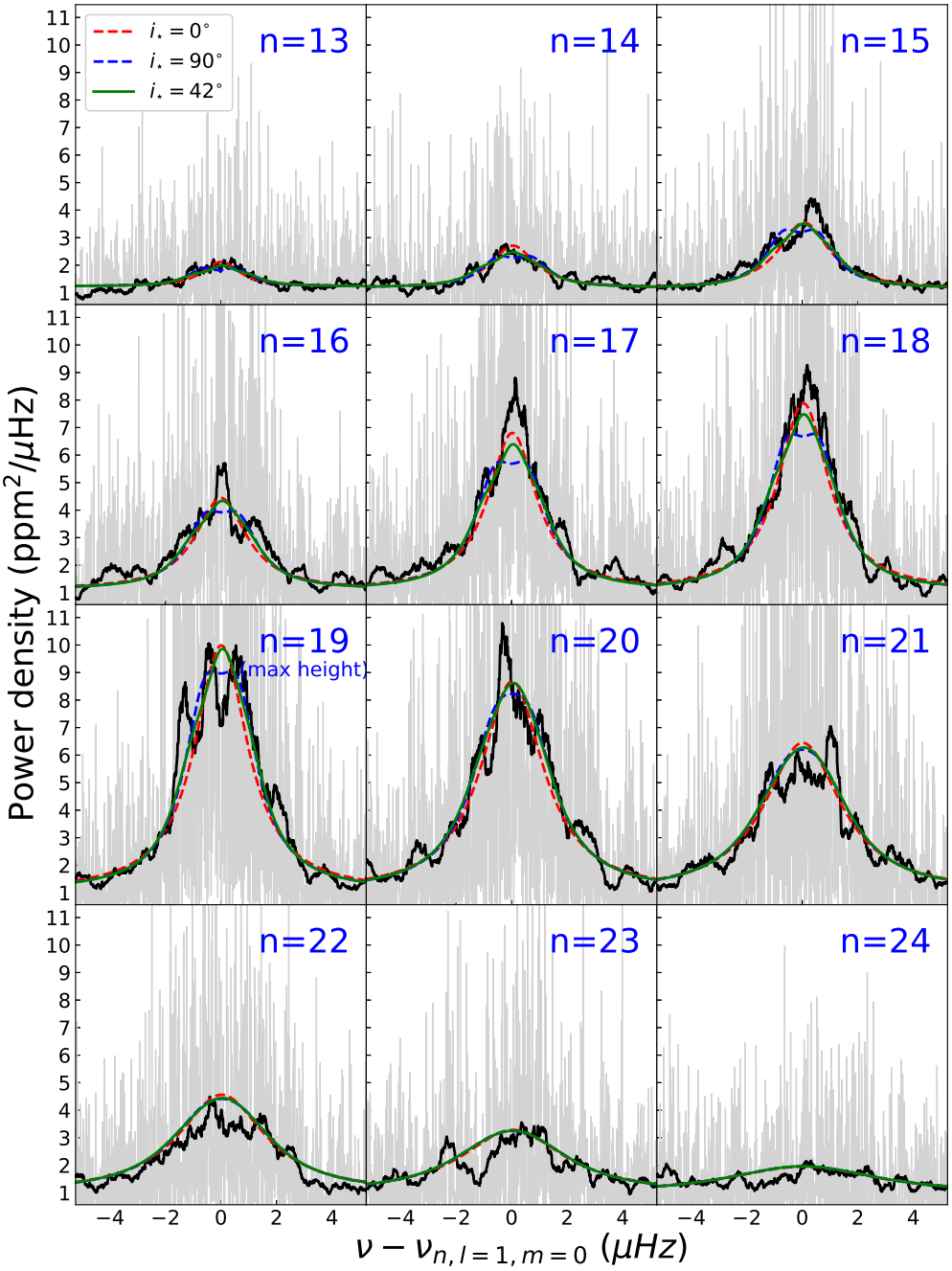

Figure 5.7: Individual profiles for dipole modes ($l = 1$) for the radial orders from $n = 13$ to 24. In each panel, the gray and black lines represent the raw data and the data after smoothing with a boxcar kernel of width 0.5 μHz, respectively. The red curve is based on a model assuming $i_\star = 0°$, the blue curve is for $i_\star = 90°$, and the green curve is for a model in which $i_\star$ is a free parameter and best-fitting value is $i_\star = 42°$.

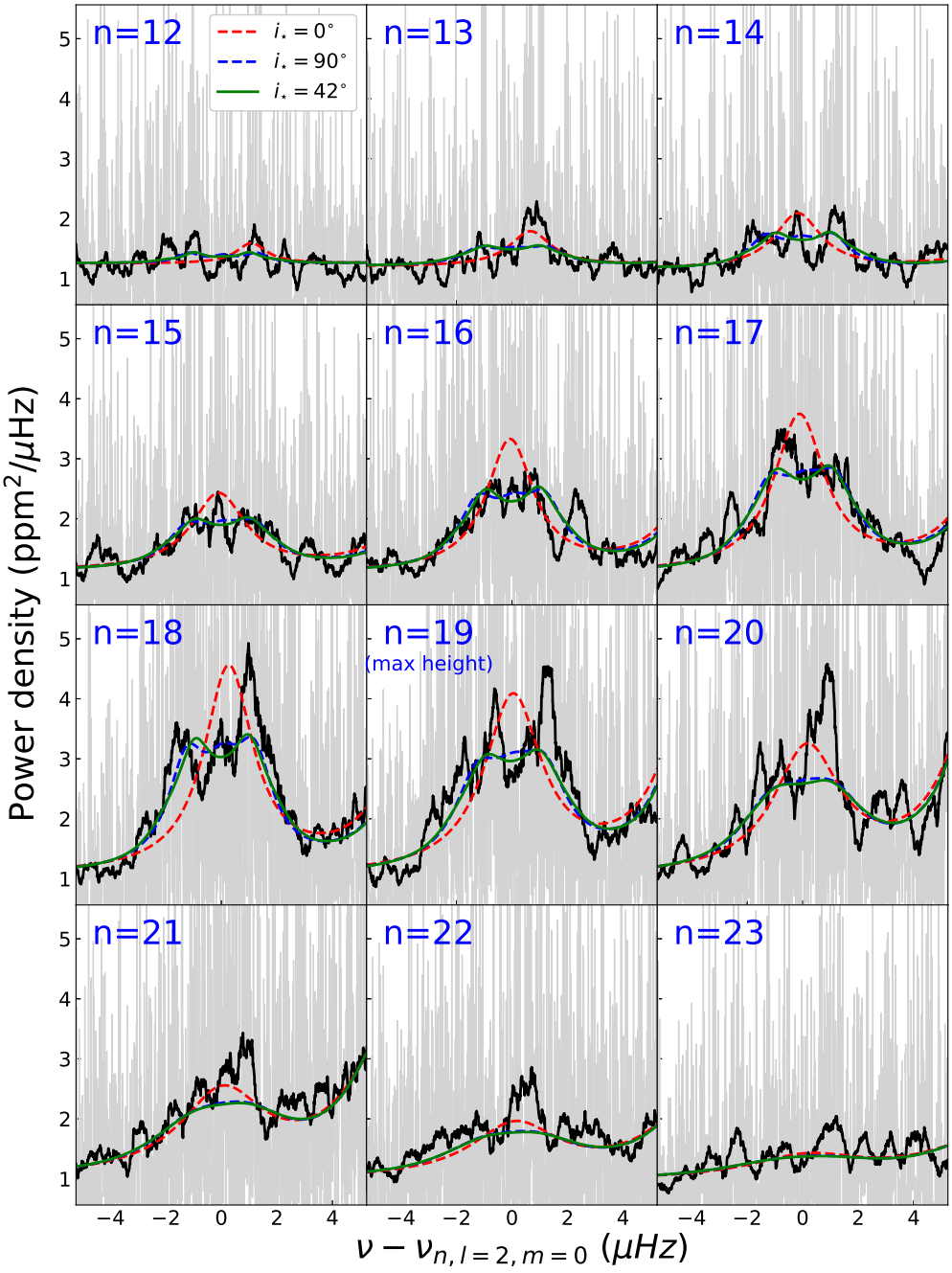

Figure 5.8: Same as Figure 5.7, but for quadrupole modes ($l = 2$).

Visual inspection of the mode profiles

The individual line profile of $l = 1$ and $l = 2$ mode is given in Figures 5.7 and 5.8, respectively. To allow for a simple visual inspection, Figure 5.9 displays the average $l = 1$ and $l = 2$ profiles, based on the combination of the data from 13 different radial orders. The profile of the average $l = 1$ multiplet (top panel) is centrally peaked, demonstrating the visibility of the $m = 0$ mode, and ruling out an inclination angle near 90°. The signal-to-noise ratio and frequency resolution are high enough that the absence of the $m = 0$ mode would have led to a flat-topped appearance, from the combination of the marginally resolved $m = +1$ and $m = -1$ modes. On the other hand, the profile of the $l = 2$ modes (bottom panel) is not centrally peaked, ruling out inclinations near zero. Together, the appearance of the modes suggests an intermediate value of the inclination.

Mode profile of $l = 2$ multiplet

The bottom panel of Figure 5.9 shows that the $l = 2$ multiplet has an asymmetric appearance, with more power at frequencies above the line center than below. This is unexpected because the geometrical factors $\mathcal{E}_{l,m}$ do not depend on the sign of m. Given the large errors present in the actual power spectra (gray lines in Figures 5.7 and 5.8), however, we find that the data do not reject our symmetric model. Therefore, the data do not prove that the observed asymmetric appearance is statistically significant. Based on this fact, we apply the symmetric model to the deta to derive stellar inclination, leading to $i_\star = 42^{+5}_{-4}$ degrees.

Despite its insignificance from a statistical point of view, estimating the effect of this asymmetric appearance on the derived parameters is of another importance. In doing so, we produced the modified power spectrum of Kepler-408, by artificially reducing the power of $m = 1$ components of $l = 2$ modes for $n = 18$ to 21 by 30%, such that $m > 0$ and $m < 0$ modes have similar power. The reduction was applied over the frequency range of Γ around $\nu(n, l = 2, m = 1)$ for $n = 18$ to 21. We performed asteroseismic analysis to this modified spectra, and obtained the inclination of $i_\star = 39^{+4}_{-3}$ (deg), consistent with the original value $i_\star = 42^{+5}_{-4}$ (deg). Based on this test, we conclude that this asymmetric appearance does not lead to any systematic bias in the results for the inclination. Consequently, the asymmetry of the $l = 2$ modes does not affect our conclusion that Kepler-408b has a significantly misaligned orbit.

Figure 5.8 suggests that the asymmetry in power is mainly due to modes of high radial order ($n = 18$ to 21). Such high-order modes are more sensitive to the conditions near the stellar surface (Sonoi et al. 2015). Thus, the asymmetric appearance may arise from the (poorly understood) magnetic and non-adiabatic processes occurring near the surface. Because the reason for the asymmetry is not clear, we tried fitting only the $l = 1$ modes and found that a low inclination (and a high stellar obliquity) are still preferred as shown in Figure 5.11c below.

Finally, we illustrate the profiles of $l = 1$ and $l = 2$ modes of other stars just for reference. Figure 5.10 shows the stacked profiles of 4 stars classified as category A (i.e., reliable stars), including KIC 12069424, the reference star used in chapter 4. The best fit curves (in red) are estimated by the fit using raw spectra (in gray). The observed spectra are intrinsically

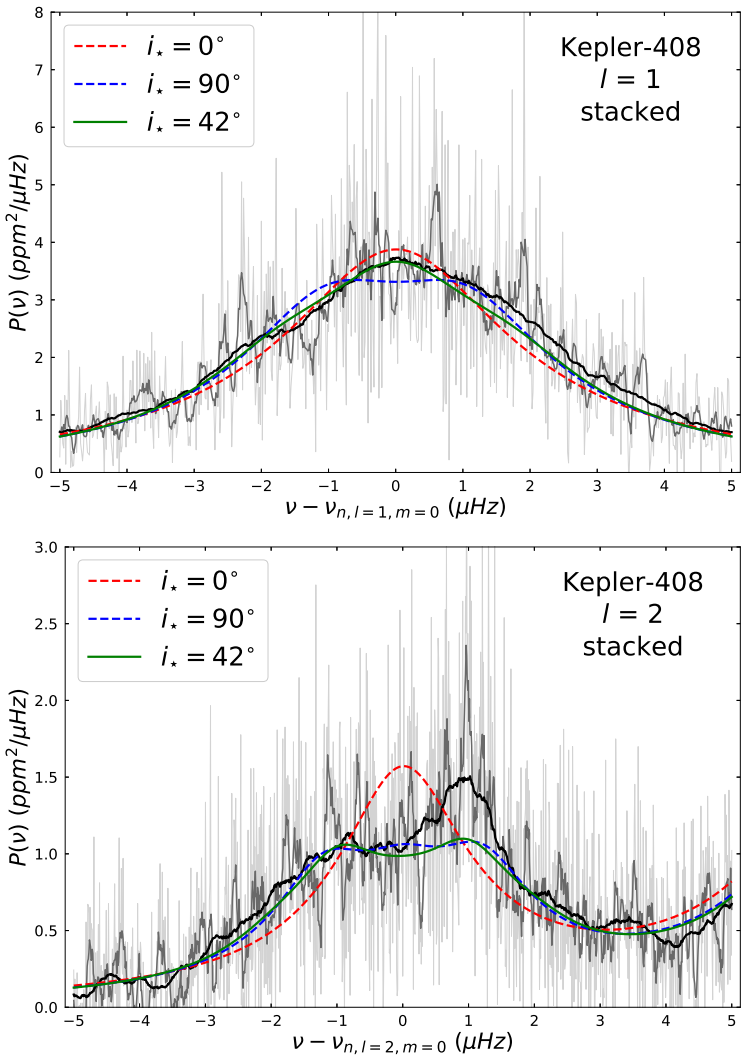

Figure 5.9: Average power spectra of rotationally split multiplets, for $l = 1$ (top) and $l = 2$ (bottom). The profiles of multiple modes have been stacked to improve the signal-to-noise ratio and allow for a visual inspection, although the quantitative fits were performed on the data without any averaging or stacking (see Figures 5.7 and 5.8). For $l = 1$, the modes with $n = 13$ to 25 were included. For $l = 2$, the modes with $n = 12$ to 24 were included. The thin gray line shows the data without any smoothing, while the thick gray and black lines show the data after smoothing over 0.05 and 0.75 μHz in frequency, respectively. Each panel also shows three model curves that were optimized to fit the data. The red curve is based on a model assuming $i_\star = 0°$, the blue curve is for $i_\star = 90°$, and the green curve is for a model in which $i_\star$ is a free parameter. For the $l = 2$ modes, the gradual rise observed at the high-frequency end is from a neighboring radial mode ($l = 0$). The asymmetry in the line profile is not understood (see text).

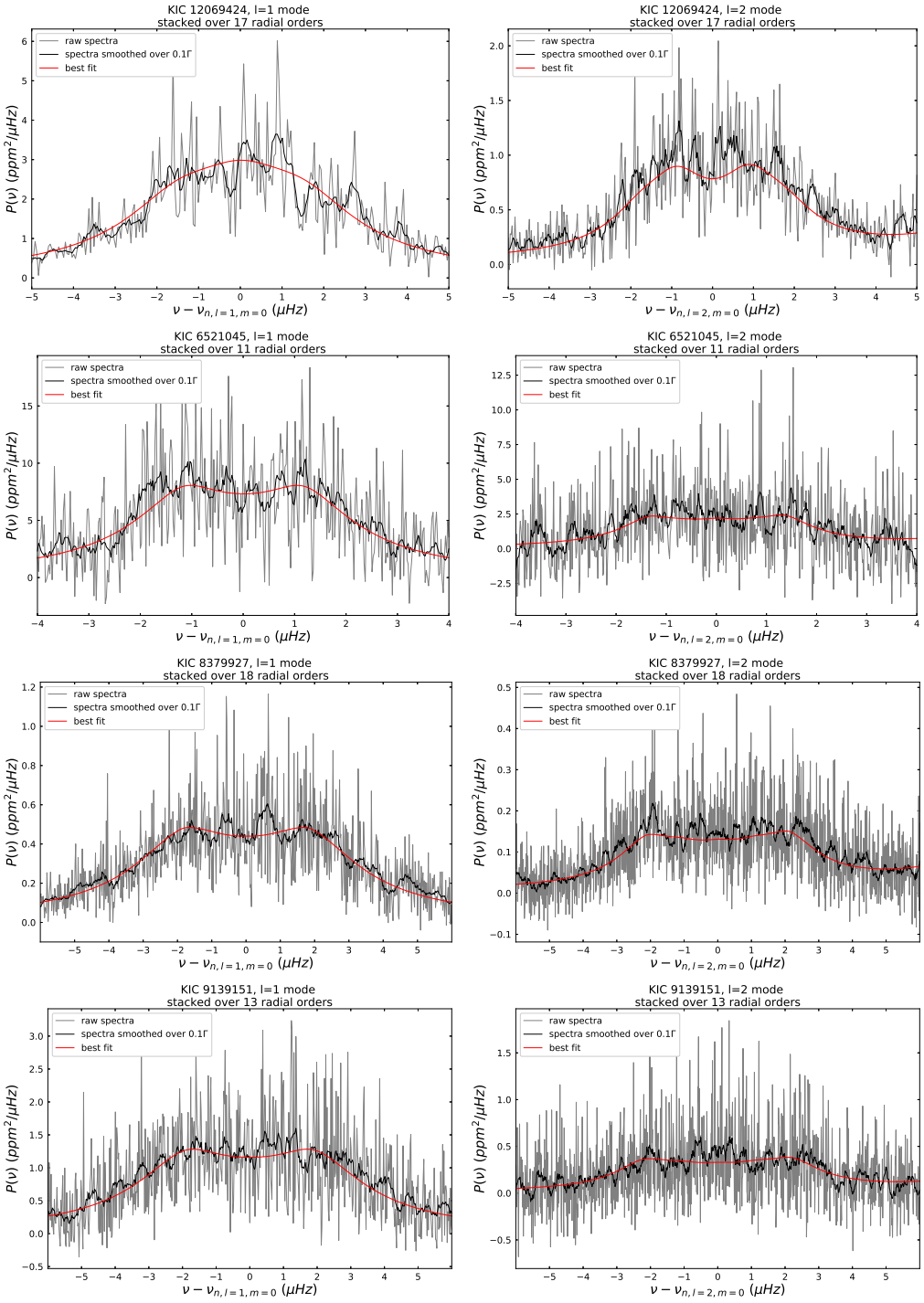

Figure 5.10: Same as Figure 5.9, but for 4 other stars. Left (right) panel shows $l = 1$ ($l = 2$) modes stacked over all fitted radial orders n. From top to bottom, we show KIC 12069424, KIC 6521045, KIC 8379927, and KIC 9139151. Red curves correspond to the best-fit model using raw spectra (gray). Black curves are spectra smoothed over 0.1Γ at $\nu_{\rm max}$ for clear visibility.

quite noisy in most cases, and we do not find any statistically-significant asymmetric profiles, similarly to the case of Kepler-408.

Dependence of the derived inclination on the choices of the modes

As further tests of robustness, we repeated the analysis for 5 different choices of the set of radial orders and angular degrees to be fitted (see Figure 5.11). This led to larger uncertainties, and small systematic changes in the derived parameters. Fitting the $l = 1$ modes tends to give lower inclinations, while the $l = 2$ modes favor higher inclinations. Such complementary roles of $l = 1$ and $l = 2$ modes are very useful in constraining $i_\star$ and $\delta\nu_\star$ reliably. While Kepler-408 is one of the stars with the clearest pulsation spectrum, its asteroseismic modelling is still subtle and careful individual tests are required for the reliable parameter extraction. In all cases, though, the results are compatible with a large spin-orbit misalignment, and the splitting is compatible with the photometric rotation period, implying that our asteroseismic inference for the Kepler-408 system is robust.

5.4.3 Comparison with previous results

We note here that our results do not agree with those of Campante et al. (2016), who found $i_\star > 54°$. In attempting to understand the reason for the discrepancy, we noted that our results use an unweighted power spectrum (Lomb-Scargle periodogram) while Campante et al. (2016) computed it using a weighted least square fitting method. By performing our analysis on their dataset, however, we could verify that the data processing cannot be the cause of the discrepancy as we found the same inclination ($i_\star = 43.7^{+9.8}_{-5.5}$ degrees). We also noticed that their best fitting model gave $\delta\nu_\star = 0.50^{+0.20}_{-0.04}\,\mu$Hz, which is inconsistent with the photometrically measured rotation period. Another difference is related to the chosen model for the background noise in the power spectrum. For the sake of uniformity, Campante et al. (2016) adopted the same model for all 25 systems of their analysis. Their model was parameterized as:

$$B(\nu) = B_0 + \left[\frac{B_1}{1 + (2\pi\nu\tau_1)^a} + \frac{B_2}{\nu^2}\right] \mathrm{sinc}^2\left(\frac{\pi\nu}{2\nu_0}\right), \tag{5.1}$$

where $\nu_0 = 8{,}496.6\,\mu$Hz is the Nyquist frequency.

While equation (5.1) is reasonable in general, it does not provide a satisfactory fit to the Kepler-408 power spectrum, as shown in Figure 5.12. In the vicinity of the oscillation modes, the best-fitting model of this form falls short of the measured background by about 10%. Formally, our model for the background spectrum is preferred over the model of Campante et al. (2016) by an "odds ratio" (based on the integrated likelihoods) of exp(855); see section 12.7 of Gregory (2005) for details.

When we replaced our model for the background with that of equation (5.1), we were able to reproduce the result of $i_\star > 54°$ reported by Campante et al. (2016). Evidently, it is essential to perform a careful subtraction of the low-frequency noise for each system, to obtain an unbiased estimate of $i_\star$ from asteroseismic analysis. Appourchaux et al. (2012b) have

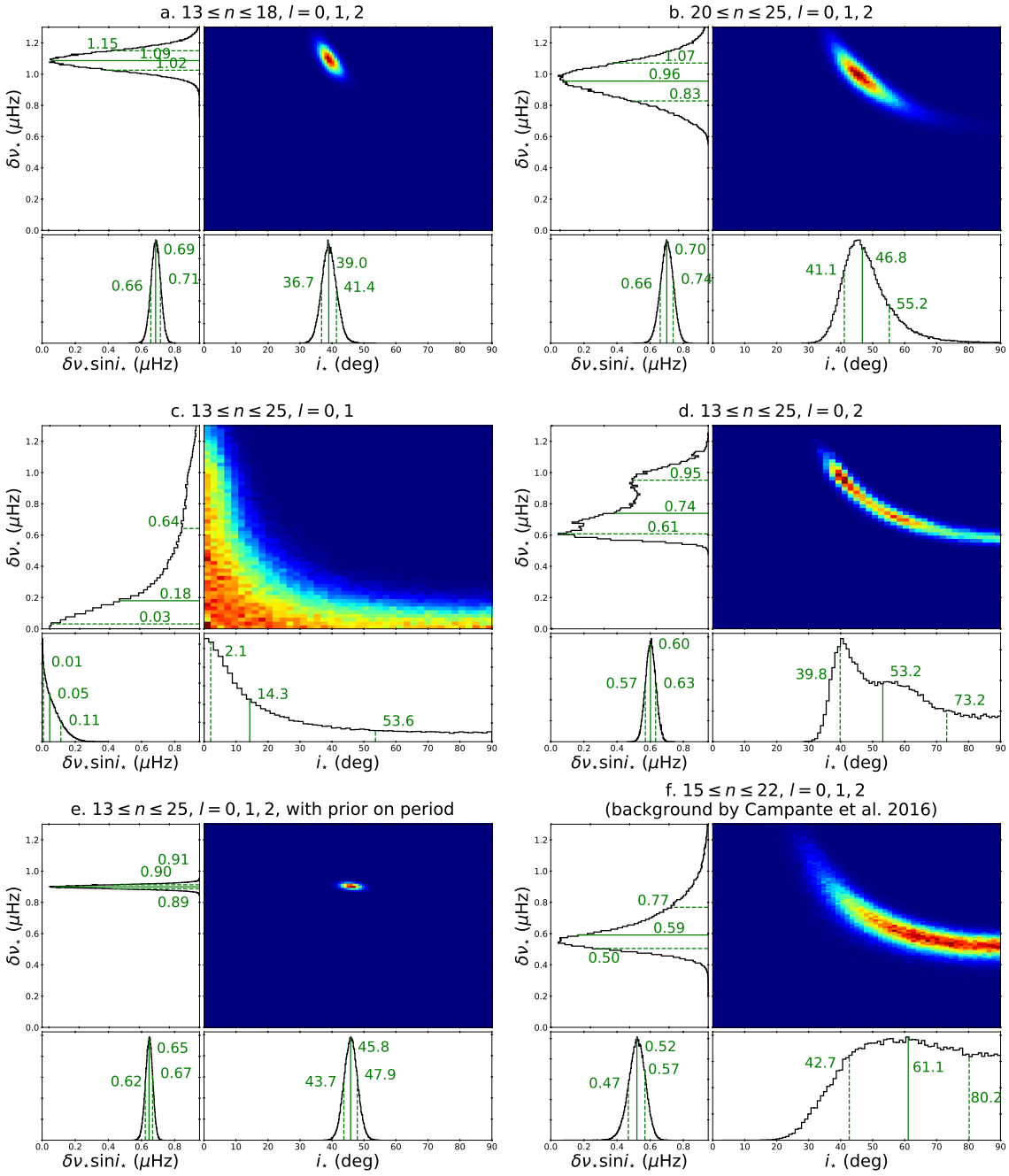

Figure 5.11: Constraints on $i_\star$ and $\delta\nu_\star$, as in Figure 5.6, after making variations in the analysis procedure. *a*: Fitting only the lower radial orders ($13 \leq n \leq 18$) and $l = 0, 1, 2$. *b*: Fitting only the higher radial orders ($19 \leq n \leq 25$) and $l = 0, 1, 2$. *c*: Fitting only the dipole modes ($l = 1$) of all orders. *d*: Fitting only the quadrupole modes ($l = 2$) of all orders. *e*: Fitting dipole and quadrupole modes of all orders, with a Gaussian prior of $\delta\nu_\star = 0.898 \pm 0.013\,\mu$Hz based on the measured rotation period (Angus et al. 2018). *f*: Fitting all orders and modes, after replacing our model for the noise background with the (unsatisfactory) model of Campante et al. (2016).

studied the systematic errors in measurements of seismic parameters caused by inaccuracies in the model for background noise. Although they did not examine the implications for inference of the inclination angle, they did note that inaccuracies can greatly impact the inferred mode heights and linewidths, which in turn may bias the measurement of the rotational splitting and inclination. Our work demonstrates that this is indeed the case: systematic errors in the background model can severely bias the measured inclination.

As an additional test, we tried replacing the background model with a simple quadratic function of frequency. By restricting the frequency range to the limited interval spanned by the oscillation modes (1,300-2,900 μHz), we found that the quadratic function also gives a satisfactory fit. The results for the inclination were the same as in our original analysis ($i_\star = 42^{+5}_{-4}$ degrees), confirming that the exact functional form of the background model does not matter, as long as it provides a satisfactory fit.

5.5 Projected rotation rate from spectroscopy

There is also evidence independent of asteroseismology that the rotational inclination is in the neighborhood of 45°, based on the measured values of the stellar radius, rotation period, and sky-projected rotation velocity (Table 5.1). The stellar radius ($R_\star$) was determined by combining the observed geometric parallax, apparent K magnitude, and spectroscopic effective temperature (Berger et al. 2018). The rotation period ($P_{\rm rot}$) was determined from the *Kepler* photometry, as noted above. The combination of these quantities implies $v = 2\pi R_\star / P_{\rm rot} = 4.92 \pm 0.21$ km/s. Meanwhile, the sky-projected rotation velocity ($v \sin i_\star$) was found to be 2.8 ± 1.0 km/s by modeling the Doppler-rotational contribution to the observed spectral line broadening (Petigura et al. 2017). Together, these data can be used to place constraints on $\sin i_\star$. To obtain the likelihood function for $\sin i_\star$, we integrated $p_1(v) \cdot p_2(v \sin i_\star)$ over v, where p_1 and p_2 are Gaussian functions representing the constraints $v = 4.92 \pm 0.21$ km/s and $v \sin i_\star = 2.8 \pm 1.0$ km/s. The result is $\sin i_\star = 0.70 \pm 0.21$, or $i_\star = 44^{+20}_{-15}$ degrees, which is consistent with our asteroseismic result.

As another consistency check, we can combine the spectroscopically determined $v \sin i_\star$ and $R_\star$ to give $\delta\nu_\star \sin i_\star = 0.51 \pm 0.19\,\mu$Hz. The white lines in Figure 5.6 show the region that is defined by this constraint, which is independent of the asteroseismic analysis. The results are again consistent to within 1σ.

5.6 An Earth-sized misaligned planet Kepler-408b

By modelling the power spectrum of p modes, we found the stellar inclination to be $i_\star = 42^{+5}_{-4}$ degrees (section 5.3). Our result in chapter 4 is similar to that reported by Nielsen et al. (2017). However, Nielsen et al. (2017) did not remark on the conflict with the analysis of Campante et al. (2016), nor did they appreciate the importance of this system for understanding the origin of the spin-orbit misalignment (as will be described below). The more thorough analysis in this chapter has resolved the conflict, by examining the individual and stacked

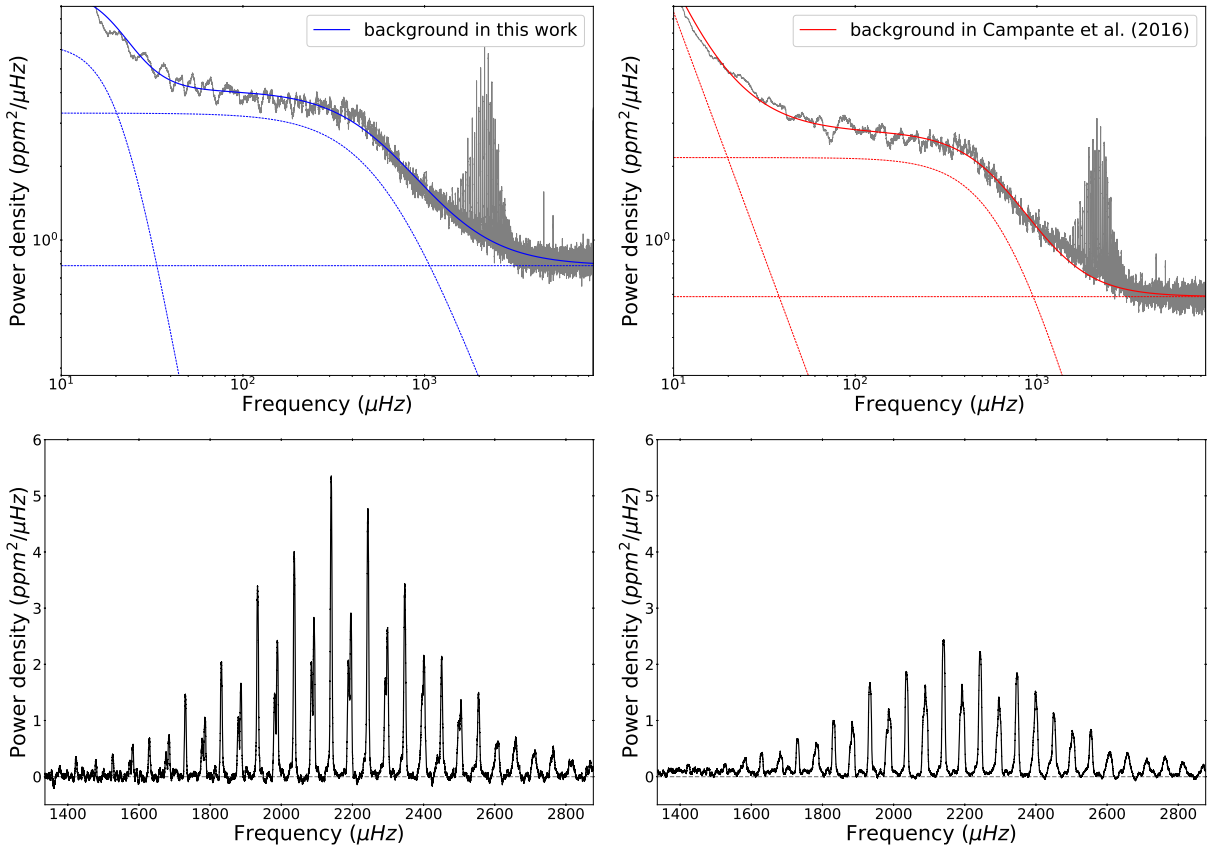

Figure 5.12: Models of the noise background. *Top panels*: The entire power spectrum of Kepler-408, along with the best-fitting model and its three separate components. The left panel shows the spectrum and model used in our analysis. The right panel shows those used in Campante et al. (2016), which does not provide a satisfactory fit to the lower envelope of the power spectrum in the vicinity of the oscillation modes. *Bottom panels*: Close-up of the oscillation modes, after subtracting the best-fitting model for the background.

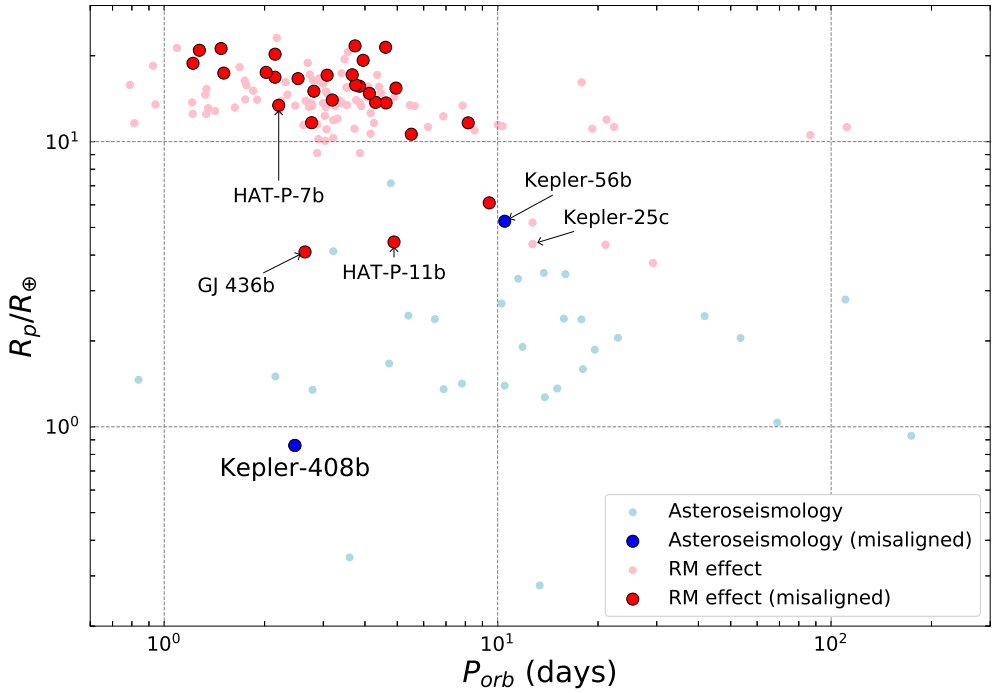

Figure 5.13: Sizes and orbital periods of planets for which the stellar obliquity has been measured, based on the Rossiter-McLaughlin effect (red) and asteroseismology (blue). The darker symbols represent those for which the stellar obliquity is known to be higher than 30° with greater than 95% confidence. Based on the compilation of Southworth (2011).

line-profiles for different modes, comparing the best-fit with and without the photometric rotation period constraint, and exploring different possibilities for the background model. This experience with Kepler-408 and the methodology presented in this chapter should allow for more robust determinations of $i_\star$ in the future, through the precise and accurate combination of asteroseismology, photometry and spectroscopy.

As for the inclination of the orbital axis, by fitting the *Kepler* light curve we found $i_{\rm orb} = 81.85 \pm 0.10$ degrees (section 5.2). Knowledge of both the rotational and orbital inclinations is not enough information to determine the stellar obliquity, because both measurements are subject to the usual degeneracy $i \leftrightarrow 180^\circ - i$, and because we do not know the position angle (λ) on the sky between the two axes. Nevertheless we may set a lower limit on the stellar obliquity of $|i_{\rm orb} - i_\star| = 40 \pm 5$ degrees for the Kepler-408 system.

Of all the planets known to have a spin-orbit misalignment, Kepler-408b is the smallest by a factor of six, as illustrated in Figures 5.13 and 5.14. Those figures also identify other systems of particular interest. Kepler-56 is an obliquely rotating star ($i_\star \approx 45^\circ$) hosting two transiting planets (Huber et al. 2013a). HAT-P-7 and Kepler-25 are the only known systems for which both the Rossiter-McLaughlin and asteroseismic measurements have been successful (Benomar et al. 2014). HAT-P-11b and GJ 436b are the smallest planets previously known to be misaligned (Winn et al. 2010b, Yee et al. 2018, Bourrier et al. 2018).

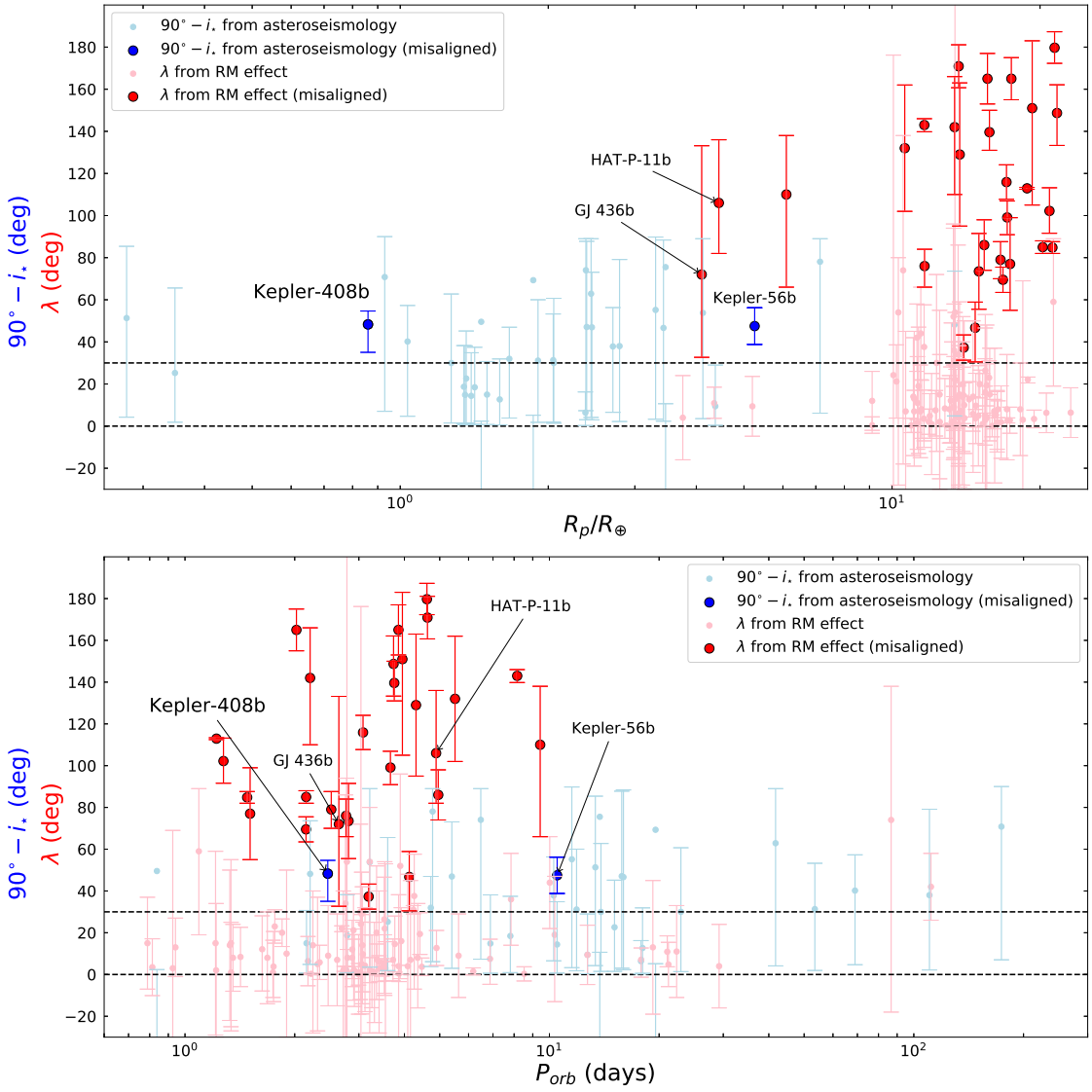

Figure 5.14: Observed spin-orbit angles for transiting exoplanets as a function of planetary radius (top) and orbital period (bottom). Red symbols are for determinations of the position angle λ based on the Rossiter-McLaughlin effect (Southworth 2011). Blue symbols are for determinations of inclination based on asteroseismology. For systems with more than one transiting planet, only the result for the innermost planet is plotted, with the sole exception of Kepler-25c. The plotted error bars correspond to 2σ (95%) confidence limits.

As such, it provides a clue about the origin of misalignments in general. Stars and their planets are thought to form in a well-aligned state. This is because the star and the protoplanetary disk inherit the same direction of angular momentum from an initial clump of gas that contracts under its own gravity. The observation of a large obliquity is an indication that something torqued the system out of alignment. The circumstances and the timing of the torque are unknown. Since all the previous cases of large obliquities involved planets larger than Neptune, some of the proposed theories have focused on giant planets. The data have often been regarded as evidence that the formation of close-orbiting giant planets, including hot Jupiters, involves processes that tilt the planet's orbit (Winn et al. 2010a, Triaud et al. 2010).

The case of Kepler-408 shows that orbit-tilting processes are not specific to giant planets, and must occur at least occasionally for "hot Earths". In a recently proposed theory for the formation of very short-period terrestrial planets (Petrovich et al. 2018), an inner planet's orbital angular momentum is reduced through chaotic long-term interactions with more distant planets, leading to spin-orbit misalignments of $10^\circ - 50^\circ$, as observed here. Another theory involves a secular resonance with a more distant giant planet (Hansen & Zink 2015), although in the case of Kepler-408, no additional transiting planets are known. The existing Doppler data do not show any signals exceeding 4 m/s on timescales less than a year (Marcy et al. 2014). Other possibilities are that stars and their protoplanetary disks are occasionally misaligned due to torques from neighboring stars (Batygin 2012) or that inner planets become misaligned due to the torque from a wider-orbiting and misaligned giant planet (Lai et al. 2018). To decide among these and other theories will require a larger and more diverse sample of planetary systems for which the stellar obliquity can be probed.

Chapter 6

Observational signatures for the spin-orbit resonance

Asteroseismology enables an independent measure of stellar rotation period in addition to the method that uses periodic variability in the observed photometry. Therefore asteroseismology is also applicable for the test of the robustness of photometrically-derived rotation periods. In this chapter, we report the observational signatures for an interesting regularities between rotation periods ($P_{\rm rot}$) of the stars and orbital periods of their planetary companions ($P_{\rm orb}$).

6.1 Tidal evolution of stellar spin and planetary orbit

As we introduced in chapter 2, there are at least two possibilities for the origin of the spin-orbit misalignment. One possibility is that the well-aligned initial condition is significantly broken via the violent dynamical evolution of planets in late stages, and the inner-most planet becomes realigned toward the stellar spin axis through the tidal interaction preferentially in cool host-star systems. Of course, it is also possible that some fraction of the observed spin-orbit misalignment is merely of primordial origin. The asteroseismic analysis by Huber et al. (2013a) revealed that the stellar inclination of Kepler-56 with two transiting planets is approximately 45°. Since it is not easy, even if not impossible, to dynamically change the orbital plane of the two planets in a coherent fashion, it is natural to expect that the spin-orbit misalignment observed for Kepler-56 simply reflects the initial condition. The two possibilities above for the origin of the spin-orbit misalignment, which we refer to as the realignment channel and the primordial channel, are not necessarily exclusive, and thus the observed distribution may be accounted for by their combination.

A possible problem for the realignment channel is that the alignment time-scale is longer than the orbit damping (Lai 2012, Rogers & Lin 2013, Xue et al. 2014). According to the conventional equilibrium tide model (Murray & Dermott 2000), the semi-major axis of the

planet, a, and the spin angular velocity of the star, $\Omega_\star$ evolve according to

$$\frac{\mathrm{d}a}{\mathrm{d}t} = -\frac{2}{Q'_\star}\frac{M_\mathrm{p}}{M_\star}\left(\frac{R_\star}{a}\right)^5 na, \tag{6.1}$$

$$\frac{\mathrm{d}\Omega_\star}{\mathrm{d}t} = -\mathrm{sign}(\Omega_\star - n)\frac{1}{\alpha_\star Q'_\star}\left(\frac{M_\mathrm{p}}{M_\star}\right)^2\left(\frac{R_\star}{a}\right)^3 n^2. \tag{6.2}$$

In the expressions above, M_p and $M_\star$ are the mass of the planet and the star, $R_\star$ is the radius of the star, n is the mean motion of the planet, $\alpha_\star$ is the inertia moment of the star in units of $M_\star R_\star^2$, and we introduce the effective tidal quality factor of the star:

$$Q'_\star \equiv \frac{2Q_\star}{3k_{2\star}} \tag{6.3}$$

with $Q_\star$ and $k_{2\star}$ being the quality factor and the 2nd Love number of the star, respectively.

Equations (6.1) and (6.2) imply the corresponding damping and synchronization (or alignment) time-scales:

$$\begin{aligned}\tau_a &\equiv \left|\frac{a}{\mathrm{d}a/\mathrm{d}t}\right| \\ &\approx 9.5\times10^{10}\left(\frac{Q'_\star}{10^6}\right)\left(\frac{M_\star}{M_\odot}\right)^{8/3}\left(\frac{10M_\mathrm{E}}{M_\mathrm{p}}\right)\left(\frac{R_\odot}{R_\star}\right)^5\left(\frac{P_\mathrm{orb}}{1\,\mathrm{day}}\right)^{13/3}\ \mathrm{yr},\end{aligned} \tag{6.4}$$

$$\begin{aligned}\tau_\mathrm{sync} &\equiv \left|\frac{\Omega_\star}{\mathrm{d}\Omega_\star/\mathrm{d}t}\right| \\ &\approx 1.4\times10^{14}\left(\frac{\alpha_\star}{2/5}\right)\left(\frac{Q'_\star}{10^6}\right)\left(\frac{M_\star}{M_\odot}\right)^3\left(\frac{10M_\mathrm{E}}{M_\mathrm{p}}\right)^2\left(\frac{R_\odot}{R_\star}\right)^3\left(\frac{P_\mathrm{orb}}{1\,\mathrm{day}}\right)^3\left(\frac{P_\mathrm{orb}}{P_\mathrm{rot}}\right)\ \mathrm{yr},\end{aligned} \tag{6.5}$$

where $P_\mathrm{orb} = 2\pi/n$ and $P_\mathrm{rot} = 2\pi/\Omega_\star$ denote the orbital period of the planet and the spin rotation period of the star, respectively.

The (re)alignment is unlikely to be completed within the age of the universe if one assumes a typical value of the tidal quality factor $Q'_\star (= 10^5 - 10^7)$. Moreover, the fact of $\tau_a \ll \tau_\mathrm{sync}$ regardless of the value of $Q'_\star$ implies that the realigned planet should have been fallen into the star. Thus the realignment channel does not seem to work in the conventional equilibrium tide model. This is why Lai (2012) proposed an alternative tidal model (see, e.g., Rogers & Lin 2013, Xue et al. 2014).

Since the spin-orbit alignment is usually supposed to proceed in a roughly similar time-scale of the orbit circularization and the spin-orbit synchronization, one may test the realignment channel hypothesis from the distribution of the eccentricity e and $P_\mathrm{orb}/P_\mathrm{rot}$. In particular, the realignment channel would imply that $P_\mathrm{rot} \approx P_\mathrm{orb}$, while no specific correlation is expected between P_rot and P_orb in the primordial channel.

While P_orb can be measured precisely for transiting planets, it is not always the case for P_rot of their host star. It is possible to estimate P_rot spectroscopically, combining the equatorial rotational velocity from Doppler broadening and the stellar radius. The estimate,

however, depends on the assumed turbulence, and also requires the stellar radius and inclination that are usually not well-determined. Although the photometric variation of the star is more directly related to $P_{\rm rot}$, the formation and dissipation of star-spots complicate the interpretation of the photometrically estimated rotation period $P_{\rm rot,photo}$.

In this respect, asteroseismology provides a complementary and indeed more reliable estimate for the stellar rotation period $P_{\rm rot,astero}$. Furthermore, since asteroseismology fits both $P_{\rm rot,astero}$ and the stellar inclination $i_\star$ as performed in previous chapters, the spin-orbit misalignment and synchronization can be examined simultaneously. Thus asteroseismology provides an unique methodology to test empirically the degree of the star-planet tidal interaction in a model-independent fashion.

The analysis of the $P_{\rm orb}/P_{\rm rot,photo}$ has been performed for *Kepler* eclipsing binaries (EBs) by Lurie et al. (2017). They measured $P_{\rm rot,photo}$ for 816 EBs from their star-spot modulation, and found that 79% of EBs with $P_{\rm orb} < 10$ days are synchronized. They also noted that the fraction of super-synchronous ($P_{\rm orb} > P_{\rm rot}$) EBs significantly increases for $P_{\rm orb} > 10$ days. The tidal interaction between the host star and planets in exoplanetary systems should be much weaker than that between stars in EBs. Nevertheless we found a similar tendency for *Kepler* transiting planetary systems, as will be shown below. The finding discussed in this chapter can give a useful empirical constraint on the star-planet tidal interaction.

The rest of the chapter is organized as follows. Section 6.2 critically compares the stellar rotation periods estimated from photometric variation and asteroseismology. We find that $P_{\rm rot,photo}$ is somewhat sensitive to the detail of the underlying assumptions and needs to be interpreted with caution. Section 6.3 describes our major finding of (quasi-)resonance of stellar spin and the planetary orbital periods. We discuss its implications and summarize our conclusion in section 6.4.

6.2 Stellar rotation period from photometric variation and asteroseismology

In general, $P_{\rm rot,photo}$ derived from photometric variation is more *precise* than $P_{\rm rot,astero}$ from asteroseismology. However, it does not necessarily imply that $P_{\rm rot,photo}$ is more *accurate* than $P_{\rm rot,astero}$. The present analysis focuses on the sample of 33 stars with transiting planets from *Kepler* data, which are analyzed with asteroseismology in chapter 4. We consider systems whose stellar rotation periods are relatively well measured from asteroseismology. Specifically we select 19 systems for which $v \sin i_\star$ from asteroseismology is inconsistent with 0 within 5σ (Table 6.1). The stellar rotation of those systems is fast enough to securely measure the rotation period from their power spectra. For reference, we also consider 48 stars without known planets, but with reliable $v \sin i_\star$ measurement, out of 61 analyzed in chapter 4. Among these $19 + 48 = 67$ stars, 30 objects are also analyzed independently by Benomar et al. (2018). We find that $P_{\rm rot,astero}$ of 26 among 30 stars agrees within 1σ and the remaining 4 have $P_{\rm rot,astero}$ consistent within 2σ, suggesting that the asteroseismic result is almost free from details of the individual analysis.

Figure 6.1 plots $P_{\rm rot,photo}$ for the 19 planet-host stars against our $P_{\rm rot,astero}$. Measured

Table 6.1: Basic stellar properties of 19 planetary systems; $T_{\rm eff}$ and $P_{\rm rot,photo}$ denote the effective temperature and photometrically-derived rotation period. The asteroseismically derived rotation period, $P_{\rm rot,astero}$, and inclination, $i_{\star,\rm astero}$, are estimated using uniform priors, while $i_{\star,\rm joint}$ is derived using the photometric rotation period as a prior in the asteroseismic analysis.

KOI	Kepler ID	$T_{\rm eff}$ (K)	$P_{\rm rot,photo}$ (days)	$P_{\rm rot,astero}$ (days)	$i_{\star,\rm astero}$ (deg)	$i_{\star,\rm joint}$ (deg)
Stars with reliable period measurement						
41	100	5825	$27.7^{+5.0}_{-4.2}$	$25.1^{+2.0}_{-2.3}$	$75.2^{+10.4}_{-12.9}$	$77.6^{+8.6}_{-11.1}$
85	65	6211	$8.2^{+0.6}_{-0.4}$	$8.2^{+0.6}_{-0.6}$	$75.0^{+9.5}_{-8.7}$	$75.4^{+9.0}_{-7.7}$
260	126	6239	$7.2^{+0.8}_{-0.5}$	$7.9^{+0.6}_{-0.6}$	$75.6^{+9.7}_{-11.2}$	$73.8^{+10.4}_{-10.2}$
262	50	6225	$8.1^{+1.1}_{-0.8}$	$7.6^{+0.6}_{-0.8}$	$71.6^{+12.3}_{-11.7}$	$75.1^{+9.9}_{-10.6}$
269	...	6477	$5.3^{+0.2}_{-0.2}$	$6.1^{+0.4}_{-0.5}$	$77.3^{+8.7}_{-10.5}$	$66.0^{+7.5}_{-5.5}$
274	128	6090	$13.2^{+1.1}_{-0.9}$	$12.4^{+1.3}_{-1.3}$	$67.4^{+12.7}_{-10.9}$	$71.5^{+10.7}_{-8.4}$
277	36	5911	$17.2^{+1.6}_{-1.6}$	$17.8^{+3.9}_{-4.0}$	$60.0^{+19.4}_{-17.5}$	$62.4^{+16.2}_{-12.7}$
280	1655	6148	$13.5^{+1.6}_{-1.2}$	$11.9^{+2.6}_{-3.4}$	$58.9^{+18.8}_{-17.7}$	$68.3^{+13.3}_{-11.9}$
288	...	6150	$13.6^{+0.8}_{-1.2}$	$10.7^{+2.2}_{-1.8}$	$52.2^{+13.1}_{-9.5}$	$67.1^{+13.0}_{-9.6}$
370	145	6022	$14.0^{+1.1}_{-1.7}$	$10.7^{+2.3}_{-3.9}$	$60.0^{+20.1}_{-21.1}$	$78.1^{+8.2}_{-11.6}$
974	...	6247	$11.0^{+0.4}_{-0.8}$	$11.0^{+1.6}_{-1.8}$	$58.7^{+18.2}_{-12.6}$	$62.1^{+12.4}_{-8.3}$
975	21	6305	$12.6^{+1.0}_{-1.0}$	$12.3^{+0.8}_{-1.2}$	$71.3^{+12.0}_{-11.0}$	$75.1^{+9.8}_{-8.8}$
1612	408	6104	$12.5^{+1.0}_{-1.0}$	$11.7^{+1.4}_{-1.0}$	$41.7^{+5.1}_{-3.5}$	$43.1^{+3.5}_{-2.9}$
Stars with no clear signal in periodogram						
2	2	6389	$30.6^{+8.1}_{-16.2}$	$12.1^{+5.5}_{-3.2}$	$41.8^{+19.6}_{-13.2}$	...
69	93	5669	$32.0^{+11.0}_{-13.2}$	$23.5^{+3.9}_{-3.0}$	$58.0^{+12.3}_{-8.1}$	...
246	68	5793	$32.5^{+9.1}_{-18.2}$	$38.0^{+16.8}_{-12.8}$	$43.1^{+27.1}_{-15.5}$	...
1925	409	5460	$12.4^{+3.3}_{-1.3}$	$28.3^{+7.9}_{-4.7}$	$49.8^{+16.5}_{-9.5}$	...
Stars with bimodal peaks in periodogram						
42	410	6273	$20.3^{+2.2}_{-1.3}$	$5.6^{+0.1}_{-0.1}$	$83.6^{+4.4}_{-5.2}$	...
244	25	6270	$22.4^{+3.3}_{-1.6}$	$7.8^{+0.5}_{-0.5}$	$80.6^{+6.6}_{-9.2}$	...

Note: $T_{\rm eff}$ is from NASA Exoplanet Archive (`https://exoplanetarchive.ipac.caltech.edu`).

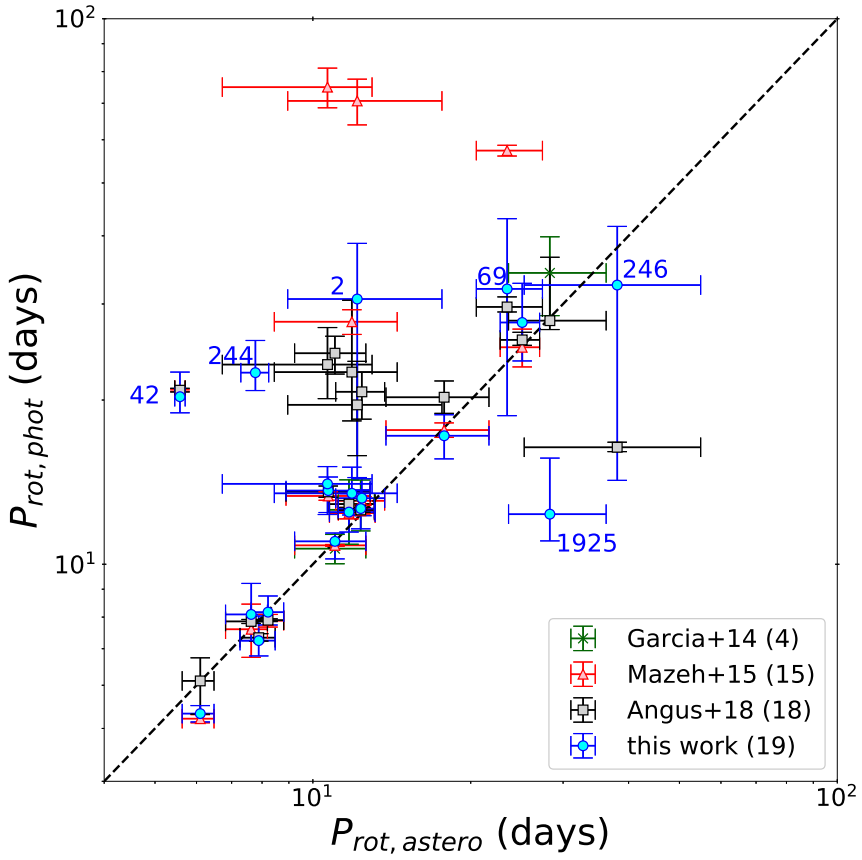

Figure 6.1: Photometric rotation periods $P_{\rm rot,photo}$ of 19 planet-host stars against their asteroseismic rotation periods $P_{\rm rot,astero}$. The values of $P_{\rm rot,astero}$ are based on four independent papers as indicated in the legend. The number in the parenthesis indicates the number of stars plotted here that are overlapped in the paper and this work. We mark 6 stars, whose $P_{\rm rot,photo}$ derived from the LS periodogram is unreliable, by their KOI IDs.

values of $P_{\rm rot,photo}$ published in literature are rather different. We plot the results by García et al. (2014) with the Morlet wavelet method in green, Mazeh et al. (2015) with the auto-correlation function in red, and Angus et al. (2018) with Gaussian process in gray. We also measure $P_{\rm rot,photo}$ using the Lomb-Scargle (LS) periodogram, which is plotted in blue. Specifically, we compute the LS periodogram using the long cadence PDCSAP lightcurves provided on the KASOC website [1]. Quarters are first concatenated by fitting the fourth-order polynomials on each quarter and extrapolating the time to the initial time of the subsequent quarter. This allows to remove jumps (due to the change of CCD when *Kepler* rotates) but preserves temporal gaps between quarters. Additionally, a smooth curve (a box-car smoothing of 50 days width) is removed from the concatenated lightcurve in order to effectively filter-out variabilities longer than ≈ 50 days.

[1] `http://kasoc.phys.au.dk`

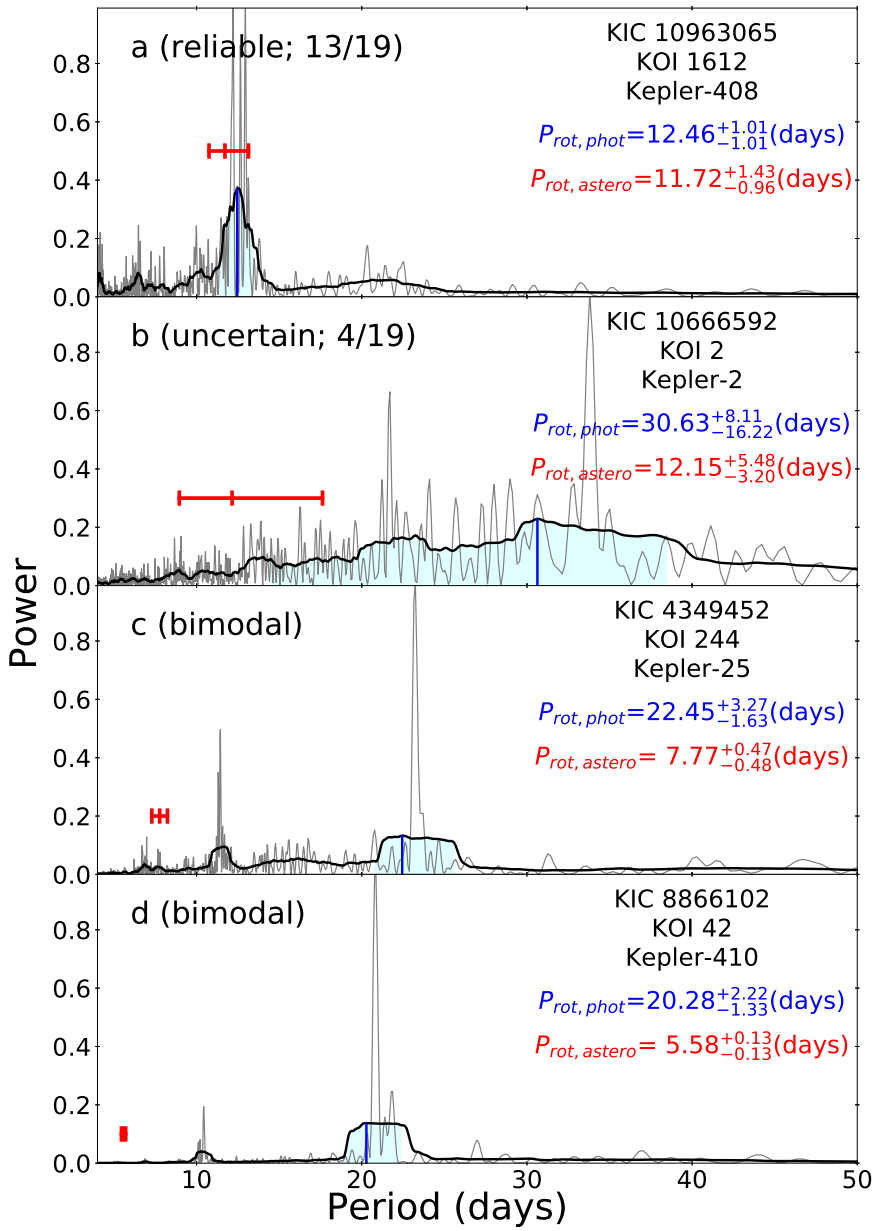

Figure 6.2: Examples of the LS periodogram for our sample. The thick black line indicates the boxcar-smoothed result (over 0.1 μHz) of the original LS periodogram (thin gray curves). The original periodogram is normalized so that the maximum power of each system is unity. The period corresponding to the maximum power of the smoothed LS curve is marked by the vertical blue line, and the associated range of its full-width-at-half-maximum is plotted as blue-shaded areas. We also show the mean and its 1σ confidence interval of the asteroseismic rotation period by the horizontal red bar. Panel *a*: Example of clear signature of the photometric rotation. Panel *b*: Example of dubious detection due to the absence of clear peak. Panels *c* and *d*: Cases showing clear double peaks, neither of which match the asteroseismic rotation period.

Effects of transits on photometric variation are minimized by trimming the lightcurve. To find the best trimming threshold, we visually inspect each lightcurve and proceed on a trial-and-error basis. We also verify that the signal from the transits is effectively removed from the low frequency part of the LS periodogram. Note that the LS periodogram is computed using an oversampling factor of four.

A low-frequency peak of the LS periodogram is interpreted as the surface rotation rate, due to surface structures co-rotating with the stellar surface. To minimize noise fluctuations, the peak position is extracted on the LS periodogram smoothed over a box-car window of width $0.1\,\mu$Hz. This value corresponds to the typical width of the observed peak and might be due to the finite lifetime of surface spots and to the effect of latitudinal differential rotation. The peak extraction is performed on the range $0.2 - 3.0\,\mu$Hz, corresponding to periods between 3.8 and 60 days.

The uncertainty on the peak position is estimated from its full-width-at-half-maximum of power in the frequency domain. We compute the corresponding frequency region in a linearly equally bin in the frequency, and convert it in the time domain, which is indicated as blue-shaded regions in Figure 6.2. This works nicely for the 13 *reliable* stars with a clear peak in the periodogram, but the resulting error-bars in $P_{\rm rot,photo}$ may be somewhat uncertain for the six *dubious* stars. Since we focus on the architecture of the 13 *reliable* stars in what follows, this does not affect our conclusion.

Figure 6.1 indicates that the measurements of $P_{\rm rot,photo}$ are somewhat dependent on the detailed methods of identifying the photometric variation, and in some cases exhibit large differences for the same systems. In particular, we note that for $P_{\rm rot,astero} \approx 10 - 20$ days, the estimates by Angus et al. (2018) are larger by a factor $\approx$ 2 (gray squares) relative to ours (blue circles). We individually examine the the LS periodograms of the 19 systems, and find that their estimates do not correspond to the highest peaks for most of the cases above.

As clearly noted in Angus et al. (2018), Gaussian Processes (GP) are prone to over-fitting and require lots of care when setting the hyper-parameters and hyper-priors. Actually, our examination of the low frequency power spectrum suggests that the GP method picks up a time-scale consistent with that of the convective turnover expected for solar-like stars (see e.g. Landin et al. 2010), rather than the stellar rotation period. Therefore, it is likely that the GP method is difficult to clearly distinguish the granulation noise (in the power spectrum it shows up as a pink noise, often referred to as the Harvey-like profile, see section 3.2) from the signal from the stellar surface rotation.

Both our asteroseismic and photometric estimates are largely consistent with the result of Mazeh et al. (2015) plotted in red triangles, but there are three stars for which their auto-correlation method gives rotational periods of more than $\approx$ 60 days. This is statistically unexpected for a solar-like star in the main-sequence phase (see McQuillan et al. 2014, and our Figure 6.4 below), and could correspond to harmonics of the true rotation period, probably more visible in the auto-correlation function than in the LS periodogram.

Our LS periodogram analysis returns unusually large uncertainties for four KOIs (KOI 2, 69, 246, and 1925), and discrepant results compared to asteroseismology for two KOIs (KOI 42 and 244), which are labelled in Figure 6.1. We carefully examine their LS periodograms, and possibly understand the origin of these anomalies as described in what follows.

Figure 6.2a shows the LS periodogram for KOI-1612 (Kepler-408) whose highest peak (blue area) is consistent with the period estimated from asteroseismology (red bars); 13 out of the 19 systems belong to this case, and will be referred to as *reliable*. Figure 6.2b for HAT-P-7 (KOI-2, Kepler-2) represents an example without any clear peak in the LS periodogram (4 out of the 19 stars). We cannot estimate the rotation period of those stars due to the large uncertainty. This may be because the star is seen near pole-on, or has a weak magnetic activity level (no large-scale surface structure).

Such systems with no clear peak in the periodogram may be regarded as good candidates for oblique systems, especially for cool stars that are supposed to exhibit detectable star-spot activity. When searching for significantly tilted planets, the absence of clear rotational peak in the LS periodogram, combined with a low inclination derived from asteroseismology, may provide a substantial hint. In particular, we note that Kepler-68, 93, and 409 may be potentially misaligned systems, in addition to HAT-P-7 for which a large *projected* spin-orbit misalignment has been discovered by Winn et al. (2009). Figure 6.3 shows the correlation map between the stellar inclination $i_\star$ and rotational splitting $\delta\nu_\star$ ($= P_{\rm rot,astero}$) derived from asteroseismic analysis in chapter 4 for these systems. They have the maximum of probability for $i_\star$ at $< 60^\circ$. This is systematically lower than the other 13 reliable detections (see Table 6.1).

Kepler-69 has three planets, including two inner Earth-sized planets ($R_{\rm p} = 2.4\,R_\oplus, 1.0\,R_\oplus$) in compact orbits ($P_{\rm orb} = 5.4$ days, 9.6 days). Kepler-93 has a close-in Earth-sized planet ($R_{\rm p} = 1.6\,R_\oplus$, $P_{\rm orb} = 4.7$ days) and a massive planet in a distant orbit ($P_{\rm orb} > 1460$ days). Kepler-409 has an Earth-sized planet ($R_{\rm p} = 1.2\,R_\oplus$) in a 69-day orbit. Because the measurement of the projected spin-orbit angle λ for such small planets is practically impossible at this point, the three systems above may be new interesting candidates for obliquity studies based on asteroseismology. As Figure 6.3 indicates, the asteroseismic analysis clearly identifies the value of $\delta\nu_\star \sin i_\star$, even if the degeneracy between $\delta\nu_\star$ ($= 1/P_{\rm rot,astero}$) and $i_\star$ is not easy to be broken. Thus reliable and independent estimates of $P_{\rm rot,photo}$ are very useful in breaking the degeneracy as our joint analysis shows (see Table 6.1 and Figure A.3). Nevertheless the fact that those four systems have relatively low inclinations around 40° may explain why they do not show any detectable periodicity in their photometric lightcurves.

As for the two stars that show a discrepancy between asteroseismology and the LS periodogram analysis, KOI-244 (Kepler-25) and KOI-42 (Kepler-410), we note that they have at least two clear peaks in the LS periodogram. As bottom panels indicate, neither peak agrees with the asteroseismic rotation period at all. We do not yet understand the origin of this bimodality. It may indicate that the transit signal is not completely removed during the lightcurve preparation, and that the residual contaminates the periodogram. It seems more likely, however, that the peaks are related to some harmonics of the true rotation period, while the true period itself is obscured for some unknown reason. Indeed $P_{\rm rot,photo}$ corresponding to the highest peak in the periodogram are $\approx 3P_{\rm rot,astero}$ and $\approx 4P_{\rm rot,astero}$ for KOI-244 and KOI-42, respectively.

Given the comparison of the different estimates of $P_{\rm rot,photo}$ described above, we decided to use our own results (blue circles in Figure 6.1) and $P_{\rm rot,astero}$ (chapter 4) as the two independent proxies for the true rotation period. Because we inspected the LS periodogram

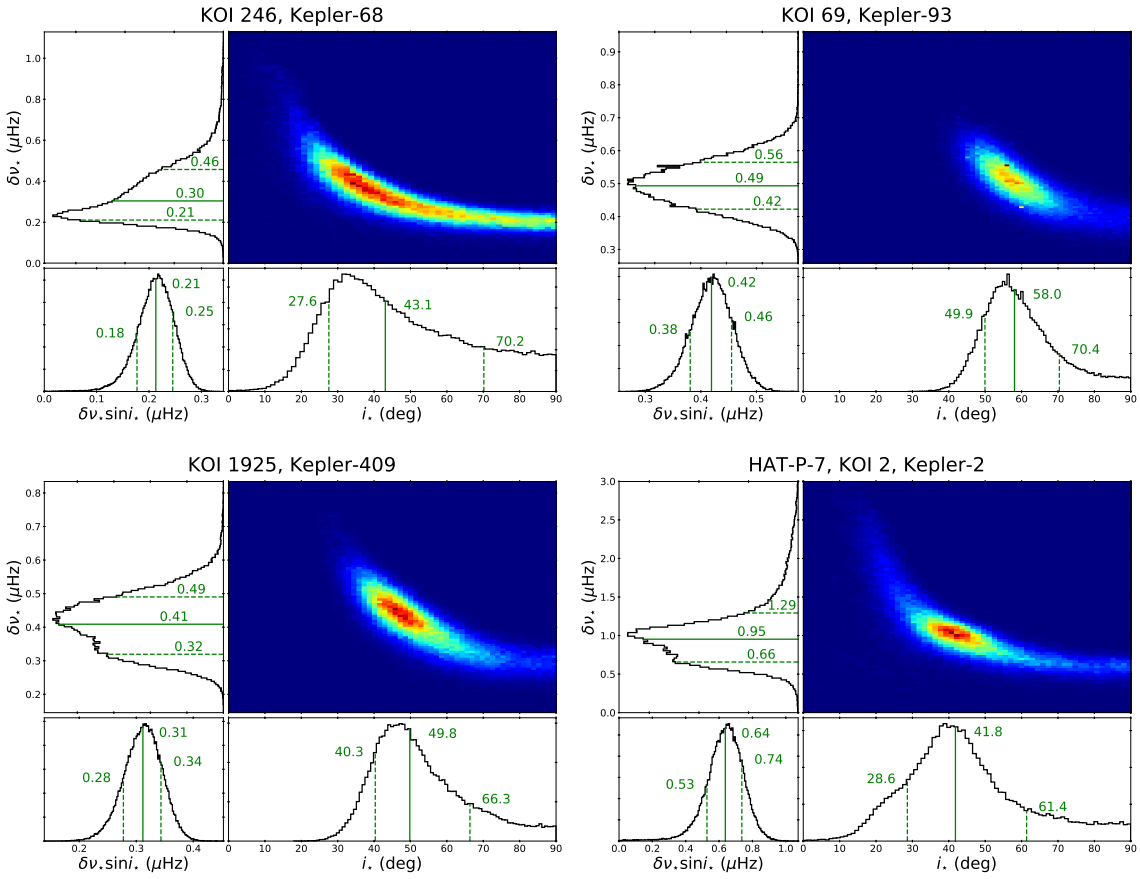

Figure 6.3: Constraints on the stellar inclination and frequency splitting from asteroseismic analysis. We plot the posterior probability density (PPD) on $i_\star$-$\delta\nu_\star$ plane, marginalized over all other parameters. The one-dimensional marginalized densities are also shown to the left and below the axes. The panel in the bottom left is the PPD of $\delta\nu_\star \sin i_\star$. Top left: Kepler-68 (KOI-246). Top right: Kepler-93 (KOI-69). Bottom left: Kepler-409 (KOI-1925). Bottom right: HAT-P-7 (Kepler-2, KOI-2).

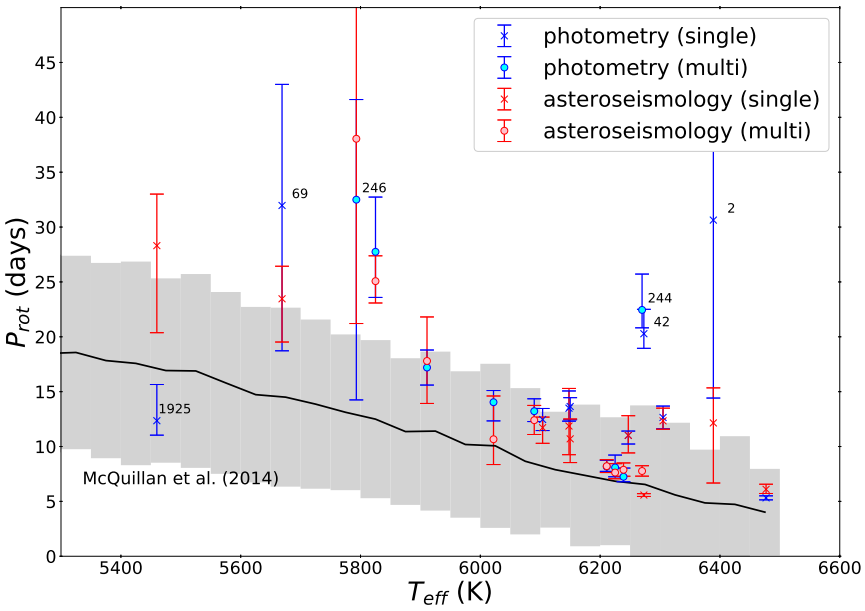

Figure 6.4: Rotation periods of the 19 stars against their effective temperature. Blue and red symbols correspond to $P_{\rm rot,photo}$ and $P_{\rm rot,astero}$ with crosses and circles indicating single and multiple planet systems, respectively. The mean and its 1σ uncertainty regions for the photometrically derived rotation period (McQuillan et al. 2014) are plotted as the thick black line and the gray area.

of the 19 systems individually and homogeneously, our estimate of $P_{\rm rot,photo}$ is more robust and reliable than those presented in the previous literature (Figure 6.1). Note that we still keep four stars (KOI-2, 69, 246, and 1925) with no clear peak and two stars (KOI-42 and 244) with two peaks in the analysis, but put their KOI number in the subsequent plots. When interpreting our following results, it would caution a possible bias due to their somewhat unreliable $P_{\rm rot,photo}$.

Incidentally Benomar et al. (2014) attempted for the first time to recover the full spin-orbit angle, instead of its projected value λ, through the joint analysis of the RM effect and asteroseismology. They considered two systems, HAT-P-7 (Kepler-2, panel *b*) and Kepler-25 (panel *c*), which are classified as *uncertain* and *bimodal*, respectively. Thus a verification of their result is difficult through an independent estimate of $P_{\rm rot,photo}$.

Figure 6.4 shows $P_{\rm rot,astero}$ (red circles) estimated by asteroseismology and $P_{\rm rot,photo}$ (blue circles) estimated by LS periodogram for those 19 planet-host stars against the stellar effective temperature $T_{\rm eff}$. For comparison, the 1σ region of $P_{\rm rot} - T_{\rm eff}$ from photometric variation analysis of $\approx$ 34,000 *Kepler* stars (McQuillan et al. 2014) is plotted as gray bands. Clearly both $P_{\rm rot,astero}$ and $P_{\rm rot,photo}$ for our sample are systematically longer than the average of *Kepler* stars. We note that the discrepancy above becomes even stronger if we use $P_{\rm rot,photo}$ by Mazeh et al. (2015) and Angus et al. (2018). We also made sure that 48 planet-less stars with secure rotational period measurement in chapter 4 exhibit the same trend, implying that

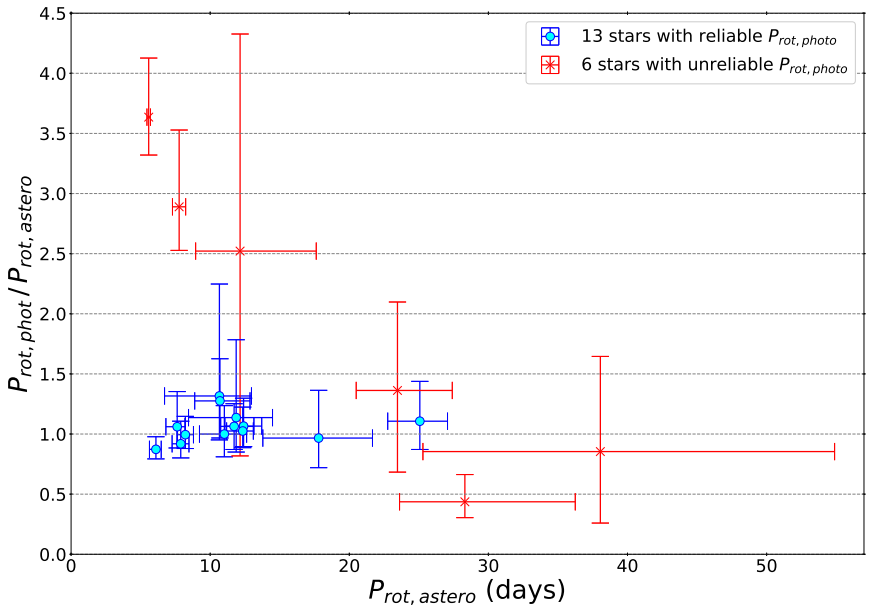

Figure 6.5: Ratio of the photometric and asteroseismic rotation periods, $P_{\rm rot,photo}/P_{\rm rot,astero}$, plotted against $P_{\rm rot,astero}$. Blue circles indicate the 13 stars with reliably-determined $P_{\rm rot,photo}$. Red crosses labeled by KOI IDs indicate the 6 stars whose $P_{\rm rot,photo}$ is not reliable.

the discrepancy is not related to the effect of the accompanying planet. The reason for this discrepancy is unclear, but we suspect that this results from (unknown) factors affecting the detectability of solar-like pulsations. For example, magnetic activity is known to damp solar pulsations so that they show reduced amplitudes (e.g., Benomar et al. 2012). The statistical distribution derived by McQuillan et al. (2014), however, is still consistent at 2σ with our estimates, and thus the apparent discrepancy may be simply due to the limited size of our sample.

Figure 6.5 plots $P_{\rm rot,photo}/P_{\rm rot,astero}$ against $P_{\rm rot,astero}$ for 19 planet-host stars; 13 systems with reliable $P_{\rm rot,photo}$ (in blue circles) and 6 systems with unreliable $P_{\rm rot,photo}$ (in red crosses). It is reassuring that there is a clear sequence around $P_{\rm rot,photo}/P_{\rm rot,astero} \approx 1$, mainly for the systems with reliable measurements of $P_{\rm rot,photo}$. Indeed all the systems whose $P_{\rm rot,photo}/P_{\rm rot,astero}$ is very different from unity correspond to the six stars classified as either uncertain or bimodal. We also note that the three stars with $P_{\rm rot,photo} \gg P_{\rm rot,astero}$ have $P_{\rm rot,astero} < 20$ days. Since both asteroseismic and photometric period measurements are expected to be more reliable for faster rotating stars, this tendency is difficult to be ascribed simply to an observational bias, but may have a yet unknown but physical explanation.

Before presenting our major results in the next section, we emphasize that strictly speaking, neither $P_{\rm rot,astero}$ nor $P_{\rm rot,photo}$ may represent the true rotation period of the star $P_{\rm rot,true}$. The surface differential rotation would lead to $P_{\rm rot,photo} > P_{\rm rot,true}$ for most stars in which the high-latitude surface rotates more slowly than the equator. Multiple formation/dissipation of star-spots may result in $P_{\rm rot,photo}/P_{\rm rot,true}$ significantly different from unity. It may be

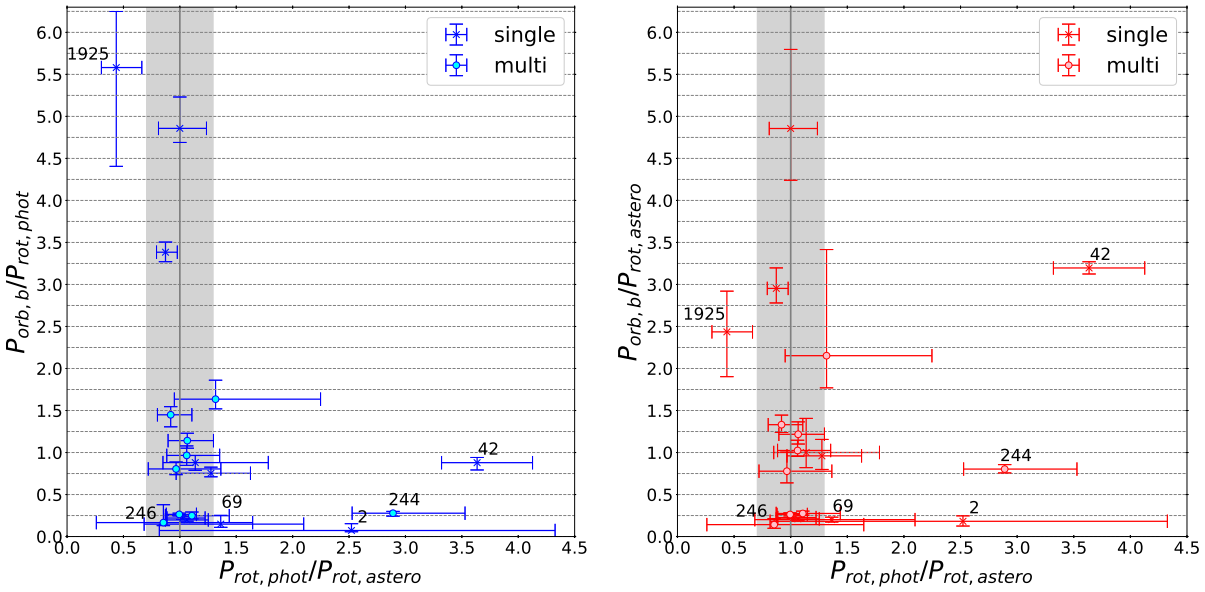

Figure 6.6: Possible spin-orbit resonance on $P_{\rm orb,b}/P_{\rm rot,photo}$-$P_{\rm rot,photo}/P_{\rm rot,astero}$ (left panel) and on the plane $P_{\rm orb,b}/P_{\rm rot,astero}$-$P_{\rm rot,photo}/P_{\rm rot,astero}$ (right panel). For multi-planetary systems, we plot the inner-most planet alone.

also the case for $P_{\rm rot,astero}$, which mainly probes the stellar internal rotation (not surface rotation) using its effect on stellar surface oscillations. Since most of our 19 stars have $P_{\rm rot,astero} \approx P_{\rm rot,photo}$, they are likely to be a good proxy for $P_{\rm rot,true}$, at least approximately, but their quantitative difference needs to be kept in mind in understanding the result presented below.

6.3 Possible signature of spin-orbit resonance

Figure 6.6 shows $P_{\rm orb,b}/P_{\rm rot,photo}$ (left) and $P_{\rm orb,b}/P_{\rm rot,astero}$ (right) against $P_{\rm rot,photo}/P_{\rm rot,astero}$ for the 19 systems, where $P_{\rm orb,b}$ is the orbital period of the inner-most planet of each system. Just for reference, the range of $0.7 < P_{\rm rot,photo}/P_{\rm rot,astero} < 1.3$ is shaded in gray, taking account of a possibility that $P_{\rm rot,photo}$ and $P_{\rm rot,astero}$ do not exactly agree with $P_{\rm rot,true}$. Indeed the ratio for the 13 stars except for the six *dubious* is within the region. Their parameters are listed in Tables 6.2 and 6.3. An interesting feature clearly visible in Figure 6.6 is that $P_{\rm orb,b}/P_{\rm rot}$ seems to be strongly clustered around 1/4 and 1, especially for the systems with $0.7 < P_{\rm rot,photo}/P_{\rm rot,astero} < 1.3$.

Figure 6.7 exhibits the trend more clearly, in which the overall spin-orbit architecture for multi- (top) and single- (bottom) planetary systems is plotted separately (see also Table 6.4). Interestingly and intriguingly, $P_{\rm orb}/P_{\rm rot}$ for multi-planetary systems does not seem to distribute in a homogeneous fashion, but rather preferentially takes discrete values.

The most straightforward interpretation is that those systems are in spin-orbit resonant

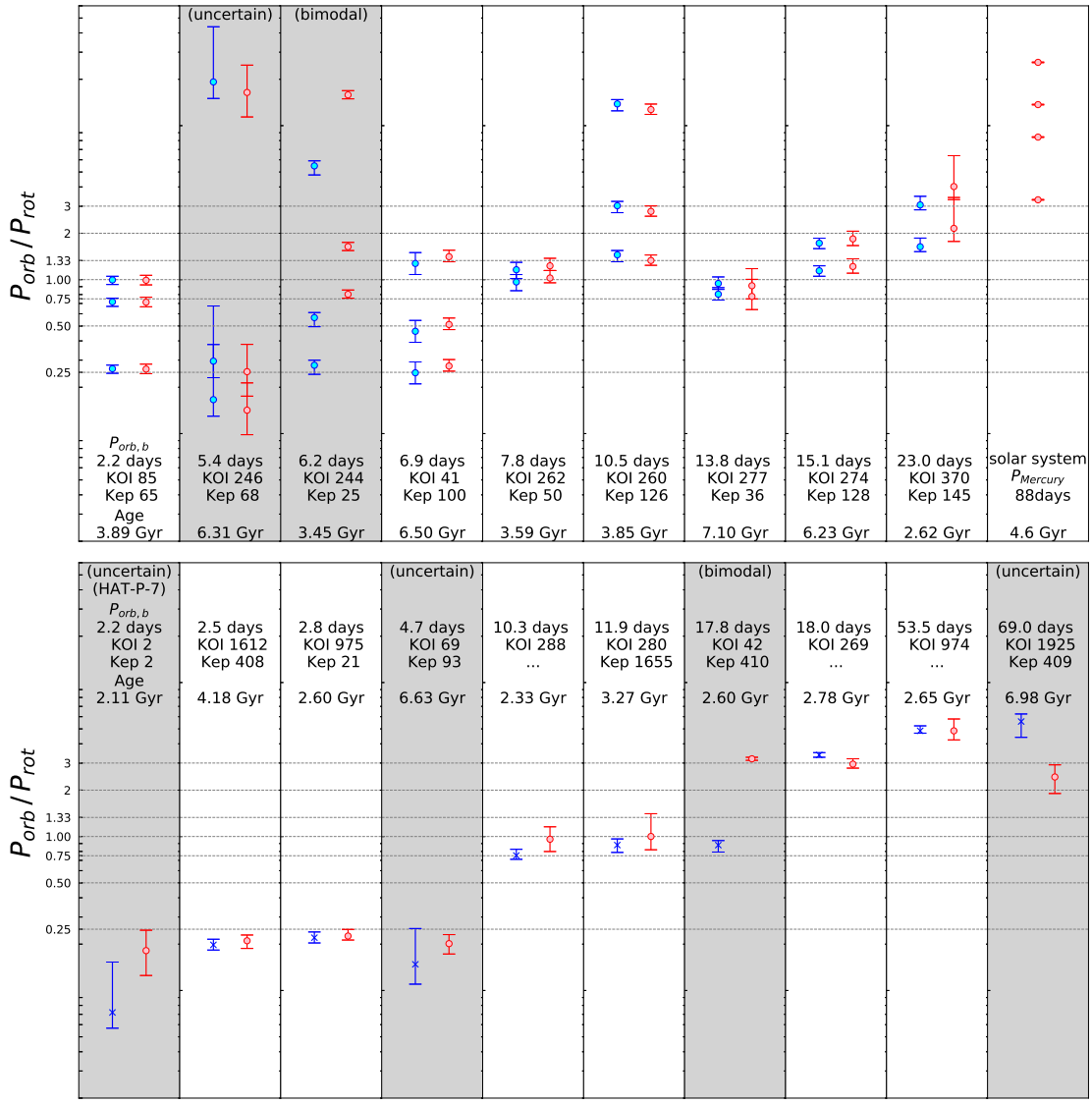

Figure 6.7: $P_{\rm orb}/P_{\rm rot,photo}$ (blue symbols) and $P_{\rm orb}/P_{\rm rot,astero}$ (red symbols) for multi- (top) and single- (bottom) transiting systems. Systems without reliable $P_{\rm rot,photo}$ measurement are gray-shaded. Just for comparison, we plot the Solar system as well in top panel.

Table 6.2: Properties of single-planetary systems.

KOI	Kepler ID	$R_{\rm p}$ ($R_\oplus$)	$M_{\rm p}$ ($M_\oplus$)	e	a (au)	$P_{\rm orb}$ (days)	$P_{\rm orb}/P_{\rm rot,photo}$	$P_{\rm orb}/P_{\rm rot,astero}$
Stars with reliable period measurement								
269	...	1.83	...	...	0.15	18.01	$3.38^{+0.12}_{-0.11}$	$2.95^{+0.24}_{-0.17}$
280	1655	2.21	5.0	...	0.10	11.87	$0.88^{+0.08}_{-0.09}$	$1.00^{+0.41}_{-0.18}$
288	...	3.04	...	...	0.10	10.28	$0.75^{+0.07}_{-0.04}$	$0.96^{+0.20}_{-0.16}$
974	...	2.52	...	...	0.29	53.51	$4.86^{+0.37}_{-0.17}$	$4.86^{+0.94}_{-0.62}$
975	21	1.64	5.08	0.02	0.04	2.79	$0.22^{+0.02}_{-0.02}$	$0.23^{+0.02}_{-0.01}$
1612	408	0.82	...	...	...	2.47	$0.20^{+0.02}_{-0.01}$	$0.21^{+0.02}_{-0.02}$
Stars with no clear signal in periodogram								
2	2	16.9	585	...	0.04	2.20	$0.07^{+0.08}_{-0.02}$	$0.18^{+0.06}_{-0.06}$
69	93	1.6	3.2	...	0.05	4.73	$0.15^{+0.10}_{-0.04}$	$0.20^{+0.03}_{-0.03}$
1925	409	1.19	...	...	...	68.96	$5.58^{+0.67}_{-1.18}$	$2.44^{+0.48}_{-0.53}$
Stars with bimodal peaks in periodogram								
42	410	2.84	...	0.17	0.12	17.83	$0.88^{+0.06}_{-0.09}$	$3.20^{+0.07}_{-0.07}$

Note: $R_{\rm p}$, $M_{\rm p}$, e, a, and $P_{\rm orb}$ are from NASA Exoplanet Archive (`https://exoplanetarchive.ipac.caltech.edu`).

states that have $P_{\rm orb}/P_{\rm rot} \approx n/m$ with n and m being simple integers. It is true that the time-scale $\tau_{\rm sync}$ of the spin-orbit synchronization ($P_{\rm orb,b}/P_{\rm rot}\approx1$) is unrealistically long at least in a conventional equilibrium tide model. Nevertheless we may speculate that there are a few dynamically stable local minima corresponding to $P_{\rm orb,b}/P_{\rm rot} \approx n/m$. In the course of the slow-down of the stellar rotation and/or the planetary migration that are not directly triggered by the tidal interaction, the star-planet system may fall into one of such quasi-resonant states temporarily. If the hypothesis is correct, the corresponding time-scale could be significantly smaller than $\tau_{\rm sync}$ based on the mere tidal interaction. Otherwise the current result would challenge the existing tidal theories if it is achieved entirely due to the star-planet tidal interaction.

Bottom panel of Figure 6.7 is the same as top panel but for single-planetary systems. Apart from the four stars classified as uncertain or bimodal, the spin-orbit resonance is still visible, even though to a lesser extent than exhibited in top panel. This may be a simple statistical fluctuation, but may suggest that the apparent spin-orbit resonance is somehow related to, or even enhanced by the orbital resonance in the overall architecture of the multi-planetary systems.

Because of the limited number of the planetary systems that allow a reliable asteroseismic estimate of the stellar rotation period, it is not easy to provide the statistical significance of the presence of the spin-orbit resonance that we propose here. Nevertheless we attempt to evaluate it using histograms of $P_{\rm orb}/P_{\rm rot,astero}$ in Figure 6.8, whose total number count is

Table 6.3: Properties of multi-planetary systems.

KOI	Kepler ID	$R_{\rm p}$ ($R_\oplus$)	$M_{\rm p}$ ($M_\oplus$)	e	a (au)	$P_{\rm orb}$ (days)	$P_{\rm orb}/P_{\rm rot,photo}$	$P_{\rm orb}/P_{\rm rot,astero}$
Stars with reliable period measurement								
41	100	1.32	7.34	0.13	...	6.89	$0.25^{+0.04}_{-0.04}$	$0.27^{+0.03}_{-0.02}$
		2.20	...	0.02	...	12.82	$0.46^{+0.08}_{-0.07}$	$0.51^{+0.05}_{-0.04}$
		1.61	...	0.02	...	35.33	$1.27^{+0.22}_{-0.19}$	$1.41^{+0.14}_{-0.10}$
85	65	1.42	...	0.02	0.04	2.15	$0.26^{+0.01}_{-0.02}$	$0.26^{+0.02}_{-0.02}$
		2.58	26.6	0.08	0.07	5.86	$0.72^{+0.04}_{-0.05}$	$0.71^{+0.06}_{-0.05}$
		1.52	...	0.10	0.08	8.13	$1.00^{+0.06}_{-0.07}$	$0.99^{+0.08}_{-0.07}$
260	126	1.52	...	0.07	0.10	10.50	$1.45^{+0.10}_{-0.14}$	$1.33^{+0.11}_{-0.09}$
		1.58	...	0.19	0.16	21.87	$3.02^{+0.20}_{-0.30}$	$2.77^{+0.24}_{-0.19}$
		2.50	...	0.02	0.45	100.28	$13.84^{+0.92}_{-1.37}$	$12.72^{+1.09}_{-0.89}$
262	50	1.71	...	...	0.08	7.81	$0.97^{+0.11}_{-0.12}$	$1.02^{+0.12}_{-0.07}$
		2.17	...	...	0.09	9.38	$1.16^{+0.14}_{-0.14}$	$1.23^{+0.15}_{-0.08}$
274	128	1.13	30.7	...	0.13	15.09	$1.14^{+0.09}_{-0.09}$	$1.22^{+0.15}_{-0.12}$
		1.13	33.3	...	0.17	22.80	$1.73^{+0.13}_{-0.14}$	$1.84^{+0.22}_{-0.18}$
277	36	1.49	4.45	0.04	0.12	13.84	$0.80^{+0.08}_{-0.07}$	$0.78^{+0.23}_{-0.14}$
		3.68	8.08	...	0.13	16.24	$0.94^{+0.10}_{-0.08}$	$0.91^{+0.27}_{-0.16}$
370	145	2.65	37.1	0.43	...	22.95	$1.63^{+0.23}_{-0.12}$	$2.15^{+1.26}_{-0.38}$
		4.32	79.4	0.11	...	42.88	$3.05^{+0.42}_{-0.22}$	$4.02^{+2.36}_{-0.71}$
Stars with no clear signal in periodogram								
246	68	2.40	6.00	...	0.06	5.40	$0.17^{+0.21}_{-0.04}$	$0.14^{+0.07}_{-0.04}$
		1.00	4.80	0.42	0.09	9.61	$0.30^{+0.38}_{-0.06}$	$0.25^{+0.13}_{-0.08}$
		...	267	0.18	1.40	625	$19.23^{+24.63}_{-4.22}$	$16.43^{+8.28}_{-5.04}$
Stars with bimodal peaks in periodogram								
244	25	2.71	9.60	...	0.07	6.24	$0.28^{+0.02}_{-0.04}$	$0.80^{+0.05}_{-0.05}$
		5.20	24.60	0.01	0.11	12.72	$0.57^{+0.04}_{-0.07}$	$1.64^{+0.11}_{-0.09}$
		...	89.90	...	...	123	$5.48^{+0.43}_{-0.70}$	$15.83^{+1.04}_{-0.90}$

Note: $R_{\rm p}$, $M_{\rm p}$, e, a, and $P_{\rm orb}$ are from NASA Exoplanet Archive (`https://exoplanetarchive.ipac.caltech.edu`).

Table 6.4: Ratios of the photometric rotation, planetary orbital and asteroseismic rotation periods.

KOI	Kepler ID	$P_{\rm rot,astero}$ (days)	$P_{\rm orb,b}$ (days)	$n_{\rm rot,astero}$	$n_{\rm rot,phot}$	$n_{\rm orb,b}$	$n_{\rm orb,c}$	$n_{\rm orb,d}$
Stars with reliable period measurement								
41	100	$25.1^{+2.0}_{-2.3}$	6.89	4.0	$4.4^{+0.9}_{-0.8}$	$1.1^{+0.1}_{-0.1}$	$2.0^{+0.2}_{-0.2}$	$5.6^{+0.4}_{-0.5}$
85	65	$8.2^{+0.6}_{-0.6}$	2.15	4.0	$4.0^{+0.4}_{-0.4}$	$1.0^{+0.1}_{-0.1}$	$2.9^{+0.2}_{-0.2}$	$4.0^{+0.3}_{-0.3}$
260	126	$7.9^{+0.6}_{-0.6}$	10.50	2.0	$1.8^{+0.2}_{-0.2}$	$2.7^{+0.2}_{-0.2}$	$5.5^{+0.4}_{-0.4}$	$25.4^{+1.9}_{-2.0}$
262	50	$7.6^{+0.6}_{-0.8}$	7.81	4.0	$4.2^{+0.7}_{-0.6}$	$4.1^{+0.3}_{-0.4}$	$4.9^{+0.4}_{-0.5}$	...
269	...	$6.1^{+0.4}_{-0.5}$	18.01	1.0	$0.9^{+0.1}_{-0.1}$	$3.0^{+0.2}_{-0.2}$	...	...
274	128	$12.4^{+1.3}_{-1.3}$	15.09	3.0	$3.2^{+0.4}_{-0.4}$	$3.7^{+0.4}_{-0.4}$	$5.5^{+0.6}_{-0.6}$	...
277	36	$17.8^{+3.9}_{-4.0}$	13.84	4.0	$3.9^{+0.9}_{-0.9}$	$3.1^{+0.7}_{-0.7}$	$3.6^{+0.8}_{-0.8}$	...
280	1655	$11.9^{+2.6}_{-3.4}$	11.87	1.0	$1.1^{+0.3}_{-0.3}$	$1.0^{+0.2}_{-0.3}$	...	...
288	...	$10.7^{+2.2}_{-1.8}$	10.28	1.0	$1.3^{+0.3}_{-0.2}$	$1.0^{+0.2}_{-0.2}$	...	...
370	145	$10.7^{+2.3}_{-3.9}$	22.95	1.0	$1.3^{+0.3}_{-0.5}$	$2.2^{+0.5}_{-0.8}$	$4.0^{+0.9}_{-1.5}$	...
974	...	$11.0^{+1.6}_{-1.8}$	53.51	1.0	$1.0^{+0.1}_{-0.2}$	$4.9^{+0.7}_{-0.8}$	...	...
975	21	$12.3^{+0.8}_{-1.2}$	2.79	9.0	$9.2^{+0.9}_{-1.1}$	$2.0^{+0.1}_{-0.2}$	...	...
1612	408	$11.7^{+1.4}_{-1.0}$	2.47	5.0	$5.3^{+0.8}_{-0.6}$	$1.1^{+0.1}_{-0.1}$	...	...
Stars with no clear signal in periodogram								
2	2	$12.1^{+5.5}_{-3.2}$	2.20	5.0	$12.6^{+6.6}_{-7.5}$	$0.9^{+0.4}_{-0.2}$	...	...
69	93	$23.5^{+3.9}_{-3.0}$	4.73	5.0	$6.8^{+2.6}_{-3.0}$	$1.0^{+0.2}_{-0.1}$	...	...
246	68	$38.0^{+16.8}_{-12.8}$	5.40	7.0	$6.0^{+3.1}_{-3.9}$	$1.0^{+0.4}_{-0.3}$	$1.8^{+0.8}_{-0.6}$	$115.0^{+50.9}_{-38.5}$
1925	409	$28.3^{+7.9}_{-4.7}$	68.96	2.0	$0.9^{+0.3}_{-0.2}$	$4.9^{+1.4}_{-0.8}$	...	...
Stars with bimodal peaks in periodogram								
42	410	$5.6^{+0.1}_{-0.1}$	17.83	1.0	$3.6^{+0.4}_{-0.3}$	$3.2^{+0.1}_{-0.1}$	...	...
244	25	$7.8^{+0.5}_{-0.5}$	6.24	4.0	$11.6^{+1.8}_{-1.1}$	$3.2^{+0.2}_{-0.2}$	$6.5^{+0.4}_{-0.4}$	$63.3^{+3.8}_{-3.9}$

Note: $T_{\rm eff}$ and $P_{\rm orb,b}$ are from NASA Exoplanet Archive (`https://exoplanetarchive.ipac.caltech.edu`).

normalized to the unity in the logarithmic scale. The top and bottom panels indicate the distributions of $P_{\rm orb}/P_{\rm rot}$ for the innermost planets alone and all planets, respectively. The vertical dotted lines indicate ratios of simple integers, which are admittedly subjective to some extent but may be useful for readers to judge the significance of our proposal.

We note here that even if the spin-orbit resonance interpretation is correct, $P_{\rm orb}/P_{\rm rot,astero}$ does not have to coincide with a ratio of simple integers *exactly*. A possible radial differential rotation would make $P_{\rm rot,astero}$ slightly different from $P_{\rm rot,true}$. Furthermore, if the planetary orbit is eccentric, the stellar rotation velocity would be more likely synchronized towards the planetary orbital velocity at the pericenter. Thus $P_{\rm rot,true}$ would deviate from $P_{\rm orb}$ to some extent.

Finally we plot the spin-orbit angles λ and $90^\circ - i_\star$ against $\tau_{\rm sync}$ in Figure 6.9. The black symbols refer to λ from the RM database (Southworth 2011), while the red symbols are based on our asteroseismic analysis. As discussed in section 6.1, the bimodal distribution of λ in Figure 6.9 may suggest the presence of both primordial and realignment channels for the spin-orbit angle. If the strong clustering around $\lambda \approx 0^\circ$ results from the realignment channel at least partially, it also indicates another tidal model because $\tau_{\rm sync}$ of the conventional equilibrium tide is too long. This may be the same situation that we encounter here in our interpretation of the spin-orbit resonance.

6.4 Discussion and conclusion

In this chapter, we find an interesting correlation between the stellar rotation and planetary orbital periods for 19 *Kepler* transiting planetary systems whose rotation periods are estimated from both photometric variation and asteroseismology. Out of the 19 systems, we find 13 *reliable* systems that have clear peaks in the LS periodogram of their photometric lightcurve. The corresponding rotation periods $P_{\rm rot,photo}$ for the 13 systems are in good agreement with the asteroseismicestimate $P_{\rm rot,astero}$ within 1σ level. Among those reliable systems, KOI-280b, 288b, 262b, 277c, and 85d are likely in the spin-orbit synchronized states, i.e., $P_{\rm rot,astero} = P_{\rm orb}$ within 1σ. Moreover, for a significant fraction of the 13 planetary systems, $P_{\rm orb}/P_{\rm rot}$ can be expressed as a ratio of simple integers, which suggests a spin-orbit (quasi-)resonance.

We emphasize that our interpretation is based on 13 stars. Due to this limited number, it is perhaps not so difficult to express their $P_{\rm orb}/P_{\rm rot}$ in terms of the ratio of *simple* integers. Also it is always possible to find a set of two integers that well approximate the observed ratios of $P_{\rm orb}/P_{\rm rot}$. On the other hand, it is not easy to explain the fact that three (KOI-280b, 288b, 262b) out of the 13 systems have $P_{\rm rot,astero} = P_{\rm orb,b}$ just by chance. In any case, a larger sample of stars would be required to confirm/refute our spin-orbit (quasi-)resonance hypothesis.

In order to select a robust sample of stars with a reliable rotation period, we focused on stars that show consistent results between asteroseismic analysis and the LS periodogram. This turned out to be particularly important because we found a relatively low-level of agreement among different published values of $P_{\rm rot,photo}$. Asteroseismology has played a key role in

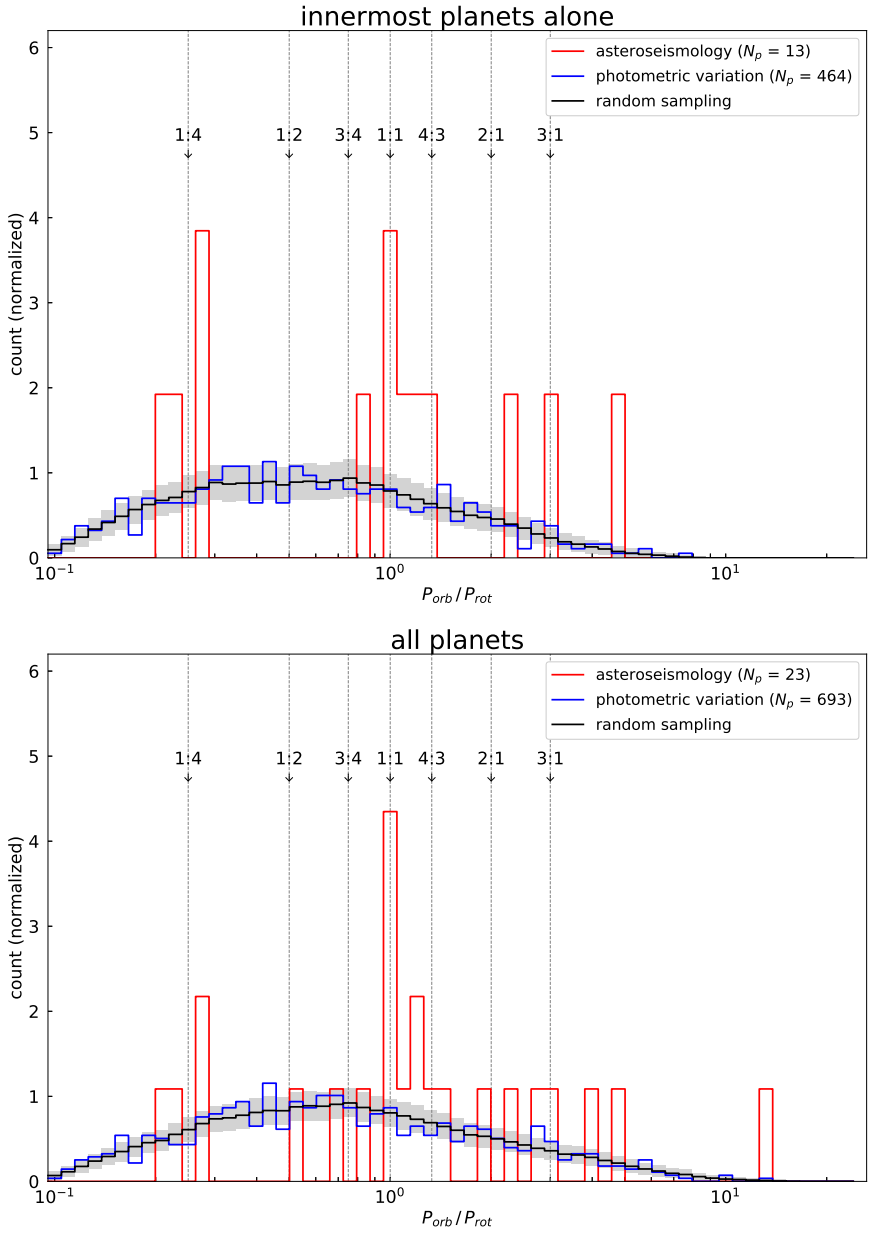

Figure 6.8: The normalized distribution of $P_{\rm orb}/P_{\rm rot}$ in logarithmic scale for innermost planets alone (top) and all planets (bottom). Red line represents the histogram for reliable asteroseismic samples, which is generated by using the median values of their posterior probability distribution (PPD) of $P_{\rm rot,astero}$. Blue line represents the histogram generated from $P_{\rm rot,photo}$ derived from photometric variation in Mazeh et al. (2015). Black line is drawn by $P_{\rm orb}$ and $P_{\rm rot,photo}$ independently sampled from the two catalogs so that this represents the case where the two are totally unrelated. Gray band are the standard deviation of 1,000 random sampling.

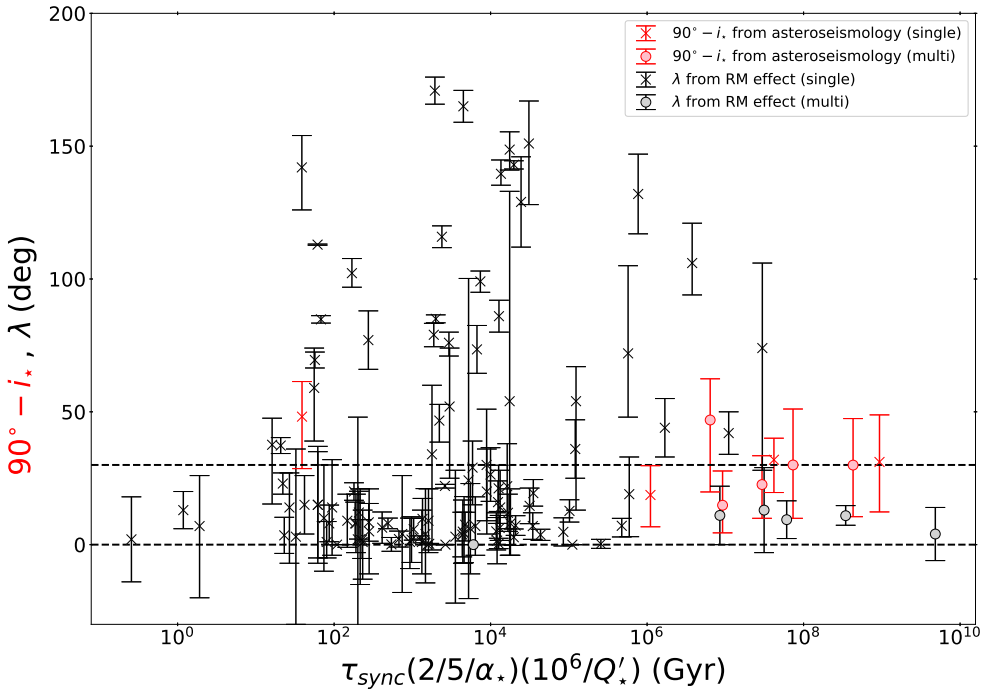

Figure 6.9: Spin-orbit angles λ and $90° - i_\star$ against $\tau_{\rm sync}$. The data for λ on the basis of the Rossiter-McLaughlin effect are taken from the compilation by Southworth (2011).

providing an entirely independent measurement of the stellar rotation. It is worth noting that a careful case-by-case examination is necessary if we use photometric variations (such as the LS periodogram) to derive $P_{\rm rot,photo}$. Indeed, the latitudinal differential rotation, the size of the star-spots and their typical formation/dissipation timescales would introduce significant differences between $P_{\rm rot,photo}$ and $P_{\rm rot,true}$. Furthermore, the planet itself induces a photometric modulation that, if not entirely removed, could be incorrectly identified as the stellar rotation period. These issues can only be circumvented by checking results independently with different methods, such as presented in this study. Unfortunately, however, measuring the rotation with asteroseismology requires high quality photometric data, so that it is difficult to increase the number of reliable stars significantly.

The spin-orbit resonance that we propose here points towards a strong tidal interaction between stars and planets. This cannot be explained in a conventional equilibrium tide model. Due to the limited number of planetary systems with a reliable stellar rotation period, the interpretation of the current data may not be conclusive, but suggestive for the spin-orbit resonance of transiting multi-planetary systems in particular.

While $\tau_{\rm sync}$, the time-scale of the spin-orbit synchronization given by equation (6.5) for planetary systems, is generally much longer than the age of the universe, quasi-synchronized states, e.g., $P_{\rm rot} = (n/m)P_{\rm orb,b}$ with n and m being simple integers, may be local minimum states of the dynamical architecture, and the time-scale to reach those states may be significantly shorter than $\tau_{\rm sync}$. This hypothesis can be, for example, modeled and tested against

numerical simulations.

Chapter 7

Summary and conclusion

Among various diversities in exoplanetary systems, the oblique orbits of planets with respect to the equatorial planes of their host stars seriously challenge the conventional theory of planet formation. Possible scenarios to explain these misaligned orbits have been proposed, and some of them ascribe the misalignment to the primordial origin, while others to the dynamical evolution of orbits after planets are born. Measuring the spin-orbit angle ψ is the key to understanding how common the oblique orbits are, and how likely these scenarios are in the actual misaligned systems. However, the measurements of spin-orbit misalignments in terms of their projected values (λ) have been ever made for planets larger than Neptune (e.g., hot Jupiters), mainly because of the observational limitations of the conventional Rossiter-McLaughlin effect. Although combined method enables the measurement of spin-orbit angles in terms of stellar inclinations $i_\star$ and is independent of planet size, it only provides weak constraints.

Asteroseismology, the study of stellar pulsations, has been made possible thanks to long and uninterrupted observation of space observatories such as CoRoT and *Kepler*. Asteroseismology is useful to infer the obliquity of planetary orbits by measuring the tilt of stellar spin axis towards the observer ($i_\star$). Importantly, asteroseismology is an unique tool to explore the orbital architecture of Earth-sized planets as well as combined method, because it relies on observing signals independent of the planet size.

In this thesis, we examined the applicability of asteroseismology to exoplanetary science, and major results are summarized as follows.

- We assessed the reliability of the parameters derived from asteroseismology, especially stellar inclination angle $i_\star$ and rotational splitting $\delta\nu_\star \approx 1/P_{\rm rot}$. Although authors in earlier studies have claimed that asteroseismology may return inaccurate values of $i_\star$ and $\delta\nu_\star$ in some cases, the dedicated study to reveal the conditions necessary for the reliable measurements has yet to be presented. In practice, stellar inclination and rotational splitting are often discussed without referring to their reliability in most literatures.

  Motivated by the necessity to remove this ambiguity, we derived analytic criteria for the secure measurement of $i_\star$ and $\delta\nu_\star$. These criteria were then verified to work well

in the actual asteroseismic analysis by performing thorough numerical simulations. We found that for the reliable determination of $i_\star$, $i_\star$ and $\delta\nu_\star$ should be at least $20^\circ \lesssim i_\star \lesssim 80^\circ$ and $\delta\nu_\star/\Gamma \gtrsim 0.5$.

We next performed asteroseismic analysis to 33 and 61 stars with and without known transiting planets, and found 9 and 22 out of them have accurate inclinations and splittings. This systematic study of 94 stars in total offers the largest catalogue of stellar inclinations and splittings ever for dwarf stars, including most of main-sequence solar-like stars with detectable pulsation signals. And then we showed statistically that asteroseismology sometimes fails to derive the correct values of $i_\star$ and $\delta\nu_\star$ (as we failed in 24 out of 33 planet-host stars and 39 out of 61 planet-less stars), which raises the caution when interpreting the derived inclination for individual system.

- The reliability of asteroseismic measurements can also be studied by comparing with other observations, such as rotational periods derived from photometric variation in stellar lightcurves. Among the reliable planet-host stars analyzed in this work, Kepler-408, a G0 type star with a sub-Earth planetary companion, is found to show unambiguous spin-orbit misalignment ($i_\star = 42^{+5}_{-4}$ degrees). Rotational splitting derived by photometry ($\delta\nu_\star = 0.898 \pm 0.013\,\mu$Hz) agrees our asteroseismic measurement ($\delta\nu_\star = 0.99 \pm 0.10\,\mu$Hz) well, making the misalignment of this system robust. Moreover, stellar inclination derived from spectroscopic $v \sin i_\star$ and $R_\star$ also predicts intermediate inclination ($i_\star = 44^{+20}_{-15}$ degrees) despite relatively large errors. Such an agreement between asteroseismology and other observations shows that joint analysis can provide quite robust measurement of stellar inclination and rotational splitting. Kepler-408, one of the most successful cases, is the first confirmation of a significant spin-orbit misalignment for planets smaller than Neptune. As a consequence, Kepler-408b is the smallest exoplanet ever known to have large misalignment. The astronomical importance of this discovery is that misalignment-enhancing mechanisms are found to work also for small planets, and spin-orbit misalignment may be common also for Earth-sized systems. The conventional RM effect cannot probe the misalignment for such a small planet. Since asteroseismology is independent of the properties of planets, this discovery clearly demonstrates that asteroseismology is a promising method to explore the orbital dynamics of Earth-sized planets.

- It is also worth emphasizing that asteroseismology offers an independent measure of stellar rotational period ($P_{\rm rot} \approx 1/\delta\nu_\star$). If asteroseismology agrees other observations such as photometry, therefore, the derived rotation period can be taken as the proxy for the true rotation period because they rely on completely different signals in observations. In this work, we find 13 exoplanetary systems where asteroseismically derived rotation period ($P_{\rm rot,astero}$) and that from photometric variation ($P_{\rm rot,photo}$) are consistent. Among them, we discovered the signature of correlation between planetary orbital motion and stellar rotation; the values of $P_{\rm orb}/P_{\rm rot}$ were turned out to preferentially take rational numbers in some systems, implying that they are in spin-orbit resonance. While dozens of planetary systems are known to be in resonant states *among* planetary

orbits, the resonance between star and planet has not been reported yet. This is partly because it is difficult to measure $P_{\rm rot,photo}$ accurately in most cases, because of the various assumptions on the star-spots. Based on asteroseismology as an independent measure of $P_{\rm rot}$, we discovered for the first time the resonance between star and planet although we have merely 13 samples. If this finding is proved to be really the case, it raises the necessity to re-consider the star-planet tidal interaction. In fact the spin-orbit synchronization ($P_{\rm rot} = P_{\rm orb}$) cannot be realized by the standard tidal theory, because estimated timescale for the synchronization is unrealistically long. Therefore it suggests that spin-orbit resonance is a (quasi-)equilibrium state during star-planet tidal evolution, or there may exist much stronger interaction beyond standard tide at play in the actual star-planet systems.

In summary, we attempted to apply asteroseismology to exoplanetary science in this work, and found observational evidence of spin-orbit misalignment for Earth-sized planet (chapter 5) and spin-orbit resonances in transiting planetary systems (chapter 6). These results are based on the careful investigation of the reliability of parameters derived with asteroseismology (chapter 4). Because these findings are difficult to be accomplished by other observations, they clearly demonstrate the asteroseismic potential as a useful and unique methodology to characterize exoplanetary systems. With these successful results enabled by asteroseismology, this work opened up a new window for the synergetic collaboration of asteroseismology and exoplanetary science.

In the near future, even more stars are expected as new asteroseismic targets by ongoing and/or future space campaigns, e.g., TESS (already under operation) and PLATO (planned for 2026). Eventually it is expected that exoplanets can be studied further both qualitatively and quantitatively, thanks to more than one million stars planned to be observed. And thus new discoveries similar to those by this work may become common outcome of asteroseismology with the rich samples by future observations. If misalignments in the orbits of small planets are discovered one after another, for example, it leads to the statistical study of the formation and evolution history of Earth-like planets. With sufficient samples of $P_{\rm rot,astero}$, on the other hand, additional tests on the accuracy of asteroseismic measurement will be made possible, as we tried with small number of samples in this work. Once asteroseismology is established as complete and independent methodology to measure stellar rotation, we can for example compare stellar internal and surface rotation statistically. This study may unveil how common stellar radial differential rotation is in the actual stars as we found in the Sun. In conclusion, asteroseismology is expected to keep bringing new discoveries in the field of stellar and planetary science with future observations in coming decades. We hope that our work will serve as a basic framework for the synergetic study of asteroseismology and planetary science in the future.

Acknowledgments

First, I would like to express my sincere gratitude to all of my collaborators. This dissertation builds on all of their kind help and support.

Above all, I would like to gratefully express thanks to my supervisor, Prof. Yasushi Suto, who provided me the opportunity to enjoy the work bridging the exoplanetary science and the stellar physics. He always seriously listened to my ideas, even though he was very busy, and gave me precious advices on what we should do next based on his great insight into various aspects of astronomy. His way of thinking and his point of view on how science and people in science should be always encouraged me to put my project forward. And then I sincerely acknowledge Dr. Othman Benomar in New York University Abu Dhabi, who guided me the stellar physics, especially asteroseismology, from the basics. I am sure that I could not have completed this dissertation without his great contribution over years to this work. Furthermore, every day's insightful discussion with him always motivated me and made advance to this project. I also would like to show my gratitude to collaborators in Princeton University, Mr. Fei Dai, Dr. Kento Masuda, and Prof. Joshua N. Winn.

Besides my collaborators above, I am also grateful to Mikkel Lund, Tiago Campante, and Martin Nielsen, who kindly shared my problems on asteroseismic data analysis and gave me materials to solve them. I also feel thankful to Thierry Appourchaux, Rafael Garcia, Jerome Ballot, Masataka Aizawa, Hajime Kawahara, and Adrien Leleu for their invaluable comments on this work, and to Benoit Marchand for his technical support on the computation.

Finally, I greatly thank my parents, Tsutomu Kamiaka and Junko Kamiaka. They always respected my decisions on the future career and patiently kept supporting me for a long, long time in all aspects.

I thank NASA *Kepler* team and the *Kepler* Asteroseismic Science Consortium (KASC) for making their data available to me. The numerical computations were carried out on PC cluster at Center for Computational Astrophysics, National Astronomical Observatory of Japan. This work is supported by Japan Society for Promotion of Science (JSPS) Research Fellowships for Young Scientists (No.16J03121).

Appendix A

Correlation of $P_{\rm orb}/P_{\rm rot}$ with stellar and orbital parameters of each system

We show $P_{\rm orb,b}/P_{\rm rot}$ as a function of stellar and orbital parameters of each system, mainly for completeness. We do not find any strong correlation nor particular bias in the following plots. Thus they are not inconsistent with our spin-orbit resonant interpretation, even if not strongly support it.

Figure A.1 shows $P_{\rm orb,b}/P_{\rm rot,photo}$ (blue symbols) and $P_{\rm orb,b}/P_{\rm rot,astero}$ (red symbols) against the transit period of the inner-most planet $P_{\rm orb,b}$ for the 19 systems; single-planet and multi-planet systems are plotted in crosses and circles, respectively. We note that our results are basically consistent with Figure 6 of Lurie et al. (2017), especially for $P_{\rm orb,b}/P_{\rm rot,astero}$. Nevertheless it may be puzzling given the fact that the star-planet tidal interaction should be significantly weaker than the star-star interaction in EBs. Since the typical time-scale $\tau_{\rm sync}$ expected from the equilibrium tidal model, equation (6.5), is too large, the result above is quite surprising unless $Q'_\star$ is unrealistically smaller than its fiducial range $10^5 - 10^7$. This is clearly shown in Figure A.2. As we mentioned in section 6.1, the alignment time-scale is basically identical to that of synchronization $\tau_{\rm sync}$. Thus systems with $P_{\rm rot}{\approx}P_{\rm orb}$ are expected to show the spin-orbit alignment. In reality, however, the stellar inclination $i_\star$ estimated from asteroseismology alone has a relatively large error-bar (chapter 4) except the notable case of Kepler-408 (KOI-1612, chapter 5). The constraint on $i_\star$ becomes more precise if combined with the independent prior on $P_{\rm rot,photo}$. Thus we selected 13 *reliable* systems in which the mean values of $P_{\rm rot,photo}$ and $P_{\rm rot,astero}$ agree within the 1σ level, and repeated asteroseismic inference adopting the Gaussian distribution of $P_{\rm rot,photo}$. The result is plotted in Figure A.3. While most systems are consistent with the spin-orbit alignment, $i_\star \approx 90^\circ$ within 2σ confidence level except Kepler-408 (KOI-1612). Nevertheless Figure A.3 is equally consistent with the primordial channel, and thus no clear conclusion cannot be drawn yet. We also plot the ratio against the eccentricity in Figure A.4, but it is difficult to interpret it either, due to the limited statistics, unlike Figure 8 of Lurie et al. (2017).

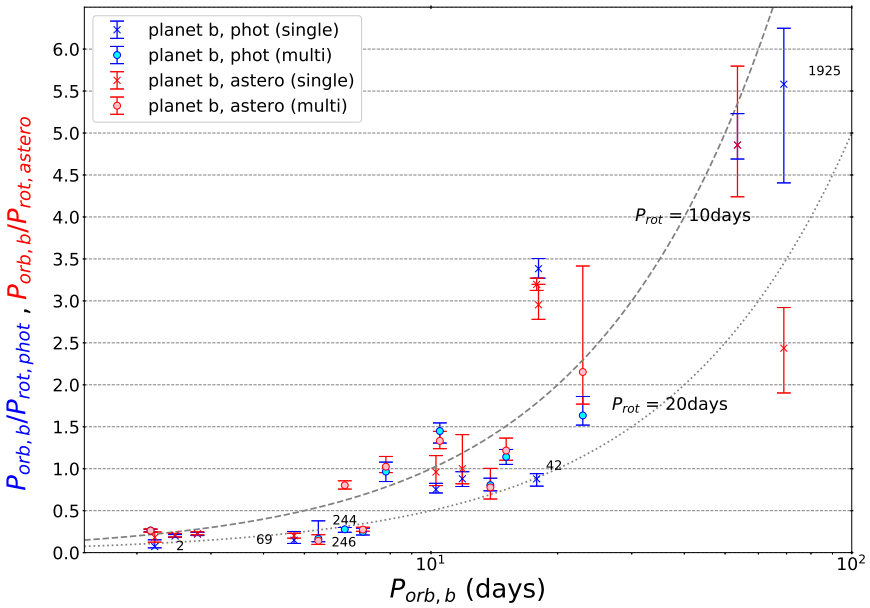

Figure A.1: $P_{\rm orb,b}/P_{\rm rot,photo}$ (blue symbols) and $P_{\rm orb,b}/P_{\rm rot,astero}$ (red symbols) against the transit period of the inner-most planet $P_{\rm orb,b}$ for 19 systems. Single- and multi-planet systems are plotted in crosses and circles, respectively. Just for reference, thick-dashed and thin-dotted lines correspond to $P_{\rm rot} = 10$ and 20 days, respectively.

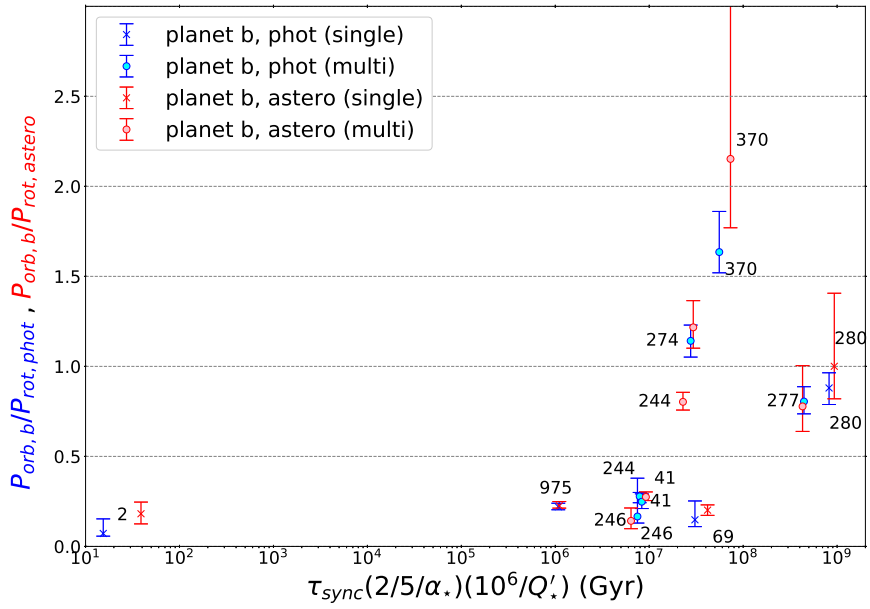

Figure A.2: $P_{\rm orb,b}/P_{\rm rot,photo}$ (blue) and $P_{\rm orb,b}/P_{\rm rot,astero}$ (red) against the synchronization time scale, equation (6.5). Single- and multi-planet systems are plotted in crosses and circles, respectively.

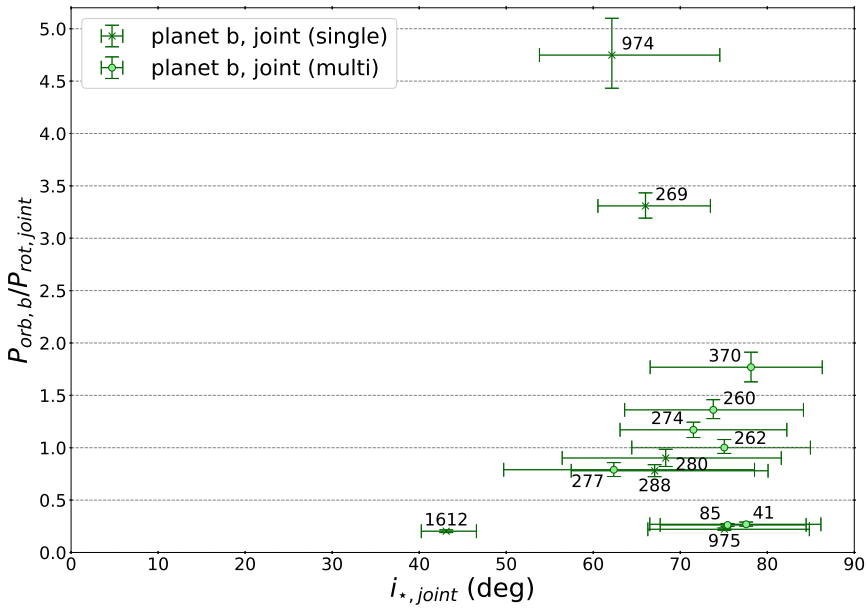

Figure A.3: $P_{\rm orb,b}/P_{\rm rot,joint}$ against $i_{\star,\rm joint}$ for 13 stars for which $P_{\rm rot,photo}$ and $P_{\rm rot,astero}$ are in good agreement. The stellar rotation period $P_{\rm rot,joint}$ and inclination angles $i_{\star,\rm joint}$ are calculated from the MCMC analysis of the asteroseismic data but using our photometrically-estimated value and errors of $P_{\rm rot,photo}$ as priors.

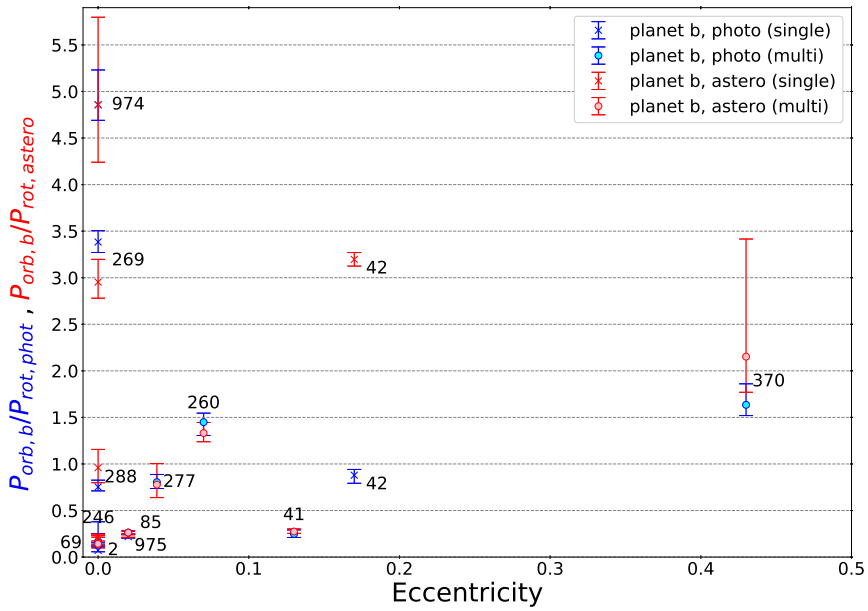

Figure A.4: $P_{\rm orb,b}/P_{\rm rot,photo}$ (blue symbols) and $P_{\rm orb,b}/P_{\rm rot,astero}$ (red symbols) against the orbital eccentricity of the inner-most planet for 19 systems. Single- and multi-planet systems are plotted in crosses and circles, respectively.

References

Agol, E., Steffen, J., Sari, R., & Clarkson, W. 2005, MNRAS, 359, 567

Albrecht, S., Winn, J. N., Johnson, J. A., et al. 2012, ApJ, 757, 18

Anderson, D. R., Hellier, C., Gillon, M., et al. 2010, ApJ, 709, 159

Anderson, D. R., Triaud, A. H. M. J., Turner, O. D., et al. 2015, ApJ, 800, L9

Anderson, E. R., Duvall, Jr., T. L., & Jefferies, S. M. 1990, ApJ, 364, 699

Angus, R., Morton, T., Aigrain, S., Foreman-Mackey, D., & Rajpaul, V. 2018, MNRAS, 474, 2094

Appourchaux, T., Samadi, R., & Dupret, M.-A. 2009, A&A, 506, 1

Appourchaux, T., Michel, E., Auvergne, M., et al. 2008, A&A, 488, 705

Appourchaux, T., Chaplin, W. J., García, R. A., et al. 2012a, A&A, 543, A54

Appourchaux, T., Benomar, O., Gruberbauer, M., et al. 2012b, A&A, 537, A134

Atchade, Y. F. 2006, arXiv Mathematics e-prints, math/0605452

Baglin, A., Auvergne, M., Barge, P., et al. 2006a, in ESA Special Publication, Vol. 1306, The CoRoT Mission Pre-Launch Status - Stellar Seismology and Planet Finding, ed. M. Fridlund, A. Baglin, J. Lochard, & L. Conroy, 33

Baglin, A., Auvergne, M., Boisnard, L., et al. 2006b, in COSPAR Meeting, Vol. 36, 36th COSPAR Scientific Assembly

Ballot, J., Appourchaux, T., Toutain, T., & Guittet, M. 2008, A&A, 486, 867

Ballot, J., Barban, C., & van't Veer-Menneret, C. 2011, A&A, 531, A124

Ballot, J., García, R. A., & Lambert, P. 2006, MNRAS, 369, 1281

Barban, C., Michel, E., Martic, M., et al. 1999, A&A, 350, 617

Barban, C., Deheuvels, S., Baudin, F., et al. 2009, A&A, 506, 51

Basu, S., Christensen-Dalsgaard, J., Schou, J., Thompson, M. J., & Tomczyk, S. 1996, Bulletin of the Astronomical Society of India, 24, 147

Bate, M. R., Lodato, G., & Pringle, J. E. 2010, MNRAS, 401, 1505

Batygin, K. 2012, Nature, 491, 418

Batygin, K., Morbidelli, A., & Tsiganis, K. 2011, A&A, 533, A7

Bazot, M., Bouchy, F., Kjeldsen, H., et al. 2007, A&A, 470, 295

Bazot, M., Ireland, M. J., Huber, D., et al. 2011, A&A, 526, L4

Beck, P. G., Montalban, J., Kallinger, T., et al. 2012, Nature, 481, 55

Bedding, T. H., & Kjeldsen, H. 1995, in Astronomical Society of the Pacific Conference Series, Vol. 83, IAU Colloq. 155: Astrophysical Applications of Stellar Pulsation, ed. R. S. Stobie & P. A. Whitelock, 109

Bedding, T. R., & Kjeldsen, H. 2003, pasa, 20, 203

Bedding, T. R., Butler, R. P., Kjeldsen, H., et al. 2001, ApJ, 549, L105

Benomar, O. 2013, in Astronomical Society of the Pacific Conference Series, Vol. 479, Progress in Physics of the Sun and Stars: A New Era in Helio- and Asteroseismology, ed. H. Shibahashi & A. E. Lynas-Gray, 161

Benomar, O., Appourchaux, T., & Baudin, F. 2009, A&A, 506, 15

Benomar, O., Baudin, F., Chaplin, W. J., Elsworth, Y., & Appourchaux, T. 2012, MNRAS, 420, 2178

Benomar, O., Masuda, K., Shibahashi, H., & Suto, Y. 2014, PASJ, 66, 94

Benomar, O., Takata, M., Shibahashi, H., Ceillier, T., & García, R. A. 2015, MNRAS, 452, 2654

Benomar, O., Bedding, T. R., Mosser, B., et al. 2013, ApJ, 767, 158

Benomar, O., Bazot, M., Nielsen, M. B., et al. 2018, Science, 361, 1231

Berger, T. A., Huber, D., Gaidos, E., & van Saders, J. L. 2018, ApJ, 866, 99

Bonanno, A., Benatti, S., Claudi, R., et al. 2008, ApJ, 676, 1248

Borucki, W. J., Koch, D., Basri, G., et al. 2010, Science, 327, 977

Bouchy, F., & Carrier, F. 2001, A&A, 374, L5

Bourrier, V., Lovis, C., Beust, H., et al. 2018, Nature, 553, 477

Broomhall, A.-M., Chaplin, W. J., Davies, G. R., et al. 2009, MNRAS, 396, L100

Brothwell, R. D., Watson, C. A., Hébrard, G., et al. 2014, MNRAS, 440, 3392

Brown, T. M., Charbonneau, D., Gilliland, R. L., Noyes, R. W., & Burrows, A. 2001, ApJ, 552, 699

Brown, T. M., Gilliland, R. L., Noyes, R. W., & Ramsey, L. W. 1991, ApJ, 368, 599

Bruntt, H., Basu, S., Smalley, B., et al. 2012, MNRAS, 423, 122

Buchhave, L. A., Latham, D. W., Johansen, A., et al. 2012, Nature, 486, 375

Campante, T. L., Lund, M. N., Kuszlewicz, J. S., et al. 2016, ApJ, 819, 85

Casagrande, L., Silva Aguirre, V., Schlesinger, K. J., et al. 2016, MNRAS, 455, 987

Chaplin, W. J., Houdek, G., Appourchaux, T., et al. 2008, A&A, 485, 813

Chaplin, W. J., Houdek, G., Karoff, C., Elsworth, Y., & New, R. 2009, A&A, 500, L21

Chaplin, W. J., & Miglio, A. 2013, ARA&A, 51, 353

Chaplin, W. J., Kjeldsen, H., Christensen-Dalsgaard, J., et al. 2011, Science, 332, 213

Chaplin, W. J., Sanchis-Ojeda, R., Campante, T. L., et al. 2013, ApJ, 766, 101

Chatterjee, S., Ford, E. B., Matsumura, S., & Rasio, F. A. 2008, ApJ, 686, 580

Correia, A. C. M., Laskar, J., Farago, F., & Boué, G. 2011, Celestial Mechanics and Dynamical Astronomy, 111, 105

Corsaro, E., Lee, Y.-N., García, R. A., et al. 2017, Nature Astronomy, 1, 0064

Damasso, M., Biazzo, K., Bonomo, A. S., et al. 2015, A&A, 575, A111

Davies, G. R., Chaplin, W. J., Farr, W. M., et al. 2015, MNRAS, 446, 2959

Davies, G. R., Silva Aguirre, V., Bedding, T. R., et al. 2016, MNRAS, 456, 2183

Dawson, R. I. 2014, ApJ, 790, L31

Deheuvels, S., Ballot, J., Beck, P. G., et al. 2015, A&A, 580, A96

Deheuvels, S., Bruntt, H., Michel, E., et al. 2010, A&A, 515, A87

Deheuvels, S., García, R. A., Chaplin, W. J., et al. 2012, ApJ, 756, 19

Deheuvels, S., Doğan, G., Goupil, M. J., et al. 2014, A&A, 564, A27

Deubner, F.-L. 1975, A&A, 44, 371

Duvall, Jr., T. L., & Harvey, J. W. 1986, in NATO Advanced Science Institutes (ASI) Series C, Vol. 169, NATO Advanced Science Institutes (ASI) Series C, ed. D. O. Gough, 105–116

Esposito, M., Covino, E., Desidera, S., et al. 2017, A&A, 601, A53

Evans, J. W., & Michard, R. 1962, ApJ, 136, 493

Fabrycky, D., & Tremaine, S. 2007, ApJ, 669, 1298

Fabrycky, D. C., & Winn, J. N. 2009, ApJ, 696, 1230

Feroz, F., Hobson, M. P., & Bridges, M. 2009, MNRAS, 398, 1601

Fielding, D. B., McKee, C. F., Socrates, A., Cunningham, A. J., & Klein, R. I. 2015, MNRAS, 450, 3306

Fukuda, Y., Hayakawa, T., Ichihara, E., et al. 1998, Physical Review Letters, 81, 1562

García, R. A., Jiménez-Reyes, S. J., Turck-Chièze, S., Ballot, J., & Henney, C. J. 2004, in ESA Special Publication, Vol. 559, SOHO 14 Helio- and Asteroseismology: Towards a Golden Future, ed. D. Danesy, 436

García, R. A., Régulo, C., Samadi, R., et al. 2009, A&A, 506, 41

García, R. A., Ceillier, T., Salabert, D., et al. 2014, A&A, 572, A34

Gaulme, P., Schmider, F.-X., Gay, J., Guillot, T., & Jacob, C. 2011, A&A, 531, A104

Gaulme, P., Rowe, J. F., Bedding, T. R., et al. 2016, ApJ, 833, L13

Gilliland, R. L., Jenkins, J. M., Borucki, W. J., et al. 2010, ApJ, 713, L160

Gizon, L., & Solanki, S. K. 2003, ApJ, 589, 1009

Gizon, L., Sekii, T., Takata, M., et al. 2016, Science Advances, 2, e1601777

Goldreich, P., & Keeley, D. A. 1977, ApJ, 212, 243

Gregory, P. C. 2005, ApJ, 631, 1198

Handberg, R., & Campante, T. L. 2011, A&A, 527, A56

Handberg, R., & Lund, M. N. 2014, MNRAS, 445, 2698

Hansen, B. M. S., & Zink, J. 2015, MNRAS, 450, 4505

Harvey, J. 1985, in ESA Special Publication, Vol. 235, Future Missions in Solar, Heliospheric & Space Plasma Physics, ed. E. Rolfe & B. Battrick

Hayashi, C., Nakazawa, K., & Nakagawa, Y. 1985, in Protostars and Planets II, ed. D. C. Black & M. S. Matthews, 1100–1153

Hébrard, G., Evans, T. M., Alonso, R., et al. 2011, A&A, 533, A130

Hellier, C., Anderson, D. R., Collier-Cameron, A., et al. 2011, ApJ, 730, L31

Hirano, T., Sanchis-Ojeda, R., Takeda, Y., et al. 2012, ApJ, 756, 66

—. 2014, ApJ, 783, 9

Hirano, T., Suto, Y., Winn, J. N., et al. 2011, ApJ, 742, 69

Holman, M. J., & Murray, N. W. 2005, Science, 307, 1288

Holt, J. R. 1893, Astronomy and Astro-Physics (formerly The Sidereal Messenger), 12, 646

Howard, A. W. 2013, Science, 340, 572

Huber, D. 2016, ArXiv e-prints, arXiv:1604.07442

Huber, D., Carter, J. A., Barbieri, M., et al. 2013a, Science, 342, 331

Huber, D., Chaplin, W. J., Christensen-Dalsgaard, J., et al. 2013b, ApJ, 767, 127

Johnson, J. A., Winn, J. N., Bakos, G. Á., et al. 2011, ApJ, 735, 24

Johnson, J. A., Petigura, E. A., Fulton, B. J., et al. 2017, AJ, 154, 108

Kamiaka, S., Benomar, O., & Suto, Y. 2018, MNRAS, 479, 391

Kamiaka, S., Benomar, O., Suto, Y., et al. 2019, accepted in AJ

Karoff, C., Campante, T. L., Ballot, J., et al. 2013, ApJ, 767, 34

Kolmogorov, A. 1941a, Akademiia Nauk SSSR Doklady, 30, 301

Kolmogorov, A. N. 1941b, Akademiia Nauk SSSR Doklady, 32, 16

Kovacs, G. 2018, A&A, 612, L2

Kozai, Y. 1962, AJ, 67, 591

Kraft, R. P. 1967, ApJ, 150, 551

Kurtz, D. W., Saio, H., Takata, M., et al. 2014, MNRAS, 444, 102

Lai, D. 2012, MNRAS, 423, 486

Lai, D., Anderson, K. R., & Pu, B. 2018, MNRAS, 475, 5231

Lai, D., Foucart, F., & Lin, D. N. C. 2011, MNRAS, 412, 2790

Landin, N. R., Mendes, L. T. S., & Vaz, L. P. R. 2010, A&A, 510, A46

Leavitt, H. S., & Pickering, E. C. 1912, Harvard College Observatory Circular, 173, 1

Leibacher, J. W., & Stein, R. F. 1971, Astrophys. Lett., 7, 191

Leighton, R. B., Noyes, R. W., & Simon, G. W. 1962, ApJ, 135, 474

Lendl, M., Triaud, A. H. M. J., Anderson, D. R., et al. 2014, A&A, 568, A81

Lin, D. N. C., & Ida, S. 1997, ApJ, 477, 781

Lomb, N. R. 1976, Ap&SS, 39, 447

Lund, M. N., Miesch, M. S., & Christensen-Dalsgaard, J. 2014a, ApJ, 790, 121

Lund, M. N., Lundkvist, M., Silva Aguirre, V., et al. 2014b, A&A, 570, A54

Lund, M. N., Silva Aguirre, V., Davies, G. R., et al. 2017, ApJ, 835, 172

Lurie, J. C., Vyhmeister, K., Hawley, S. L., et al. 2017, AJ, 154, 250

Mancini, L., Esposito, M., Covino, E., et al. 2015, A&A, 579, A136

—. 2018, A&A, 613, A41

Mandel, K., & Agol, E. 2002, ApJ, 580, L171

Marcy, G. W., Isaacson, H., Howard, A. W., et al. 2014, ApJS, 210, 20

Mayor, M., & Queloz, D. 1995, Nature, 378, 355

Mayor, M., Pepe, F., Queloz, D., et al. 2003, The Messenger, 114, 20

Mazeh, T., Krymolowski, Y., & Rosenfeld, G. 1997, ApJ, 477, L103

Mazeh, T., Perets, H. B., McQuillan, A., & Goldstein, E. S. 2015, ApJ, 801, 3

McLaughlin, D. B. 1924, ApJ, 60, doi:10.1086/142826

McQuillan, A., Mazeh, T., & Aigrain, S. 2013, ApJ, 775, L11

—. 2014, ApJS, 211, 24

Metcalfe, T. S., Chaplin, W. J., Appourchaux, T., et al. 2012, ApJ, 748, L10

Metcalfe, T. S., Creevey, O. L., Doğan, G., et al. 2014, ApJS, 214, 27

Miglio, A., Chaplin, W. J., Brogaard, K., et al. 2016, MNRAS, 461, 760

Miglio, A., Chiappini, C., Mosser, B., et al. 2017, Astronomische Nachrichten, 338, 644

Molenda-Żakowicz, J., Sousa, S. G., Frasca, A., et al. 2013, MNRAS, 434, 1422

Mosser, B., Michel, E., Belkacem, K., et al. 2013, A&A, 550, A126

Mosser, B., Benomar, O., Belkacem, K., et al. 2014, A&A, 572, L5

Mosser, B., Belkacem, K., Pinçon, C., et al. 2017, A&A, 598, A62

Muñoz, D. J., & Perets, H. B. 2018, ArXiv e-prints, arXiv:1805.03654

Murray, C. D., & Dermott, S. F. 2000, Solar System Dynamics

Nagasawa, M., Ida, S., & Bessho, T. 2008, ApJ, 678, 498

Naoz, S., Farr, W. M., Lithwick, Y., Rasio, F. A., & Teyssandier, J. 2011, Nature, 473, 187

Narita, N., Sato, B., Hirano, T., & Tamura, M. 2009, PASJ, 61, L35

Nielsen, M. B., Schunker, H., Gizon, L., & Ball, W. H. 2015, A&A, 582, A10

Nielsen, M. B., Schunker, H., Gizon, L., Schou, J., & Ball, W. H. 2017, A&A, 603, A6

Ohta, Y., Taruya, A., & Suto, Y. 2005, ApJ, 622, 1118

Paxton, B., Bildsten, L., Dotter, A., et al. 2011, ApJS, 192, 3

Paxton, B., Cantiello, M., Arras, P., et al. 2013, ApJS, 208, 4

Paxton, B., Marchant, P., Schwab, J., et al. 2015, ApJS, 220, 15

Paxton, B., Schwab, J., Bauer, E. B., et al. 2018, ApJS, 234, 34

Petigura, E. A., Howard, A. W., Marcy, G. W., et al. 2017, AJ, 154, 107

Petrovich, C., Deibert, E., & Wu, Y. 2018, ArXiv e-prints, arXiv:1804.05065

Ragazzoni, R., Magrin, D., Rauer, H., et al. 2016, in Proc. SPIE, Vol. 9904, Space Telescopes and Instrumentation 2016: Optical, Infrared, and Millimeter Wave, 990428

Rasio, F. A., & Ford, E. B. 1996, Science, 274, 954

Rogers, T. M., & Lin, D. N. C. 2013, ApJ, 769, L10

Rogers, T. M., Lin, D. N. C., & Lau, H. H. B. 2012, ApJ, 758, L6

Rossiter, R. A. 1924, ApJ, 60, doi:10.1086/142825

Salabert, D., Ballot, J., & García, R. A. 2011, A&A, 528, A25

Sanchis-Ojeda, R., Winn, J. N., Marcy, G. W., et al. 2013, ApJ, 775, 54

Scargle, J. D. 1982, ApJ, 263, 835

Schlaufman, K. C. 2010, ApJ, 719, 602

Schlesinger, F. 1910, Publications of the Allegheny Observatory of the University of Pittsburgh, 1, 123

Schou, J., Antia, H. M., Basu, S., et al. 1998, ApJ, 505, 390

Scott, D. W. 1992, Multivariate Density Estimation

Silva Aguirre, V., Davies, G. R., Basu, S., et al. 2015, MNRAS, 452, 2127

Silva Aguirre, V., Lund, M. N., Antia, H. M., et al. 2017, ApJ, 835, 173

Sonoi, T., Samadi, R., Belkacem, K., et al. 2015, A&A, 583, A112

Southworth, J. 2011, ArXiv e-prints, arXiv:1108.2976

Suto, Y., Kamiaka, S., & Benomar, O. 2019, submitted to AJ

Takada-Hidai, M., Kurtz, D. W., Shibahashi, H., et al. 2017, MNRAS, 470, 4908

Tamayo, D., Triaud, A. H. M. J., Menou, K., & Rein, H. 2015, ApJ, 805, 100

Tassoul, M. 1980, ApJS, 43, 469

—. 1990, ApJ, 358, 313

Thies, I., Kroupa, P., Goodwin, S. P., Stamatellos, D., & Whitworth, A. P. 2011, MNRAS, 417, 1817

Thompson, M. J., Christensen-Dalsgaard, J., Miesch, M. S., & Toomre, J. 2003, ARA&A, 41, 599

Thompson, S. E., Coughlin, J. L., Hoffman, K., et al. 2018, ApJS, 235, 38

Toutain, T., & Froehlich, C. 1992, A&A, 257, 287

Toutain, T., & Gouttebroze, P. 1993, A&A, 268, 309

Triaud, A. H. M. J. 2017, The Rossiter-McLaughlin Effect in Exoplanet Research, 2

Triaud, A. H. M. J., Collier Cameron, A., Queloz, D., et al. 2010, A&A, 524, A25

Ulrich, R. K. 1970, ApJ, 162, 993

—. 1986, ApJ, 306, L37

Valenti, J. A., & Fischer, D. A. 2005, ApJS, 159, 141

Van Eylen, V., Albrecht, S., Huang, X., et al. 2018, ArXiv e-prints, arXiv:1807.00549

Walker, G., Matthews, J., Kuschnig, R., et al. 2003, PASP, 115, 1023

Weidenschilling, S. J., & Marzari, F. 1996, Nature, 384, 619

White, T. R., Bedding, T. R., Gruberbauer, M., et al. 2012, ApJ, 751, L36

Winn, J. N. 2010, ArXiv e-prints, arXiv:1001.2010

Winn, J. N., Fabrycky, D., Albrecht, S., & Johnson, J. A. 2010a, ApJ, 718, L145

Winn, J. N., & Fabrycky, D. C. 2015, ARA&A, 53, 409

Winn, J. N., Johnson, J. A., Albrecht, S., et al. 2009, ApJ, 703, L99

Winn, J. N., Johnson, J. A., Howard, A. W., et al. 2010b, ApJ, 723, L223

Winn, J. N., Howard, A. W., Johnson, J. A., et al. 2011, AJ, 141, 63

Winn, J. N., Sanchis-Ojeda, R., Rogers, L., et al. 2017a, AJ, 154, 60

Winn, J. N., Petigura, E. A., Morton, T. D., et al. 2017b, AJ, 154, 270

Xue, Y., Suto, Y., Taruya, A., et al. 2014, ApJ, 784, 66

Yee, S. W., Petigura, E. A., Fulton, B. J., et al. 2018, AJ, 155, 255

Zahn, J.-P. 1977, A&A, 57, 383

—. 1989, A&A, 220, 112